Organization and scaling of coherent structures in the outer region of high-Reynolds-number turbulent boundary layers

A DISSERTATION
SUBMITTED TO THE FACULTY OF THE
UNIVERSITY OF MINNESOTA
BY

Michael Heisel

IN PARTIAL FULFILLMENT OF THE REQUIREMENTS
FOR THE DEGREE OF
DOCTOR OF PHILOSOPHY

Michele Guala

May 2020

Acknowledgements

Perhaps contrary to the spirit of a dissertation, my doctoral thesis research was not the outcome of a singular individual effort. The name on the cover and the words on the following pages are my own, but this thesis is the outcome of collective contributions from many wonderful colleagues. Foremost to thank is my advisor Professor Michele Guala. Beyond the mechanics of how to conduct experiments, he taught me how to approach turbulence research as an art in order to untangle meaning from the chaos. He also spent countless hours providing feedback and guidance, and is most responsible for my development as a researcher. To encapsulate my feelings I must invoke the words of Tina Turner: *you're simply the best, better than all the rest*.

The experiments presented here, and those not included in the thesis, were conducted at St. Anthony Falls Laboratory (SAFL). The construction and setup of the experiments in many cases were carried out by the skillful engineering staff at SAFL. Specifically, my work was directly or indirectly facilitated by Chris Feist, Chris Milliren, Dr. Chris Ellis, Jim Tucker, Erik Steen, Aaron Ketchmark, and Ben Erickson. They spared me from scrapes and bruises and prevented further destruction of the wind tunnel facility. I would also like to thank the IT staff (Charles Nguyen, Patrick Arnold, Matt Jansen, among others) for their help with all things computer, including maintenance of the high-performance computing resources used for data processing.

My research was continuously advanced through the input of several faculty at the University of Minnesota. Professors Jiarong Hong and Filippo Coletti provided insight as co-investigators on the atmospheric study during both group meetings and independent conversations. I am grateful to Drs. Hong and Coletti, in addition to Professors Vaughan Voller and Ellen Longmire, for serving on my doctoral exam committee and providing valuable feedback to this work.

I have benefited from several rewarding relationships outside of Minnesota. Much of my thesis relies on the output of a collaboration with the University of Melbourne. I am grateful to Professors Charitha de Silva, Nicholas Hutchins, and Ivan Marusic for contributing their time, experimental data, and expertise to help bring this work to fruition. I would also like to thank Professor Gabriel Katul of Duke University for his mentorship. While the findings of our ongoing collaboration are not represented in this thesis, Dr. Katul has been invaluable to the development of my future research goals and professional career.

Finally, and this work would not have been possible without sponsorship. The following organizations have funded my various research projects as a graduate student: the National Science Foundation, the Institute on the Environment, the Minnesota Department of Transportation, and the Graduate School at the University of Minnesota.

Dedication

to Papa Bear

Abstract

Recent advances in high-Reynolds-number turbulence have suggested there is a general self-organization of coherent structures in the logarithmic and wake regions of boundary layer flows. The organization comprises large-scale velocity structures known as uniform momentum zones (UMZs) separated by thin internal shear layers (ISLs). While the velocity structures have been extensively studied in more specific forms such as momentum streaks, streamwise rolls, and bulges, the shear layers have received less attention outside the context of the hairpin packet paradigm. In the present thesis, the universality of this self-organization is evaluated using a novel field-scale particle image velocimetry (PIV) experiment in the logarithmic region of the atmospheric surface layer. The field measurements are validated using collocated sonic anemometry. The experiment reveals the same organization of UMZs and ISLs occurs for atmospheric flows. The properties of the UMZs and ISLs are then compared using ten PIV experiments and a direct numerical simulation, which together span a wide range of surface roughness and three orders of magnitude in Reynolds number. The UMZs unambiguously scale with the friction velocity and wall-normal distance in the logarithmic region, regardless of Reynolds number and surface roughness. The scaling behavior is in agreement with Prandtl's mixing length theory and Townsend's attached eddy hypothesis. The results show that the hypothetical eddies of the logarithmic law of the wall manifest in the structural organization of the flow. Separate analysis focusing on the smaller structures shows that the ISLs and large vortices are both governed by the friction velocity and Taylor microscale. Preliminary evidence suggests these ISL and vortex scaling behaviors both result from mutual interaction with the local large-scale UMZs, possibly through a stretching mechanism. Additional experiments in three dimensions are required to verify the dynamics. The overall findings support the universality of large-scale structures in the outer region and provide promising clues for better understanding scale interaction and energy transfer mechanisms.

Table of contents

List of tables

List of figures

Nomenclature

The standard meteorological coordinate system is used in this text. The position in the direction of the flow (i.e. streamwise position) is given by x, the position transverse to the flow (i.e. spanwise) is y, and the distance from the wall (i.e. wall-normal position) is z. The flow velocity in the streamwise, spanwise, and wall-normal directions are given by u, v, and w, respectively. Velocities are decomposed as $u = U + u'$ where lowercase (u, v, w) is the total velocity, uppercase (U, V, W) is the ensemble average, and prime (u', v', w') is the fluctuation from the mean. In general, lower-case lettering is used for the instantaneous value of a variable and upper-case lettering is used for the mean. The mean value is also indicated by overbars ($\overline{\cdot}$) or angled brackets ($\langle\cdot\rangle$). Finally, the superscript "+" indicates normalization in viscous units, e.g. $x^+ = xu_\tau/\nu$ or $u^+ = u/u_\tau$ with u_τ and ν defined below.

The following non-comprehensive lists provide the abbreviations and notation used most frequently throughout the thesis text. These definitions also appear at the first usage of each abbreviation or variable. In a small number of cases, the same notation is used for multiple variables of lesser importance, e.g. pressure and probability density both given by p. The duplicity in notation does not occur within the same chapter and the relevant definition is specified where necessary.

Abbreviations

ABL	atmospheric boundary layer
AEH	attached eddy hypothesis
ASL	atmospheric surface layer
DNS	direct numerical simulation
FOV	field of view
ISL	internal shear layer
pdf	probability density function
rms	root mean square of deviations from the mean
PIV	particle image velocimetry
SAFL	St. Anthony Falls Laboratory
SLPIV	super-large-scale particle image velocimetry
TNTI	turbulent/non-turbulent interface
UMZ	uniform momentum zone

Standard notation

k_s	equivalent sandgrain roughness
L	integral length scale
ℓ_e	characteristic eddy length scale
Re_τ	friction Reynolds number
Ri_f	flux Richardson number
S	mean velocity gradient $\partial U/\partial z$
St	Stokes number
T	large eddy turnover time scale
u_e	characteristics eddy velocity scale
u_{rms}	streamwise root-mean-squared velocity
u_η	Kolmogorov velocity scale
u_τ	friction velocity scale
w_I	interrogation window size for particle image velocimetry
Δx	vector spacing in particle image velocimetry fields
z_o	aerodynamic roughness length
α	strain rate
δ	average boundary layer thickness
δ_{SL}	atmospheric surface layer thickness
ϵ	turbulent kinetic energy dissipation rate
η	Kolmogorov length scale
κ	von Kármán constant
λ_{ci}	swirling strength
λ_T	Taylor microscale (length scale)
ν	fluid kinematic viscosity

ρ	fluid density
σ	standard deviation
ω_y	spanwise vorticity

Uniform momentum zone properties

h_m, H_m	wall-normal thickness (instantaneous, mean)
ℓ_m, L_m	streamwise length (instantaneous, mean)
$\mathcal{L}_x$	streamwise distance contributing to momentum zone detection
u_m, U_m	modal velocity (instantaneous, mean)
ΔU_m	velocity difference across the shear layer between adjacent momentum zones (mean)
z_m	wall-normal midheight

Internal shear layer properties

u_i, U_i	streamwise advection velocity (instantaneous, mean)
w_i, W_i	wall-normal advection velocity (instantaneous, mean)
z_i	wall-normal midheight
δ_ω	average thickness (notation following the vorticity thickness)

Spanwise vortex properties

d_ω, D_ω	diameter (instantaneous, mean)
u_ω, U_ω	streamwise advection velocity (instantaneous, mean)
$\Delta u_\omega, \Delta U_\omega$	azimuthal velocity difference across the vortex diameter (instantaneous, mean)
w_ω, W_ω	wall-normal advection velocity (instantaneous, mean)
x_ω	streamwise center position
z_ω	wall-normal center position

1 Introduction

We are surrounded by turbulence, even if we do not pay much attention to it. More specifically, we live in a turbulent boundary layer, the lower part of the atmosphere where the wind interacts with the Earth's surface. The turbulent air is not readily seen, owing to its transparency, unless it has a visual aid such as a frosty breath during a frigid Minnesota winter. The seemingly random swirling eddies often used to describe turbulence are more apparent on water surfaces as depicted in Leonardo da Vinci's sketch in figure 1.

From da Vinci's early illustrations of turbulence circa 1500 to the present, scientists have grown to appreciate the importance of turbulent fluids in our lives, where air and water are the most common fluids. A running example in this text will be the aforementioned atmospheric boundary layer, though turbulent boundary layers are ubiquitous in environmental and engineering applications including pipeline infrastructure (Moody 1944), naval shipping (Prandtl & Schlichting 1934), aeronautics (Anderson 2016), river channel hydraulics (Chow 1959), and marine ecosystems (Thorpe 2005). Just within the ABL example, there are several research sub-topics of practical importance. For instance, atmospheric turbulence affects the performance and lifetime of wind turbine farms (Stevens & Meneveau 2017), imposes non-stationary loads on buildings and structures (Simiu & Yeo 2019), disperses source pollutants such as car exhaust (Nicholson 1975), and enhances the exchange of heat and water between the earth surface and the atmosphere (Brutsaert 1982). The summation of local turbulence effects related to heat, water, and wind contribute to weather and climate at the regional and global scales (Hartmann 2016).

Having expressed the importance of the turbulent boundary layers, it is now prudent to provide a proper definition for *turbulence*, *boundary layer* and other basic concepts of the research topic. Note that a satisfactory definition of turbulence has eluded scientists for centuries and the definition provided here may be better classified as a qualitative description. Following these definitions, the research goals are given to introduce the questions addressed in the remaining chapters of the thesis.

Figure 1. A sketch by Leonardo da Vinci circa 1500 of a water jet flowing into a turbulent pool, from his notebook *Codex Leicester* (Laurenza & Kemp 2019).

1.1 What is turbulence?[1]

Turbulence ultimately results from the physical laws governing the movement of a fluid, which are remarkably simple given the complexity of the result. One law is the conservation of mass. If the fluid is incompressible, i.e. if the density ρ is constant as in this research, the conservation law simplifies to the continuity equation:

$$\nabla \cdot \mathbf{u} = 0, \tag{1}$$

where $\mathbf{u}$ is the velocity vector and $\nabla \cdot$ is the divergence with vector gradient operator ∇ and inner product "$\cdot$". Equation (1) states that any flow region must have an equal amount of fluid entering and exiting the region at a given time. Another law is Newton's second law of motion $\mathbf{F} = m\mathbf{a}$ which relates the net force $\mathbf{F}$ on a region "parcel" of fluid to its acceleration $\mathbf{a}$ (Newton 1687). Evaluation of the acceleration and internal forces yields the Navier-Stokes equations (Navier 1821; Stokes 1845):

$$\underset{\text{(I)}}{\frac{\partial \mathbf{u}}{\partial t}} \;+\; \underset{\text{(II)}}{(\mathbf{u}\cdot\nabla)\,\mathbf{u}} \;=\; \underset{\text{(III)}}{-\frac{1}{\rho}\nabla p} \;+\; \underset{\text{(IV)}}{\nu\nabla^2\mathbf{u}} \;+\; \underset{\text{(V)}}{\mathbf{f}_{ext}}. \tag{2}$$

Here, p is the pressure, ν is the kinematic viscosity, and $\mathbf{f}_{ext}$ is an external force per unit mass. The new operators are the partial derivative $\frac{\partial}{\partial t}$ with respect to time t and the Laplacian ∇^2. The first term (I) represents storage of momentum (temporal acceleration), (II) is the advection of momentum (spatial acceleration), (III) acts to redistribute momentum through the pressure field (distribution of force across a pressure gradient), (IV) acts to diffuse momentum by viscosity (smooth the velocity differences through viscous shear stresses), and (V) represents any external forces acting on the fluid including gravity. The viscous term (IV) used here is specific to Newtonian fluids, and results from Newton's law of viscosity $\tau = \rho\nu\nabla\mathbf{u}$, where τ is the shear stress. While the Navier-Stokes equations strictly describe the conservation of momentum within the fluid continuum, it is conceptually useful to consider each term in the framework of force and acceleration as given in parentheses above.

From Poisson's equation relating the pressure to the velocity field, it is known that the pressure and advective terms (II,III) have similar magnitude. The response of the fluid to an external perturbation (i.e. a small, disruptive force) then depends on the relative magnitude of the viscous term (IV). Two scenarios are depicted in the figure 2 cartoon. If the viscous term is greater, the velocity difference imposed by the external force is dampened faster than it can advect and grow. If the viscosity is too small, the perturbation advects and grows as an instability. Because the advection is non-linear, the perturbation from the base flow similarly grows non-linearly, affecting the surrounding flow and eventually leading to unsteady conditions known as turbulence throughout the flow geometry. From this description, a generic definition for turbulence emerges,

---

[1] This section is based on my accumulated knowledge from graduate courses and research texts. The ideas draw most heavily from the introductory chapters of the textbooks sitting at my desk: Monin & Yaglom (1971); Schlichting & Gersten (1999); Pope (2000); Davidson (2015). Additional references are cited where appropriate.

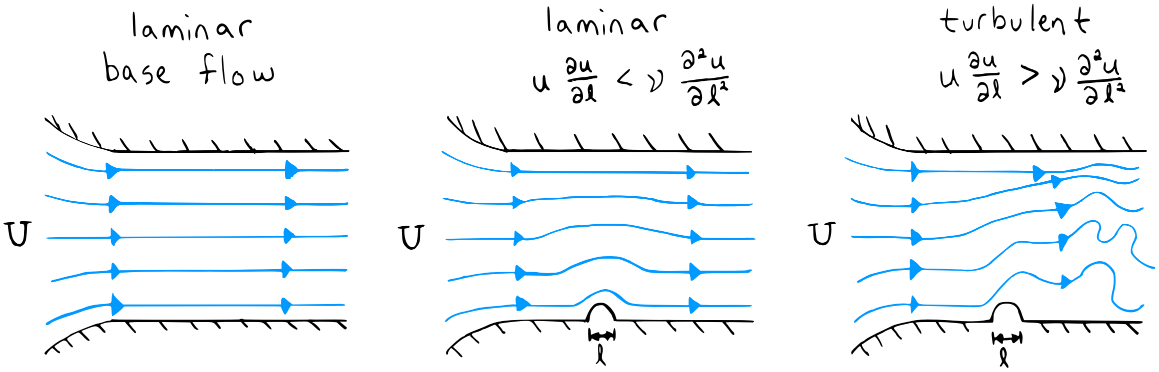

Figure 2. A cartoon of laminar flow streamlines perturbed by an obstacle: (*left*) the base flow; (*middle*) perturbed flow remaining laminar; (*right*) perturbed flow becoming turbulent.

adapted from Davidson (2015):

> Turbulence is the spatially complex distribution of fluid motion that propagates in a non-linear and chaotic manner, changing in both space and time.

There are certainly more attributes of turbulent flows, but at some point a (admittedly ambiguous) distinction must be made between a characteristic and a defining feature. Among other characteristics of turbulence, the fluid velocities are three dimensional and rotational, and the viscosity continuously works to diffuse the momentum and dissipate the turbulent kinetic energy. Turbulence will decay and the flow re-laminarizes in the absence of energy supply (Tennekes & Lumley 1972).

Returning to the figure 2 cartoon, the competing terms can be compared using dimensional analysis. The advective and pressure terms scale as $\mathbf{u} \cdot \partial \mathbf{u}/\partial \mathbf{x} \sim u^2/\ell$ and the viscous term scales as $\nu\, \partial^2 \mathbf{u}/\partial \mathbf{x}^2 \sim \nu u/\ell^2$, where u and ℓ are a characteristic velocity and length, respectively[2]. The ratio of the terms yields the Reynolds number $Re = u\ell/\nu$, which characterizes the relative importance of advective and diffusive (or inertial and viscous) effects (Stokes 1851; Reynolds 1883). The flow is turbulent if the Reynolds number is large ($Re \gg 1$) and any small perturbation is present to disrupt the flow. In practice, the vast majority of flows are turbulent; air and water have low viscosities leading to large Reynolds numbers, and disruptions due to imperfections (e.g. surface roughness, temperature gradient, unsteady inflow conditions) are ubiquitous outside of specially designed facilities.

In theory, equations (1) and (2) form a deterministic system. There are four unknown quantities (u, v, w, p) and four equations (the continuity equation and one Navier-Stokes expression each for x, y, and z directions). *A priori* knowledge of the initial conditions and all external forces allows for calculation of future flow fields. However, the computational resources required to fully resolve any atmospheric flow is well beyond current capabilities, and more importantly, the initial conditions and external forces are never perfectly known. To the second point, any infinitesimal error in the initial condition grows non-linearly, quickly making future predictions inaccurate. For this reason, the instantaneous solution to a turbulent flow is considered chaotic and unpredictable in practice (Manneville 2010).

---

[2] Throughout the text, "$\sim$" means "scales with" such that the two terms have the same order of magnitude.

To circumvent the chaos, turbulent flows are often treated statistically in an attempt to solve for the mean, standard deviation, covariance, or other statistics rather than each instantaneous flow realization (Monin & Yaglom 1971). Most commonly, the Reynolds decomposition treats the mean velocity $\mathbf{U}$ and deviations from the mean $\mathbf{u}'$ separately as $\mathbf{u} = \mathbf{U} + \mathbf{u}'$ prior to averaging the governing equations (Reynolds 1895). While this approach has led to many advances in our understanding of turbulence, it also introduces a new problem of closure: there are always more unknown statistical variables than statistical equations such that the equations cannot be solved directly. This is due to the dastardly non-linear advective term in equation (2) which creates a new unknown variable when the equation is Reynolds decomposed and averaged. The workaround to the closure problem is the aptly named "closure model" which uses a semi-empirical expression to relate two of the unknown statistics (Boussinesq 1887; Durbin 2018). The model replaces an unknown statistic to close the system of equations, where experimental data are often used to tune any model parameter(s). This modeling approach to problems in turbulence motivates the primary question for future expansion of this thesis work: *how can the present results be leveraged to inform and improve turbulence modeling tools?*

1.2 What is a boundary layer?

Thankfully, it is easier to define *boundary layer* than *turbulence*. Consider the simple case of a fluid moving parallel to a wall as depicted in the figure 3 cartoon. Friction along the wall exerts a shear stress τ_w on the fluid, where τ_w is a function of the fluid viscosity, velocity U_∞ and the surface properties (e.g. roughness). The wall stress retards the fluid, and in most cases it is valid to assume a no-slip condition where the fluid at the wall adheres to the surface and does not move relative to it (Schlichting & Gersten 1999). The wall therefore imposes a velocity difference equal to U_∞ between flow at the wall and the unobstructed flow. From the Navier-Stokes equations, we know the viscosity will diffuse the velocity difference, and thus the shear stress τ, away from the wall. The result is a distribution of the velocity and shear stress, where the velocity profile resembles that shown in figure 3. The definition of the boundary layer is directly related to the region where the effect of viscosity is felt:

> The boundary layer is the fluid region near to a surface where the velocity deficit and shear stress are non-negligible due to the effects of viscosity.

This concept of a boundary layer was first introduced by Ludwig Prandtl (1904) and was slow to gain acceptance outside of Prandtl's research group until the 1920's (Tani 1977).

Typically, the free-stream condition above the boundary layer is approximately laminar. The flow within the boundary layer can be either laminar or turbulent based on the Reynolds number and perturbations as previously discussed, but only turbulent boundary layers are studied here. Specifically, the boundary layers in the present research have an approximately zero-pressure-gradient free-stream condition, as opposed to internal flows such as pipe flow that have a positive pressure gradient. The bulk mean velocity difference "supplies" energy to sustain the turbulence. This flow case is known as *shear-driven* turbulence.

In addition to the diffusion of momentum by viscosity, in a turbulent boundary layer the vertical motions

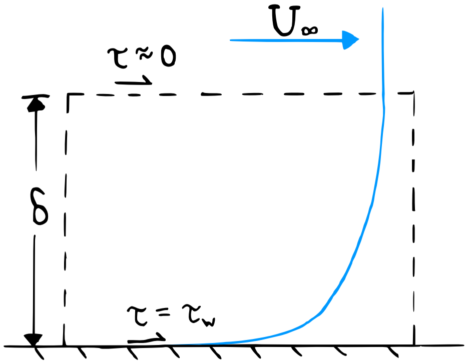

Figure 3. A cartoon of a boundary layer formed by flow over a wall. The boundary layer is the region of thickness δ above the wall where the wall shear stress τ_{w} is felt by the fluid.

also transfer momentum. For instance, when a turbulent motion high in the boundary layer carries a fast-moving parcel downward into a lower-speed region, the momentum at the new position is increased. The average transport (flux) of momentum due to turbulence is given by the covariance $\rho\overline{u'w'}$. The covariance is always negative because, on average, momentum is transferred downward toward the wall. The momentum flux is known as the *Reynolds shear stress* because it is an apparent stress dimensionally consistent with the viscous shear stress that similarly acts to transfer momentum (Schlichting & Gersten 1999).

Because the velocity and shear stress distributions approach the free-stream condition asymptotically, it is common to define the boundary layer thickness where the velocity is 99% of the free stream, i.e. $\delta = z(U{=}0.99U_\infty)$ with z indicating the distance from the wall. The characteristic velocity for a turbulent boundary layer is the friction velocity $u_\tau \equiv \sqrt{\tau_{\mathrm{w}}/\rho}$ corresponding to the average wall shear stress. Despite having a definition fabricated from dimensional grouping, u_τ successfully characterizes turbulent velocities throughout the boundary layer as will be seen later. Using δ as the characteristic length yields the friction Reynolds number $Re_\tau \equiv u_\tau\delta/\nu$ for boundary layers.

Besides indicating whether a flow is likely to be turbulent, a second useful purpose of the Reynolds number is to quantify the difference between the largest and smallest turbulent motions. The largest motions are limited by the flow geometry, in this case δ (Kovasznay *et al.* 1970), and the smallest are given by the Kolmogorov length scale η (Kolmogorov 1941). The ratio of these lengths scales with the Reynolds number as $\eta/\delta \sim Re_\tau^{-3/4}$ (Pope 2000), indicating that higher-Reynolds-number flows have a wider range of turbulent motions.

1.2.1 The atmospheric boundary layer [3]

Compared to laboratory boundary layers such as in a wind tunnel, the composition of the atmospheric boundary layer (ABL) is more complicated. The free stream condition is similar, i.e. the free atmosphere is characterized by laminar flow or low-level turbulence and negligible average shear stress. However, additional forces are present within the boundary layer that must be considered in the Navier-Stokes equations. The

---

[3] The primary source of information for this section is the textbook by Stull (1988).

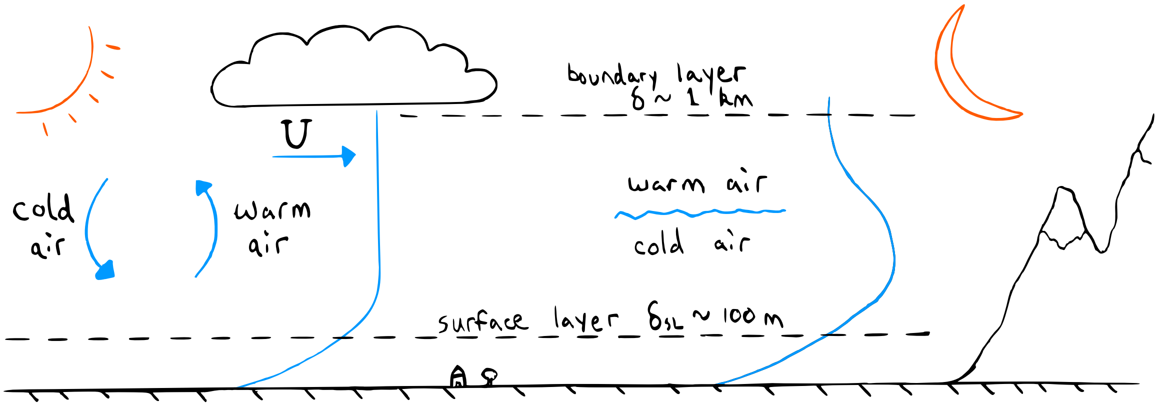

Figure 4. A cartoon of an atmospheric boundary layer formed by wind over the earth's surface during the day (left) and night (right).

frame of reference for atmospheric flows is the Earth's surface. The rotation of the Earth about its axis means the frame of references similarly rotates. The influence of the rotation on the relative wind speed is accounted for in equation (2) by introducing a Coriolis force (Coriolis 1835).

The second effect of the rotation is the resulting diurnal variation in temperature depicted in the figure 4 cartoon. Gradients in temperature lead to small differences in air density, and thus buoyancy forces. During the day, the sun heats the Earth's surface, causing the air near the ground to be warmer and lighter than the air higher in the atmosphere. The lighter air rises and the denser air falls, leading to vertical mixing and motions known as convective or *buoyancy-driven* turbulence and a thermally unstable ABL. The thickness δ grows throughout the day as the convective motions entrain air from the free atmosphere into the boundary layer.

The opposite temperature gradient occurs at night, when warm and light air is situated above cooler air near the surface. The net buoyancy acts to resist vertical turbulent motions generated by the shear. The negative buoyancy results in lower turbulence intensity and a *stably stratified* boundary layer. The upper portion of the stable boundary layer is characterized by residual turbulence from the daytime conditions. In the early morning and late evening there is a short transition period between stable and unstable conditions when the ABL has a constant temperature profile and is *neutrally stratified*.

The buoyancy effects are incorporated in the Navier-Stokes equations by allowing the density ρ to be a function of time and space instead of a constant. Boussinesq (1897) showed that the small density differences are only significant to the weight difference from the gravitational force, and the density can otherwise be assumed constant in equation (2). This assumption is known as the Boussinesq approximation.

The lowest portion of the ABL shown in figure 4 is known as the atmospheric surface layer (ASL). Turbulence generated by shear is primarily concentrated within the surface layer thickness δ_{SL}, and the turbulent motions within the ASL are small enough that Coriolis effects can be neglected (Sutton 1953; Kaimal & Finnigan 1994). In this research, shear-driven atmospheric turbulence is compared to shear-driven turbulent boundary layers at the laboratory scale. The appropriate atmospheric outer length scale is therefore δ_{SL} which characterizes the region with high shear, rather than the total depth δ which is strongly dependent on buoyancy.

1.3 Coherent structures, eddies, and other terminology

Thus far, the general term *turbulent motions* has been used to describe the complex movement of a turbulent fluid. Other terminology specific to turbulence research has been avoided because it can have various meanings depending on the reader (and author). To avoid confusion, important jargon is given below along with a precise definition and purpose.

The definition of a *coherent structure* is borrowed and modified from Robinson (1991):

> A coherent structure is a spatial region of the flow over which a flow variable (e.g. velocity or vorticity) is similar to itself relative to the surrounding regions.

The definition is purposely subjective to account for various types of structures and identification methods. For example, a *vortex* is a coherent structure characterized by high vorticity and rotation around a central core. A vortex is *prograde* if the direction of rotation is consistent with the mean velocity gradient (i.e. negative vorticity in this study). In the opposite case the vortex is *retrograde* (positive vorticity). Other coherent structure types are introduced in §2.2.

The term *eddy* is reserved for turbulent motions described statistically rather than as instantaneous structures. For example, the energy spectrum defines the average energy content of eddies at each scale. An eddy is *wall-dependent* if it is influenced by the presence of the wall such that its size is a function of its distance from the wall. Townsend's (1976) terminology of an "attached" eddy is only used in the context of the corresponding hypothesis and model.

A boundary layer has a *smooth* wall if the surface asperities are negligibly small compared to the viscous length scale ν/u_τ, and otherwise it has a *rough* wall. Following Pope (2000), the *outer region* of the boundary layer corresponds to the region where viscosity (for smooth walls) and asperities (for rough walls) have a negligible direct effect on velocity statistics, thus excluding the near-wall region.

1.4 Research questions

The previous sections have systematically introduced concepts relevant to this thesis entitled *Organization and scaling of coherent structures in the outer region of high-Reynolds-number turbulent boundary layers*. This research uses a series of experiments to investigate velocity fields in turbulent boundary layers ranging from the laboratory to the atmosphere. For each experiment, I identified coherent structures in the outer region of the boundary layer and quantified their properties. Through a comparison of the results across experiments, the thesis explores the following questions:

1. In the absence of buoyancy effects, is the atmospheric surface layer structurally similar to laboratory-scale boundary layers?
2. If so, what parameters determine the average coherent structure properties?
3. Is there a persistent organization of the structures that relates to overall flow statistics?

4. Is there a dynamical relationship between the structures that can be inferred from the results?

As previously discussed, a key motivation for these questions is the improvement of turbulence modeling. If the turbulent flow tends to organize into a specific arrangement of coherent structures with known average properties, the flow could be represented in a structural model that reflects the known behavior with a reduced level of complexity compared to flow simulations. Similar existing reduced-order models are summarized in the subsequent literature review. The remaining chapters of the thesis are as follows:

Chapter 2: Further background on the composition of turbulent boundary layers and a review of previous literature on coherent structures

Chapter 3: Methodology for and validation of a field experiment in the atmospheric surface layer

Chapter 4: Identification and analysis of coherent structures from the field measurements

Chapter 5: Organization and scaling of velocity structures and their relationship to the mean velocity profile

Chapter 6: Organization and scaling of vortex structures

Chapter 7: Phenomenological interpretation of the results

Chapter 8: Concluding remarks and avenues for future research

2 Literature review and further background

2.1 The regions of a turbulent boundary layer and related theory

In the introduction, it was said the Reynolds number indicates the separation between the smallest and largest turbulent scales (see §1.2). The friction Reynolds number Re_τ also describes the separation between the parameters governing the fluid stress at the wall (ν and τ_w) and the bulk flow geometry (δ). In a smooth wall turbulent boundary layer, distinct regions emerge based on which of these parameters are of leading-order importance. Prandtl (1925) first proposed there is a thin layer very near the wall where the viscous shear stress is primarily responsible for the mean flow behavior, and a relatively larger layer farther from the wall where the bulk parameters are important. At high Reynolds number (i.e. $Re_\tau \gtrsim 10^3$), there is an additional intermediate layer sufficiently far from both boundaries (i.e. $z^+ {=} z u_\tau/\nu \gg 1$ and $z/\delta \ll 1$) such that the direct effects of both ν and δ can be neglected (Schlichting & Gersten 1999; Pope 2000). This intermediate layer is known as the inertial or *logarithmic (log) region*. The various regions of a turbulent boundary layer are shown in figure 5 and are characterized as follows (Pope 2000):

1. **Viscous sublayer** ($z^+ \lessapprox 5$). Region closest to the wall where the viscous shear stress governs the flow. The mean flow is $U^+ = z^+$ to first-order accuracy.

2. **Buffer layer** ($5 \lessapprox z^+ \lessapprox 3Re_\tau^{1/2}$). Transition region between the viscous sublayer and logarithmic region where the viscous stress becomes increasingly less important relative to momentum transfer due to turbulence. Viscosity loses leading-order importance near $z^+ \approx 3Re_\tau^{1/2}$ (Wei *et al.* 2005).

3. **Logarithmic region** ($3Re_\tau^{-1/2} \lessapprox z/\delta \lessapprox 0.2$). Overlap region where direct effects of both ν and δ are negligible and the logarithmic law holds, discussed further in §2.1.1.

4. **Wake region** ($z/\delta \gtrapprox 0.2$). Outermost region specific to boundary layers with a free-stream condition. The bulk parameters δ and U_∞ are relevant in the wake and the velocity can be modeled using a wake function (Coles 1956; Krug *et al.* 2017). Present within the wake is the turbulent/non-turbulent interface (TNTI) separating the boundary layer turbulence from the free-stream flow. The TNTI is highly convoluted and can instantaneously reach positions as low as $z/\delta \approx 0.4$ (de Silva *et al.* 2013; Chauhan *et al.* 2014). There is an analogous center-most region in internal pipe and closed channel flows where the mean pressure gradient is relevant (George 2007).

Importantly, the limits given above for each region are approximate. As demonstrated by the buffer layer in figure 5, there is a gradual transition between each region as parameters like ν and δ slowly lose or gain importance, and the region limits are merely general thresholds for when the parameter can/cannot be neglected. As a result of these transitions and indefinite limits, researchers have proposed additional intermediate or alternative regions such as the so-called mesolayer (see, e.g., Long & Chen 1981).

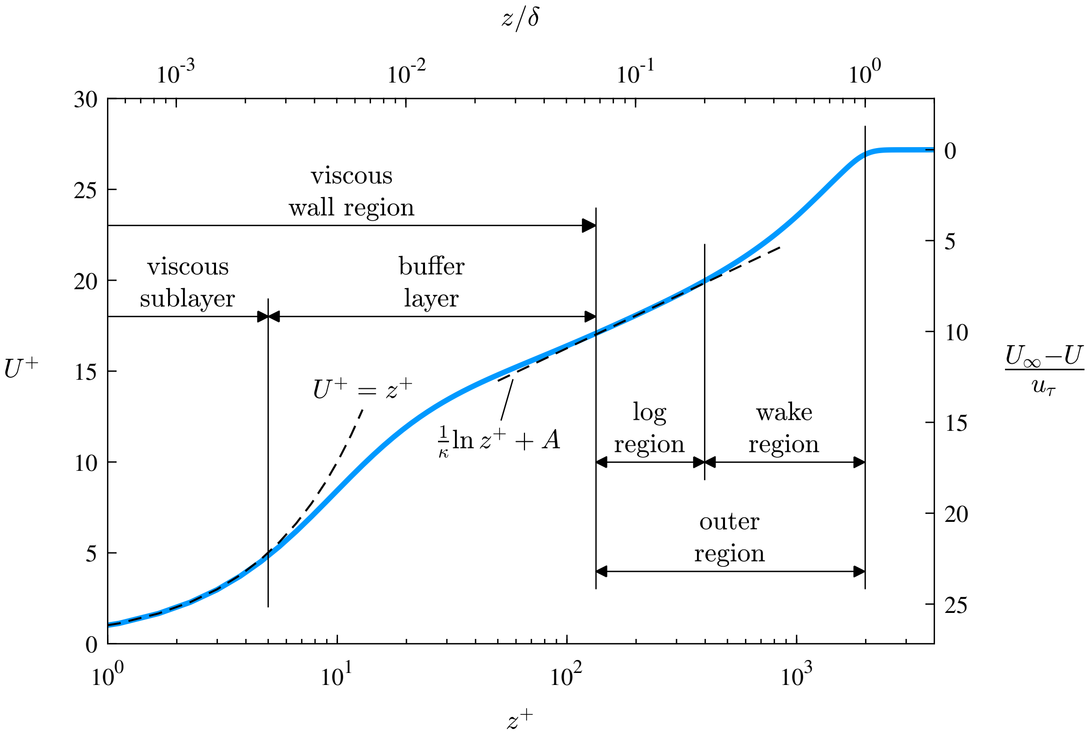

Figure 5. Profile of the mean velocity U demonstrating the regions of a turbulent boundary layer. The plotted data are from the simulation with $Re_\tau = 2\,000$ by Sillero *et al.* (2013).

2.1.1 The logarithmic region

Considerable research attention is paid to the log region, despite it occupying less than 20% of the boundary layer. The attention is in part due to a strong theoretical basis for the log region unlike the wake, and is also because more than half the turbulent kinetic energy production occurs within the logarithmic region at high Reynolds numbers (Jiménez 2004). A remarkable aspect of the log region is that the large turbulent energy production P is approximately matched by the dissipation rate ϵ of turbulent energy into heat. The log region is considered an equilibrium layer, where net transfer of energy to/from other regions of the flow is not required to balance the energy budget. In this sense, the local turbulent motions are determined by local conditions without significant net influence by non-local transport processes from other parts of the flow (Townsend 1961).

The remote position of the boundaries (i.e. $z^+ \gg 1$ and $z/\delta \ll 1$ as given above) and the negligible net effect of non-local processes are the basis for deriving the mean flow behavior within the log region. From this point, dimensional arguments directly derive the equation for the mean velocity (see, e.g., Millikan 1938) and for the constant Reynolds shear stress profile $-\overline{u'w'} \approx u_\tau^2$ (Townsend 1976). However, the approach shown here will follow the earliest derivations which instead apply a closure model in the spirit of Boussinesq's eddy viscosity (1887). Scaling assumptions by Prandtl (1925) and Theodore von Kármán (1930) led independently to the same relationship between the shear stress and the velocity gradient:

$$\tau = \rho {\ell_e}^2 \left(\frac{\partial U}{\partial z}\right)^2 . \tag{3}$$

Here, ℓ_e is the so-called mixing length corresponding to the size of hypothetical "eddies" responsible for momentum transfer (Prandtl 1925). Because the direct effects of the viscous length scale ν/u_τ and boundary layer thickness δ are negligible in this region, the only relevant length scale is the distance from the wall z. From this scaling, Prandtl (1932) introduced the common form of the mixing length $\ell_e = \kappa z$, where κ is the von Kármán constant. Using this mixing length with the approximation $\tau \approx \tau_\mathrm{w} = \rho u_\tau^2$ applicable for large Reynolds numbers, equation (3) simplifies to scaling for the mean shear:

$$\frac{\partial U}{\partial z} = \frac{u_\tau}{\kappa z}. \tag{4}$$

The integral of equation 4 is the so-called *logarithmic law of the wall*, hereon referred to as the log law:

$$U^+ = \frac{1}{\kappa} \ln z^+ + A. \tag{5}$$

The von Kármán constant $\kappa \approx 0.39$ and the smooth-wall constant $A \approx 4.3$ are believed to be universal (Marusic *et al.* 2013).

The existence and universality of the log law has been questioned at times, usually without regard to the constraints on equation (5) to high-Reynolds-number flows in the specific region $3Re_\tau^{-1/2} \lessapprox z/\delta \lessapprox 0.2$. Prior to the log law derivation, empirical power law relationships $U \sim z^m$ were developed based on Blasius' friction law (1912), where $m \approx 1/7$ was known to depend on the Reynolds number (von Kármán 1930). Barenblatt (1993) refined this relationship to argue for the superiority of a power law over the log law, but the power law only performs better above the log region into the wake region (Panton 2002). Above the log region, the log law must be supplemented by a wake function for boundary layers (Coles 1956) or a pressure gradient term for internal flows (Luchini 2017). Within the log region, numerous high-Reynolds-number experiments have shown the log law to be robust (George 2007; Marusic *et al.* 2013).

In the atmosphere, the logarithmic region is analogous to the surface layer. Under neutrally stratified conditions, the ASL is characterized by the same logarithmic mean velocity profile as in equation (5) and the Reynolds shear stress is approximately constant (Kaimal & Finnigan 1994). Under stable and unstable conditions, the buoyancy effects are accounted for through a stability correction function in the velocity equations (Monin & Obukhov 1954; Katul *et al.* 2011).

2.1.2 Townsend's attached eddy hypothesis and outer layer similarity

In addition to his work on the equilibrium layer discussed above, A. A. Townsend contributed two hypotheses in his seminal textbook *The Structure of Turbulent Shear Flow* (1976) that are worth discussing here. Townsend's *attached eddy hypothesis* (AEH) postulates that the main energetic turbulent eddies in the log region are directly influenced by the presence of the wall such that the eddy size is proportional to the distance from the wall and in a sense extends to the wall (Townsend 1976, p. 150). From this, Townsend considered a

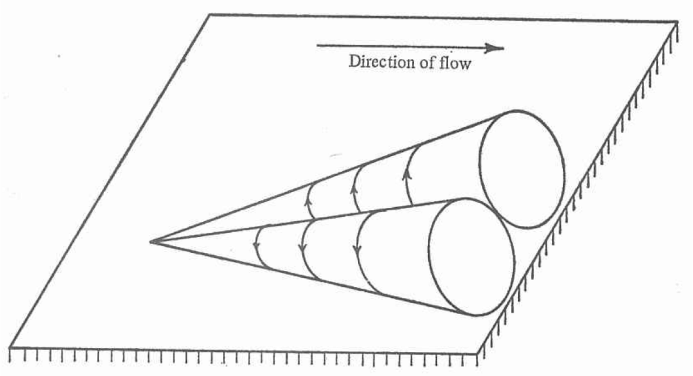

Figure 6. Figure 5.8 of Townsend (1976) showing a double-cone eddy proposed as a possible representative "attached" eddy.

random superposition of eddies, where the size increased with z and the eddy number density decreased with z in order to satisfy the Reynolds shear stress condition $-\overline{u'w'} \approx u_\tau^2$. The field of superimposed eddies led Townsend to logarithmic equations for the profiles of the second-order velocity statistics (variances) which have been confirmed experimentally (Hultmark *et al.* 2013; Marusic *et al.* 2013). While a specific eddy geometry is not required to derive the variance equations, Townsend originally proposed the double-cone eddy shown in figure 6 as a potential representative attached eddy. The ambiguity of the phrasing "extends to the wall" has led some researchers to interpret "attached eddy" somewhat literally (see, e.g. Lozano-Durán *et al.* 2012), while others have read it to mean that the eddy is influenced by the wall, even if it does not physically extend to it (Marusic & Monty 2019).

The second of Townsend's hypotheses concerns similarity. Townsend proposed that the influence of the wall in the fully turbulent region of the boundary layer is limited to the transfer of shear stress away from the wall. The Reynolds number similarity hypothesis, now known as outer layer similarity, postulates that the motions in the turbulent outer region depend on the wall stress and flow geometry δ and are independent of Reynolds number (Townsend 1976, p. 133). The hypothesis has been supported by showing that turbulence statistics such as the streamwise variance are universal in the outer region of boundary layers when normalized by u_τ and δ (see, e.g., Perry & Abell 1975; Chung *et al.* 2014).

2.1.3 Rough-wall boundary layers

The discussion so far has focused on the composition of smooth-wall boundary layers. Research on the effect of surface roughness on boundary layer turbulence began around the same time the log law was first derived (Nikuradse 1933), and the dynamics of rough-wall turbulence are now understood fairly well. When the asperities of a rough surface protrude into the buffer layer as shown in figure 7, there are two primary effects (Jiménez 2004): (i) the roughness disrupts the viscous cycle responsible for drag and momentum transport in the buffer layer (Jiménez & Moin 1991), and (ii) the roughness geometry induces a form drag on the flow. In most practical cases, the additional form drag (ii) exceeds the drag reduction (i), thus increasing the overall drag on the fluid. When the roughness partially disrupts the viscous cycle the surface is considered

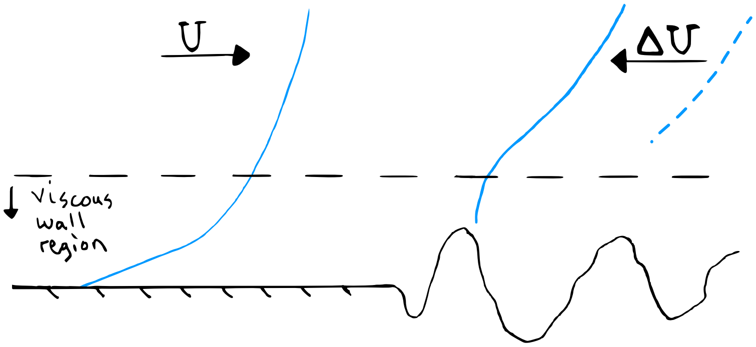

Figure 7. Cartoon comparing a smooth-wall (left) and rough-wall (right) boundary layer near the surface.

transitionally rough, and it is *fully rough* upon complete disruption which occurs when the roughness height k extends far into the buffer layer, i.e. $k^+ \gtrsim 50-100$ (Jiménez 2004). The viscous effects are negligible relative to roughness geometry and form drag in the fully rough regime. In typical atmospheric conditions with $u_\tau{\sim}O(0.1\ \mathrm{m\,s^{-1}})$ and $\nu \approx 1.5{\times}10^{-5}\ \mathrm{m^2\,s^{-1}}$, the flow is fully rough if $k \gtrsim 1$ cm such that all but the flattest and smoothest environments are within the fully rough regime.

The turbulence generation in the vicinity of the rough surface is altered by the complex wakes of the roughness geometry. For example, the disruption of the viscous cycle reduces the streamwise variance near the surface (Grass 1971), and events bringing high-momentum flow downward to the surface are relatively more important (Raupach 1981). The region where these direct roughness effects are felt is the *roughness sublayer* which replaces the viscous wall region from the smooth-wall case. The extent of the roughness sublayer is often taken to be proportional to the roughness height, i.e. $5k$ (Raupach *et al.* 1991; Flack *et al.* 2007), though more complex relationships have also been proposed (Mehdi *et al.* 2013).

Above the roughness sublayer, the additional drag results in a bulk reduction in the velocity known as the roughness function ΔU shown in figure 7. The roughness function is subtracted from the smooth-wall constant A, and the mean flow otherwise follows the log law equation. Johann Nikuradse (1933) applied sand grains of various diameters k_s to the walls of a pipe to determine the relationship between k_s and ΔU:

$$\Delta U^+ = \frac{1}{\kappa}\ln k_s^+ + A - A_{FR}, \tag{6}$$

where $A_{FR} = 8.5$ is the fully rough constant. While the relationship is specific to sand grain surfaces in fully rough conditions, equation (6) has become a standard benchmark for comparing various roughness geometries: ΔU^+ is determined experimentally for a roughness with size k, and the equivalent k_s is calculate from equation (6). In this sense, k_s is the sand grain size required to achieve an equivalent bulk velocity decrease ΔU^+. By subtracting ΔU^+ from the right-hand side of equation (5) and rearranging terms, the velocity can be re-expressed as $U^+ = \kappa^{-1}\ln z/k_s + A_{FR}$. Closely related to this is the standard form of the log law in micrometeorology (Raupach *et al.* 1991):

$$U^+ = \frac{1}{\kappa}\ln\frac{z}{z_o}, \tag{7}$$

where z_o is the aerodynamic roughness length with $z_o = k_s \exp(-\kappa A_{FR}) \approx k_s/30$ for fully rough conditions. The length z_o describes the wall-normal displacement of the mean velocity profile due to roughness, which is perhaps more meaningful than the equivalent length k_s. Values of z_o for a variety of land surfaces are commonly provided in micrometeorolgy literature (Stull 1988; Garratt 1994).

Regarding the turbulence statistics in the logarithmic and wake regions of rough-wall flows, Townsend (1976) explicitly extended his similarity hypothesis to rough surfaces, where the outer layer turbulence is independent of k except in its effect on the wall stress. Outer layer similarity for rough surfaces has been confirmed by numerous studies using one- and two-point statistics (see, e.g., Perry & Abell 1977; Raupach *et al.* 1991; Volino *et al.* 2007; Flack & Schultz 2014; Squire *et al.* 2016a,b). The most notable evidence against similarity is from P. Å. Krogstad and co-authors (1992; 1994; 1999) based on mesh and rod-type roughness experiments. These contrary results are the minority, and my own later results using mesh roughness support similarity. It is possible the roughness geometry extended into the logarithmic region and directly altered the turbulence production in the outer region (i.e., k/δ was somewhat too large per Jiménez 2004).

2.2 A brief history of coherent structure research and related models

In the classical description of turbulence put forth by Lewis Richardson (1920), large eddies are generated at the expense of the mean flow energy (production), and energy is transferred to successively smaller eddies until the smallest eddies convert the energy into heat via viscosity (dissipation). Over the intervening decades, a major thrust of turbulence research has investigated the following questions: Beyond hypothetical eddies, are there specific types of deterministic coherent motions responsible for much of the production and dissipation of turbulence? What is the relationship between these structures and the turbulence statistics? The following is a brief and non-comprehensive overview of previous research into these questions, with a primary focus on boundary layer turbulence.

2.2.1 From the horseshoe vortex to the attached eddy model

There are perhaps no other research trajectories in wall turbulence literature that follow as straight and continuous a line as the progression from the horseshoe vortex to the attached eddy model. Theodorsen (1952) first conceptualized the horseshoe vortex shown in figure 8 as a structure consistent with the governing Navier-Stokes equations. Vortices resembling Theodorsen's horseshoe were visualized using injected dye shortly thereafter by (Hama *et al.* 1957)[4]. The horseshoe vortex did not otherwise gain wide acceptance in the 1950's, as early visualization of boundary layer structures was more focused on *low-speed streaks* (Corrsin 1957; Kline & Runstadler 1959; Reiss & Hanratty 1963; Runstadler *et al.* 1963). The streaks, as seen in figure 9, are long low-momentum regions in the buffer layer with consistent spanwise spacing of approximately 100 viscous units (Kline *et al.* 1967).

---

[4] In a remarkable instance of unintended foreshadowing, Hama *et al.* (1957, p. 393) made the following statement: "To describe fully-developed turbulence as a system of horse-shoe vortices seems to be straining a concept which is most valuable in the initial stages."

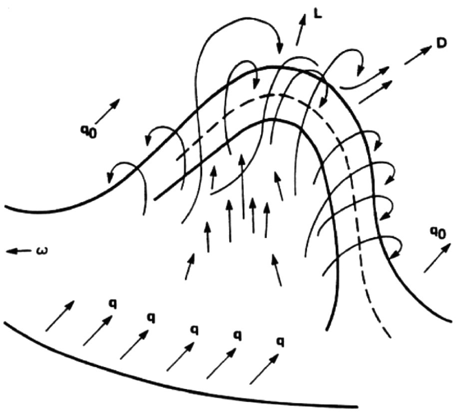

Figure 8. Figure 5 of Robinson (1991) depicting the horseshoe vortex conceptualized by Theodorsen (1952).

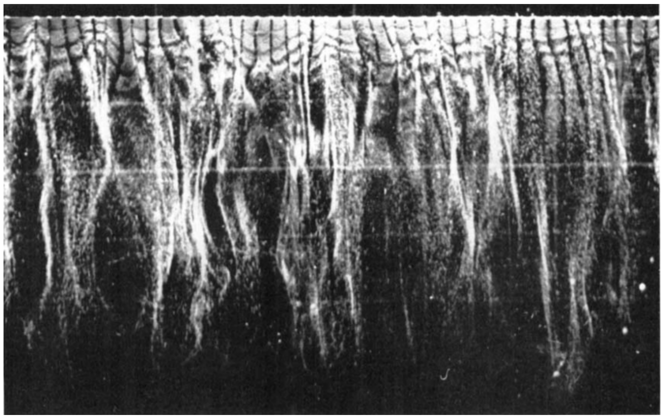

Figure 9. Figure 10(a) of Kline *et al.* (1967) showing a photograph of low-speed streaks at wall-normal position $z^+ = 2.7$. The view is from above the flow, whose mean direction is downward. The streaks are visualized using hydrogen bubbles.

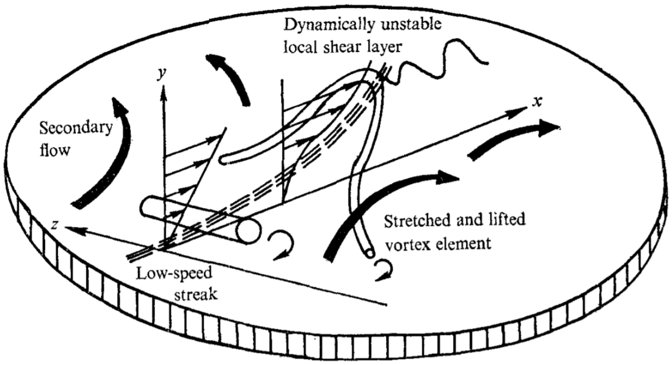

Figure 10. Figure 3(a) of Offen & Kline (1975) depicting their conceptual model in which a horseshoe-type vortex forms from a “bursting” low-speed streak.

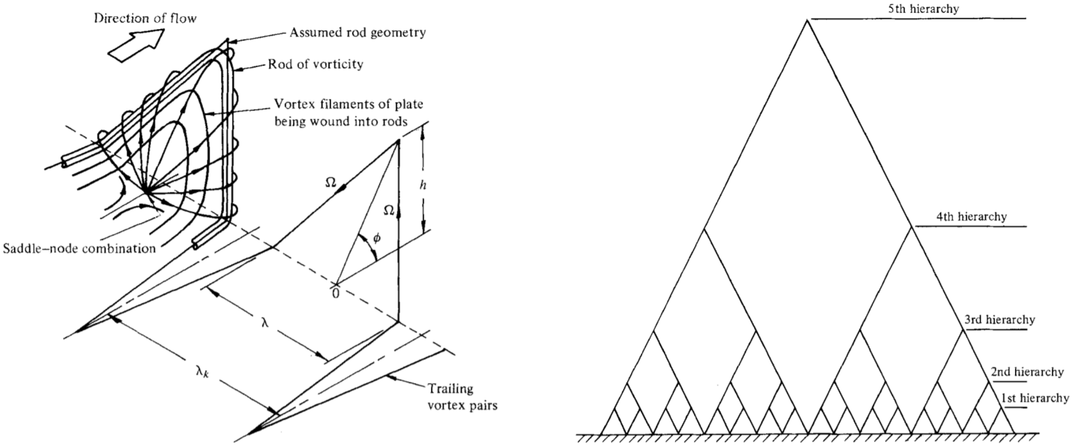

Figure 11. Figures 2 (left) and 14 (right) of Perry & Chong (1982) depicting their attached eddy model. (*left*) The representative Λ-vortex. (*right*) A symbolic representation of the vortex hierarchy.

Kline & Runstadler (1959) hypothesized that these streaks are separated by streamwise vortices, which was subsequently confirmed (Praturi & Brodkey 1978; Blackwelder & Eckelmann 1979). These vortices are now known as *quasi-streamwise vortices*. The initial prediction that each streamwise vortex had a counter-rotating pair was contradicted by later studies (Robinson 1991). These vortices are believed to be responsible for "bursts" where the streamwise vortex draws fluid in the low-momentum streak upward into a high-momentum region (Kline *et al.* 1967; Corino & Brodkey 1969). Around this time, several conceptual models were introduced to explain the bursting process (Kline *et al.* 1967; Offen & Kline 1975; Hinze 1975; Smith 1984). In the typical model such as in figure 10, an upward-bursting low-speed streak induces a streamwise vortex which is subsequently lifted (stretched) by a burst until it resembles the horseshoe vortex of Theodorsen (1952). In a separate approach using hot-wire anemometry, Klebanoff *et al.* (1962) identified *hairpin* structures similar in shape to the horseshoe, though the authors argued the hairpin to be distinct from a vortex loop.

The horseshoe vortex concept came to prominence following visualization of structures in flows with higher Reynolds number than the earlier studies. In particular, Head & Bandyopadhyay (1981) used smoke to visualize inclined structures in the outer region of the boundary layer which the authors attributed to a series of hairpin vortices. In contrast to the earlier hairpin definition, Head & Bandyopadhyay (1981) classified the hairpin as a horseshoe vortex with legs elongated due to the higher Reynolds number. The authors further noted that the legs of hairpin vortices farthest from the wall may diffuse into each other such that the hairpin head is the only remaining feature.

Based on the visual evidence of Head & Bandyopadhyay (1981) and their own study (Perry *et al.* 1981), Perry & Chong (1982) created a structural model of boundary layer turbulence now known as the *attached eddy model* (AEM). The model incorporated a Λ-vortex defined from Biot-Savart law as the representative eddy following Townsend's (1976) attached eddy hypothesis. Perry & Chong (1982) populated the boundary layer with Λ-vortices whose size increased with z and the number density decreased, resulting in a hierarchy

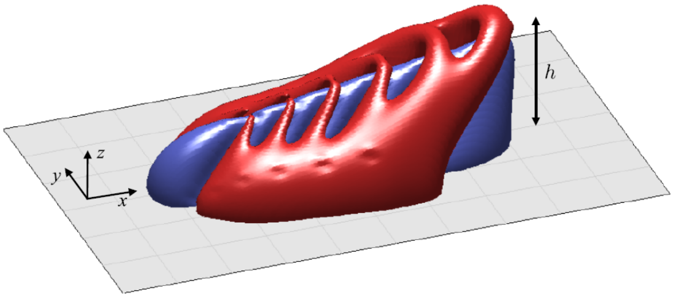

Figure 12. Figures 1 of Woodcock & Marusic (2015) showing a current representation of the representative attached eddy.

as shown in figure 11. The authors envisaged the vortices to generate at the wall from the low-speed streaks and streamwise vortices as previously discussed, diffuse outward as the vortex head is stretched, and induce a low-speed region below the vortex arch.

Since its introduction, the AEM has been occasionally refined based on experimental observations and theoretical advances such that the current model accurately reproduces second-order statistics (see, e.g., Perry & Marusic 1995; Marusic 2001; Nickels *et al.* 2007; Woodcock & Marusic 2015). The representative eddy has been updated to include a packet of Λ-vortices as shown in figure 12. And while the AEM originated from a mechanistic argument for near-wall structures, the current model does not explicitly require a generation mechanism and the vortex packet need not physically extend to the wall (Marusic & Monty 2019). The AEM provides a useful framework for implementing Townsend's attached eddy hypothesis and understanding the importance of "attached" behavior to turbulence statistics. Considering the model's simplicity and absence of dynamics, the AEM is meant to be statistically representative and is not intended to provide a complete picture of every instantaneous feature.

2.2.2 Experimental advances and conflicting evidence on hairpin vortices

Our ability to identify and characterize spatially coherent features of turbulence improved significantly in the 1980's due to advances in computational and physical experimental techniques. The first direct numerical simulations (DNS) of boundary layer turbulence occurred in the second half of the decade (Spalart 1986; Kim *et al.* 1987). In DNS, the flow domain is represented by a volumetric computational grid with sufficiently small spacing between grid points to directly solve the Navier-Stokes equations and resolve the smallest turbulent scales η. Due to the computation costs associated with the required number of grid points $N{\sim}Re^{9/4}$ (Moin & Mahesh 1998), the simulations to date are limited to moderately-high Reynolds number $Re_\tau{\sim}O(10^3)$ (Lee & Moser 2015).

The particle image velocimetry (PIV) technique was also developed around this time (Adrian 1984, 1991). For PIV, small tracer particles are introduced to a laboratory flow and images of the flow are taken while the particles are illuminated by a laser. Typically, cross-correlations are used to estimate the displacement of the particles between consecutive images and infer the fluid velocity at different points in space (Raffel *et al.* 2007). Standard PIV is used to estimate two velocity components in a two-dimensional measurement plane

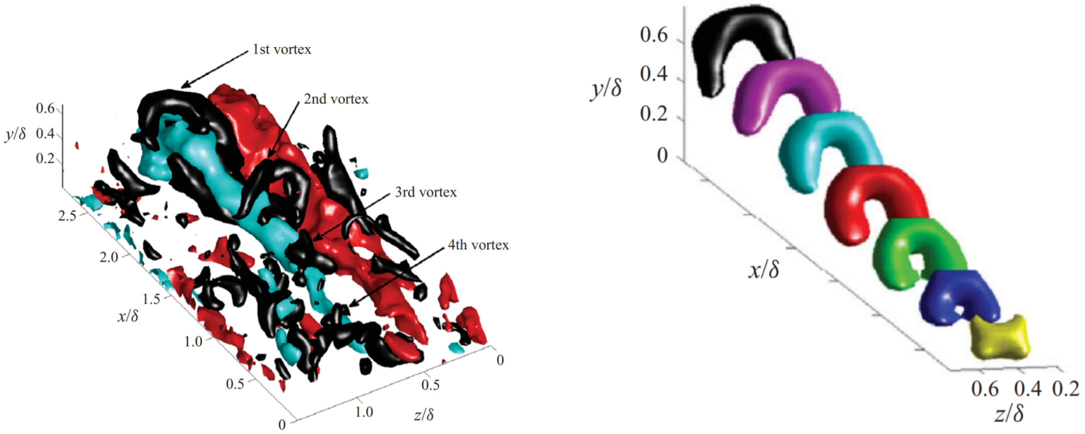

Figure 13. Figures 6 (left) and 16 (right) of Dennis & Nickels (2011) visualizing coherent structures identified from three-dimensional stereoscopic PIV. (*left*) Iso-surfaces showing instantaneous coherent structures. (*right*) Iso-surfaces of conditionally-averaged structures.

with sample frequency too slow to capture the time evolution of structures (i.e. it is not time-resolved), but more complex setups allow for PIV measurements to be time-resolved (Vogel & Lauterborn 1988), three-dimensional (Elsinga *et al.* 2006), or both (Schmid *et al.* 2012).

Both DNS and PIV have been used to provide evidence for hairpin vortices, packets of hairpins, and their statistical signature (Zhou *et al.* 1999; Adrian *et al.* 2000b; Christensen & Adrian 2001; Ganapathisubramani *et al.* 2003; Lee & Sung 2011; Jodai & Elsinga 2016, among many many others). The clearest visual evidence for a preponderance of instantaneous hairpin vortices is within the buffer layer of moderate-Reynolds-number flows (Wu & Moin 2009). The evidence becomes murkier at higher Reynolds numbers and above the buffer layer into the outer region. Gao *et al.* (2011) showed that vortex structures with strong rotation *statistically* have shape and inclination similar to a hairpin, while weaker vortices have less preference in their orientation. Consider the identified structures from Dennis & Nickels (2011) shown in figure 13. The instantaneous vortex structures hardly look like a hairpin, but the conditionally-averaged structures do resemble the hairpin arch. The figure illustrates two points: (i) the instantaneous fluid rotation often appears disorganized; (ii) a large number of messy realizations reveals the statistically representative features which are befitting of an arched vortex packet.

The primary argument against hairpin vortices in the outer region concerns their proposed generation mechanism. The mechanism assumes the hairpins originate from near-wall streaks and quasi-streamwise vortices, then are lifted up higher in the boundary layer (Adrian 2007). To date, there is no strong evidence of buffer layer hairpins consistently migrating upward into the outer region. This idea that the outer flow structure is dependent on the near-wall features is also contradictory to Townsend's outer layer similarity. The near-wall structures in the presence of surface roughness are dependent on the roughness geometry such that the proposed near-wall hairpin generation is unlikely to be viable. Yet Volino *et al.* (2007) still identified the statistical signature of hairpin vortices in the outer region of a rough-wall boundary layer. In a DNS study, (Mizuno & Jiménez 2013) replaced the viscous wall region with a boundary condition and still achieved the theoretical logarithmic behavior. These two results suggest the buffer layer (or roughness sublayer) structures are unimportant to the outer layer statistics.

My interpretation of the evidence is as follows: hairpin vortices are present in the buffer layer for smooth-wall conditions, and are particularly evident for low to moderate Reynolds numbers. In the outer region, the *average* representative vortex structure shares several statistical features with the hairpin model regardless of the wall conditions. The generation mechanism for these outer region eddies therefore should consider local conditions rather than near-wall features.

2.2.3 Velocity and vorticity structures in the logarithmic region

Besides the hairpin vortex, the velocity structures in the log region are also qualitatively similar to near-wall features. Several studies have identified streaks of coherent streamwise momentum in the log region that are remarkably similar to the low-speed streaks in the buffer layer (see, e.g., Tomkins & Adrian 2003; Hwang 2015; Hwang & Sung 2018). These *low-momentum streaks* have been associated with an instability and subsequent breakdown similar to bursting in the buffer layer Flores & Jiménez (2010). Despite the buffer layer analogue, the log region streaks exist independently of the near-wall structures (Flores *et al.* 2007). Further, the log region streaks are much larger than their buffer layer counterparts (Jiménez 2013) and the low-momentum streaks are flanked by high-momentum regions (Dennis & Nickels 2011).

It is likely that the momentum streaks are closely related to the low-speed region underneath the Λ-vortex packet in the representative attached eddy of figure 12. Consistent with the attached eddy hypothesis, the streaky structures increase in size with wall-normal distance and are self-similar in their geometry (Hwang 2015; Hwang & Sung 2018). Further, the vorticity accompanying the alternating streaks produces the signature of the hairpin legs (Tomkins & Adrian 2003).

A more subtle characteristic of the momentum streaks is their weak, diffuse average rotation which forms a *streamwise roller* (del Álamo *et al.* 2006). Figure 14 shows instantaneous and conditionally-averaged structures from Jiménez (2018) associated with the momentum streaks. Much like the hairpin signature in the previous figure, the roller is mainly apparent from the conditionally-averaged flow field. Based on the vectors in figure 14, the low-momentum region is associated with the upward motion of the roller, and the high-momentum region with the downward motion. The average streamwise roller therefore contributes to the transfer of momentum in the log region. Jiménez (2018) referred to the iso-surface structures in figure 14 specifically as Q2–Q4 pairs, which are briefly discussed in §2.2.4. The streamwise rollers and Q2–Q4 pairs have the same wall-normal distance scaling are their associated streaks (del Álamo *et al.* 2006; Jiménez 2018).

There exist larger structures in the log region that have similar geometry to the momentum streaks, but distinct scaling. Very-large-scale motions (VLSMs) scaling with δ contribute a majority of the turbulent energy in the log region (Kim & Adrian 1999; Guala *et al.* 2006). The VLSMs span numerous boundary layer thicknesses in streamwise length (Hutchins & Marusic 2007a; Smits *et al.* 2011) and closely resemble the wall-dependent z-scaled streaky structures (Monty *et al.* 2007; Lee *et al.* 2014). The VLSMs often meander in the spanwise direction, likely due to an instability that leads to their eventual breakdown (Hwang & Cossu

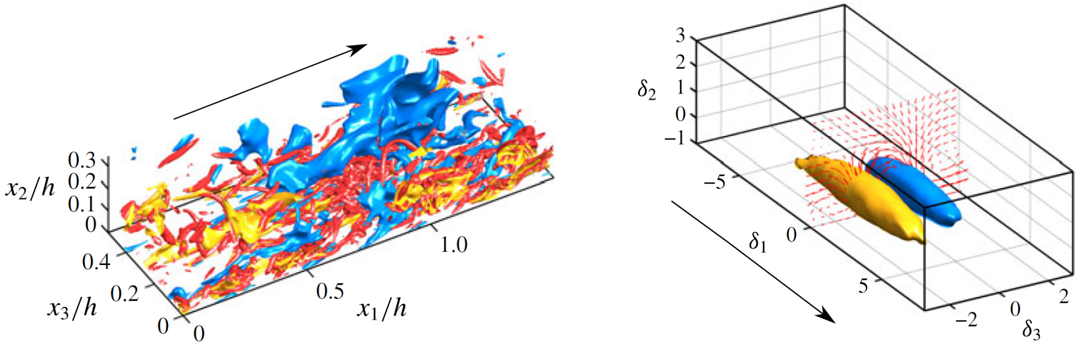

Figure 14. Figure 18 of Jiménez (2018) visualizing coherent structures identified from DNS. (*left*) Iso-surfaces showing instantaneous low-speed (yellow), high-speed (blue), and vortical (red) regions. (*right*) Iso-surfaces of conditionally-averaged structures and the associated rotation (arrows).

2010; Kevin *et al.* 2019). The arrangement of VLSMs is also similar to the wall-dependent streaks: the low-velocity VLSMs are flanked by high-velocity structures and conditional averaging reveals the signature of a δ-scaled streamwise roll mode between the velocity structures (Hutchins & Marusic 2005; Marusic & Hutchins 2008). To my knowledge, there is unfortunately no current consensus on terminology to distinguish by name the wall-dependent streaks and rolls from their δ-scaled counterparts. In this work, *momentum streak* and *streamwise roll* refer to the wall-dependent structures. How the wall-dependent structures and VLSMs relate to one another is a subject of ongoing research. For instance, the VLSMs may comprise a series of wall-dependent structures (Adrian *et al.* 2000b) where the VLSMs modulate the behavior of the wall-dependent structures (Hutchins & Marusic 2007b).

To identify the strongly-rotating coherent vortex structures in the log region, researchers often use one of two methods: (i) apply a threshold of a criterion for rotation (Haller 2005; Chakraborty *et al.* 2005); or (ii) fit the local flow field to a vortex model that is consistent with the Navier-Stokes equations, e.g. the Oseen (1912) or Burgers (1948) model. Both methods have led to similar statistics for the strongly-rotating vortex cores, where the average core diameter is on the order of ten times the Kolmogorov length scale (Tanahashi *et al.* 2004; Herpin *et al.* 2013; Wei *et al.* 2014; Jiménez 2018). This diameter is the cross-section of elongated *vortex tubes*. The tubes often occur in clusters and are not uniformly distributed in space (Wu & Christensen 2006; Kang *et al.* 2007; Jiménez 2013). In particular, del Álamo *et al.* (2006) identified "attached" clusters of vortices that have the same self-similar size behavior as the momentum streaks.

2.2.4 Momentum transfer events and the issue of Reynolds decomposition

Whereas the horseshoe vortex and velocity streaks were conceived as a coherent structure before they were related to turbulence statistics, research on momentum transfer events took a somewhat opposite approach. The importance of the Reynolds shear stress has long been understood, and researchers have since worked to better understand the turbulent structures leading to the statistic $\overline{u'w'}$ (Wallace 2016). Kinematic momentum transfer events were mentioned earlier in this text: high-momentum fluid moving downward is

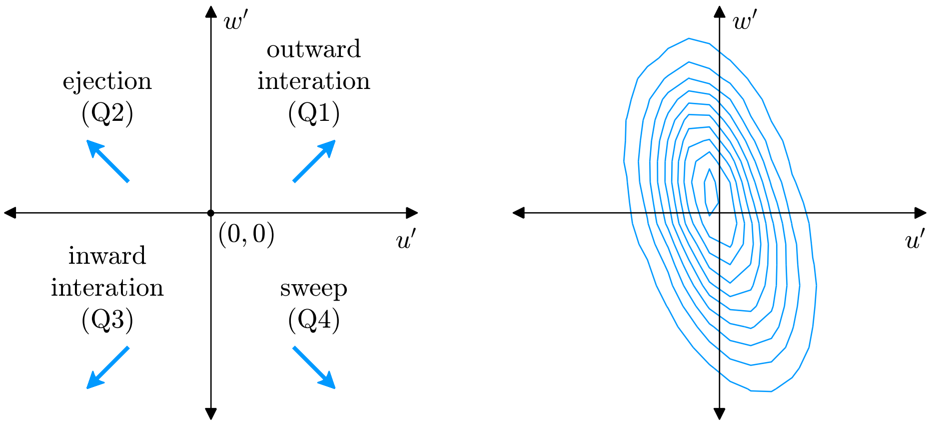

Figure 15. Classification of instantaneous $u'w'$ events based on quadrants following Wallace *et al.* (1972). (left) The four quadrants of the $u'-w'$ plane and the flow direction relative to the mean for each quadrant. (right) Joint probability contours of u' and w' at $z/\delta = 0.1$ based on the DNS results of Sillero *et al.* (2013).

hereon referred to as a *sweep*, and low-momentum fluid moving upward is hereon an *ejection*. In some cases, sweeps and ejections are related to other structures. For instance, the bursting process of a low-speed streak is a type of ejection (Kline *et al.* 1967), and the evolution of a hairpin-shaped vortex involves fluid ejected from below the arch and swept in from behind (Adrian *et al.* 2000b).

Following Corino & Brodkey's (1969) visualization of coherent sweeps and ejections, Wallace *et al.* (1972) classified the events statistically using the quadrants of the $u'-w'$ plane shown in figure 15. As a reminder, u' is the fluctuation from the mean velocity based on Reynolds decomposition $u' = u - U$ (Reynolds 1895). Conditional statistics allowed researchers to investigate the relative importance of each quadrant (Wallace *et al.* 1972; Nakagawa & Nezu 1977; Raupach 1981). For example, the probability contours in figure 15 shows that ejections contribute more to the Reynolds shear stress than sweeps at the given wall-normal position. More recently, spectral analysis has shown that δ-scaled turbulent motions are mostly responsible for the Reynolds shear stress (Jiménez 1998; Guala *et al.* 2006; Balakumar & Adrian 2007), which suggests that sweeps and ejections are either large-scale structures or a large "packet" of smaller-scale structures.

Researchers have used the quadrant classification to identify spatial Q2 and Q4 regions (see, e.g., Lozano-Durán *et al.* 2012; Jiménez 2018). For instance, the average streamwise rollers in figure 14 form a Q2–Q4 pair. The quadrant system provides a useful tool for point measurements and statistics, but there is a caveat in extending the quadrants to coherent structures. In the Reynolds decomposition of a boundary layer velocity field, the mean shear profile is subtracted. This mean shear results from the net momentum transfer due to viscosity and turbulence at each wall-normal position, where turbulence effects are dominant at high Reynolds numbers. In searching for the structures that lead to momentum transfer, why should the net effect of the momentum transfer be removed? In other words, the fluctuation field distorts the physical flow structures with a time-averaged statistic resulting from those same structures. The present research instead uses the full instantaneous velocity fields to identify coherent structures.

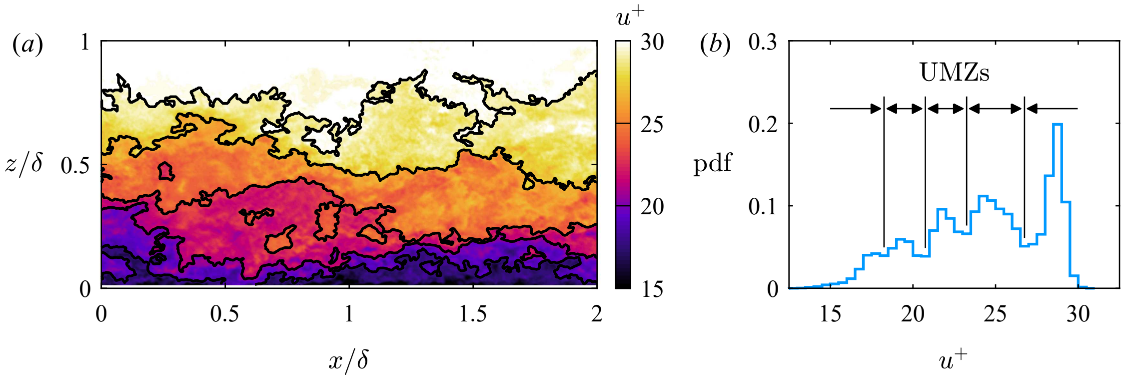

Figure 16. Example of uniform momentum zones (UMZs) based on the $Re_\tau = 17\,000$ boundary layer PIV data of de Silva *et al.* (2014). (*a*) PIV field where color indicates streamwise velocity u and black lines indicate the UMZ boundaries. (*b*) Histogram corresponding to the velocity field, where each local peak is assumed to represent the streamwise momentum of a distinct UMZ.

2.2.5 Uniform momentum zones and internal shear layers

Over the past few decades, a more general classification of coherent structures has emerged for higher-Reynolds-number boundary layers. The *uniform momentum zone* (UMZ) introduced by Meinhart & Adrian (1995) is a spatial region with relatively uniform velocity. Meinhart & Adrian (1995) assessed PIV vector fields across the entire boundary layer, i.e. an $O(\delta)$ measurement field in x and z, and noted the existence of large regions with uniform momentum relative to the entire flow field. They further observed that instances of high instantaneous shear $\partial u/\partial z$ and vorticity were preferentially concentrated along the boundaries of the uniform regions (Meinhart & Adrian 1995). The term *internal shear layer* (ISL) will be used here to describe these regions of high shear and vorticity, noting that various other names have been introduced in the literature (Priyadarshana *et al.* 2007; de Silva *et al.* 2017). Figure 16(*a*) identifies the UMZ boundaries in an example PIV velocity field, and the relative uniformity in color within each bounded region shows visually the coherence of UMZs.

The quantitative detection of UMZs was introduced by Adrian *et al.* (2000b), who used histograms of the streamwise velocity to identify the speeds of each UMZ. Figure 16(*b*) shows the histogram corresponding to the 16(*a*) velocity field. The coherent velocity regions lead to numerous PIV vectors with similar u value such that the UMZs manifest as local peaks in the histogram. The shear region between each UMZ is characterized by a large velocity gradient across a short distance such that the velocities within the shear region are represented by a small number of vectors. The ISLs can therefore be approximated as the minima between each local histogram peak. The UMZ boundaries in figure 16(*a*) are contours of the local minima in the histogram.

It is important to acknowledge the term *relative* in the UMZ definition. Each UMZ is uniform *relative* to the surrounding flow, and low-level turbulent fluctuations within the zone are neglected. How much of the surrounding flow is considered in the detection will impact the identified zones and the extent of neglected turbulence. This issue is quantified by the streamwise length $\mathcal{L}_x$ of the vector field used in the histogram detection (de Silva *et al.* 2016). For instance, the length is $\mathcal{L}_x = 2\delta$ in figure 16. The choice of $\mathcal{L}_x$ and its effect on the detected UMZs is discussed in the later analysis. If $\mathcal{L}_x$ is chosen properly, the variability of u within the detected UMZs is a small fraction of the overall time-averaged variance (de Silva *et al.* 2016), and a majority of the instantaneous shear is aligned with the ISLs (de Silva *et al.* 2017). In this sense, de Silva *et al.* (2016, 2017) showed statistically that the outer region self-organizes into relatively uniform zones separated by concentrated shear regions.

Beyond the simple existence of UMZs, several studies have related these structures to turbulent behavior in the outer region. Klewicki (2013a) used scaling arguments to show that the organization of UMZs and ISLs in the log region is consistent with the Navier-Stokes equations for the mean flow. These same scaling arguments lead to the wall-normal distance scaling and the log law (Klewicki *et al.* 2009; Klewicki 2013b). de Silva *et al.* (2017) showed that the average velocity difference across the ISL is proportional to u_τ throughout the boundary layer, and multiple studies showed that the ISL thickness is proportional to the Taylor microscale λ_T (Wei *et al.* 2014; Eisma *et al.* 2015; de Silva *et al.* 2017). Assuming the UMZs are large-scale features whose size is proportional to either δ or the integral length scale L, the ratio of the ISL and UMZ thicknesses is $\lambda_T/L \sim Re_L^{-1/2}$ (Pope 2000). The scale separation between the ISLs and UMZs therefore increases with Reynolds number, and the segregation of shear and vorticity into thin layers becomes more apparent. In high-Reynolds-number cases, the arrangement of UMZs and ISLs results in instantaneous velocity profiles that resemble a step-like function more than a smooth continuous profile (Meinhart & Adrian 1995), and the logarithmic mean velocity is only achieved by averaging many step-like profiles. Recognizing the potential importance of the UMZ-ISL organization, de Silva *et al.* (2017) related the organization statistically to the mean velocity, Chini *et al.* (2017) proposed a conceptual model for a self-sustaining process of UMZs and ISLs, and Bautista *et al.* (2019) used the organization and scaling arguments to model instantaneous velocity profiles.

In addition to turbulent boundary layers, UMZs have be identified for closed channel flows (Kwon *et al.* 2014), pipe flows (Chen *et al.* 2020), hypersonic boundary layers (Williams *et al.* 2018), and uniform shear flows (Vanderwel & Tavoularis 2011). A majority of UMZ studies used a two-dimensional streamwise–wall-normal measurement plane to detect and characterize the structures, though researchers have also conducted three-dimensional studies (Chen *et al.* 2020).

The UMZ coherent structure classification is closely associated with the histogram detection technique (or alternatively the fuzzy clustering method; Fan *et al.* 2019). Given the generic definition of UMZs, many of the coherent structures discussed above are identified as UMZs or ISLs when histogram detection is employed. The most straightforward example is the relationship between streamwise momentum streaks and UMZs, where each streak would be detected as a distinct UMZ due to its coherent velocity. UMZs are also related to "bulges" of coherent velocity in the wake region near the non-turbulent interface (Kovasznay *et al.* 1970; Saxton-Fox & McKeon 2017). The connection to sweeps and ejections is less direct. Laskari *et al.* (2018) associated the number of UMZs at a given instant to quadrant events; one or two large UMZs were detected during a relatively long-lived Q4 (sweep-type) events, and numerous UMZs appeared during shorter Q2 (ejection-type) events with increased small-scale turbulent activity. The ISLs are often populated by vortex cores resembling the heads of a vortex packet or cluster, and the average forward inclination of the ISLs is consistent with observations of inclined vortex packets (Squire 2017).

Considering the overlap in these labels, it is perhaps better to treat UMZs and ISLs as two classes of coherent structures. The UMZ class includes any structures with coherent velocity such as streaks, bulges, sweeps, and ejections. The ISL class describes coherent regions with concentrated velocity gradient statistics (e.g. shear, vorticity, strain) such as vortex clusters, and only includes individual Kolmogorov-scale features as they relate to the larger collective cluster. Whereas the UMZs are critical to the kinematics, the ISLs are dynamically important. A limitation to this categorization is that UMZs are currently detected based only on coherence of the streamwise velocity. The detection methodology should be extended to include additional velocity components, which would distinguish a sweep/ejection from a streak.

2.2.6 Coherent structures and their measurement in atmospheric turbulence

Determining spatial coherence in the atmospheric surface layer requires significant up-scaling of the experimental facilities and simulations. The most common measurement technique in atmospheric studies is to use an array of sensors and anemometers mounted to a meteorological tower. Remote sensing instrumentation such as doppler lidar is also common, but the measurements are limited in both spatial and temporal resolution (Kaimal & Finnigan 1994).

Vertical and spanwise arrays of sonic and hotwire anemometers have been specially constructed in very flat field environments for the purpose of fundamental boundary layer research at high Reynolds numbers. At these facilities, measurements are acquired during neutrally stratified conditions and velocity coherence is inferred from multi-point correlations across the array. Two such facilities are the Surface Layer Turbulence and Environmental Science Test (SLTEST) site in the salt flats of Utah (Metzger & Klewicki 2001) and the Qingtu Lake Observation Array (QLOA) on a dry lake bed in western China (Wang & Zheng 2016). At the SLTEST facility, flow visualization by fog and smoke has also been utilized to observe coherent structures near the surface (Klewicki *et al.* 1995; Hommema & Adrian 2003; Morris *et al.* 2007).

DNS of atmospheric turbulence is not feasible due to the required grid resolution and corresponding computational cost. In this case, large-eddy simulation (LES) is used to circumvent the required resolution (Deardorff 1970). In LES, the Navier-Stokes equations are low-pass filtered with a relatively coarse computational grid to resolve the large-scale turbulence, and a closure model is used to approximate the effect of the unresolved small scales (Louis 1979; Meneveau & Katz 2000). Simulation of the ASL is viable using LES due to the reduction in computational cost.

A number of coherent structures have been identified in the ASL through a combination of field experiments and LES. Fog visualization by Klewicki *et al.* (1995) in the buffer layer at the quasi-smooth-wall SLTEST facility revealed near-wall low-speed streaks matching the viscous behavior of the near-wall streaks in lower-Reynolds-number flows. In the log region, the large-scale streaks of alternating low- and high-momentum fluid have been identified using sensor arrays (Wilczak & Tillman 1980; Hutchins *et al.* 2012), doppler lidar (Träumner *et al.* 2015), and LES (Salesky & Anderson 2018). In an approach similar to figure 14, Foster *et al.* (2006) used conditional statistics with LES to show these alternating streaks are part of streamwise rolls with a corresponding sweep and ejection. These rolls are distinct from the convective rolls observed to span the entire atmospheric boundary layer (Etling & Brown 1993). In another LES study, (Lin *et al.* 1996) observed regions of high vorticity along the shear interfaces separating sweeps and ejections.

There has been similar success in the search for hairpin characteristics. Hutchins *et al.* (2012) used velocity correlations to identify the statistical signature of hairpin vortices up to 30 meters above the surface. Flow visualization at the SLTEST facility revealed the presence of forward-inclined *ramp-like* structures (Hommema & Adrian 2003) consistent with a vortex packet. These structures share the same broad characteristics as hairpin packets – namely their forward inclination – without necessarily distinguishing individual vortices. The statistical consequence of ramp-like structures is an inclined two-point correlation. The observed inclination angle in the neutrally-stratified ASL (Guala *et al.* 2011; Hutchins *et al.* 2012) matches lower-Reynolds-number flows in both smooth- and rough-wall conditions (Ganapathisubramani *et al.* 2005; Guala *et al.* 2012; Squire *et al.* 2016a). As buoyancy becomes increasingly important in thermally unstable conditions, the inclination angle increases (Chauhan *et al.* 2013; Liu *et al.* 2017) and buoyancy forces modulate the long momentum streaks until they are eventually replaced by short convective cells (Salesky *et al.* 2017; Salesky & Anderson 2018).

The studies described here seem to confirm that the ASL is populated by the same streaks, rolls, sweeps, ejections, and inclined vortical structures as laboratory flows, at least in conditions where the turbulence is shear-driven. The ASL appears structurally similar to lower-Reynolds-number flows, suggesting similar turbulence production mechanisms are occurring at the larger scale. Note the current focus is canonical boundary layer turbulence, and turbulence phenomena related specifically to meteorology and weather-scale patterns are not discussed here.

2.2.7 A possible universal organization of structures

The final literature topic to discuss is the recent advances in isotropic turbulence research. Unlike boundary layer turbulence which has a directionality due to the mean velocity and shear, isotropic turbulence has no preferential orientation and turbulent statistics are the same in any direction. Based on Kolmogorov's 1941 theory, in high-Reynolds-number flow the small turbulent motions are not influenced by the boundary conditions or forcings and behave in a universal and isotropic manner. In this regard, isotropic turbulence research is relevant to the small-scale features in boundary layer flows. The validity of universal small-scale isotropy for high-order statistics is the subject of numerous studies (see, e.g., Warhaft 2009, and references therein), and is not discussed here.

Consistent with the boundary layer case, the velocity gradients in isotropic turbulence are concentrated in thin regions. Figure 17 shows DNS results of Ishihara *et al.* (2009) where the velocity gradient statistics (dissipation and enstrophy, in this case) are clustered and intermittent. Several studies have observed the clustering of worm-like vortex tubes (see, e.g., She *et al.* 1990; Moisy & Jiménez 2004), where the core diameter of the tubes is proportional to the Kolmogorov length scale (Jiménez *et al.* 1993). The length of the tubes and the cluster is proportional to the integral length scale (Jiménez *et al.* 1993; Ishihara *et al.* 2009), as is the distance between clusters (Ishihara *et al.* 2013).

The intense vortex tubes primarily reside within thin shear layers whose thickness is proportional to the Taylor microscale (Ishihara *et al.* 2013; Elsinga *et al.* 2017). Several researchers have suggested the shear

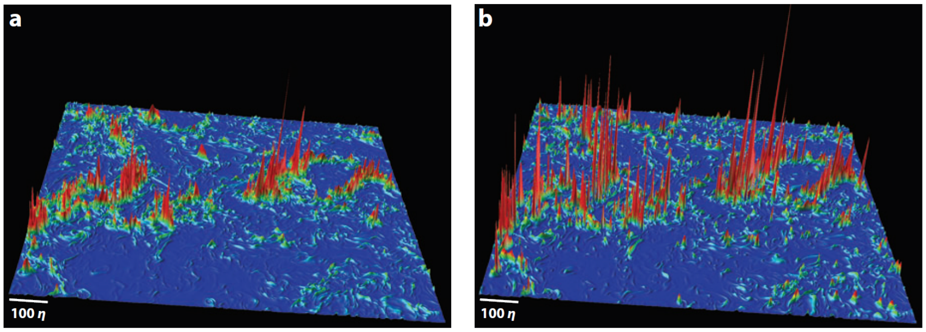

Figure 17. Figure 4 of Ishihara *et al.* (2009) showing a cross-section of DNS in isotropic turbulence. The (*a*) dissipation rate and (*b*) enstrophy fields demonstrate the clustering of small-scale turbulence into thin, sparse regions.

layers roll-up into vorticity sheets due to a Kelvin-Helmholtz instability (Ruetsch & Maxey 1992; Vincent & Meneguzzi 1994; Passot *et al.* 1995). In particular, Pirozzoli (2012) showed the average flow field away from the vortex tube core is consistent with vorticity sheets, but the existence of these sheets is a subject of debate (Davidson 2015).

Based on these observations, the organization of clustered vortex tubes into intermittent shear layers has been proposed as an important component of small-scale dynamics (Hunt *et al.* 2010; Elsinga & Marusic 2010; Ishihara *et al.* 2013; Hunt *et al.* 2014; Elsinga *et al.* 2017). The organization is consistent with intermittency principles, where the clustering of strong velocity gradients leads to heavy-tailed probability distributions which influences high-order statistics (She & Leveque 1994; Sreenivasan & Antonia 1997). The same organization is present in boundary layer turbulence, where the ISLs represent the concentrated velocity gradients, and the UMZs are the separation between clusters. These findings suggest a possible universal self-organization of structures. Yet caution must be taken in interpreting the similarity in organized intermittency as a similarity in dynamics. In shear flows such as a boundary layer, the preferential direction and persistence of the ISLs in the presence of the mean flow leads to vortices which span the entire ISL, and these larger vortices are not present in the isotropic case (da Silva & Taveira 2010). The thesis results pertaining to the interaction of UMZs and ISLs therefore may not be entirely relevant to every turbulent flow case, despite the similarities.

3 Atmospheric surface layer measurements using particle image velocimetry

Chapter 3 comprises an edited version of sections 2 and 3 of the article below, published in the *Journal of Fluid Mechanics*, © Cambridge University Press 2018. Please cite the published article when referencing content in this chapter.

Heisel, M., Dasari, T., Liu, Y., Hong, J., Coletti, F., and Guala, M. (2018). The spatial structure of the logarithmic region in very-high-Reynolds-number rough wall turbulent boundary layers. *J. Fluid Mech.* **857**, pp. 704-747. https://doi.org/10.1017/jfm.2018.759.

3.1 Methodology

Previous attempts to characterize ASL turbulence using flow imaging, discussed in §2.2.6, include seeding the flow with artificial smoke or fog (Hommema & Adrian 2003; Morris *et al.* 2007). In these experiments, the concentrated particle regions were close to ground level (within 1-2 m) where the particles were introduced, thus limiting the imaging field to a small fraction of the surface layer depth. In a major advancement of field-scale PIV, Jiarong Hong and colleagues exploited the frigid Minnesota winters by using natural snowfall as the seeding particles (Hong *et al.* 2014).

Using natural snow has numerous advantages over artificial seeding (Toloui *et al.* 2014): (i) there is no economic or environmental cost; (ii) no machinery or structures are required to introduce the seeding particles, thus avoiding intrusive flow obstructions; (iii) natural snow is well-distributed throughout the boundary layer, greatly expanding the viable measurement domain in space and time; (iv) the crystal structure of snowflakes results in strong scattering of light in multiple directions (Kokhanovsky & Zege 2004), reducing the required power of the illumination source. Points (iii) and (iv) are particularly important, as they allow for the traditional laser to be replaced by a searchlight and snowflakes can be illuminated more than 100 m above the light source (Dasari *et al.* 2019).

Owing to the unprecedented size of the imaging field, the snow-driven measurements are known as *super-large-scale* particle image velocimetry (SLPIV). Since the method was first validated (Toloui *et al.* 2014), a majority of the SLPIV studies have characterized the inflow or wake of the utility-scale wind turbine located at the field site described later in §3.1.1 (Hong *et al.* 2014; Dasari *et al.* 2019; Abraham *et al.* 2019; Abraham & Hong 2020; Li *et al.* 2020). However, in the experiment described here, SLPIV was used to measure turbulence in the ASL far from any influence of the turbine. The following sections provide experimental details related to the field site, the experimental setup, and the data processing. The justification for using snowflakes as seeding particles is discussed last.

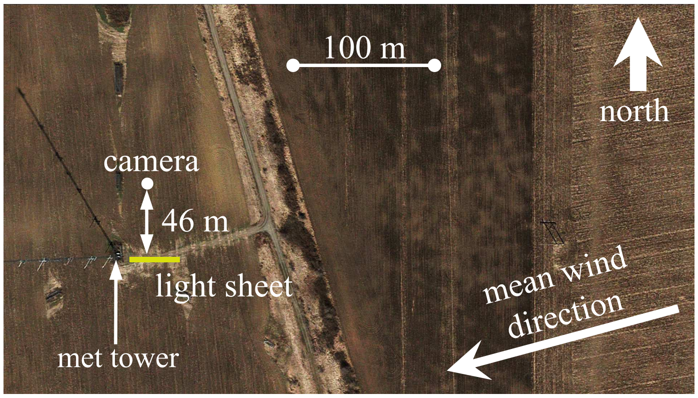

Figure 18. Google Earth aerial satellite image of the Eolos field site with enhanced brightness and contrast. Adapted from Figure 1(a) of Heisel *et al.* (2018).

3.1.1 Eolos field site

The SLPIV experiment took place at the University of Minnesota Eolos Wind Research Field Station in Rosemount, Minnesota. The field deployment occurred early morning 11 December 2016 between 00:30 and 02:00 central standard time. The area surrounding the measurement site is primarily flat farmland with trees and sparse two-story buildings farther away. At the time of the deployment, the farmland was harvested such that the soil was overturned and short, cut vegetation protruded through the snow cover. The roughness of the overturned soil was evident through the shallow snow cover. The primary wind direction during the deployment was from east to west. Upwind of the measurement location, there was a shallow ditch with shrubs 100 m away followed by 1 km of flat farmland. The approximate height of the shrubs was less than 1 m. A meteorological (met) tower was situated 17 m downwind of the imaging field. Aside from the met tower, the nearest downstream obstruction was a row of trees 200 m away. The utility-scale wind turbine was more than 100 m north of the image field, transverse to the mean wind direction. An aerial view of the site is shown in figure 18.

The position of the imaging field was selected to be collocated with the met tower to supplement and validate the SLPIV results. The 130 m tall met tower has three CSAT3 sonic anemometers (heights $z = 10$, 30, and 80 m) and six cup-and-vane anemometers (heights $z = 7$, 27, 52, 77, 102, and 126 m). The sonic anemometers measure velocity in three directions as well as temperature at 20 Hz. The 1 Hz cup-and-vane anemometers are each paired with temperature and relative humidity sensors. The met tower measurements are time-stamped and uploaded approximately in real time to an online database.

3.1.2 Experimental setup

The SLPIV experimental apparatus includes equipment to generate a sheet of light for illuminating snowflakes, and a camera to capture images. The position of the light sheet and camera are indicated in the figure 18 aerial image, and the setup for the light sheet is shown in figure 19. The light source was a 5 kW xenon arc lamp searchlight powered by a 6 kW portable generator. The searchlight beam projected

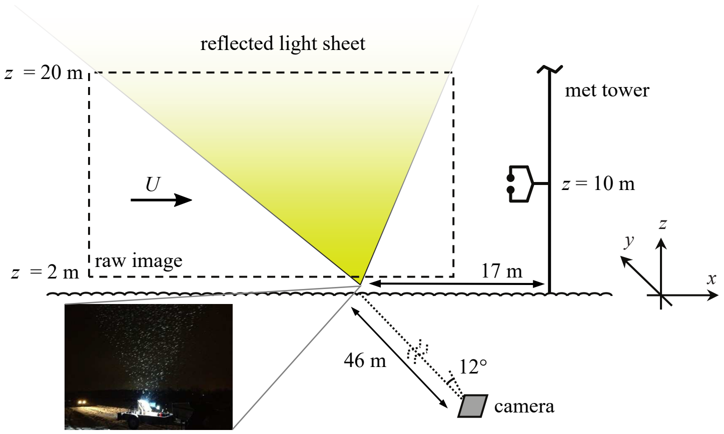

Figure 19. Schematic of the super-large-scale PIV (SLPIV) imaging field upwind of the meteorological (met) tower. Adapted from Figure 1(c) of Heisel *et al.* (2018).

horizontally, then was reflected upward from a convex aluminum panel. The curvature of the convex panel can be adjusted to create a tall and narrow light sheet or a broad and short sheet. A broader sheet was favored for the experiment to capture a wider field of view (FOV), while still reaching a measurement height close to 20 m above the surface. The light beam was 0.3 m thick at the searchlight, and broadened to approximately 0.4 m thick through the imaging field. The light sheet width (in x) also increased with height (in z), creating a non-rectangular imaging field as seen in figure 19. The light sheet was positioned upwind of the met tower and was oriented with the anticipated mean wind direction based on weather forecasts and current conditions measured by the met tower.

To capture the illuminated snowflakes with the desired FOV, the camera was positioned at a standoff distance of 46 m and tilted upward 12° from the horizontal. The Nikon D600 CMOS camera was equipped with a 50 mm Nikon lens to acquire full HD (2.1 megapixel) images at a 30 Hz frame rate. Three image sets were captured, each approximately 15 minutes in duration. An example raw image frame is shown in figure 20(*a*).

The camera height, inclination, and standoff distance determined the center of the FOV, namely its height and its object distance from the camera. The magnification and corresponding pixel resolution at the FOV center were calculated using the object distance and the thin lens formula, yielding a 17 mm pixel^{-1} resolution. The pixel resolution is related to the magnification through the camera sensor resolution. Due to the inclination of the camera, the object distance from the camera to the light sheet increased with increasing height, resulting in non-uniform magnification and resolution values. The FOV extent was determined based on the known FOV center position and the resolution gradient throughout the FOV. Following Toloui *et al.* (2014), the images were corrected to achieve a uniform 17 mm pixel^{-1} resolution with the FOV center as the anchored reference point. The pixel resolution and the FOV height was confirmed using a reference object with a known size and position at the FOV bottom. Despite the confirmation, the estimated uncertainty in the calibrated resolution is 0.7 mm pixel^{-1}, assuming conservative uncertainties of 2 m in the camera standoff distance and 1° in the measured tilt angle.

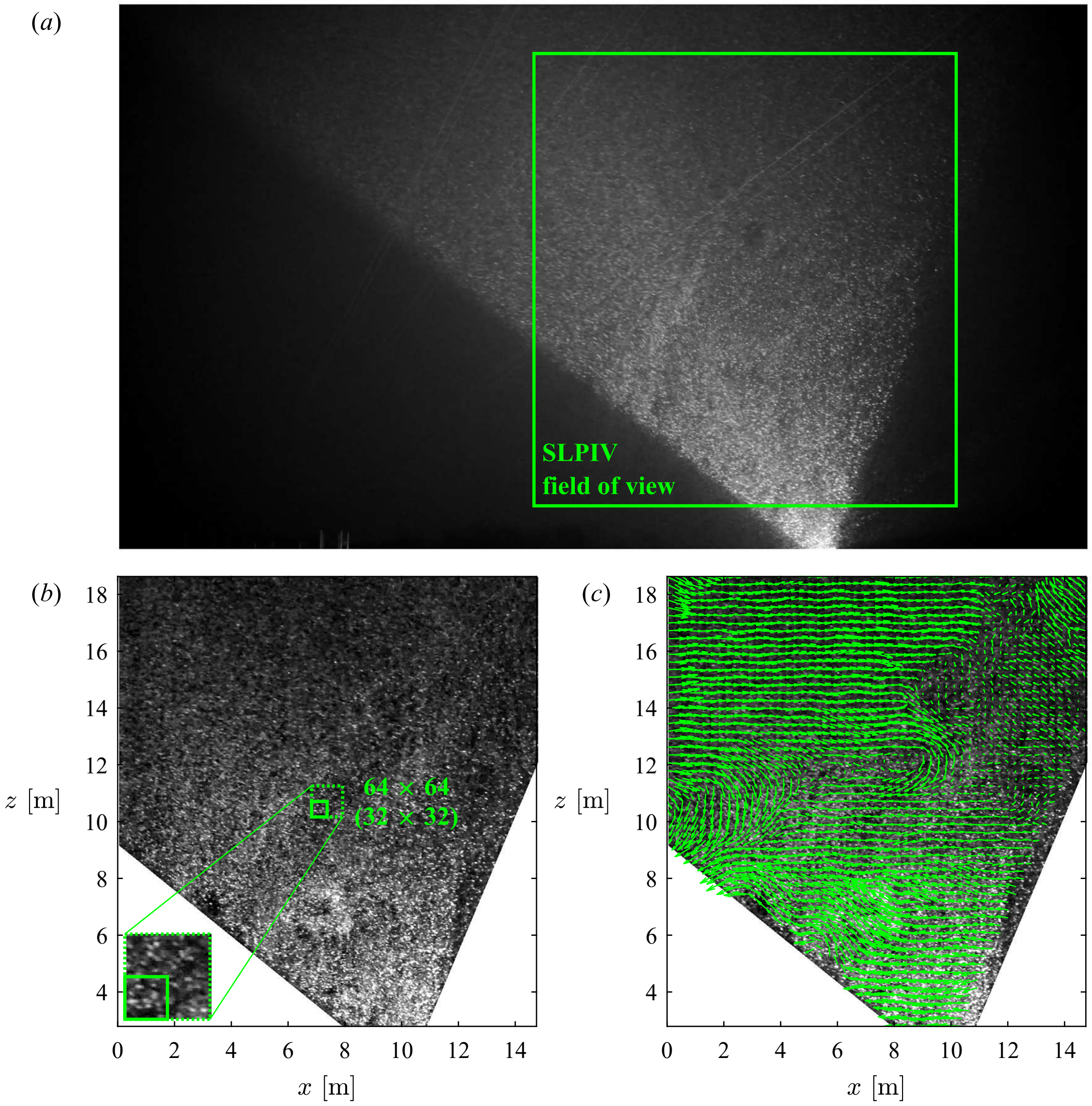

Figure 20. Example SLPIV image field: (*a*) raw image; (*b*) image after cropping, masking, and background subtraction; (*c*) velocity vector field, where a bulk velocity is subtracted to visualize the turbulent motions.

3.1.3 Data processing

Following the magnification correction of the raw images, the images were pre-processed using minimum intensity background subtraction and were masked to exclude non-illuminated areas, resulting in filtered images such as in figure 20(*b*). To estimate velocities between two consecutive frames, cross-correlations on the filtered images were computed using an iterative adaptive correlation scheme (Nemes *et al.* 2015). The scheme used an in-house algorithm on the St. Anthony Falls Laboratory (SAFL) performance computing

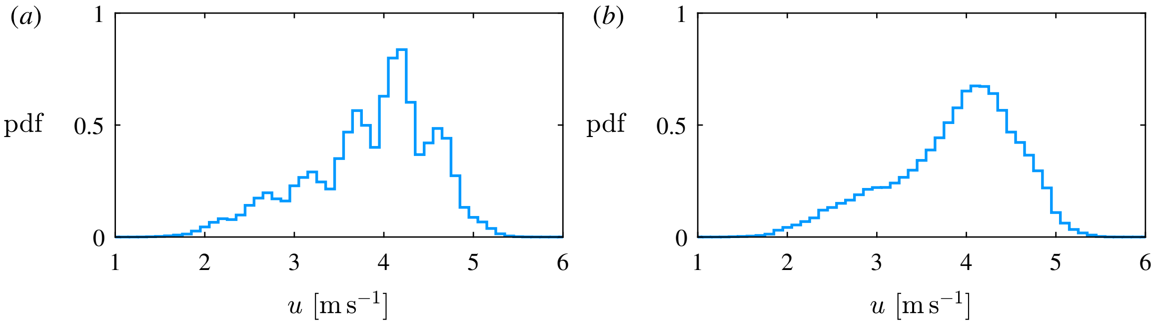

Figure 21. Demonstration of the peak-locking effect on estimated SLPIV velocities: histograms of measured streamwise velocities (*a*) before and (*b*) after histogram equalization to correct for peak locking.

cluster. The interrogation window size for the correlation code was 64 × 64 pixels in the first pass and 32 × 32 pixels in the second pass. A final window deformation pass was performed to improve accuracy of the detected correlation peaks (Scarano 2001). In all passes, a 50% overlap of the windows was employed. Figure 20(*b*) shows the window sizes with respect to the FOV. Outlier vectors were detected and replaced using the criteria of Westerweel & Scarano (2005). To exclude regions where the percent of rejected vectors exceeded 10%, the field of view was cropped to the extents shown in figure 20(*c*). An example velocity field is shown in figure 20.

The resulting velocity vectors exhibited moderate peak locking. This effect occurs when the PIV correlation peak is very narrow, i.e. the peak is much higher at a given pixel displacement than at neighboring values. The routine to estimate the sub-pixel displacement – a Gaussian fit in the peak neighborhood in this case – then strongly favors the peak value, and the pixel displacements are biased towards integer values (Westerweel 1997). The effect of peak locking is evident from the histogram of all velocity values shown in figure 21(*a*) where u is biased towards specific values. Peak locking typically occurs when the imaged particles occupy a small number of pixels, e.g. less than two pixels across the particle diameter, but the particles appear to be larger in the figure 20(*b*) example. Nevertheless, peak locking effects can be mitigated in post-processing using histogram equalization (Roth & Katz 2001). The procedure assumes the correct distribution of sub-pixel displacements is uniform, and maps the observed biased displacements onto the uniform distribution. The equalization was performed separately for each position in the vector field (Hearst & Ganapathisubramani 2015), resulting in the corrected histogram in figure 21(*b*).

From the pixel resolution, final window size in pixels, and percent overlap of windows, the window size was w_I =0.54 m and the spacing between velocity vectors was Δx = 0.27 m. With a surface layer depth $\delta_{SL} \sim O$(100 m), the spatial resolution relative to outer units was $\Delta x/\delta_{SL} \sim O(10^{-3})$. This resolution is finer than previous field studies using met-mounted anemometers, and is also an improvement compared to many previous laboratory studies.

Considering separately the 0.7 mm pixel^{-1} resolution uncertainty and a nominal pixel displacement uncertainty of 0.2 pixels, the roughly-estimated measurement uncertainty for each velocity vector was 0.1 m s^{-1}.

The statistical uncertainty was estimated using 95% confidence bounds, and the total uncertainty was calculated as the magnitude of the measurement and statistical uncertainties. Uncertainty ranges for parameters such as u_τ are discussed later in the text and reflected in figures using error bars.

The SLPIV results yielded a non-zero mean wall-normal velocity due to the settling velocity of the snow W_s. The true mean wall-normal velocity was assumed to be zero such that the measured mean velocity was equal to the settling velocity $W_{piv} = W_s \approx 1.3\ \mathrm{m\,s^{-1}}$. Instantaneous velocities were decomposed from the settling velocity as $w(x, z) = w_{piv}(x, z) - W_s(z)$ and the resulting velocities were treated as the turbulent fluctuations. The validity of this decomposition is discussed below.

3.1.4 Snowflakes as flow tracers

The primary assumption regarding the seeding particles in PIV is that the particles instantaneously respond to flow accelerations. If this is true, the particle velocity is the same as the flow velocity, and measurements of particle movement by PIV provide an accurate representation of the flow. If the particle has finite mass, the particle inertia results in a slower response time to the flow accelerations, and there is a discrepancy between the particle and local flow velocities. The suitability of a particle for seeding a PIV experiment is given by the Stokes number $St_\eta = \tau_p/\tau_\eta$, where τ_p is the particle response time and τ_η is the Kolmogorov time scale corresponding to the shortest time between turbulent flow accelerations. When $St_\eta \ll 1$, the particle responds to a flow acceleration and equilibrates with the flow velocity well before the next turbulent fluctuation, and the particle is a "faithful" tracer of the turbulent fluctuations (Raffel *et al.* 2007).

It is therefore important to estimate the response time τ_p of the snowflakes, which are hereafter referred to as "snow particles" or simply "particles". The standard estimate for the response time of inertial particles is the Stokes drag relationship with a correction for finite particle Reynolds number $Re_p = W_s D_p/\nu$, where D_p is the particle diameter. The corrected formula is $\tau_p = \rho_p D_p^2/18\mu(1 + 0.15Re_p^{0.687})$, where ρ_p is the particle density and μ is the dynamic viscosity of air (Crowe *et al.* 1998). The snow particle properties D_p and ρ_p vary significantly depending on meteorological conditions which affect the snow crystal shape and growth (Nakaya 1954), and must be characterized based on the specific deployment conditions. The snow crystal shape and size was identified using the digital in-line holography system detailed in Nemes *et al.* (2017). Based on 196 particle samples captured by the holography and fresh snow samples from the ground for verification, the observed particles were individual ice crystals in the shape of plates. The hexagonal prism is the most basic ice crystal structure, and these prisms form plates when the preferential growth direction favors the hexagonal face (Pruppacher & Klett 1997). Plates occur when temperatures are within the range –9° to –22° C (Pruppacher & Klett 1997), which is consistent with the surface air temperature –10° to –11° C measured by the met tower during the deployment. The average size of the particles included the face diameter $D_p = 0.61$ mm and the thickness $H_p = 0.25$ mm.

The snow particle density could not be measured directly with the experimental setup, and an empirical model was used to estimate the bulk density. Most existing density models follow a power law relationship $\rho_p = aD_p^b$, where $a = 100$ to 200, $b = –0.9$ to –1, the unit for D_p is mm, and the unit for ρ_p is $\mathrm{kg\,m^{-3}}$ (Brandes *et al.* 2007). Using the suggested values for a and b from three recent references, the estimated bulk density of the particles was $\rho_p = 167$, 213, or 281 $\mathrm{kg\,m^{-3}}$ (Heymsfield *et al.* 2004; Thompson *et al.* 2008; Brandes *et al.* 2007, respectively). The true density was assumed to be within the range of these estimates, and the limits were used to approximate the uncertainty bounds as $\rho_p = 167$ to 281 $\mathrm{kg\,m^{-3}}$.

Based on the measured W_s from the SLPIV, measured D_p from the holography, and estimated ρ_p range from empirical models, the particle Reynolds number was response time was $Re_p \approx 62$ and the response time range was $\tau_p \approx 0.056$ to 0.095 s. Note that the drag correction assumes a solid spherical particle. This assumption can underestimate the snow particle drag and overestimate the response time (Nemes *et al.* 2017). It was also assumed the hexagonal face was always normal to the flow such that the projected area was maximized, thus maximizing τ_p. In the absence of a more accurate drag coefficient estimate, these assumptions were used with the corrected drag formula above and the resulting τ_p is considered conservative.

From the met tower measurements discussed later, the Kolmogorov time scale in the field conditions was $\tau_\eta {\sim} O(0.01$ s). The resulting Stoke number $St_\eta {\sim} O(1$–$10)$ is overly penalizing because the SLPIV interrogation windows did not resolve the Kolmogorov scales. The smallest flow time scale captured by each interrogation window is given by the time for a fluctuation to travel across the window. The relevant SLPIV time scale was $\tau_f = w_I/\sigma_u$, where $\sigma_u = 0.6\ \mathrm{m\,s^{-1}}$ was the maximum measured streamwise root-mean-square (rms) velocity characterizing the turbulent fluctuations. The limiting measurement time scale was therefore $\tau_f = 0.9$ s. The corresponding particle Stokes number range was $St = \tau_p/\tau_f = 0.06$ to 0.11, making the snow particles reasonable tracers for the selected interrogation window size. However, inertial effects are non-negligible for $St {\sim} O(0.1)$. While the largest turbulent motions are well captured by the snow particles as evidenced by the agreement with met tower measurements presented in §3.3, the particles likely cannot trace the most intense acceleration events, specifically small vortices with strongly rotating cores.

Besides the response time, the effect of gravity poses an additional concern for the inertial snow particles. The simplified equation for the particle motion is given by $\partial \mathbf{u}_p/\partial t = (\mathbf{u} - \mathbf{u}_p)/\tau_p - (1 - \rho/\rho_p)\mathbf{g}$, where $\mathbf{u}_p$ is the particle velocity, $\mathbf{u}$ is the local flow velocity, and $\mathbf{g}$ is the gravitational constant (Adrian & Westerweel 2011). The simplified expression already neglects numerous force terms such as lift from the full governing equation (Maxey & Riley 1983), which may be important for non-spherical inertial snow particles. The specific assumption regarding gravity is that the effect of $\mathbf{g}$ in the above expression is uncoupled from the drag force of the flow field such that the mean fall speed W_s can simply be subtracted from the results. It is already known that the flow turbulence can enhance the gravitational settling (Nemes *et al.* 2017; Petersen *et al.* 2019), and the question of whether the gravity force affects the particle fluctuations is not trivial. Finally, it is assumed the snow particles do not affect the turbulent motions, i.e. one-way coupling. The volume fraction of snow particles has been estimated as $O(10^{-7})$ for other SLPIV deployments (M. Guala, private communication), which is within the regime where the one-way coupling assumption should be valid (Elghobashi 1994).

While the snow particles make these measurements possible, many inertial effects cannot be quantified here and are instead neglected. Considering also the known limitations posed by terms such as the Stokes number, care must be taken in interpreting any SLPIV result as an effect of turbulence rather than of particle inertia. Results and trends presented in this thesis are either validated against direct met tower measurements or are shown to be consistent with laboratory-scale experiments and previous literature findings.

Table I. Overview of meteorological conditions during the three SLPIV measurement periods: average wind speed U and direction β at $z = 10$ m, and the local flux Richardson number Ri_f for the listed heights. Adapted from Table 1 of Heisel *et al.* (2018).

	start time	duration	U	β	thermal stability: Ri_f		
data set	[CST]	[min]	[$\mathrm{m\,s^{-1}}$]	[°]	$z = 10$ m	$z = 30$ m	$z = 80$ m
1	2016-12-11 00:31	13	4.1	74	-0.01	0.05	0.24
2	2016-12-11 01:00	15	4.5	72	-0.01	0.06	0.29
3	2016-12-11 01:29	15	4.7	77	-0.01	0.03	0.17

3.2 Meteorological conditions

The goal of the experiment was to study the ASL as a canonical high-Reynolds-number boundary layer. Here, "canonical" means standard flow conditions, such that the field results can be objectively compared with previous studies. Requirements for canonical conditions include stationary (constant) mean wind conditions, negligible buoyancy effects, and no external forcings unique to the field site. The last condition is achieved at the Eolos field site, as the Coriolis parameter can be neglected within the surface layer and the roughness of the farmland is similar across a long distance upstream of the measurements. The first two conditions, however, are harder to achieve as the mean wind conditions frequently vary due to weather and buoyancy forces are often present during the diurnal temperature cycle. The average meteorological conditions for each of the three SLPIV data acquisition periods are given in table I. The wind conditions and thermal stability for these periods are discussed in greater detail in the following subsections.

3.2.1 Mean wind conditions

The mean wind conditions varied throughout the experimental deployment, both in the wind direction and speed. A time series of the average meteorological conditions for the night of the field deployment is provided in figure 22. The wind direction in figure 22(a), measured by a cup and vane anemometer at $z = 7$ m, was aligned with the light sheet at the onset of the deployment, but changes in the mean conditions led to an offset from the light sheet during the three SLPIV data acquisition periods. With the light sheet oriented at 90° (clockwise from north), the average wind directions listed in table I corresponded to an average misalignment of 16°, 18°, and 13° for the three respective SLPIV data periods.

The misalignment of the mean flow and the light sheet can create out-of-plane effects in the PIV correlation. If illuminated particles frequently disappear between consecutive frames because they travel out of the illuminated area, the correlation peaks and the signal-to-noise ratio both decrease (Raffel *et al.* 2007). Considering here the second SLPIV data set which has the highest misalignment, the mean wind speed and direction listed in table I result in an average $1.4\ \mathrm{m\,s^{-1}}$ out-of-plane velocity. Based on the 0.4 m thickness of the light sheet and 30 Hz sampling rate of the camera, the mean expected residence time of particles in the light sheet was 8 frames. The snow particles entering and exiting the light sheet plane from the mean out-of-plane motion did not significantly impact the correlations because a majority of particles remained in the plane for numerous frames.

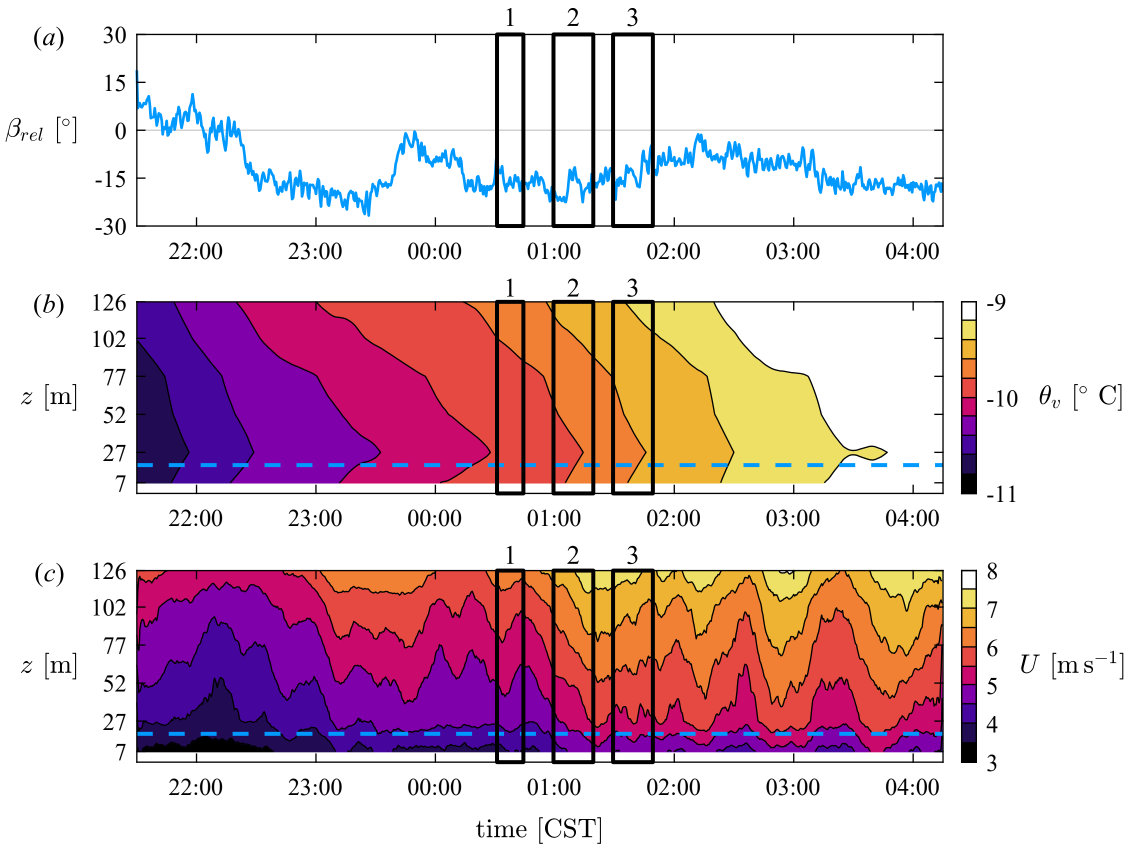

Figure 22. Extended time series of meteorological conditions as measured by met tower sensors. (*a*) 1-minute moving average wind direction β relative to the light sheet orientation, measured at $z = 7$ m. (*b*) Virtual potential temperature θ_v space-time contour. (*c*) Horizontal wind speed U space-time contour. The three SLPIV data periods are indicated by the numbered boxes. The contour plots in (*b*) and (*c*) were interpolated from 10-minute moving averages at the six measurements altitudes shown in the vertical axes. The blue dashed lines in (*b*) and (*c*) represent the top height of the SLPIV imaging field. Adapted from Figure 2 of Heisel *et al.* (2018).

To calculate velocity statistics presented in §3.3, I rotated the met tower measurements into the mean wind direction for each data period. I also projected the SLPIV streamwise velocity statistics onto the mean wind direction to compensate for the misaligned light sheet. The projection followed the standard coordinate rotation formula

$$u_{piv} = u_\perp \cos\beta_{rel} - v_\perp \sin\beta_{rel}, \tag{8}$$

where "⊥" indicates the coordinate system aligned with the mean wind and β_{rel} is the light sheet misalignment. For the mean velocity, the spanwise component was $V_\perp = 0$ by definition of the coordinate system, and $U_\perp$ could be estimated directly. As an example, the compensation for SLPIV data set 2 was an approximate 5% increase: $U_\perp = U_{piv}/\cos 18^\circ = 1.05U_{piv}$. For instantaneous vector fields, $v_\perp \neq 0$ and $u_\perp$ cannot be estimated directly from equation (8). Rather than attempt any projection with an assumed spanwise velocity,

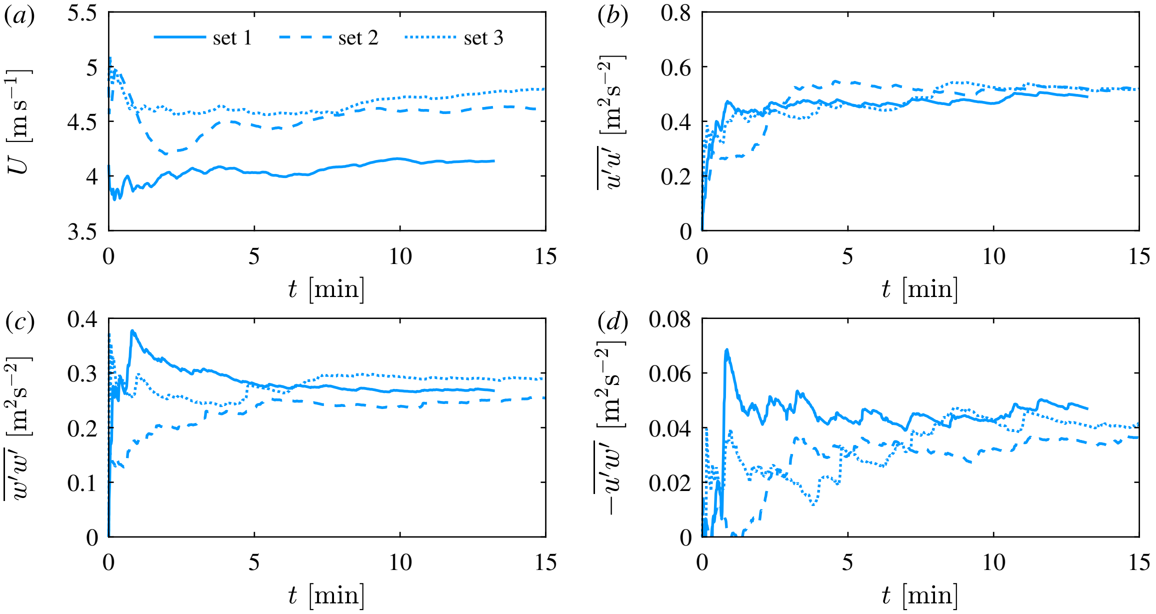

Figure 23. Convergence of first- and second-order velocity statistics for the three SLPIV data set periods. The statistics are based on sonic anemometer measurements at $z = 10$ m projected onto the mean wind direction. (*a*) The mean velocity U. (*b*) The streamwise variance $\overline{u'u'}$. (*c*) The wall-normal variance $\overline{w'w'}$. (*d*) The Reynolds shear stress $-\overline{u'w'}$. Adapted from Figure 3 of Heisel *et al.* (2018).

the analysis in chapter 4 was based on the original light sheet orientation. The misalignment may lead to underestimated streamwise velocity statistics by up to 5% and this effect was incorporated into the estimated uncertainties.

Variations in the mean wind condition can lead to unconverged statistics. Velocity statistics will continue to change if the mean conditions are changing (i.e. non-stationarity). Figure 23 depicts the statistical convergence for the three SLPIV data periods using sonic anemometer measurements at $z = 10$ m. The statistics at a given time t were calculated as the average up to that time, e.g. $U(t) = \frac{1}{t}\int^{t} u(t_*)\,dt_*$ where t_* is a dummy variable for time. The mean velocities in figure 23(*a*) increased slowly towards the end of the period, most noticeably for sets 2 and 3, which indicates slowly-varying wind conditions. To account for the increasing mean, the streamwise velocity fluctuations of the met tower and SLPIV data were calculated by subtracting a linear slope from the velocity series rather than a single time-averaged mean.

Velocity statistics, particularly higher-order turbulent quantities, will also be unconverged if an insufficient number of the largest turbulent events are recorded. Statistical convergence of the velocity variances, based on the linear detrending, are shown in figure 23(*b-d*). The streamwise and wall-normal variances in 23(*b,c*) are relatively well converged. The effect of large-scale motions on the Reynolds shear stress is visible in 23(*d*), where the average value for $-\overline{u'w'}$ is still fluctuating after 10 minutes. The very-large-scale motions contributing to the turbulent stresses have streamwise extent up to 5δ (Smits *et al.* 2011), which corresponds to an approximate two minute turnover time based on the mean wind speed and $\delta_{SL}{\sim}O(100\text{ m})$. This turnover time is consistent with the variations in figure 23(*d*), which may be due to intense sweep events increasing the average $u'w'$, followed by a gradual decrease in the average before the next large sweep. While the shear stress data do not appear fully converged due to the limited number of these events, the changes in $-\overline{u'w'}$ for data set 1 are less than 4% in the final two minutes of the acquisition period.

3.2.2 Thermal stability

As discussed in §1.2.1, temperature differences lead to density differences and corresponding buoyancy forces in the atmosphere that either promote vertical air movement (positive buoyancy, thermally unstable) or act against the movement (negative buoyancy, stably stratified). Because the forces are due to gravity, the buoyancy only acts directly on the vertical velocity component in the Navier-Stokes equations, which here is the wall-normal component w. After applying the Reynolds decomposition, the Navier-Stokes equation for w can be premultiplied by w' and averaged to reveal the statistical terms that contribute to the wall-normal velocity variance $\overline{w'w'}$. The resulting budget equation for the wall-normal variance includes the buoyancy term

$$B = \frac{g}{\theta_v}\overline{w'\theta_v'}. \tag{9}$$

where θ_v is the virtual potential temperature. The buoyancy term directly results from the density fluctuations ρ', but density is difficult to measure experimentally. The virtual potential temperature is the temperature that dry air at standard atmospheric pressure must have to equal the density of air described by a given temperature, moisture content, and pressure. Removing the effects of moisture and pressure allows for θ_v to be directly related to ρ through the ideal gas law as $\rho'/\overline{\rho} = -\theta_v'/\overline{\theta_v}$ (Stull 1988). The temperature, which is relatively easy to measure, then replaces density in equation (9). The heat flux $\overline{w'\theta_v'}$ describes the extent to which the temperature fluctuations enhance (positive correlation $\overline{w'\theta_v'} > 0$) or suppress (negative correlation) the wall-normal movement.

Same as the wall-normal component, the Navier-Stokes equation for u can be premultiplied by u' to derive the budget equation for the streamwise velocity variance. The equation includes the previously mentioned shear production term

$$P = -\overline{u'w'}\frac{\partial U}{\partial z}. \tag{10}$$

While the buoyancy and mean shear production statistics arise from different velocity components, they are related through the mean turbulent kinetic energy $\mathrm{TKE} = \frac{1}{2}(\overline{u'u'} + \overline{v'v'} + \overline{w'w'})$. The relative importance of buoyancy and shear production to the turbulent kinetic energy is expressed by the dimensionless flux Richardson number Ri_f, which is simply the ratio of B and P:

$$Ri_f = \frac{\dfrac{g}{\theta_v}\overline{w'\theta_v'}}{\overline{u'w'}\dfrac{\partial U}{\partial z}}, \tag{11}$$

where the negative sign from the shear production is dropped by convention (Stull 1988). Each term in equation (11) can be estimated from the Eolos met tower measurements aside from the mean shear $\partial U/\partial z$

which requires multiple anemometers positioned close together to approximate the gradient. The shear can instead be assumed to follow equation (4) for the neutrally stratified log region. For surface measurements, e.g. at $z = 10$ m, if $\partial U/\partial z = u_\tau/\kappa z$ and $\overline{u'w'} \approx -u_\tau^2$ are substituted into equation (11), the flux Richardson number is then equivalent to the Monin-Obukhov stability parameter $\zeta = z/L_o$, where L_o is the Obukhov length $L_o = -u_\tau^3\overline{\theta_v}/\kappa g\overline{w'\theta_v'}$ (Monin & Obukhov 1954).

The ASL is considered near-neutrally stratified with negligible buoyancy effects when $B \ll P$ such that the magnitude of Ri_f or ζ are small, e.g. $|\zeta| \lesssim 0.1$ (Högström *et al.* 2002). The convective, thermally unstable ASL corresponds to negative Ri_f values, and the stably stratified ASL corresponds to positive Ri_f. Turbulent energy production in thermally stable conditions is sustained in the ASL until negative buoyancy matches shear production, i.e. $Ri_f \approx 1$, and above this point the flow may be laminar (Stull 1988).

The met tower measurements were used to estimate Ri_f during the SLPIV deployment. The virtual potential temperature θ_v was calculated using 1 Hz temperature, pressure, and relative humidity measurements. The pressure and relative humidity were required to convert the measured temperature θ to the virtual potential temperature θ_v based on ideal gas and partial pressure laws (Stull 1988). Because the virtual temperature conversion was only possible for the 1 Hz measurements, the heat flux was approximated as $\overline{w'\theta'}$ using detrended 20 Hz sonic anemometer measurements. The momentum flux $\overline{u'w'}$ was also estimated with the sonic anemometer data. Lastly, the previously described shear assumption $\partial U/\partial z = u_\tau/\kappa z$ was applied. Determination of u_τ is described in §3.3.

The estimated Ri_f values at the three sonic anemometer heights are given in table I. For each data period, the Ri_f values near the surface were small and buoyancy was negligible compared to the strong shear production, but at higher elevations, e.g. $z = 80$ m, the flow was stably stratified. The Ri_f values are consistent with the potential temperature θ_v space-time contour in figure 22(*b*). The stability conditions at the surface were near-neutral where the temperature gradient $\partial\theta_v/\partial z$ was flatter. The gradient was increasingly negative at higher elevations where Ri_f values indicated increased stability.

The $Ri_f(z)$ trends in table I appear consistent between the three data periods, but the effects of stability were not equal. The space-time contour of wind speed in figure 22(*b*) shows an extended period of relatively constant (low-pass filtered) wind speed at the second measurement height ($z = 27$ m) between 23:00 and 01:00 local time. The wind speed increased significantly beginning at 01:00. Very long motions with a period of 45 to 60 minutes are apparent in the contours throughout the remainder of the morning. These motions were likely waves associated with stably stratified flows (Mahrt 2014). The waves appear to have propagated down below the top of the SLPIV imaging field during data sets 2 and 3, and they may have modulated the near-surface turbulence. The velocity profiles are next analyzed to assess whether the SLPIV measurements were affected by the weakly stable stratification.

Table II. Scaling parameters for the Eolos field site during the three SLPIV data acquisition periods. Adapted from Table 2 of Heisel *et al.* (2018).

data set	symbol	u_τ [m s^{-1}]	ν/u_τ [mm]	η [mm]	δ_{SL} [m]	z_o [m]	k_s [m]	k_s^+	ΔU^+	Re_τ
1	$\circ$	0.30±0.03	0.042	0.7±0.2	70–200	0.04	1.2	29 000	22.1	$1.7-4.7\times10^6$
2	$\times$	0.32±0.03	0.039	0.7±0.2	70–200	0.04	1.2	31 000	22.3	$1.8-5.1\times10^6$
3	$+$	0.33±0.03	0.038	0.7±0.2	70–200	0.04	1.2	32 000	22.4	$1.8-5.3\times10^6$

3.3 Measurement validation

3.3.1 Site parameterization

The methods used to calculate the velocity statistics, described in the previous sections, are summarized here: the mean snow settling speed was subtracted from the SLPIV vertical velocities, the velocities were linearly detrended to estimate the turbulent fluctuations, and the streamwise statistics were projected onto the mean wind direction. The compensated velocity profiles were used to estimate separate values of the friction velocity u_τ for each data set. The values of u_τ were determined manually by collapsing the velocity profiles of the three sets and aligning the slope of the mean velocity with the theoretical log law slope κ^{-1} given in equation (5). The determination of u_τ also considered the theoretical Reynolds shear stress peak $-\overline{u'w'}^+_{max} \approx 1$. A least squares fit of the profiles was not employed to define u_τ due to the fact that multiple profiles and conditions were considered simultaneously. The resulting values are given in table II. The estimated 10% uncertainty bounds for u_τ includes the experimental and convergence uncertainty for $-\overline{u'w'}_{max}$.

With u_τ defined for each data set, a single value for the aerodynamic roughness length z_o (k_s) was determined. Because the conditions are well within the fully rough regime, z_o and k_s depended only on the surface geometry and did not change between data sets. The length z_o was calculated using a non-linear least squares fit of all the mean velocity data points up to $z = 70$ m to achieve alignment with the log law formulation in equation (7). The estimated aerodynamic roughness length for the Eolos site was $z_o = 0.04$ m, which is within the expected range $z_o = 0.01$ to 0.05 m for farmland (Stull 1988; Garratt 1994). Because the snow cover was shallow and had not concealed the underlying roughness, the surface asperities from the overturned soil accounted for some of the aerodynamic roughness. The roughness z_o therefore corresponded to a combination of the asperities and protruding vegetation, where the vegetation was consistent with early wheat of roughness height $k = 0.4$ m (Raupach *et al.* 1991). The equivalent sand grain roughness was then calculated as $k_s \approx 30z_o \approx 1.2$ m, and the roughness function ΔU^+ was estimated from equation (6).

To evaluate the smallest flow scale, i.e. the Kolmogorov length scale $\eta \equiv (\nu^3/\epsilon)^{1/4}$, the turbulent energy dissipation rate ϵ must first be approximated. A common assumption for the log region is an equilibrium between shear production and dissipation $\epsilon \approx P$, and in the log region the production follows the theoretical form $P = -\overline{u'w'}(\partial U/\partial z) = u_\tau^2(u_\tau/\kappa z) = u_\tau^3/\kappa z$ for high-Reynolds-number boundary layers. This leads to the Kolmogorov length scale estimate $\eta = (\kappa z \nu^3/u_\tau^3)^{1/4}$. For the SLPIV field of view $z = 3$ to 18 m, the estimate yields $\eta \approx 0.7\pm0.2$ mm.

The largest flow scale given by the surface layer depth δ_{SL} was generally unknown for the Eolos field site. The mean velocity profile deviated strongly from the expected log law behavior near $z = 70$ m, which is why the log law was not fitted above 70 m for determining u_τ and z_o. The mean velocity profiles are shown in figure 24 and are discussed in greater detail in the following subsection. The surface layer definition is in some ways analogous to the log region of a conventional boundary layer, such that a conservative estimate for the depth is $\delta_{min} \approx 70$ m where the logarithmic behavior ends. However, the departure from the log law may have been due to the stable stratification at higher elevations. Alternatively, the depth can be estimated following the traditional laboratory definition using the free stream condition. The free-stream velocity was not reached by the top of the met tower ($z = 130$ m) based on the mean velocity profiles in figure 24, and I chose a nominal maximum estimate $\delta_{max} \approx 200$ m. A more accurate estimation of δ_{SL} is not feasible without additional velocity measurements above the met tower. The Reynolds number range resulting from the δ_{SL} limits is $Re_\tau \approx 2{-}5{\times}10^6$, which is comparable to other atmospheric studies (Kunkel & Marusic 2006; Hutchins *et al.* 2012; Wang & Zheng 2016). The Re_τ values, in addition to the other parameters discussed above, are listed in table II.

3.3.2 Velocity profiles

The compensated mean velocity profiles for the three data sets, normalized in viscous units following the log law form in equation (5), are shown in figure 24(*a*). Included for reference are velocity profiles from rough-wall laboratory studies (Krogstad *et al.* 1992; Schultz & Flack 2007; Flack *et al.* 2007; Squire *et al.* 2016b; Morrill-Winter *et al.* 2017) as well as atmospheric studies at the SLTEST (Kunkel & Marusic 2006; Hutchins *et al.* 2012) and QLOA (Wang & Zheng 2016) facilities. Additional atmospheric measurements from other met-mounted anemometer studies (Clarke *et al.* 1971; Tieleman 2008) are also included. The displacement of each profile from the smooth wall reference line is given by the roughness function ΔU^+ as previously discussed.

The Eolos profiles exhibit the expected log-linear increase in mean velocity up to approximately $z = 70$ m. The log-linear range was captured by the SLPIV (blue markers), sonic anemometers (magenta) and cup and vane anemometers (green). The upper limit of the range is somewhat arbitrary due to the low spatial resolution of the met tower. There was close agreement in the mean velocity estimate between the SLPIV and sonic data at $z = 10$ m. The higher velocity from the cup and vane measurements at $z = 7$ m was likely overestimated based on the discrepancy with both the nearest SLPIV and sonic estimates.

The fully rough flow cases shown in figure 24(*a*), including the Eolos data, are re-plotted in figure 24(*b*) following the standard meteorological log law form in equation (7). Only the fully rough cases are included, for which z_o can be calculated directly from the k_s values reported in the cited literature. The collapse of the experimental data along the theoretical line validates the values of u_τ and z_o for both the Eolos data and the cited studies.

The variance profiles for the three Eolos data sets are shown in figure 25 with the same literature comparison as the mean velocity profiles. The expected log-linear decrease in streamwise variance is observed

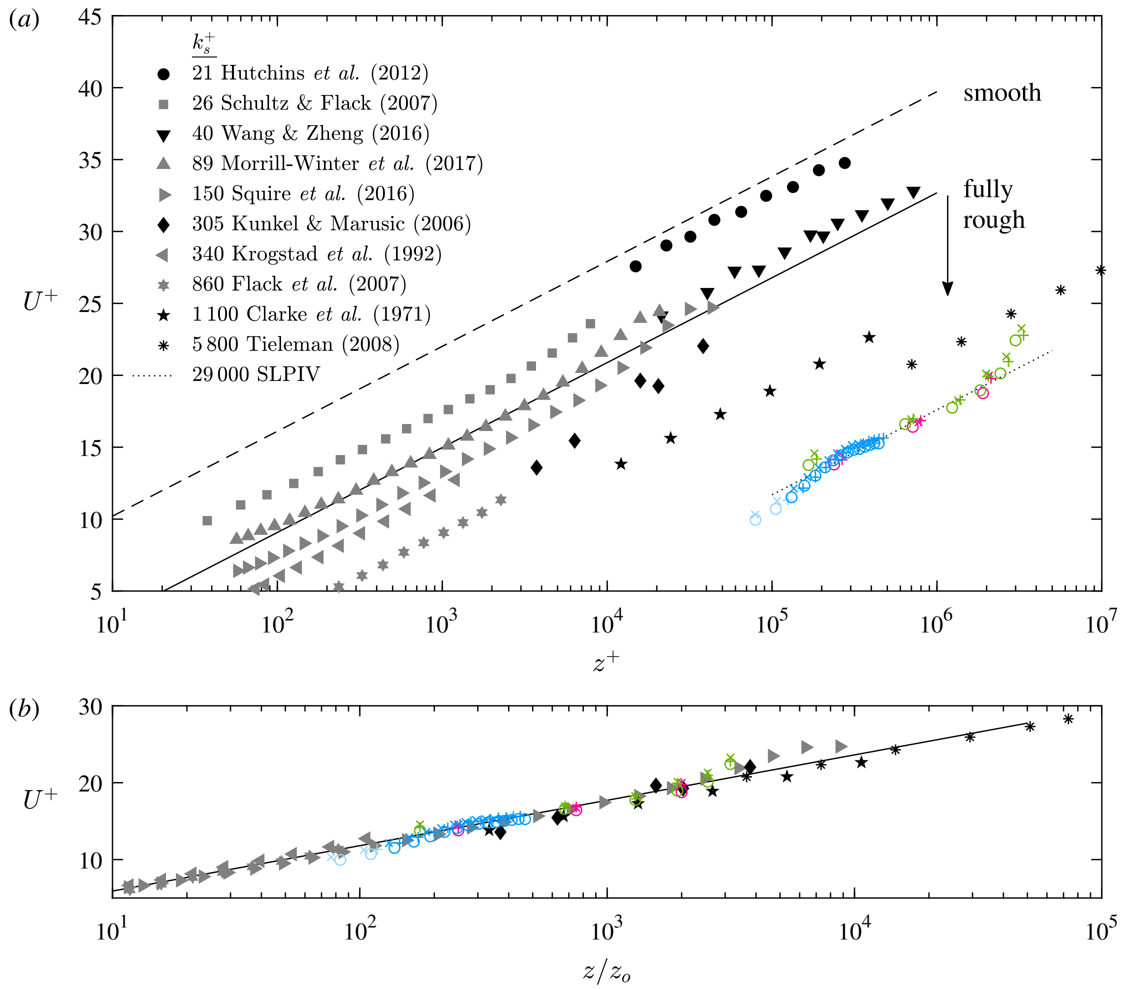

Figure 24. Mean velocity profiles for the three SLPIV data sets compared with selected results of laboratory (gray symbols) and atmospheric (black symbols) studies. The wall-normal position is normalized using (*a*) viscous wall units and (*b*) the aerodynamic roughness length. Reference lines in (*a*) for smooth wall (– –), transition to fully rough (——), and the present data (· · ·) have slope κ^{-1}. Symbols for the SLPIV (blue), sonic (magenta), and cup (green) data are defined in table I. Every fourth SLPIV data point is shown for clarity. Adapted from Figure 4 of Heisel *et al.* (2018).

beginning at $z = 5.5$ m ($z^+{=}2.2{\times}10^5$). Together with the agreement between the Eolos mean velocity profiles and equation (5) up to $z = 70$ m, the log-linear behavior of $\overline{u'u'}^+$ suggests a log region from $z = 5.5$ to 70 m. The region below 5.5 m is assumed to be the roughness sublayer. The data points in the sublayer are shown with transparency in figures 24 and 25. The extent of the roughness sublayer exceeds somewhat the $5k \approx 2$ m limit suggested by Flack *et al.* (2007), but the sublayer height likely depends on the specific roughness geometry and the agreement is reasonable considering the disparity in flow scales between the present work and the cited study.

The SLPIV data do not capture a near-wall streamwise variance peak in figure 25(*a*). However, the near-wall peak would have been below the field of view, and the peak was very likely not present due to

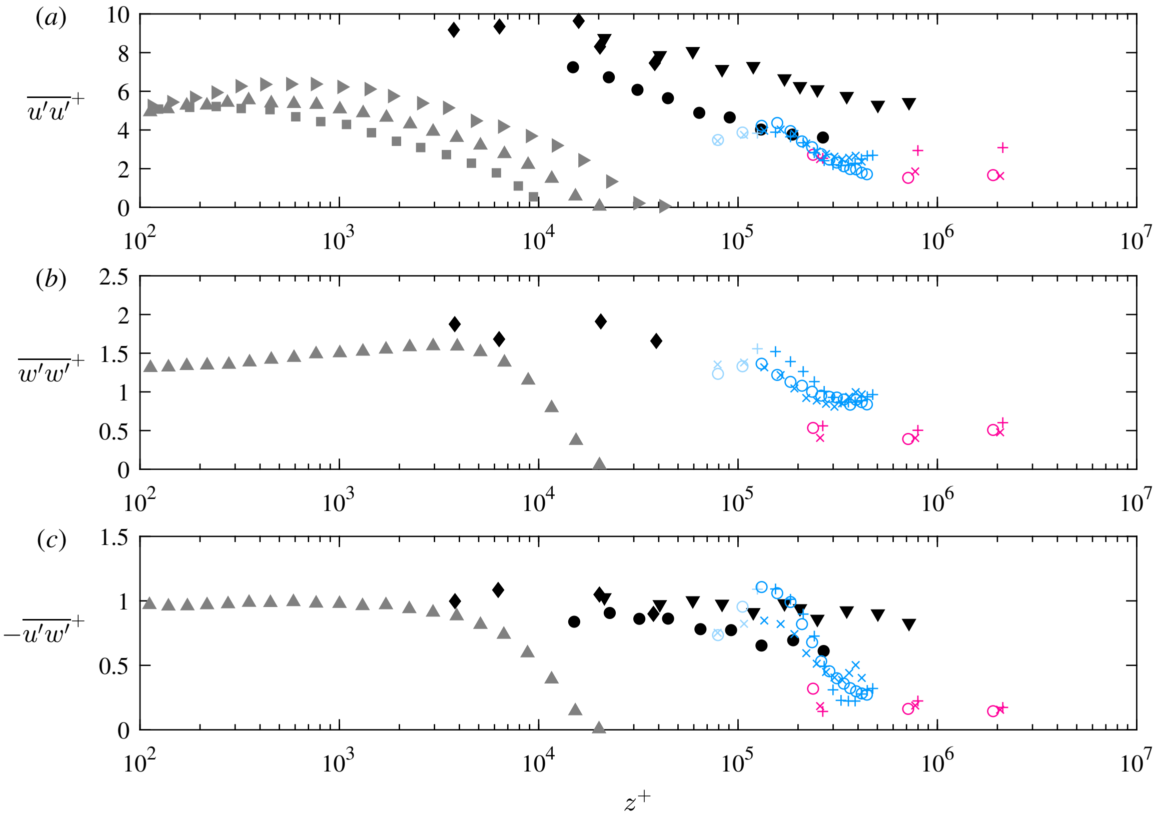

Figure 25. Turbulent velocity profiles for the three SLPIV data sets and selected literature results. (*a*) The streamwise variance $\overline{u'u'}^+$. (*b*) The wall-normal variance $\overline{w'w'}^+$. (*c*) The Reynolds shear stress $\overline{u'w'}^+$. Literature symbols are defined in the figure 24 legend. Symbols for the SLPIV (blue) and sonic (magenta) data are defined in table I. Every fourth SLPIV data point is shown for clarity. Transparent points are within the estimated roughness sublayer. Adapted from Figure 5 of Heisel *et al.* (2018).

destruction of the near-wall turbulence cycle by the roughness elements (Grass 1971). The peak values in each variance profile are otherwise in agreement with previous literature. In particular, the streamwise variance in figure 25(a) and wall-normal variance in 25(b) are consistent with other field measurements. Further, the SLPIV streamwise rms velocity σ_u was within 6% of the sonic anemometer measurements at $z = 10$ m. The difference between the SLPIV and sonic results was much greater for the wall-normal rms velocity. For the first Eolos data set, the σ_w measured by the sonic anemometer was 27% lower than the SLPIV result. This discrepancy is likely responsible for the similar large difference in the Reynolds shear stress in figure 25(c). Based on the agreement of the SLPIV wall-normal variance peak $\overline{w'w'}^+ \approx 1.25$ with previous literature, I assume the error was primarily in the sonic anemometry result. Multiple studies have demonstrated scenarios leading to underestimates and errors in the vertical velocity measured by sonic anemometers. These scenarios include non-orthogonality of the anemometer (Frank *et al.* 2013), flow distortion from the met tower mast mount (Grant & Watkins 1989), and a combination of snow precipitation and icing conditions (Makkonen *et al.* 2001). The last explanation is the most probable, considering the weather conditions during measurement.

3.4 Canonical or not?

Ideally, the variances in figure 25 would be plotted as z/δ and the outer region results would collapse with the rough-wall literature in accordance with Townsend's outer layer similarity. Unfortunately, the lack of an accurate δ_{SL} estimate and the effect of stable stratification on the turbulence statistics prevent such a collapse. The stability effects are most apparent in the sharp decline of the Reynolds shear stress in figure 25(*c*). The decline begins well below the uncertainty range of the surface layer depth δ_{SL} = 70 to 200 m, and the mean velocity continues to follows a logarithmic trend up to 70 m.

A second explanation for the Reynolds shear stress decrease follows Hunt & Carlotti (2001) and Drobinski *et al.* (2004). In their argument, the surface layer is further separated into two sublayers: a near-wall region where turbulent motions interact directly with the wall (i.e. the "attached" eddies) and an upper region where top-down turbulent motions are "detached" from the wall. The extent of the near-wall region predicted by Hunt & Carlotti (2001) depends on the roughness, and for the Eolos field site roughness the prediction matches well with the observations.

A likely possibility is that both explanations have merit. The partitioning of the boundary layer into a near-neutral, shear-dominated region close to the ground and a stably stratified upper region is qualitatively similar to the classification by Hunt & Carlotti (2001). Top-down motions from the stable upper region, including the waves observed in figure 22(*c*), may have sporadically interacted with the shear-driven region. This possible top-down interaction may have created the stability effects near the top of the SLPIV imaging field, which were stronger than the local stability parameter would indicate (i.e. Ri_f = 0.05 at z = 30 m). A final possibility is that the SLPIV measurement noise was greater near the top of the field of view, which may explain some of the covariance decrease.

Regardless of the cause, the Reynolds shear stress statistics begin to depart from the theoretical log region profile above z = 11 m. Below z = 11 m and above the roughness sublayer, the mean velocity and variance statistics follow the canonical behavior for the log region. This region is therefore the focus of the analysis in chapter 4. The remainder of the analysis uses only data set 1 (circles). The steadiest meteorological conditions occurred during set 1 with respect to the wind direction in figure 22(*a*), the potential thermal stability effects in figure 22(*c*), and the converged wind speed in figure 23(*a*). Further, the velocity variance profiles for set 1 in figure 25 exhibited the least variability near the top of the SLPIV field ($z^+ \approx 5\times10^5$). Data set 1 was therefore inferred to most closely represent a canonical rough-wall boundary layer.

4 Detection of coherent structures in the surface layer

Chapter 4 comprises an edited version of sections 4 through 7 of the article below, published in the *Journal of Fluid Mechanics*, © Cambridge University Press 2018. Please cite the published article when referencing content in this chapter.

Heisel, M., Dasari, T., Liu, Y., Hong, J., Coletti, F., and Guala, M. (2018). The spatial structure of the logarithmic region in very-high-Reynolds-number rough wall turbulent boundary layers. *J. Fluid Mech.* **857**, pp. 704-747. https://doi.org/10.1017/jfm.2018.759.

4.1 Hairpin-like packet signature

Before assessing the coherent structures in the ASL in the framework of uniform momentum zones and internal shear layers, it is worth investigating other structural features seen in previous laboratory-scale PIV studies. In particular, this section presents evidence of the hairpin packet signature in the rough-wall ASL.

4.1.1 Visual evidence

I used the instantaneous SLPIV vector fields to identify possible hairpin-like structures. An example realization from data set 1 is shown in figure 26(*a*). To highlight the spanwise vortices and make their circular core apparent, a bulk advective velocity U_c approximately equal to the local velocity of the vortices was subtracted from the SLPIV field. The resulting vector field shares the same signatures of hairpin vortices as the visualizations in figures 10 and 11 of Adrian *et al.* (2000b): (i) the spanwise vortices are at the head of a shear layer and both are advected at the same speed; (ii) the shear layer has a forward inclination of approximately 35° above horizontal; (iii) the shear layer separates an ejection event from below and a sweep event from above. To more clearly identify the cores of the vortex heads, figure 26(*b*) shows a color plot of the two-dimensional swirling strength λ_{ci} (Adrian *et al.* 2000a), where the sign of λ_{ci} is based on the out-of-plane vorticity ω_y. The regions of negatively-signed swirl indicate prograde vortices rotating in a direction consistent with the mean shear, i.e. clockwise in the figure 26 reference frame.

Given the presence of multiple vortex heads along the single shear layer, the signature resembles the hairpin vortex packet rather than the individual hairpin vortex. This signature has previously been observed for rough-wall boundary layers in laboratory studies (see, e.g., Volino *et al.* 2007; Hong *et al.* 2011). Despite the striking similarities between the vortex structure in figure 26 and a hairpin packet, the visualization is limited to the two-dimensional $x - z$ plane, and the three-dimensional shape of the vortex tubes is unknown. Additionally, the example was certainly "cherry-picked", and most instances did not have a clear hairpin

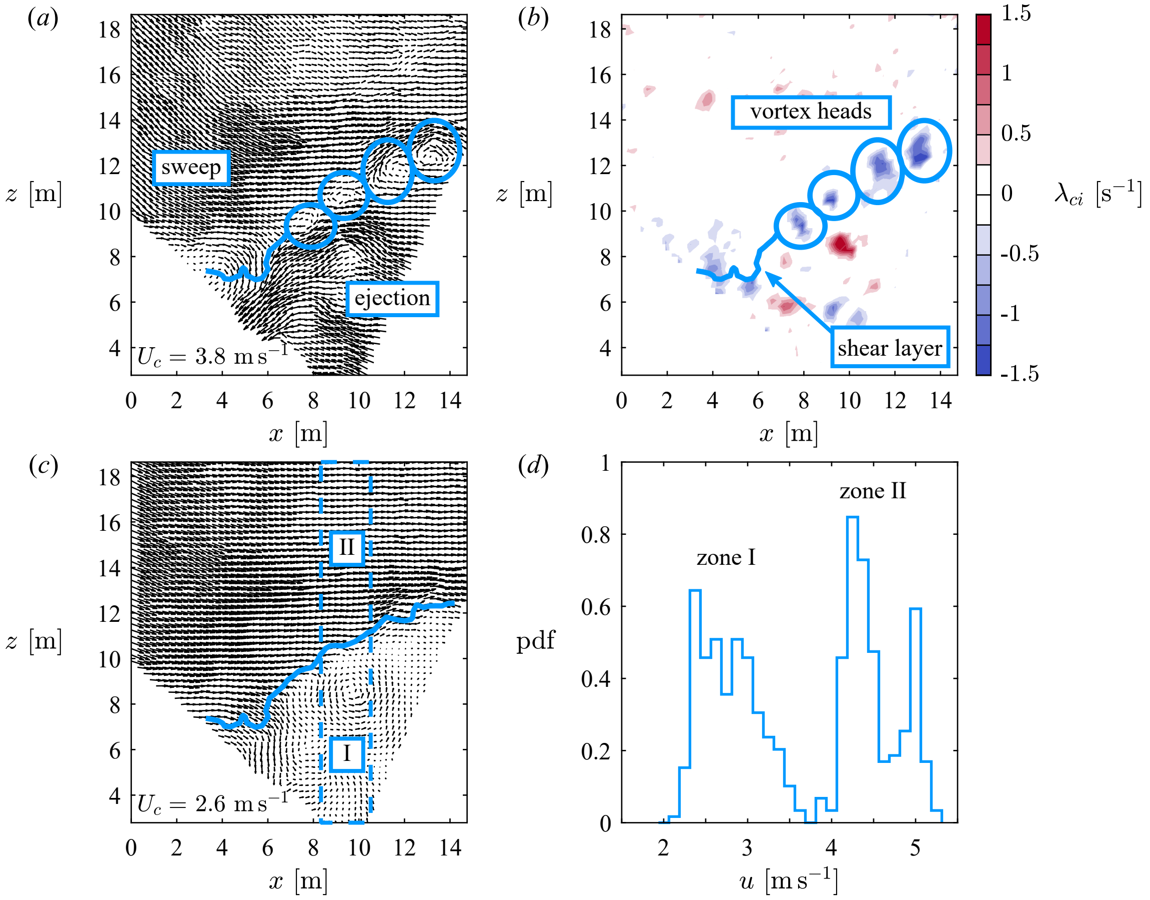

Figure 26. Realization of a vortex structure having the signature of a hairpin-like packet with four vortex heads along an inclined shear layer. (*a*) Sweep and ejection regions on either side of the shear layer. (*b*) Identification of the vortex cores by the swirling strength λ_{ci}. (*c*) Zones of uniform momentum separated by the shear layer. (*d*) Histogram of streamwise velocities for vectors within the dashed box of (*c*). The quiver plot reference frames in (*a*) and (*c*) use the advective velocity $W_c = -1$ m s^{-1} and the listed U_c. The shear layer line in (*a*-*c*) is a contour of $u = 3.75$ m s^{-1}, the minimum occurrence velocity between the histogram peaks in (*d*). Adapted from Figure 6 of Heisel *et al.* (2018).

signature. Nevertheless, the example provides anecdotal evidence of an inclined vortex structure extending up to $z = 12$ m that shares features similar to a hairpin packet and the representative attached Λ-packet eddy. The influence of these inclined shear layer events on overall statistics is investigated in the following subsection.

In a generalized description of the velocity signature in figure 26(*a*), the shear layer separates two regions of distinct momentum, leading to the UMZ-ISL classification introduced by (Meinhart & Adrian 1995). The UMZs are more visually apparent when a new advective velocity U_c equal to the speed of lower momentum region is subtracted from the flow field. The vector field resulting from this new U_c value is shown in figure 26(*c*). The vector field clearly shows a low- and high-momentum region below and above the shear layer, respectively. As discussed in §2.2.5, the presence of UMZs is shown statistically using histograms of the streamwise velocities in the vector field as seen in figure 26(*d*). To avoid selection bias in the non-rectangular SLPIV field, I limited the vectors contributing to the histogram to the rectangular area outlined by the dashed box in figure 26(*c*). The contour for the shear layer in figure 26(*a-c*) is represented statistically by the minimum in the histogram at $u = 3.75\ \mathrm{m\,s^{-1}}$. The presence of a signature for both a hairpin-like packet and a UMZ in the figure 26 realization highlights the effect of the reference frame on the classification of the structure. It is therefore important to recognize the overlap in the definition of hairpin-type packets and UMZs when interpreting structures in instantaneous velocity fields.

In figure 26 and many later figures, I chose to present the distances x and z dimensionally rather than normalized by δ_{SL} or ν/u_τ. This choice hopefully allows the reader to appreciate the extreme physical scale of these turbulent features compared to previous laboratory studies. Further, the correct scaling parameter is likely the wall-normal distance z. The vortex structure in figure 26 reaches heights far from both the rough wall ($z^+{\sim}10^5$, $z/k{\approx}30$) and the top of the ASL ($z/\delta_{SL}{\sim}0.1$) such that z is the relevant length scale in accordance with theory for the log region.

4.1.2 Statistical evidence

As discussed in §2.2.6, the signature of inclined shear layers and ramp-like structures is apparent from the shape of the two-point correlation. The correlation is a statistical measure of velocity coherence, and the two-point correlation is inclined if the statistically relevant coherent velocity structures are similarly inclined. The present analysis is specifically for correlations of the streamwise velocity. For a given reference height z_{ref}, the two-point correlation ρ_{uu} is defined at each height z and streamwise separation distance r_x as

$$\rho_{uu}(r_x, z, z_{ref}) = \frac{\langle u'(x, z_{ref})u'(x + r_x, z)\rangle}{\sigma_u(z_{ref})\sigma_u(z)}, \tag{12}$$

where the brackets $\langle\cdot\rangle$ indicate the average correlation across each x position at the reference height. The correlation definition uses the fluctuations u', such that the mean shear is absent from the reference frame for the statistic. The inclination of ρ_{uu} is therefore not strictly representative of the average structure shape, but the result provides a qualitative assessment of the inclines structures. An alternative is to calculate the fluctuations in equation (12) as $u`(z) = u(z) - U(z_{ref})$ to avoid subtraction of the mean shear. Figure 27 compares a sample correlation map ρ_{uu} resulting from the standard and alternative fluctuation definitions. In

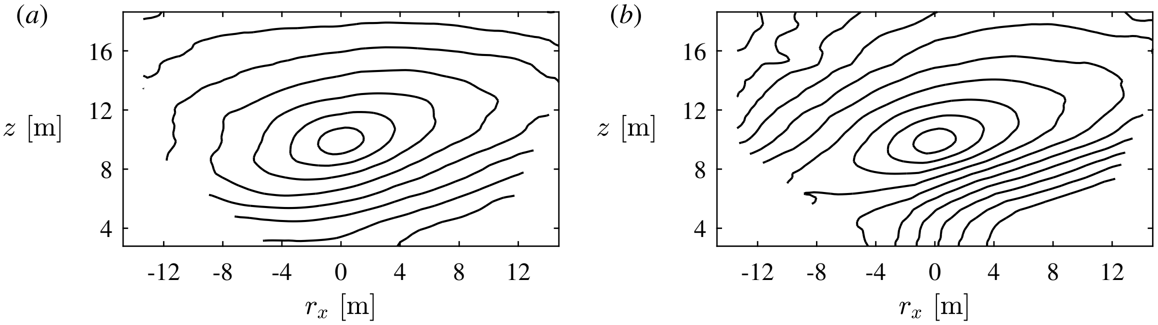

Figure 27. Comparison of two methods for calculating the two-point correlations of the streamwise velocity ρ_{uu} at reference height $z_{ref} = 10$ m: (*a*) fluctuations for equation (12) calculated by standard Reynolds decomposition $u'(z) = u(z) - U(z)$; (*b*) fluctuations calculated relative to the reference height $u^{\backprime}(z) = u(z) - U(z_{ref})$.

both cases, the well-correlated regions are elongated along the streamwise direction and inclined at a shallow angle from the horizontal, indicative of the statistical persistence of the ramp-like structures in the flow. For $u^{\backprime}$ in figure 27(*b*), the structure inclination is more apparent across larger height differences $|z_{ref} - z|$ where the effect of subtracting the mean shear is greater, particularly above the reference height. Additionally, the correlation values decrease faster across height differences such that the correlation aspect ratio becomes more elongated in the streamwise direction.

I calculated the ρ_{uu} correlation maps for each reference height within the SLPIV field using the traditional fluctuation definition. While the $u^{\backprime}$ results are revealing, the use of u' allows for a direct comparison with previous studies in the literature. Further, the alternative definition $u^{\backprime}$ introduces mathematical inconsistencies in the normalization of the correlation. The correlation contours resulting from equation (12) are shown in figure 28 for four reference heights. To determine the inclination angle γ of the spatial correlation, I fitted ellipses to each contour (using finer contour intervals than shown in figure 28), identified the major axis edge points for each ellipse, and used a least-squares linear fit to form a line through all the major axis points. A similar method was employed by Volino *et al.* (2007). The contour fit was only applied to the correlation range $\rho_{uu} = 0.6$ to 1. The line resulting from the linear fit and the angle γ are included in figure 28. The inclination angle $\gamma \approx 12°$ at lower positions ($z_{ref} = 4$ and 8 m) is in excellent agreement with the 10 to 15° range observed in numerous literature (see, e.g., Adrian *et al.* 2000b; Christensen & Adrian 2001; Dennis & Nickels 2011; Guala *et al.* 2011; Liu *et al.* 2017). This agreement further confirms that the signature of ramp-like structures is qualitatively similar, at least in the inclination, across a range of scales independent of surface roughness (Volino *et al.* 2007; Guala *et al.* 2012; Squire *et al.* 2016a).

Towards the top of the SLPIV field, e.g. at $z_{ref} = 12$ m and 16 m in figure 28(*c*-*d*), the elongated shape of the correlations is maintained, but the estimated inclination angle is smaller. Volino *et al.* (2007) observed a similar flattening in their outer region ($z/\delta > 0.7$) entirely above the log region, but other studies found an increase in γ with increasing z (Dennis & Nickels 2011; Hutchins *et al.* 2012; Squire *et al.* 2016a) due to a bulging of the structures (Kovasznay *et al.* 1970; Dennis & Nickels 2011). The discrepancy of the SLPIV findings with the latter studies may be due to methodology. In Hutchins *et al.* (2012) and Squire *et al.* (2016a), the inclination of higher positions was estimated from the shape of low-correlation contour lines

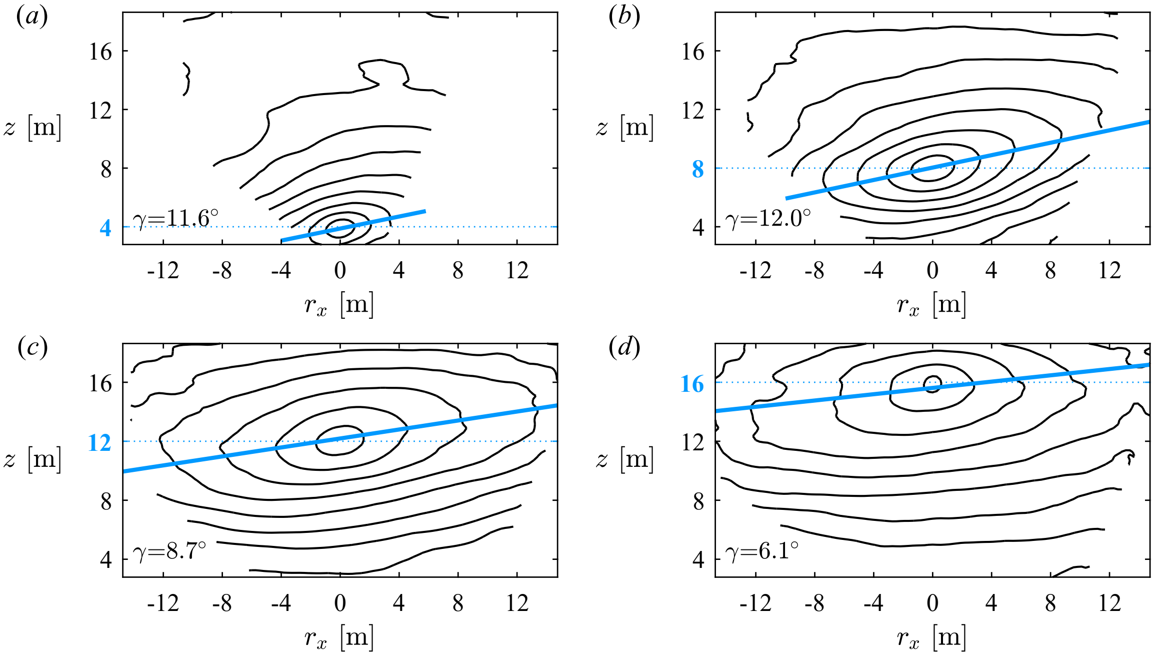

Figure 28. Two-point correlations of the streamwise velocity ρ_{uu} for the four reference heights indicated by the dotted lines: (*a*) $z_{ref} = 4$ m, (*b*) $z_{ref} = 8$ m, (*c*) $z_{ref} = 12$ m, and (*d*) $z_{ref} = 16$ m. The blue line indicates the inclination angle γ of the contours. Contour lines start at $\rho_{uu} = 0.9$ and decrease in intervals of 0.1. Adapted from Figure 7 of Heisel *et al.* (2018).

conditional to a z_{ref} nearer the wall (see e.g. figure 11 of Hutchins *et al.* 2012). In figure 11 of Dennis & Nickels (2011), a higher local z_{ref} was used, but the increased inclination is mainly apparent from the tails of the correlation contours away from the reference point. Considering the positive correlations extend multiple surface layer thicknesses in the streamwise direction (Hutchins *et al.* 2012; Wang & Zheng 2016), the SLPIV field is restricted relative to the correlation and there is likely not sufficient separation distance across the field of view to capture the statistical signature of the bulged structures.

To further investigate the flattening of the correlation contours at the top of the SLPIV field, the wall-normal profile of the inclination angle is given in figure 29. The error bars for each inclination angle represents the 95% confidence interval of the fitted slope. These error bars are likely underestimated, as other sources of uncertainty from the correlation calculations are difficult to quantify and carry forward to the uncertainty of the final result. For example, the ellipse fit was only applied to contours completely enclosed within the field of view. For higher z_{ref}, many of the contours extended above the field limit and the γ estimate was based primarily on the highest ρ_{uu} region which may have been less inclined than the lower correlation regions.

A more physical explanation for the decreased inclination is modulation of the inclined structures by the negative buoyancy. The stratification limits the vertical motions and interactions between different wall-normal regions, leading to more layered, flatter structures. The decrease in inclination has been observed previously for stably stratified turbulence (Sullivan *et al.* 2016; Liu *et al.* 2017). Particularly similar to the present results, Chauhan *et al.* (2013) noted a decrease in the inclination away from the surface in stable

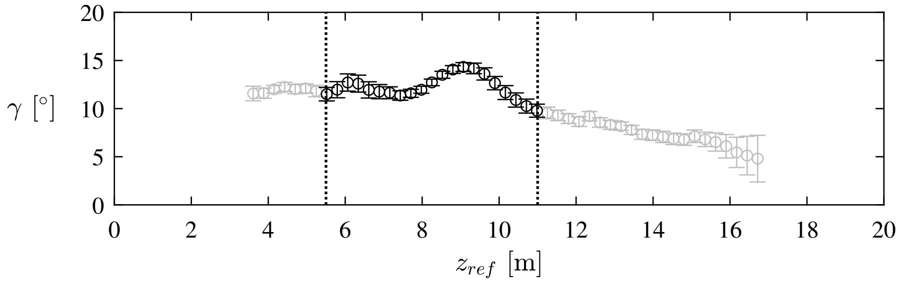

Figure 29. Wall-normal profile of the two-point correlation inclination angle γ. The dotted lines correspond to the limits of the region exhibiting canonical log layer behavior. Adapted from Figure 19 of Heisel *et al.* (2018).

conditions, and a positive inclination relatively close to the surface where the shear production was highest. The decrease in $\overline{u'w'}$ and γ within the same region, i.e. $z \gtrapprox 11$ m, indicates the increased influence of negative buoyancy to be the likeliest reason for the trend in the two-point correlations.

4.2 Uniform momentum zones

I now return the the UMZ classification. While the hairpin-like vortex packets and ramp-like structures have a statistical signature, their presence is not apparent in every realization of the flow. The generalized definition of the UMZs in figure 26(*c,d*) make it possible to extend the UMZ detection to entire data set and systematically characterize the coherent velocity structures in the surface layer.

4.2.1 Histogram construction

Detecting UMZs as local peaks in the velocity histogram via an algorithm, as opposed to visually, requires statistically converged histograms. Limiting the histogram contributions to a rectangular field as shown in figure 26(*c*) results in 8 (streamwise) columns which span the 59 (vertical) rows of the vector field. A single frame is not sufficient to properly converge the histogram as seen in figure 26(*d*). To improve the convergence, and to track the properties of UMZs across time, I extended the two-dimensional representation in figures 26(*c,d*) across consecutive SLPIV frames. Specifically, I combined the 8 central columns in the field of view across 15 SLPIV frames to construct each histogram. The number of vectors contributing to each histogram was therefore $8{\times}59{\times}15{\approx}7{\times}10^3$, which is a similar value to previous studies (de Silva *et al.* 2016; Laskari *et al.* 2018). The histogram space-time (x, z, t) contributions are visualized in figure 30(*a*): the full SLPIV field in space-time (dotted lines) is reduced to a 15-frame rectangular prism (thick black lines). The resulting histogram is shown in figure 30(*b*).

Aside from convergence, another consideration is the scale of the detected velocity regions. The issues of convergence and scale are both addressed by the choice of the parameter $\mathcal{L}_x$ introduced in §2.2.5. Unfortunately, distinguishing the two effects is not trivial. For $\mathcal{L}_x$ much smaller than most of the velocity structures, the limiting factor is convergence of the peaks for the existing structures. However, when $\mathcal{L}_x$ is larger than some of the structures, multiple regions with different momentum contribute to the histogram, which can

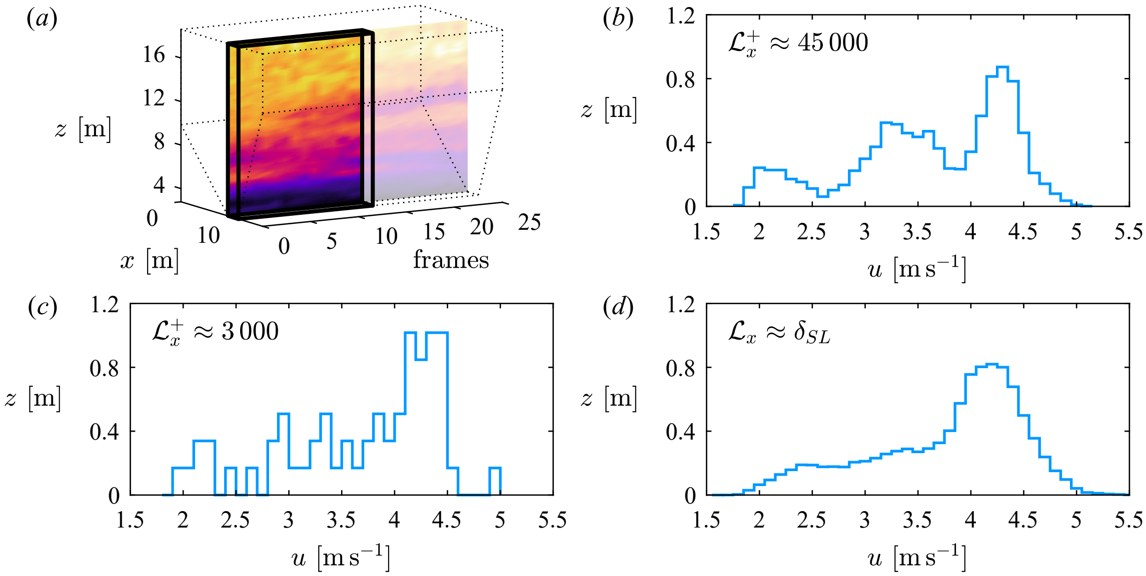

Figure 30. Illustration of the vector field contributions to the histograms used to detect UMZs. (*a*) Dotted lines representing the full SLPIV field in space (x–z) and time (frames) reduced to a 15-frame rectangular prism (thick black lines). (*b*) Histogram of the u values within the 15-frame rectangular prism in (*a*). (*c*) Histogram of u from a single frame and column, scaled in inner wall units. (*d*) Histogram of u from 550 frames, scaled in outer wall units. The three histograms begin at the same SLPIV frame. The conversion from frames to streamwise extent is $\mathcal{L}_x = U_B(\text{frames}/f_s)$ where $U_B \approx 4$ m s^{-1} was the bulk mean velocity and $f_s = 30$ Hz was the sampling frequency. Adapted from Figure 8 of Heisel *et al.* (2018).

mask the smallest local peaks. In this case, a smoother histogram may be due the low-pass filtering effect of $\mathcal{L}_x$ in addition to improved convergence.

To assess the scaling of $\mathcal{L}_x$ for the SLPIV results, the frame extent must be converted to an equivalent streamwise length. The temporal extent of the 15-frame histogram contributions was 0.5 s. Using Taylor's frozen turbulence hypothesis, the streamwise spatial extent can be approximated by multiplying this time to the bulk mean velocity $U_B \approx 4$ m s^{-1}, yielding $\mathcal{L}_x \approx 0.5U_B \approx 2$ m. The streamwise extent can be normalized as $\mathcal{L}_x/\delta_{SL} \approx 0.03$ or $\mathcal{L}_x^+ \approx 45\,000$. If $\mathcal{L}_x$ were limited to a single SLPIV column and frame, i.e. the shortest possible value for the SLPIV data, the resulting length $\mathcal{L}_x^+ \approx 3\,000$ is comparable to the value $\mathcal{L}_x^+ = 2\,000$ suggested by de Silva *et al.* (2016). The corresponding histogram is shown in figure 30(*c*). The histograms in figures 30(*b,c*) exhibit the same general shape and high probability velocity regions, but the short extent does not allow statistical convergence of the zones and automated peak detection. Increasing $\mathcal{L}_x$ to scale instead with δ_{SL} results in the figure 30(*d*) histogram based on 550 SLPIV frames. The low velocity modes seen in figure 30(*b*) are no longer apparent due to the contribution of many structures with slightly different momentum to the histogram. Considering the changes in the modal velocities, $\mathcal{L}_x$ should be small compared to the boundary layer depth to avoid filtering all but the largest zones, in agreement with de Silva *et al.* (2016).

The value $\mathcal{L}_x^+ = 2\,000$ proposed by de Silva *et al.* (2016) was intended to detect the long momentum streaks in the buffer layer whose extent is approximately $1\,000\,\nu/u_\tau$, in addition to larger structures in the log and wake regions. The viscous-scaled streaks are not relevant to fully rough flow. This is demonstrated by the qualitative similarity of the two histograms in figure 30(*b,c*), despite a factor of 15 difference in $\mathcal{L}_x$. Later results indicate the more relevant length scale for the UMZs in the log region is the wall-normal distance z. When normalized by z, the chosen extent is $\mathcal{L}_x/z \sim 0.1$ to 1 throughout the SLPIV field of view.

In addition to the 15-frame temporal extent, further smoothing is introduced by including the 8 central columns in each frame as opposed to a more simple two-dimensional $z{-}t$ plane. I included the multiple columns to improve convergence without increasing too much the temporal extent. The inclusion and smoothing is at the expense of the smallest measurable UMZs whose histogram peak may be eliminated. The smoothing and convergence effects induced by the choice of $\mathcal{L}_x$ represent the primary uncertainty in the UMZ analysis. Sensitivity analysis of $\mathcal{L}_x$ and the histogram parameters yielded up to 30% changes in the calculated average UMZ streamwise extent based on a 2 000 frame sample. The analysis included halving the span to 7 frames (i.e. halving $\mathcal{L}_x$) and doubling the span to 30 frames. The range ±30% is used to represent uncertainty in later UMZ results.

Besides the frame span, another important consideration for the histogram construction is the bin width. I selected a bin width of $0.1\ \mathrm{m\,s^{-1}}$, which is the same as the experimental uncertainty in the velocity vectors. The bin width results in approximately 30 bins per histogram. The normalized bin width is $0.33u_\tau$, which is comparable to the $0.5u_\tau$ width employed by Laskari *et al.* (2018). de Silva *et al.* (2017) showed the streamwise velocity difference between vertically adjacent UMZs to be one to two times u_τ. This jump corresponds approximately to the velocity difference between modes in the histogram. The normalized bin width $0.33u_\tau$ is therefore small enough to allow for the average mode-to-mode velocity difference to be separated by multiple histogram bins. As a result, adjacent UMZs appear as distinct modes in the histogram.

4.2.2 Tracking methodology

The following description provides a brief overview of the methodology employed to identify momentum zones using the histograms and track the UMZs in time. Local peaks in a given histogram were considered as distinct UMZ modes by a peak detection algorithm based on a calibrated set of parameters. The parameters included the minimum distance between two peaks (2 bins), the minimum peak height (0.05), and minimum peak prominence (0.05), where the prominence is the height difference between the peak and its neighboring minima. Importantly, the height and prominence parameters require the histograms to be normalized as probability density functions (pdfs) with integral equal to unity. Similar parameter values were used by Laskari *et al.* (2018). From the detected peaks, the modal velocities u_m were determined using a local three-point Gaussian fit of the peaks, and the edge velocities were determined using a three-point parabolic fit of the minima between peaks. The example histogram in figure 31(a) shows the detected modes and edge velocities.

To determine the edge height, the 8-column streamwise velocity time series was reduced to the central (fifth) column, resulting in a $z{-}t$ velocity series at the center x position. The UMZ edge location within the velocity field was estimated from a contour of the detected edge velocity, and the edge z position at a given time t was taken as the height of the contour at that time. The detected edge heights are shown in figure 31(b), where the given time t =2.5 s is the the center of the frame span. The bottom and top edge heights were

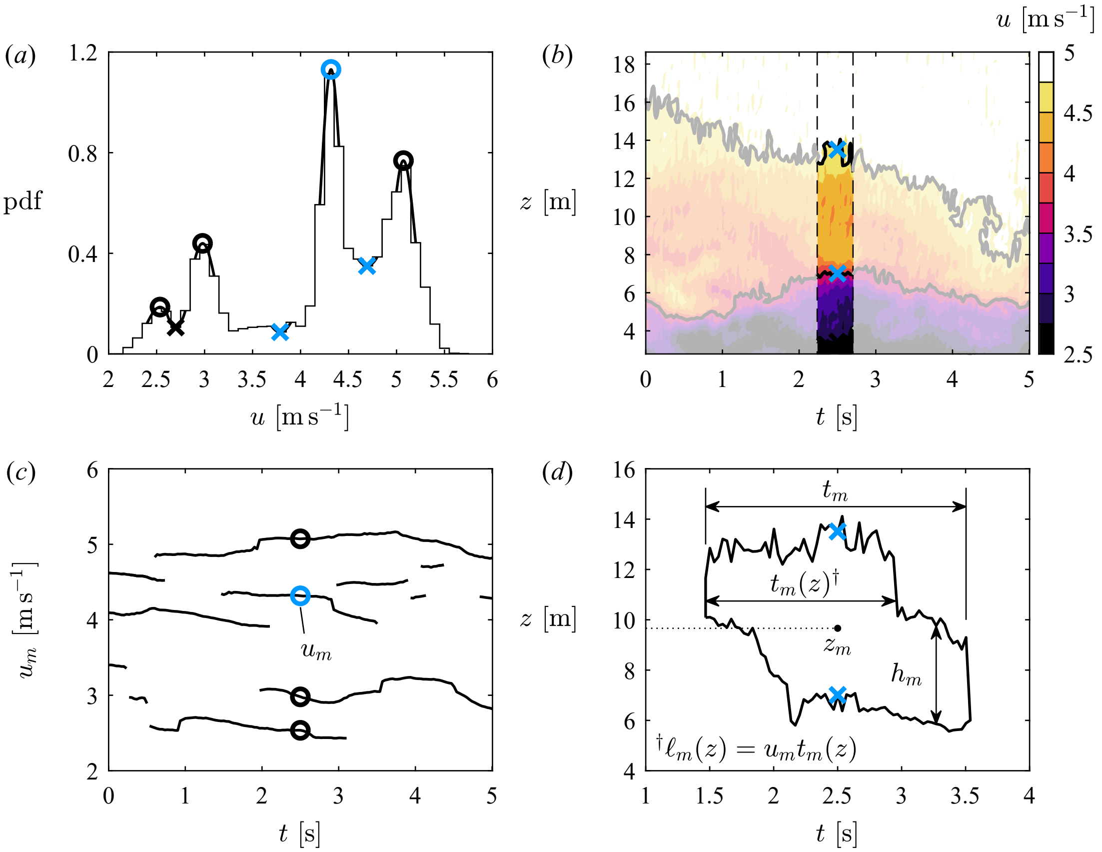

Figure 31. Demonstration of the UMZ tracking methodology. (*a*) Histogram of u values with the detected modal velocities u_m (○) and zone edge velocities (×). (*b*) Color plot of u in space z and time t, including the 15-frame histogram span (bounded by the dashed lines) and contours of the edge velocities from (*a*) used to detect the edge heights for $t = 2.5$ s. (*c*) UMZ velocities u_m in time where the histogram in (*a*) corresponds to $t = 2.5$ s. (*d*) Definitions of zone average midheight z_m, total time duration t_m, wall-normal thickness h_m, and height-dependent length $\ell_m(z) = u_m t_m(z)$. Blue markers in each plot indicate attributes associated with the zone featured in (*d*). Adapted from Figure 9 of Heisel *et al.* (2018).

assigned to each modal velocity by matching the u_m values with the mean of the streamwise velocity vectors between each edge height (including the bottom and top of the field). The mode and edge detection was repeated by shifting forward one frame and computing the new histogram. Because the frame shift between histograms was shorter than the 15-frame span of the histogram construction, there was overlap in the vectors contributing to consecutive histograms. The effect of the vector overlap is quantified using the frame span sensitivity analysis discussed above.

Following the calculation of modal velocities and edge heights for every frame, the UMZs were tracked temporally using a nearest-neighbor routine, resulting in the tracked zone speeds in figure 31(*c*). The algorithm connected UMZ modes between frames if the modal velocity difference was less than 1.5 bin widths. The duration of the connected UMZ modes defines the extent of the zone. UMZs lasting only one frame were considered short-lived and were removed (Laskari *et al.* 2018). The boundaries of each remaining UMZ were converted from scattered bottom and top heights to an enclosed shape as shown in figure 31(*d*). The velocity vectors belonging to each zone are those within the UMZ boundaries. Properties computed for each UMZ include those defined in figure 31(*d*): the average midheight z_m, total time duration t_m, wall-normal thickness h_m, and height-dependent streamwise length $\ell_m(z) = u_m t_m(z)$. The height, thickness, and duration properties are based on the position of the UMZ boundaries in the $z{-}t$ plane. The use of Taylor's frozen turbulence hypothesis to convert the time duration to streamwise length is justified here due to the fact that each UMZ moves with a uniform velocity by definition. However, the hypothesis still assumes "frozen" turbulence where the structures do not evolve in time, which may underestimate the length if the entire UMZ did not pass through the SLPIV field prior to its breakup.

More than 1 300 UMZs were identified from the tracking routine. Figure 32 provides results of the UMZ edge tracking routine for two 5-second sample periods. The interfaces align well with the shear identified in figure 32(*c,d*) and the vortices based on swirling strength in figure 32(*e,f*). However, the inherent requirement for a substantial number of velocity vectors in a given zone to manifest a histogram peak is apparent in two ways. First, it results in the inability to detect zones only partially in the field of view. For instance, the high shear at the bottom of the field in figure 32(*d*) indicates a potential shear layer, but insufficient vectors are present to detect the UMZ that likely appears just below the field of view. Second, an emerging zone may not immediately correspond to a histogram peak. When the zone is detected in these cases, the vertical extent of the UMZ is already substantial, leading to an apparent vertical front edge. This can be seen for both samples in figure 32(*a,b*) near $z = 10$ m and $t = 2.5$ s. The result of these limitations in the tracking methodology are potentially biased statistics near the top and bottom of the field as well as underestimated durations for certain UMZs to the favor of the surrounding zones. In consideration of the field edge effects, later figures and discussion of wall-normal UMZ trends clearly acknowledge the regions where bias is observed. The results are interpreted using only the central region of the field where the statistics are most reliable.

In addition to the visual samples, the efficacy of the tracking methodology can be assessed by measuring the uniformity of each UMZ. I used the rms of the velocity vectors σ_m in a given UMZ to represent the uniformity. Figure 33 shows the average σ_m in intervals of z, where the appropriate interval for each UMZ was based on its midheight z_m. The overall time-averaged rms profiles are also shown for reference. The relatively low turbulence levels within the UMZs confirm the uniformity of the zones. The streamwise velocity deviations $\sigma_m(u)$ are 20% to 40% of the time-averaged rms profile and the wall-normal deviations $\sigma_m(w)$ are 40% to 60%. The decrease for $\sigma_m(w)$ is appreciable considering the w velocity is not considered in the UMZ detection, and demonstrates the correlation between u and w at the scale of the UMZs. I assume the w uniformity would be further improved by detecting each UMZ as a region with coherent u and w values simultaneously. Note also that the estimates for σ_m include the vectors along the UMZ edges that were within the thickness of the shear layers. These shear layer vectors likely have higher deviations than the UMZ interior such that the estimated uniformity is conservative.

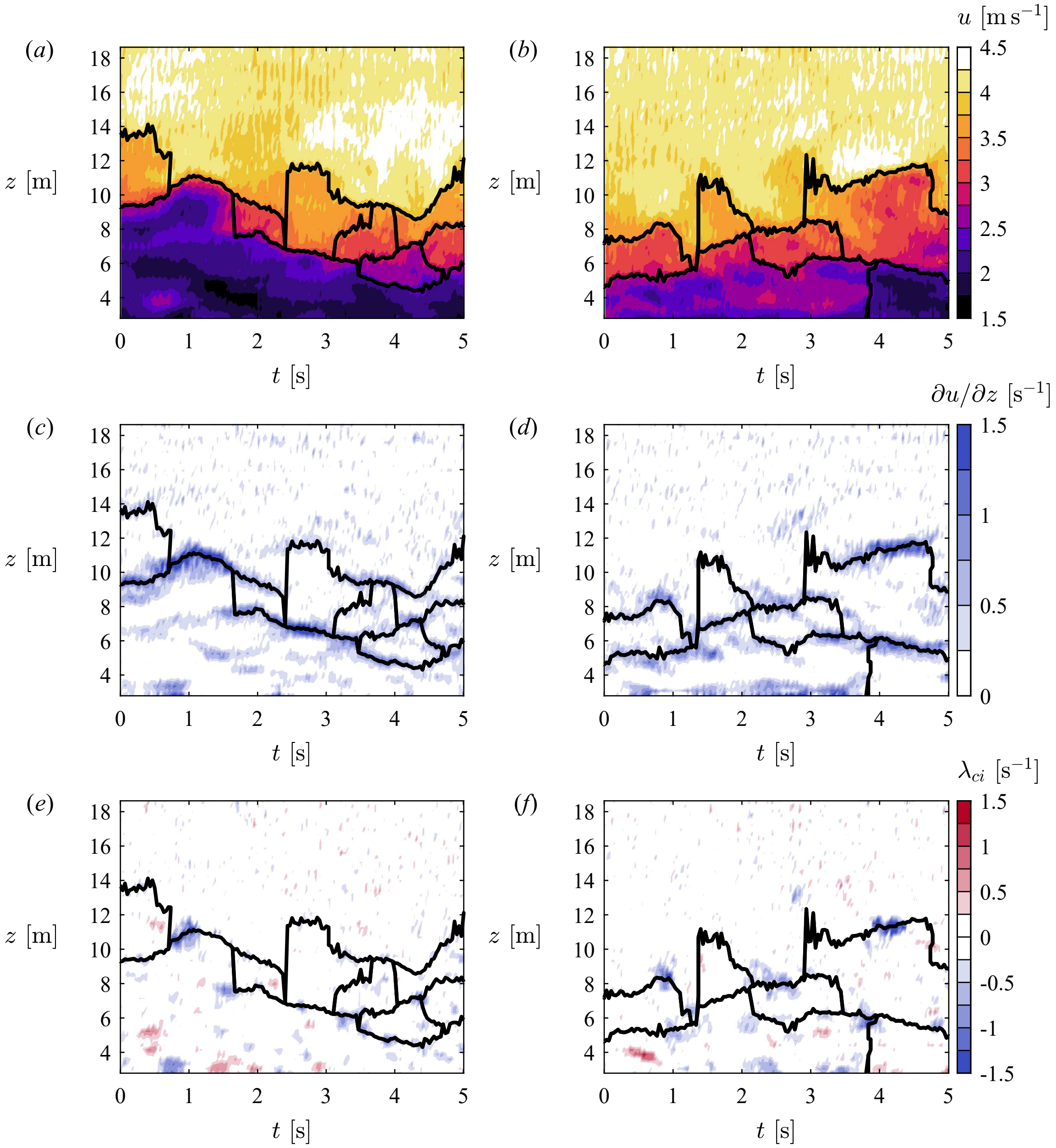

Figure 32. Temporally tracked UMZ edges in the $z-t$ plane for two example 5-second periods (*a,b*) overlaid on streamwise velocity color plots, (*c,d*) overlaid on instantaneous shear color plots, and (*e,f*) overlaid on swirling strength color plots. Adapted from Figure 10 of Heisel *et al.* (2018).

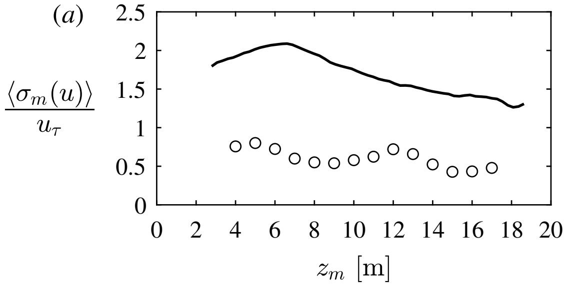

Figure 33. Binned averages of the velocity standard deviation σ_m in each UMZ (circles) compared with the time-averaged rms velocity profiles (lines) for (*a*) the streamwise velocities u and (*b*) the wall-normal velocities w. The bins are based on the UMZ midheight z_m. Adapted from Figure 11 of Heisel *et al.* (2018).

4.2.3 Length statistics

The tracking described above yielded an estimated total streamwise length ℓ_m for each UMZ. The probability distribution of ℓ_m is shown in figure 34(*a,b*). The bins used to estimate the distribution are spaced logarithmically to better capture the probability tail. The tail follows a power law relationship as shown by the fit in figure 34(*b*). The bin spacing here results in a -2 power law exponent, while the linear bins used in the original analysis predicted a -2.2 exponent. In either case, the exponent indicates the mean value for ℓ_m is statistically well-defined. The longest tracked event, $\ell_m = 160$ m, is on the order of δ_{SL}. This extent is consistent with the longest UMZs tracked by Laskari *et al.* (2018) and approaches the range of very-large-scale motions (VLSMs) identified using turbulence spectra in the logarithmic layer (see, e.g., Guala *et al.* 2006; Balakumar & Adrian 2007; Smits *et al.* 2011). Hutchins & Marusic (2007a) identified longer, meandering superstructures over 20δ in length using a spanwise array of point measurements. Consistent with Laskari *et al.* (2018), I note the possibility that the tracked UMZs may be part of larger structures: if a tracked UMZ were to meander, the UMZ could be lost, then reappear as a new UMZ due to the lack of spanwise measurements.

A quantitative analysis of the longest UMZs is precluded by the discussed limitations in defining the UMZ length, namely the underestimated duration of emerging zones, the application of Taylor's hypothesis, and the inability to follow meandering structures. While there may be a link between the longest zones and VLSMs, UMZs with length $\ell_m \gtrsim \delta_{SL}$ are rare and represent 0.5% of the tracked zones. The majority of tracked UMZs have length $\ell_m \lesssim 0.1\delta_{SL}$. The maximum size of UMZs may be bounded by δ_{SL} scaling, but the average UMZ does not appear to by influenced by δ_{SL} in the present measurements.

A profile of the height-dependent average UMZ length $L_m(z)$ is shown in figure 34(*c*). The average $L_m(z) = \langle\ell_m(z)\rangle$ was determined from the contributions of each zone at a given height such as the example in figure 31(*d*). The profile exhibits a wall-normal dependence up to approximately $z = 11$ m, above which the zone length is relatively constant. The increase of UMZ length with height is in agreement with theoretical scaling for the log region and is discussed further in §4.5. The behavior above $z = 11$ m is consistent with the two-point correlation results and the influence of stable stratification. The errors bars in figure 34(*c*) correspond to the forementioned sensitivity analysis based on changing $\mathcal{L}_x$ by a factor of two. Importantly,

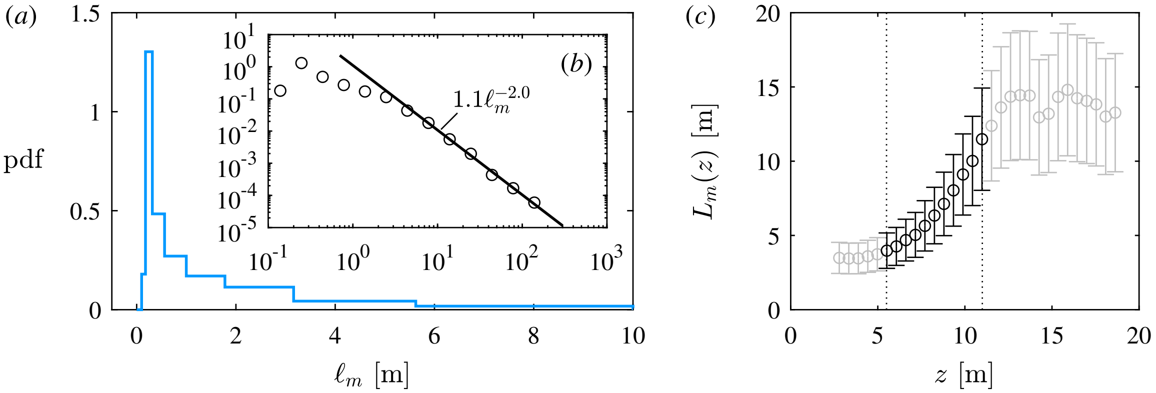

Figure 34. Statistics of the UMZ streamwise length $\ell_m = u_m t_m$. (*a*) Histogram of ℓ_m. (*b*) The same histogram in log-log scale with a power law fit to the distribution tail. (*c*) Profile of the average height-dependent length $L_m(z)$ with every second data point shown for clarity. The dotted lines correspond to the limits of the region exhibiting canonical log layer behavior. See figure 31(*d*) for definitions of t_m and $\ell_m(z)$. Adapted from Figure 12 of Heisel *et al.* (2018).

varying $\mathcal{L}_x$ affects neither the wall-normal dependency nor the conclusions drawn from the trends. Changes in $L_m(z)$ due to the choice of $\mathcal{L}_x$ were approximately uniform across all heights.

4.3 Internal shear layers

In the previous section, I referred to the tracked points between zones as UMZ edges. Hereon, I assume the tracked edges correspond to the midheights of internal shear layers (ISLs), and adopt the latter terminology. Previous studies have shown the ISLs to carry a majority of the instantaneous shear (see, e.g., Adrian *et al.* 2000b; Eisma *et al.* 2015; de Silva *et al.* 2017), which is consistent with the visual evidence from the SLPIV data in figure 32(*c,d*).

To evaluate the statistical properties of the ISLs, I followed the same conditional averaging procedure as de Silva *et al.* (2017). For each tracked point, the reference frame was adjusted relative to the ISL midheight z_i and statistics were compiled as functions of the wall-normal distance from the ISL, i.e. $z{-}z_i$ and $\langle u{-}u_i \rangle$. Figure 35(*a*) shows an example UMZ edge contour with the nearest SLPIV vectors (blue dots) and the neighboring coordinates (black dots) used to represent the ISL reference frame. The ISLs were conditionally sampled before computing the averaged velocity profiles. To avoid offsetting effects, shear layers with high-speed UMZs *below* low-speed UMZs, e.g. the ISL at $z_i \approx 10$ m for frames 4 and 5 in figure 35(*a*), were excluded from the averaging. These "inverted" shear layers represented 14% of all ISLs. Instantaneous ISL profiles were also excluded if there was another shear layer within $5\Delta z$ in the same frame. Approximately 20% of the remaining profiles were excluded based on this condition such that 69% of the overall interfaces were used for the analysis. Figure 35(*b*) shows the resulting conditionally-averaged streamwise velocity profile relative to the ISL.

The parameter ΔU_m, shown as a blue line in figure 34(*b*), describes the average streamwise velocity difference across the ISL between adjacent UMZs. Figure 35(*c*) compares the normalized value of ΔU_m

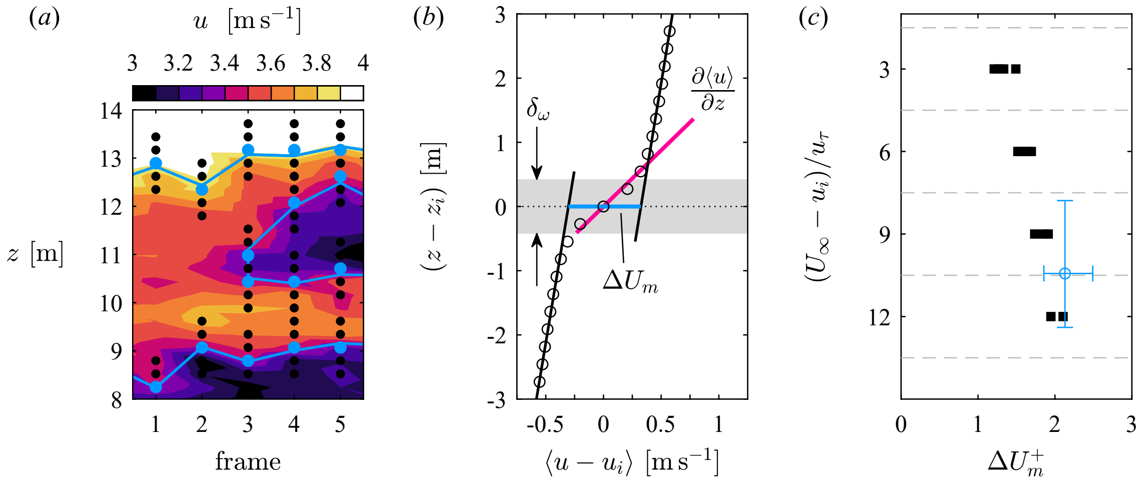

Figure 35. Demonstration of the internal shear layer (ISL) conditional profile following Figure 7 of de Silva *et al.* (2017). (*a*) Color plot sample of u with tracked UMZ edges (blue lines), SLPIV vectors located at the ISL midheight z_i (blue dots), and vector coordinates surrounding the ISL (black dots). (*b*) Streamwise velocity profile in the frame relative to the ISL midheight z_i and velocity u_i, averaged for all tracked edges. The profile indicates the maximum shear $\partial \langle u - u_i \rangle / \partial z|_{max}$ (magenta line slope) and average streamwise velocity difference ΔU_m (blue line length) used to calculate the interface thickness δ_ω. (*c*) Average difference ΔU_m normalized by u_τ, following Figure 13(*a*) of de Silva *et al.* (2017). Closed squares in (*c*) correspond to de Silva *et al.* (2017) and the blue circle corresponds to the SLPIV results. Adapted from Figure 14 of Heisel *et al.* (2018).

from the SLPIV data with the experimental results of de Silva *et al.* (2017), where the vertical axis is the deficit in momentum from the free stream U_∞. To normalize the velocities, I used the u_τ value from table II and a nominal estimate $U_\infty = 6.6$ m s^{-1} which is the mean velocity at the top of the met tower ($z = 130$ m). The momentum deficit corresponds to a wall-normal position z approximately in the center of the SLPIV field, and the vertical error bars represent the estimated momentum deficits at the top and bottom of the field. The close agreement for ΔU_m^+ in figure 35(*c*) confirms the velocity difference across the shear layers is $\Delta U_m {\sim} O(u_\tau)$ as suggested by de Silva *et al.* (2017). Binning the conditional profiles based on wall-normal distance revealed ΔU_m to decrease slowly with increasing wall-normal distance. The wall-normal trend is investigated further in chapter 5.

Following Brown & Roshko (1974) and de Silva *et al.* (2017), I assumed the average ISL acts as a shear mixing layer to calculate the ISL thickness δ_ω as

$$\delta_\omega = \frac{\Delta U_m}{\partial \langle u - u_i \rangle / \partial z|_{max}}, \tag{13}$$

where $\partial \langle u - u_i \rangle / \partial z|_{max}$ is the maximum shear at the center of the ISL. Each element of equation (13) is demonstrated in figure 35(*b*), including the average interface thickness $\delta_\omega \approx 0.85$ m. To assess the effect of SLPIV spatial resolution on the ISL results, I reanalyzed a subset of the SLPIV images using coarser resolution, i.e. 64×64 and 128×128 pixel interrogation window size as opposed to 32×32 pixels. I then repeated the UMZ tracking and conditional ISL profiles to compare the results. The estimate of ΔU_m relies on the conditional profile away from the shear layer and was insensitive to the resolution, suggesting the ΔU_m

results are robust. However, the maximum shear $\partial\langle u{-}u_i\rangle/\partial z|_{max}$ is susceptible to the spatial resolution within the shear layer and decreases for coarser resolutions. The SLPIV results for δ_ω are therefore not reliable. The influence of resolution on the ISL thickness is investigated further in chapter 6.

4.4 Vortex structures

The visualization at the beginning of this chapter in figure 26(*b*) showed strongly rotating vortex cores associated with the shear layer separating UMZs. Here, "strong" is a qualitative term indicating the local values associated with rotation, i.e. vorticity ω and swirling strength λ_{ci}, are high relative to their mean. In this section I discuss properties of these prograde vortex cores to demonstrate their relationship to UMZs and ISLs.

4.4.1 Tracking vortex events

The vortex events were tracked in the same space-time plane (x, z, t) as the UMZs, except the entire SPLIV field was used to identify vortices as opposed to the rectangular prism for UMZs. In this chapter, I identified vortices based on values of the swirling strength λ_{ci} in the vector field (see, e.g., Adrian *et al.* 2000a) as previously shown in figure 26(*b*). To discriminate vortex cores from the background flow field, I applied a high-pass cutoff threshold $\lambda_{thr} = 0.55$ s^{-1}. The choice of λ_{thr} is discussed further in 4.4.2. Contiguous regions above the threshold in the three-dimensional spatio-temporal domain were identified as a vortex event if the region extended for at least 8 frames, i.e. 0.25 s. The temporal (frame) filter was required to exclude measurement noise which was enhanced in the derivative calculation. The combination of the cutoff threshold, temporal filtering, and SLPIV spatial resolution limit the focus of the tracking procedure to relatively large, persistent vortex events. Almost 4 000 vortex events in SLPIV data set 1 were identified as a result of the tracking. An example of detected vortices for the same frame as figure 26 is given in figure 36(*a*) and isosurfaces of tracked vortices in time are shown in 36(*b*).

For each frame in an identified vortex event, the vortex area A_ω was estimated based on the region within the contours of the threshold λ_{thr}. The vortex center was then calculated as the geometric centroid of the region weighted by the swirling strength values. Using the vortex area, the characteristic size was determined assuming the vortex was circular. The equivalent radius of the vortex in each frame is defined as $r_\omega = \sqrt{A_\omega/\pi}$ and the equivalent diameter d_ω is twice the radius. Figure 36(*a*) provides an example of the threshold contours, detected centroid position, and equivalent diameter.

To assess the circularity of the vortices, I defined a shape factor SF based on the SLPIV vectors associated with the vortex. The value for SF is the ratio of vortex vectors within r_ω of the centroid to the total number of vectors in the vortex. For SF=1, all vortex vectors are enclosed by the equivalent radius such that the centroid and r_ω fully characterize the vortex size. In figure 36(*a*), the green dashed circles representing r_ω match closely with the vortex outlines. Figure 36(*c*) shows the average shape factor in intervals of the diameter. The high SF value regardless of d_ω indicates the equivalent diameter is representative of the vortex size.

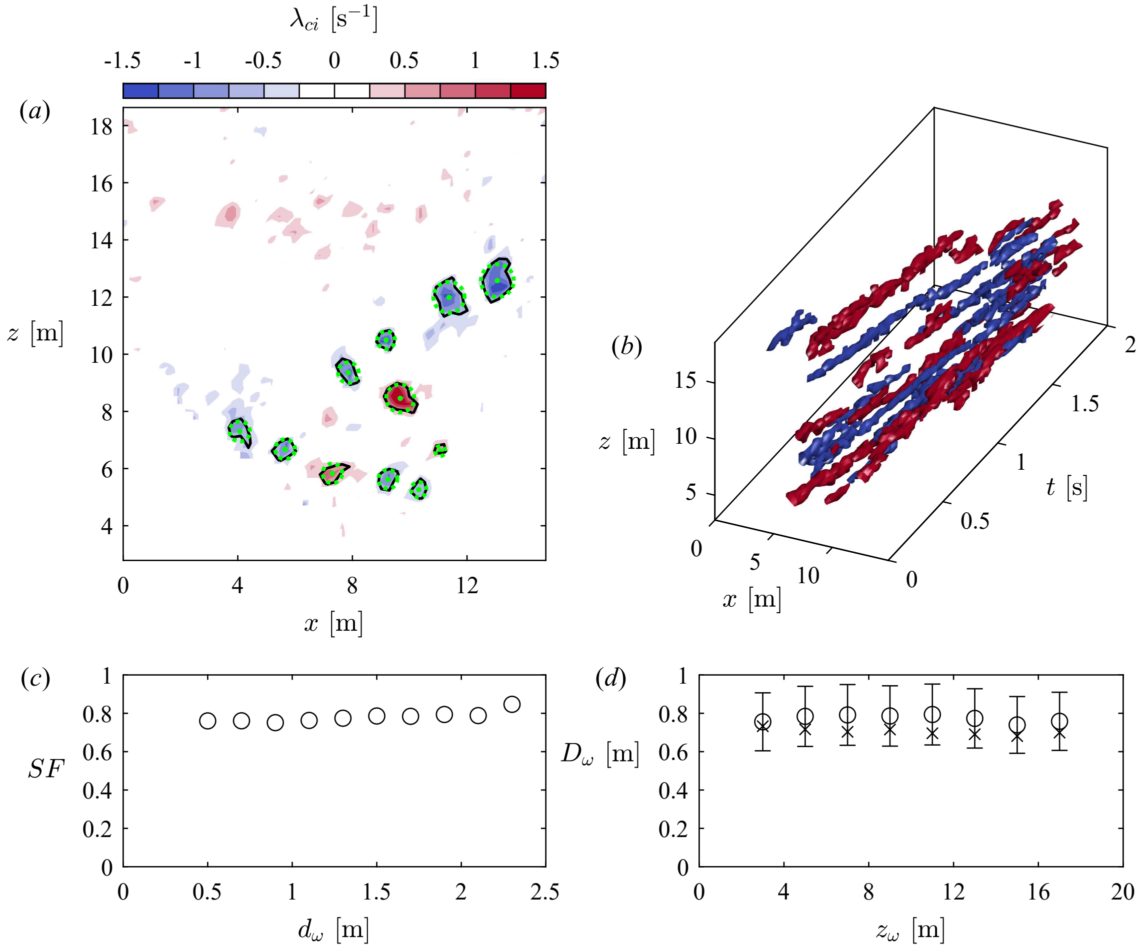

Figure 36. Demonstration of the vortex event tracking methodology. (*a*) Color plot of the swirling strength λ_{ci} for an example velocity field. The color plot is overlaid with contours of the cutoff threshold λ_{thr} (black lines), tracked vortex centroids (green dots), and circular representations of the equivalent diameter d_ω (green dashed circles). (*b*) Isosurfaces of tracked prograde (blue) and retrograde (red) vortices for a two-second sample time period. (*c*) Average shape factor SF for intervals of the vortex diameter. (*d*) Average diameter D_ω of prograde (○) and retrograde (×) vortices in intervals of the vortex centroid height z_ω with ±20% uncertainty bounds. Adapted from Figure 20 of Heisel *et al.* (2018).

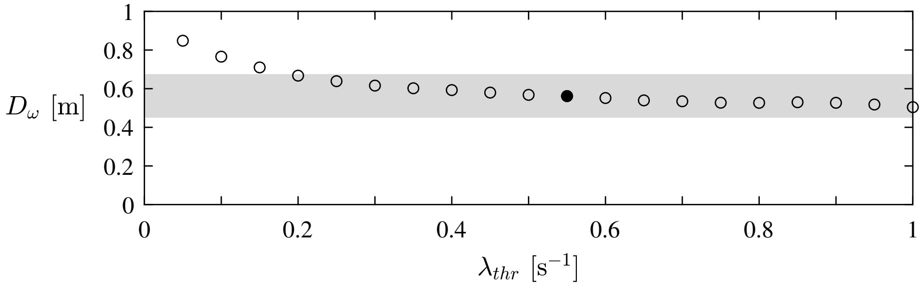

Figure 37. Average vortex diameter D_ω as a function of the detection threshold λ_{thr} for a 2 000 frame sample, where the filled data marker indicates the λ_{thr} value used for the full analysis and the shaded region is within $\pm 20\%$ of D_ω at the filled marker. Adapted from Figure 20(*d*) of Heisel *et al.* (2018).

The average prograde vortex diameter D_ω is shown in figure 36(*d*) as a function of the vortex position z_ω. The size of the large vortex cores appears to be independent of wall-normal distance within the field of view. The prograde vortices have a thicker probability tail and slightly larger average size than the retrograde vortices. The error bars represent the sensitivity of the vortex diameter to the cutoff threshold. Note that the sensitivity uncertainty is small compared to the effect of spatial resolution. Given the expected vortex core size is $D_\omega{\sim}O(10\eta){\sim}O(10\text{ mm})$ (Herpin *et al.* 2013), the SLPIV data cannot resolve most of the small-scale vortices. Vortices smaller than 0.5 m (800η) are either not detected within the vector field, or are augmented by the averaging of the velocity across each interrogation window. Similar to the δ_ω statistic, D_ω is not reliable for the SLPIV data, and no conclusions on vortex size are made here. Chapter 6 analyzes vortex size behavior using experimental data with higher spatial resolution.

4.4.2 Threshold sensitivity

As there is no universal physics-based cutoff threshold value for identifying vortices, the choice of λ_{thr} is somewhat arbitrary. To test how the cutoff value affects the results, the vortex tracking procedure was repeated across a range of λ_{thr} values for a 2 000 frame sample of the SLPIV data. The average diameter in the tested range is shown in figure 37. The vortex size is only weakly sensitive to λ_{thr} across an order of magnitude such that selecting any of the thresholds in the range would not change the general results. Decreasing λ_{thr} by 70% or increasing λ_{thr} by 100% results in less than 20% change in the equivalent diameter (represented by the shaded region in figure 37). I used $\pm 20\%$ as a nominal estimate of the uncertainty in d_ω due to the choice of λ_{thr}, noting again that spatial resolution is the leading cause of uncertainty for the size results.

Previous studies have used a percentage of the maximum λ_{ci} (Ganapathisubramani *et al.* 2006) and a factor of the rms swirling strength (Wu & Christensen 2006) as the cutoff threshold. For the SLPIV results, the only effect of these choices is to change the number of detected vortex events. The results are similarly insensitive to the detection method. There were no appreciable differences in vortex statistics using the Γ_2 function to detect vortex cores, where the Γ_2 function is the relation of strain and rotation such that the cutoff threshold has a physical basis (Graftieaux *et al.* 2001).

The velocity gradients used to calculate λ_{ci} (and all other derivatives for the ASL analysis) were estimated

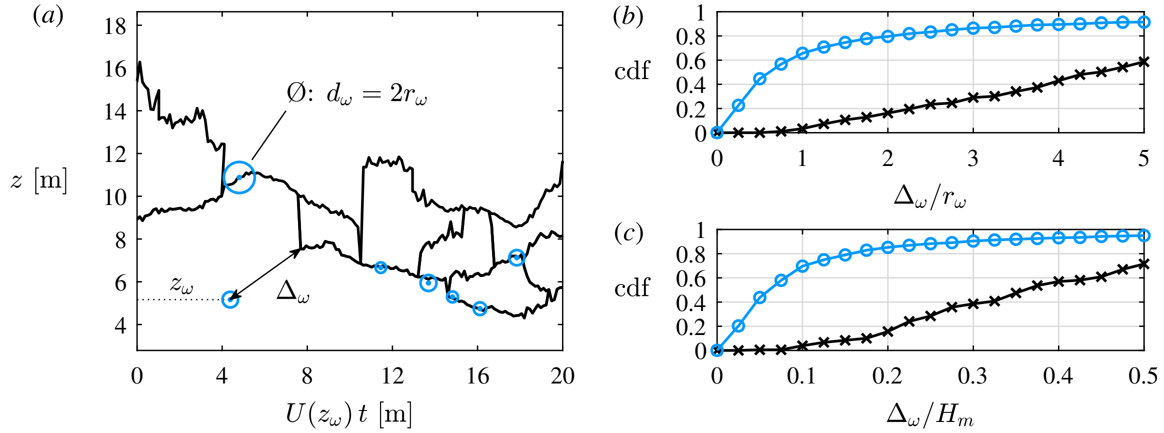

Figure 38. The proximity of tracked vortices to tracked UMZ edges. (*a*) An example of UMZ edges (black lines), prograde vortex centroids (blue dots), and vortex areas based on the equivalent radii (blue circles). The vortex proximity Δ_ω is the shortest distance from the centroid to the nearest UMZ edge. (*b,c*) Cumulative distribution functions (cdfs) of Δ_ω for prograde (○) and retrograde (×) vortices normalized by its own radius r_ω and the average UMZ thickness H_m, respectively. Adapted from Figure 13 of Heisel *et al.* (2018).

using a second-order accurate central difference scheme. The order of the scheme has a filtering effect: higher order numerical difference formulas are calculated using a larger neighborhood of vectors around the given point which results in a smoothing of the λ_{ci} estimate. The second-order accurate scheme uses a 3×3 neighborhood to estimate λ_{ci}.

4.4.3 Proximity of vortices to shear layers

The primary reason for tracking vortex events was to relate their position to the internal shear layers. The position statistics are less sensitive than the vortex size to the spatial resolution effects, except in the selection bias where only the strongest vortex events are detected. Figures 26(*b*) and 32(*e,f*) suggest that the strongest prograde vortices were collocated with the internal shear layers. The outputs of the tracking procedure described above include the vortex centroid position in space (x_ω,z_ω) and time (t_ω) and the equivalent radius r_ω of each vortex. Because the tracked UMZ edges are at a single streamwise location x, the vortex centroid values were narrowed to include only the centroid height z_ω and time t_ω when the vortex crossed the center x position, yielding approximately 800 events. I then calculated the shortest path distance from each vortex centroid to the nearest tracked UMZ edge in the streamwise-wall-normal plane. I refer to this distance as the proximity Δ_ω. The local mean velocity $U(z{=}z_\omega)$ was used with Taylor's hypothesis to convert the time difference to streamwise distance in the $z{-}t$ plane. An example of the vortex proximity is shown in figure 38(*a*).

The cumulative distributions of Δ_ω in figures 38(*b,c*) normalize the proximity by the vortex equivalent radius r_ω and average UMZ thickness H_m, respectively. More than 60% of prograde vortices are within their own radius of the nearest UMZ edge such that a majority of tracked vortices overlap with an internal shear layer. The proximity Δ_ω is also small relative to the zone thickness, with more than 60% of vortices within $0.1H_m$ of the nearest shear layer. Note that outliers such as the vortex at the bottom of figure 24(*a*) are in part due to the inability of the UMZ tracking procedure to detect shear layers along the bottom of the field, leading to long distribution tails (5% occurrence of $\Delta_\omega > 5r_\omega$).

In contrast, the proximity of retrograde vortices is uniformly distributed, as indicated by the linear trends in each cdf. The lack of an observed relationship between the locations of the retrograde vortices and shear layers shows that the proximity of prograde vortices is a robust result and not an artifact of the methodology. Therefore, in addition to the ISLs carrying a majority of the instantaneous shear (de Silva *et al.* 2017), figure 38 shows the strong prograde vortices to primarily reside within these layers. While this result is unsurprising, I am not aware of any previous studies providing statistical evidence such as the Δ_ω distributions.

4.5 Results in the context of Townsend's attached eddies

To this point in the chapter, I have provided evidence showing the structural organization of the log region in the fully rough, high-Reynolds-number ASL to be qualitatively similar to laboratory-scale flows. The UMZ-ISL organization is apparent in both cases, where the flow is populated by thin regions of strong local shear and rotation separating relatively larger regions of uniform momentum (Meinhart & Adrian 1995; de Silva *et al.* 2016). Instantaneous realizations of these features show their relation to the signature of inclined hairpin-type packets and ramp-like structures. The Λ-vortex packet, a specific variant of the hairpin packet discussed in §2.2.1, is currently used as the representative eddy in model applications of Townsend's attached eddy hypothesis (AEH). In this section, I further explore the interconnectedness of the UMZ-ISL organization, the representative attached eddy, and the principles of the AEH.

The AEH, summarized in §2.1.2, leads to three primary average properties of the main eddies responsible for the velocity statistics in the log region: (i) the eddy size increases proportionally with the distance from the wall to eddy center; (ii) the population density of eddies is inversely proportional with the distance from the wall; (iii) the characteristic eddy velocity is u_τ. The first property is the direct result of the hypothesis, and the last two properties are required to meet the condition $\overline{u'w'} = u_\tau^2$. Additional requirements exist for the eddy behavior close to the wall (relative to the eddy size) in order to satisfy the wall boundary conditions (Townsend 1976). The size and velocity scaling of the eddies is consistent with the mixing length model of Prandtl (1932) and arguments leading to the log law in equation (5).

In the UMZ-ISL classification, the characteristic structure size and velocity are L_m (or H_m) and ΔU_m, respectively. Figure 35 already demonstrated that the characteristic velocity ΔU_m is proportional to the friction velocity u_τ. Figure 39 provides the number density and size of tracked UMZs and tracked vortices as a function of wall-normal distance z. The number density N in figure 39(*a*) is the number of unique tracked zones or vortices occurring at each position z normalized as a probability. The definition for N used here is equivalent to a pdf of z_m or z_ω. The number density exhibits a near-linear decrease with increasing z for both UMZs and vortices in the canonical log region above the roughness sublayer and below the region where thermal stability effects are felt. Assuming each UMZ is separated in the streamwise direction by a shear layer where the vortices primarily reside, the number density of UMZs and vortices should be similar. This is confirmed by the agreement in the canonical region of the two distributions in figure 39(*a*) which result from independent tracking methodologies. The linear decrease in number density of spanwise vortices is in

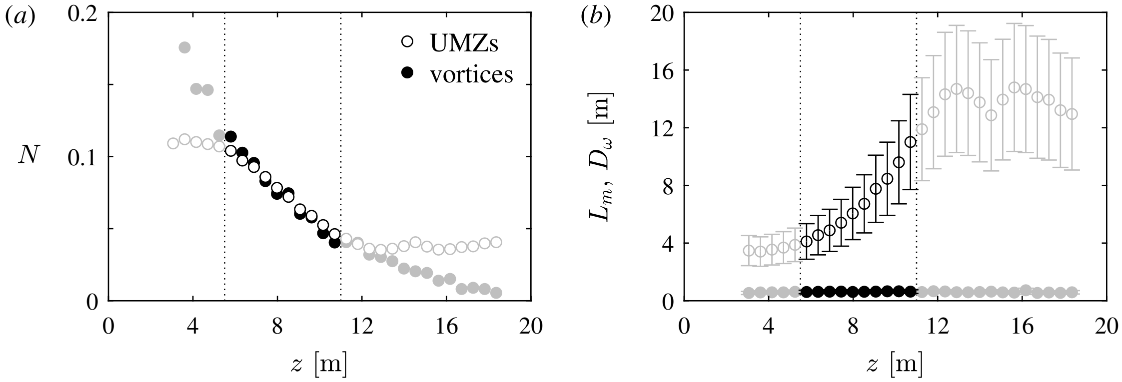

Figure 39. Comparison of UMZ (open circles) and vortex (closed circles) properties as a function of wall-normal distance: (*a*) the number density N and (*b*) the characteristic UMZ length L_m and vortex size D_ω. The dotted lines correspond to the approximate limits of the region exhibiting canonical behavior. Error bars for D_ω are included, but do not exceed the marker size. Adapted from Figure 15 of Heisel *et al.* (2018).

agreement with previous studies (Wu & Christensen 2006; Herpin *et al.* 2013).

The characteristic sizes of UMZs and vortices, provided in previous figures, are shown together in figure 39(*b*). Whereas the vortices appear to be smaller-scale features relatively independent of the wall-normal distance, the UMZ length L_m increases with z. The departure from canonical behavior above $z \approx 11$ m is consistent with the two-point correlation results and the Reynolds shear stress profile. The UMZs occupy a majority of the field above $z \approx 11$ m, leading to a relatively constant average length L_m. There are fewer shear layers and correspondingly fewer vortices in this region. With longer zones with limited vertical motion and fewer shear layers, the structures become statistically flatter and the Reynolds shear stress decreases. Within the canonical region below $z \approx 11$ m, figure 39 demonstrate that the UMZs share the three main properties of attached eddies describe above; the trends of velocity, number density, and size are all in agreement with the AEH.

By the AEH, the population of the main attached eddies corresponds directly to the velocity mean and variance profiles. If UMZs are the representative eddy in physical space, the tracked UMZ properties should also relate closely to the profiles for the mean U and rms σ_u. The previous UMZ tracking procedure provided the modal velocities u_m and edge locations of UMZs in a single $z-t$ plane. I used these properties to create an artificial velocity signal by assigning each vector index the u_m value of the UMZ to which the vector belonged. The resulting signal, the stepwise function shown in figure 40(*a*), contains no information relating to the shear layers except for the velocity jump between zones. The UMZ signal works similarly to a low-pass filter such that large-scale trends equal to and greater than the UMZ duration are captured. The mean profile of the UMZ signal in figure 40(*b*) matches closely with the SLPIV profile, except for the bottom and top of the image field where the tracking methodology is biased as previously discussed. Previous studies on UMZs have found similar agreement with the mean velocity (de Silva *et al.* 2017; Bautista *et al.* 2019). The streamwise turbulence in figure 40(*c*) is fairly well represented, though the energy is overestimated by the UMZ signal at lower heights (due to excluding the relatively smoother transitions across the zone interfaces) and underestimated at higher z values (due to excluding fluctuations within zones).

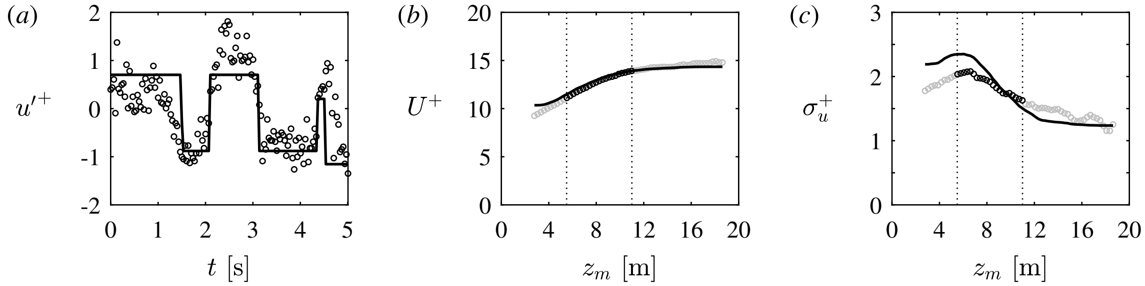

Figure 40. A comparison of the SLPIV signal (circles) with an artificial velocity signal based on UMZ modal velocities u_m (lines). (*a*) A 5-second sample time signal at $z = 10$ m. (*b*) The streamwise mean velocity profile. (*c*) The streamwise rms velocity profile. The dotted lines correspond to the approximate limits of the region exhibiting canonical behavior. Adapted from Figure 16 of Heisel *et al.* (2018).

Qualitatively, figure 40(*c*) demonstrates that the UMZs, along with larger-scale motions, govern the variance in the streamwise velocity. The variance profile, realized in the passing of successive UMZs, confirms the importance of the UMZ passing frequency (which scales with z, consistent with the length and number density) and the velocity jump between zones (which scales with u_τ). The UMZs are therefore related to the representative attached eddy in terms of both their average properties and their contribution to the velocity statistics.

While the UMZs are kinematically important, they lack the dynamics such as vorticity necessary to fully describe the evolution of structures and the generation of new ones. To capture both the flow statistics and dynamics, the representative eddy must include both the UMZ and corresponding ISL. Additionally, based on the shape of the two-point correlation, the average ISL must have a forward inclination. These features of the combined UMZ and ISL are compatible with the basic framework of the hairpin-type packet structure. de Silva *et al.* (2016) specifically showed that a synthetic velocity field created from Λ-vortex packet can reproduce the UMZ properties measured by their experiments.

An intriguing question moving forward is which perspective to take: are the shear layers separated by uniform flow regions, or are the uniform regions separated by shear interfaces? The more useful perspective depends on the generation mechanism of this organization, which has not been proven. Like many other complex systems, the answer is probably similarly complex, where the UMZs and ISLs act on each other and are in some way both responsible for generating new structures.

5 Uniform momentum zones and the mean velocity profile

Chapter 5 comprises an edited version of the article below, published in the *Journal of Fluid Mechanics*, © Cambridge University Press 2020. Please cite the published article when referencing content in this chapter.

Heisel, M., de Silva, C. M., Hutchins, N., Marusic, I., and Guala, M. (2020). On the mixing length eddies and logarithmic mean velocity profile in wall turbulence. *J. Fluid Mech.* **887**, pp. R1. https://doi.org/10.1017/jfm.2020.23.

5.1 The unanswered question

The results in chapter 4 and previous studies (de Silva *et al.* 2017; Bautista *et al.* 2019) have demonstrated a relationship between the UMZs and the mean velocity profile, where an ensemble of many UMZs and ISLs with varying wall-normal position leads to the continuous function $U(z)$. The specific evidence in §4.5 suggests the UMZs scale with u_τ and z in the log region, and are related to representative attached eddies whose population is consistent with the mean velocity and variance profiles (Townsend 1976). The scaling is not unique to UMZs, and many studies have identified wall-normal distance scaling using various analysis methods. Examples include detection of regions with coherent velocity fluctuations such as momentum streaks (Hwang 2015; Hwang & Sung 2018) and Q2–Q4 pairs (Lozano-Durán *et al.* 2012; Jiménez 2018), analysis of vortex clusters (del Álamo *et al.* 2006), modal decomposition (Cheng *et al.* 2019), and resolvent analysis (Sharma & McKeon 2013; Sharma *et al.* 2017). These results are not mutually exclusive. For instance, the histogram signature of a UMZ is consistent with streaks and rolls as previously discussed and also with resolvent modes (Saxton-Fox & McKeon 2017; McKeon 2019). In a generalization, the community of wall turbulence researchers uses different experimental methods[5] and conceptual frameworks to works towards an improved understanding of the same problem. Despite the collective research efforts, an important question remains unanswered: beyond scaling behavior, what are the exact properties of the flow structures leading to the mean velocity profile, and are these properties universal across a range of flow conditions?

These properties, referred to here as the average eddy size ℓ_e and velocity u_e, are at the heart of models for the mean velocity profile. The closure model in equation (3) with $u_e = u_\tau$ and $\ell_e = \kappa z$ is one of the earliest derivations of the log law (Prandtl 1932). Townsend (1976) used similar eddy properties to derive the velocity profiles. The scaling of these hypothetical eddies is well supported, yet the exact eddy properties have not been shown experimentally, e.g. the constant C in $\ell_e = Cz$ is assumed. Further, the universality of C has not been demonstrated for a range of Reynolds number and surface conditions.

---

[5] Each method is like a different pair of goggles that filters your view to a certain perspective, as my advisor would say.

Rather than observe the eddy properties directly (which is admittedly difficult), previous approaches have estimated the properties working backward from the mean velocity profile. The proportionality constant κ in the mixing length model $\ell_e = \kappa z$ was first estimated from mean velocity measurements (von Kármán 1930). The measurements more specifically apply then to the model ratio u_e/ℓ_e, but the constant κ was attributed solely to ℓ_e (Prandtl 1932), perhaps for simplicity. The mixing length $\ell_e = \kappa z$ is often used as a length scale in empirical meteorological models (Stull 1988) despite no direct estimate of ℓ_e. In a similar approach, L'vov *et al.* (2008) used experimental velocity profiles to fit an eddy model for the entire outer region, where the model transitioned from $\ell_e \propto z$ in the log region to $\ell_e \propto \delta$ in the wake and included a Reynolds number dependency.

The previous works cited above relating UMZs and the mean velocity have their own set of limitations. de Silva *et al.* (2017) used their detected UMZ edge statistics to estimate the average velocity jump ΔU_m as a function of z and probability distributions of the jump locations. The velocity profile modeled from the jump positions and intensities matched well with the measured mean velocity (de Silva *et al.* 2017), but the model assumed a fixed number of UMZs and did not quantify the size properties. Bautista *et al.* (2019) developed a similar model for instantaneous streamwise velocity profiles. The average characteristic velocity $\Delta U_m \approx \phi_c u_\tau$ and thickness $H_m \approx z/\phi_c$ of the UMZs in the log region were determined from scaling of the averaged Navier-Stokes equations. Similar to previous eddy models, the so-called Fife similarity parameter $\phi_c = \kappa^{-1/2} \approx 1.62$ was estimated from fits of experimental velocity profiles rather than direct observation of the UMZs (Klewicki 2013b). The probability distributions for the UMZ parameters were assumed to be Gaussian, and the distribution standard deviations were adjusted by trail and error until the resulting average model profile matched experimental velocity profiles (Bautista *et al.* 2019).

Given the limitations of the previous studies, this chapter evaluates the properties of UMZs across a variety of flow conditions, with an emphasis on high-Reynolds-number, zero-pressure-gradient boundary layers. The specific properties of interest are the average velocity difference ΔU_m and thickness H_m within the log region, i.e. above the viscous (or roughness) sublayer and below $z \lesssim 0.15\delta$. The goal of the analysis is to provide a systematic description of the UMZ properties in order to reconcile the structural composition of UMZs with previous eddy models and the derivation of the log law of the wall.

5.2 Methodology

The central aspect of the analysis was to detect UMZs for a range of flow conditions and compare the results. The most valuable dataset for the comparative analysis is the SLPIV measurements in the ASL, which has significantly larger surface roughness (k_s^+), Reynolds number (Re_τ), and scale separation than any laboratory-scale boundary layer. At the laboratory scale, I conducted new PIV experiments in the wind tunnel at St. Anthony Falls Laboratory (SAFL). My advisor and I also established a collaboration with the fluid mechanics research group at the University of Melbourne to extend the range of the laboratory-scale conditions. I visited their research group in 2019 to access and analyze previous PIV experimental data. Lastly, I downloaded instantaneous velocity fields from a direct numerical simulation (DNS) of a $Re_\tau \approx 2\,000$ boundary layer whose data are publicly available (Sillero *et al.* 2013). The experiments provide a uniquely

Table III. Experimental DNS and PIV datasets used in the comparison of uniform momentum zone (UMZ) properties. In addition to the SLPIV case at the Eolos field site, PIV measurements were conducted in the St. Anthony Falls Laboratory (SAFL) wind tunnel at the University of Minnesota and High Reynolds Number Boundary Layer Wind Tunnel (HRNBLWT) at the University of Melbourne.

Dataset	Label	Symbol	Facility	Re_τ	k_s^+	Source
direct numerical simulation	DNS	∗	computation	2 000	–	Sillero *et al.* (2013)
smooth wall	sw1	×	SAFL	3 800	–	Heisel *et al.* (2020)
smooth wall	sw2	+	SAFL	4 700	–	Heisel *et al.* (2020)
smooth wall	sw3	○	HRNBLWT	6 600	–	de Silva *et al.* (2014)
smooth wall	sw4	□	HRNBLWT	12 000	–	de Silva *et al.* (2014)
smooth wall	sw5	◊	HRNBLWT	17 000	–	de Silva *et al.* (2014)
mesh roughness	m1	△	SAFL	10 100	430	Heisel *et al.* (2020)
mesh roughness	m2	▽	SAFL	13 900	620	Heisel *et al.* (2020)
sandpaper roughness	sp1	▷	HRNBLWT	12 000	64	Squire *et al.* (2016a)
sandpaper roughness	sp2	◁	HRNBLWT	18 000	104	Squire *et al.* (2016a)
atmospheric surface layer	ASL	•	Eolos	$O(10^6)$	30 000	Heisel *et al.* (2018)

large range of both Reynolds number $Re_\tau \sim O(10^3 - 10^6)$ and surface roughness $k_s^+ \sim O(10^0 - 10^4)$, where $k_s \sim 1$ corresponds to hydraulically smooth conditions (Jiménez 2004). Details of the ASL measurements are provided in chapters 3 and 4. The remaining previous and new experiments are discussed in the subsections below.

5.2.1 Previous experiments

I accessed the streamwise velocity data for seven previously published boundary layer experiments which were performed under approximately zero-pressure-gradient conditions. The experiments are summarized in table III. The case with the lowest Reynolds number is from the DNS experiment of Sillero *et al.* (2013). Two-dimensional slices in the streamwise–wall-normal ($x - z$) plane were extracted from the DNS results to match the measurement plane of the remaining PIV experiments. Three of the smooth-wall and the two sandpaper roughness cases are based on large-field-of-view PIV measurements from the High Reynolds Number Boundary Layer Wind Tunnel (HRNBLWT) at the University of Melbourne, which were previously published by de Silva *et al.* (2013, 2014) and Squire *et al.* (2016a). Further details on the measurements can be found in the references cited in table III.

5.2.2 New experiments

To complement the existing databases, new PIV measurements were acquired for two smooth wall and two woven wire mesh roughness cases in the boundary layer wind tunnel at SAFL. The test section of the closed-loop wind tunnel is 16 m downstream of the contraction and has cross-sectional dimensions of 1.7×1.7 m^2 under approximately zero-pressure-gradient conditions. For the rough-wall cases, the test section and entire 16 m fetch were covered with woven wire mesh. The mesh had 3 mm wire diameter and 25 mm opening size, i.e. distance between wires, resulting in equivalent sand grain roughness $k_s = 17$ mm.

Table IV. Additional details and dimensional flow parameters for the new PIV measurements from the SAFL wind tunnel.

Dataset	Label	Symbol	U_∞ [m s^{-1}]	u_τ [m s^{-1}]	δ [mm]	k_s [mm]	w_I^+ ($w_I u_\tau/\nu$)
smooth wall	sw1	$\times$	7.1	0.27	220	–	26
smooth wall	sw2	$+$	10.1	0.37	200	–	36
mesh roughness	m1	$\triangle$	7.1	0.39	400	17	38
mesh roughness	m2	$\bigtriangledown$	10.1	0.56	390	17	55

Because the mesh cases were in fully rough conditions, the roughness k_s was estimated using equation (6) and a fit to the mean velocity profile.

I used the previous wire mesh experiment by Flack *et al.* (2007) to predict *a priori* the relationship between the mesh dimensions and the roughness sublayer extent. I selected the mesh size to maximize the roughness length scale k_s while maintaining a roughness sublayer less than 50% of the log region extent. These conditions allow for maximum separation between the roughness and viscous length scales as quantified by the roughness Reynolds number k_s^+, while also preventing the roughness from modifying turbulent energy generation in the log region to an extent where outer layer similarity does not hold (Jiménez 2004).

Cross-hotwire anemometer measurements of the full boundary layer profile were used to estimate flow parameters such as δ. The Dantec cross-wire probes were aligned to measure the u and w velocities simultaneously. The probes were connected to an A.A. Lab anemometer system. The anemometer system was calibrated using a separate temperature-controlled calibration box with laminar flow output. The temperature of the box was fixed to the same temperature as the wind tunnel which also has temperature controls for both the floor and free stream. The calibration box was operated for a series of flow velocities and angles to establish calibration points spanning the range of expected instantaneous velocity measurements. After calibration, the probes were mounted to a motorized traverse to acquire the velocity measurements at different wall-normal positions. Measurements were acquired at 10 kHz for 240 seconds.

The PIV setup in the tunnel test section included a Big Sky 532 nm Nd:YAG double-pulsed laser oriented in the streamwise–wall-normal plane, a TSI Powerview 4 MP camera, and TSI Insight 4G synchronizer and acquisition software. Atomized olive oil was used as tracer particles for the flow imaging. The field of view was limited to the lowest 25% of the boundary layer in the rough-wall case where $\delta \approx 400$ mm (50% in the smooth-wall case where $\delta \approx 200$ mm) to enhance the spatial resolution in the logarithmic region. A total of 10 000 image pairs were captured for each of two smooth-wall cases and two rough-wall cases. For the rough-wall cases, 5 000 image pairs were captured for two planes within the roughness pattern. Velocities were calculated from the image pairs using the same in-house cross-correlation code employed for the SLPIV measurements. The code performed two passes, with a final interrogation window size of 24 by 24 pixels and 50% window overlap. An overview of the scaling parameters for the new measurements is provided in table IV. Wall-normal profiles of the velocity statistics for the new and previous experiments are shown in figure 41.

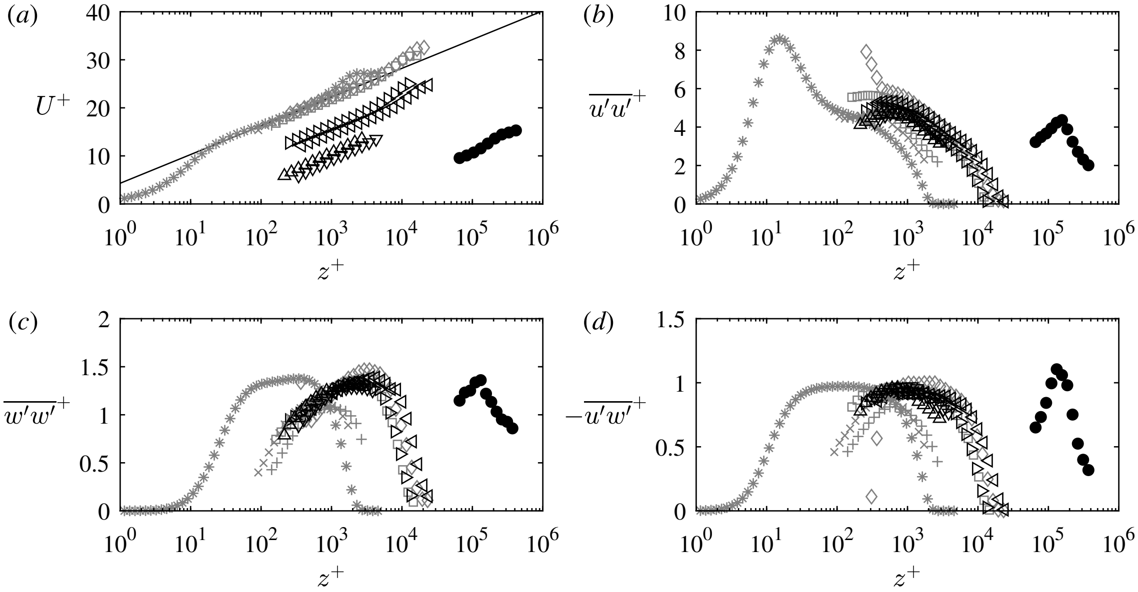

Figure 41. Velocity profiles for the datasets used in the comparison of UMZ properties: (*a*) mean streamwise velocity; (*a*) streamwise variance; (*c*) wall-normal variance; (*d*) Reynolds shear stress. Data symbols correspond to the experimental datasets in table III and the line in (*a*) is the log law for smooth wall conditions. Data symbols are shown with logarithmic spacing for clarity. Adapted from Figure 1 of Heisel *et al.* (2020).

5.2.3 Detection of uniform momentum zones

I detected UMZs using the same histrogram method detailed in §4.2.1. Owing to the inclusion of new datasets, the streamwise length $\mathcal{L}_x$ of the vector fields used for each histogram is revisited here. The lowest wall-normal position reported in later results is fixed to $z = 0.05\delta$ in order to exclude most of the roughness sublayer in the rough-wall cases, and because some of the PIV experiments did not measure nearer to the wall. The position $z = 0.05\delta$ is also the approximate start of the log region for the DNS case with the lowest Reynolds number. The aspect ratio of the streamwise extent and wall-normal position of wall-attached structures is between 10 and 15 (Baars *et al.* 2017) such that the average length of structures at $z = 0.05\delta$ is approximately 0.5δ. I selected the length $\mathcal{L}_x = 0.1\delta$ to be short enough for smaller-than-average structures to manifest distinct peaks in the histograms, while also large enough to yield statistically converged histograms in the dataset with the coarsest resolution. The sensitivity of the results to the choice of $\mathcal{L}_x$ is discussed in §5.2.4. The other change to the histogram detection was an increase in the bin width from $0.33u_\tau$ to $0.5u_\tau$. The new bin width is still smaller than the average velocity difference ΔU_m, and the corresponding decrease in number of bins improved the histogram statistical convergence.

I reanalyzed the SLPIV vector data using the new histogram parameters with $\delta_{SL} \approx 70$ m, and detected UMZs and their edges for the remaining experimental datasets using the same parameters. Many of the experimental datasets measured the entire boundary layer thickness, and therefore included PIV vectors in the free-stream flow. Because the extent of free-stream vectors in each PIV field can influence the height of the UMZ peaks in the normalized histogram, the free-stream vectors must be excluded from the histogram detection (de Silva *et al.* 2016). I detected the TNTI separating the boundary layer turbulence from the free-stream region using a threshold of the local kinetic energy. I tuned the threshold for each dataset following the suggested procedure in Chauhan *et al.* (2014). Figure 42(*a,b*) shows an example vector field and histogram with the free-stream region above the TNTI excluded. As before, the internal shear layers were located using isocontours of the histogram minima u_i. Figure 42(c) shows the shear layers between the detected UMZs, where the velocity throughout each UMZ is represented by its modal velocity u_m.

As discussed in §2.2.5, the scale separation between the ISL thickness $\delta_\omega{\sim}O(\lambda_T)$ and the UMZ thickness $H_m{\sim}O(L)$ increases with Reynolds number, and the shear layers are thin (i.e. small δ_ω/δ) for high-Reynolds-number flows. In the log region of the present lab-scale datasets, the ISLs cover up to approximately 15% of the measurement area, and the interior of UMZs covers the remaining 85%. The UMZ coverage is greater for the ASL case. Here, I consider the UMZ and its corresponding ISL to be a single unit that defines the representative eddy. The thickness of the UMZ interior and the ISL are combined in a single parameter h_m which is the wall-normal distance between the center of adjacent ISLs. Combining the thicknesses does not affect the conclusions of the study. In this approximation, the low-amplitude turbulence within the UMZ interior is also neglected, and the velocity difference Δu_m is assumed to occur instantaneously, as opposed to occurring across the Taylor microscale-thickness of the ISL.

Figure 42(*d*) shows an instantaneous velocity profile overlaid with the detected UMZ signature. The profile highlights the organization of relatively uniform regions separated by sharp velocity jumps, demonstrated by the agreement between the UMZ approximation and the measured velocity. An ensemble of these instantaneous step-like profiles leads to the mean velocity profile also shown in figure 42(*d*). The mean profile is well captured by the UMZ approximation given by U_m.

The analysis yielded instantaneous UMZs profiles for every column in every PIV frame. From these profiles I compiled at least 10^6 instantaneous h_m values for each dataset. To evaluate the thickness as a function of the wall-normal distance, I calculated ensemble averages of h_m in intervals of z/δ, where the UMZ midheight z_m was used to determine the z/δ interval for each UMZ.

I calculated the velocity difference ΔU_m following the same conditional averaging procedure as in §4.3. Similar to h_m, the velocity profiles relative to the detected ISL were compiled for each ISL in every PIV column and frame. However, the conditional averaging does not allow for instantaneous estimates Δu_m. Based on the ISL wall-normal position, the profiles were sorted using the same z/δ intervals as for h_m. For each interval, the relative profiles were ensemble averaged and ΔU_m was computed using linear fits to the average profile in the same manner as before. The conditional averaging did not discriminate between internal shear layers and the TNTI such that the TNTI behavior contributes to ΔU_m, particularly as z/δ approaches one.

5.2.4 Sensitivity analysis

To assess the sensitivity of the results to the choice of $\mathcal{L}_x$, I calculated UMZ thickness statistics for a range of $\mathcal{L}_x$ using a small sample of each dataset. Figure 43 plots the average UMZ thickness $H_{m,log}$ within the log region as a function of $\mathcal{L}_x$. The thickness H_m increases moderately with $\mathcal{L}_x$ due to the exclusion of the

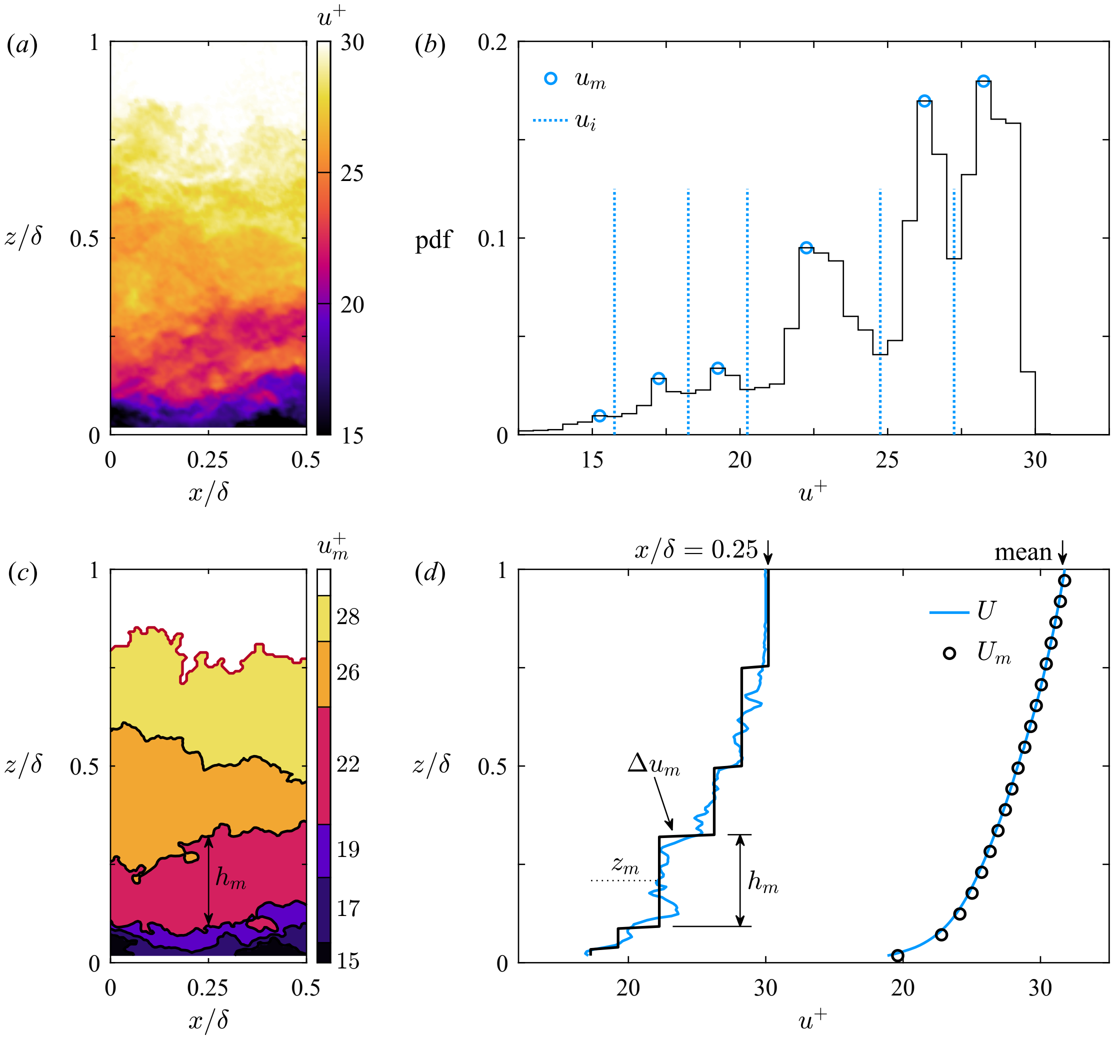

Figure 42. Example detection of UMZs from experiment “sw5” in table III. (*a*) Streamwise velocity field $u(x, z)$. (*b*) Histogram of the vectors in (*a*) with the detected modes u_m and minima u_i. (*c*) Estimated UMZ field including internal shear layers corresponding to u_i (black lines) and the turbulent/non-turbulent interface (red line). (*d*) Instantaneous and time-averaged profiles of u (blue lines) and u_m (black lines/markers). Adapted from Figure 2 of Heisel *et al.* (2020).

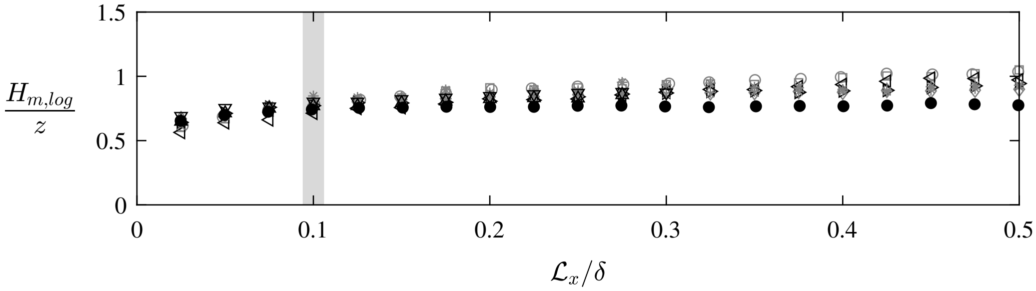

Figure 43. Average UMZ thickness $H_{m,log}$ in the log region as a function of the detection parameter $\mathcal{L}_x$, where $\mathcal{L}_x = 0.1\delta$ is the value used for later results. Data symbols correspond to the experimental datasets in table III. Adapted from Figure 3 of Heisel *et al.* (2020).

smallest structures by the filtering effect discussed in §4.2.1. The difference between the ASL and laboratory-scale datasets for larger $\mathcal{L}_x$ may be due to the underestimated size of the largest UMZs exceeding the spatially limited field of view in the SLPIV measurements. Considering the orders-of-magnitude difference in H_m, the agreement of results across datasets is minimally affected and the conclusions drawn from the later results do not change within the range of $\mathcal{L}_x$ shown. Figure 43 therefore shows $\mathcal{L}_x = 0.1\delta$ to be appropriate for studying H_m in the range of z/δ presented here, both in terms of the scaling parameter and the proportional constant.

I also compared the UMZ results with an alternative detection method for a single dataset. I detected the position of the shear layers directly from the PIV fields using a high-pass cutoff threshold of the instantaneous shear $\partial u/\partial z$. I selected the threshold to be a factor of the height-dependent rms value for $\partial u/\partial z$. The UMZ thicknesses h_m were the wall-normal distances between the midheight of detected shear regions. Using a threshold equal to the shear rms, the resulting $H_m(z)$ statistics were both qualitatively and quantitatively similar to the histogram detection results. However, changing the threshold to a different factor of the rms had a similar effect on the results as the $\mathcal{L}_x$ parameter, where a higher factor detected fewer shear regions and increased the average UMZ thickness. The findings presented here are therefore not specific to the histogram detection method.

5.3 Average momentum zone properties and the mean shear

Wall-normal profiles of the average UMZ properties are shown in figure 44. The approximately continuous ensemble-averaged UMZ profiles result from variability in the UMZ size, velocity, and position throughout the averaging period. The stochastic behavior of the shear layer position was studied in de Silva *et al.* (2017), and variability in the UMZ size is addressed later in the next section. As seen in figure 44(*a,b*), the UMZ characteristic velocity ΔU_m scales unambiguously with the friction velocity u_τ. The result agrees with the log law formulation and highlights u_τ as the relevant turbulent velocity scale across the entire boundary layer. The observed moderate decrease from $\Delta U_m \approx 1.8u_\tau$ in the log region to $\Delta U_m \approx u_\tau$ near the edge of the boundary layer compliments previous laboratory-scale results for ISLs and the TNTI (Chauhan *et al.*

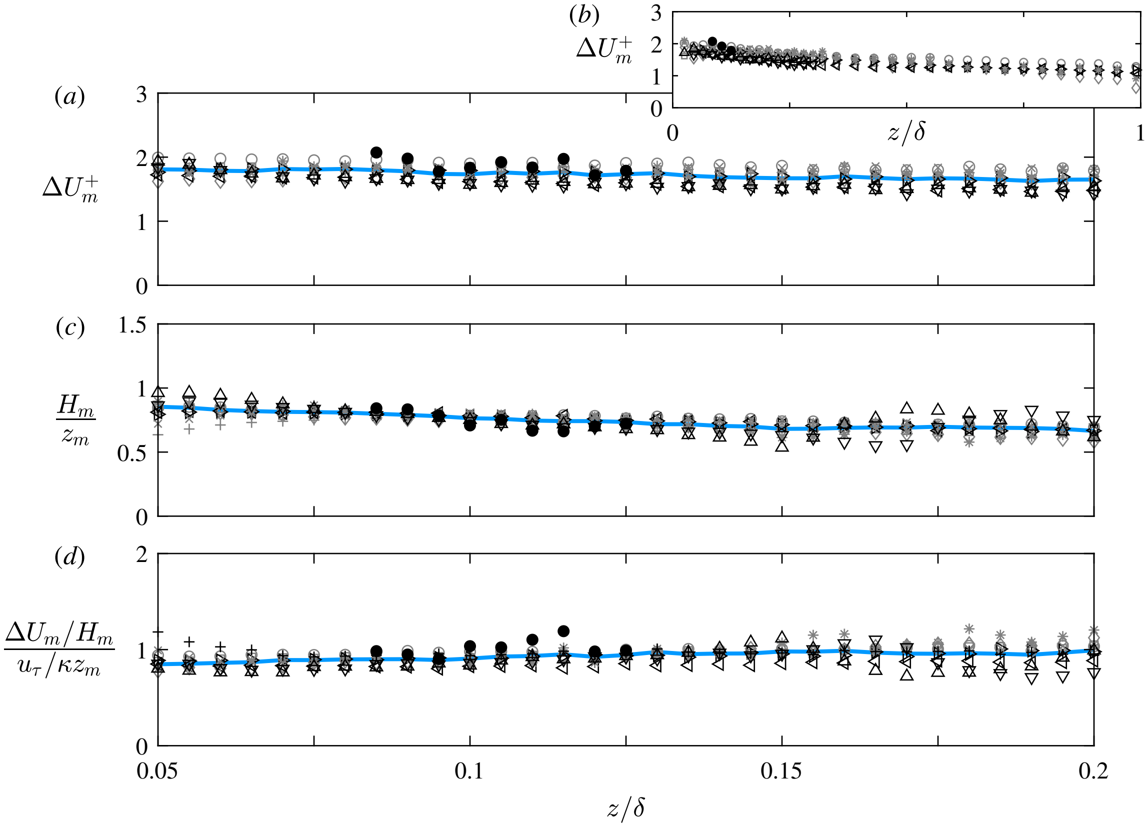

Figure 44. Profiles of average UMZ properties in the log region. (*a*) Velocity difference ΔU_m between adjacent UMZs. (*b*) Same as (*a*), but for the entire boundary layer thickness. (*c*) Thickness H_m of UMZs. (*d*) Comparison of UMZ properties with the mean shear scaling $u_\tau/\kappa z$. Data symbols correspond to the experimental datasets in table III and the blue line is the average. Adapted from Figure 4 of Heisel *et al.* (2020).

2014; de Silva *et al.* 2017), and the present work extends the u_τ scaling to a wider range of Reynolds number and surface roughness.

The consistent u_τ scaling of coherent structure characteristic velocities seems reasonable from a statistical approach (what other velocity scale should matter?), but it is worth considering the result in terms of phenomenology. Recalling the definition $u_\tau \equiv \sqrt{\tau_\mathrm{w}/\rho}$ from dimensional grouping, how does the wall shear stress manifest itself as a local velocity ΔU_m within (and between) coherent structures? How do the features far from the wall, particularly the TNTI, "know" u_τ? I do not have the answers to these questions, though perhaps the latter question is related to interdependence. The bulk velocity difference across the boundary layer (U_∞) is fixed. If the log region and sublayer structures follow u_τ scaling, the remaining velocity difference becomes related to u_τ in some form. This is a variation on the bottom-up mechanism where the velocity information near the wall is propagated throughout the boundary layer, possibly through the pressure field, even if the physical structures do not all originate at the wall.

Returning to the results, the average UMZ thickness H_m is given in figure 44(*c*). The agreement across datasets with wall-normal distance scaling shows z to be the appropriate length scale for UMZs in the log region. To emphasize the success of the normalization, note that the dimensional range represented in figure 44(*c*) is $H_m = 0.0065$ to 6.3 m. Based on the observed functional dependence $H_m \propto z_m$ in this region, the UMZs exhibit the wall-dependent behavior predicted by the mixing length model and the attached eddy hypothesis. Any differences between the smooth- and rough-wall profiles are within the uncertainty of the results.

Figures 44(*a-c*) highlight the similarity of UMZs relative to the log law scaling parameters u_τ and z across a three order-of-magnitude range in Reynolds number. In figure 44(*d*), the mean shear $\partial U/\partial z$ is estimated from the average UMZ properties $\Delta U_m/H_m$ and is compared with the shear scaling argument $u_\tau/\kappa z$. The values near unity demonstrate the fundamental interdependence of the UMZ properties and the shear scaling parameters in the log region, where the distribution of UMZs relates directly to the mean velocity gradient as $\Delta U_m/H_m \approx u_\tau/\kappa z$.

Before proceeding further, I would like to wax philosophical on the chicken-and-egg question of wall turbulence: which came first, the structures or the mean shear? Following the above discussion on u_τ, the only fixed velocity condition for every flow realization is the net velocity difference across the entire boundary layer. The UMZ results so far have shown that the boundary layer self-organizes at each instant into relatively uniform flow regions and relatively intense shear layers to accommodate the velocity difference. The mean shear is not present or “felt” in each of these instances. It is rather a statistical quantity resulting from an ensemble of many realizations of this self-organization. Figure 44(*d*) is consistent with this argument: the mean shear matches the behavior of the ensemble of many UMZs and ISLs. In this sense, the structures lead to the mean shear, and the mean shear and mean velocity profile describe the net result of the average structure.

Within the log region, the behavior of the average structure is governed by the theoretical scaling parameters u_τ and z, regardless of Reynolds number or surface rougness. The findings provide experimental evidence that the hypothetical eddies assumed in Prandtl’s mixing length model and Townsend’s attached eddy hypothesis have a well-defined and persistent physical representation in the layered structure of boundary layer turbulence. The log law is successful because the eddy scaling behavior and complete Reynolds number similarity assumed in derivations of the law are correct, and the present work shows that this behavior is exhibited in realizations of the UMZ-ISL organization. As this is a critical point of the thesis, I again note here that the UMZ-ISL organization is in many ways compatible with other structures such as momentum streaks and hairpin-type packets. The advantage of the UMZ classification is that it allows for a generalized framework to systematically quantify the velocity organization at every measured realization of the flow.

Assuming the UMZ and its associated ISL are the representative eddy, the average UMZ properties can be compared to previous model predictions. The results in figure 44(*a,c*) suggest u_e/u_τ and ℓ_e/z may both be weakly dependent on the wall-normal position within the log region. This may be an effect of finite Reynolds number, or an artifact of the detection methodology. The average properties in the log region are $\Delta U_m^+ = 1.73 \pm 0.13$ and $H_m/z = 0.74 \pm 0.07$, where the uncertainty is represented by one standard deviation of all the data point in figure 44, noting that additional uncertainty exists in the $\mathcal{L}_x$ sensitivity. These values are approximately twice the mixing length model $u_e = u_\tau$ and $\ell_e = \kappa z$ (Prandtl 1932), and are closer to

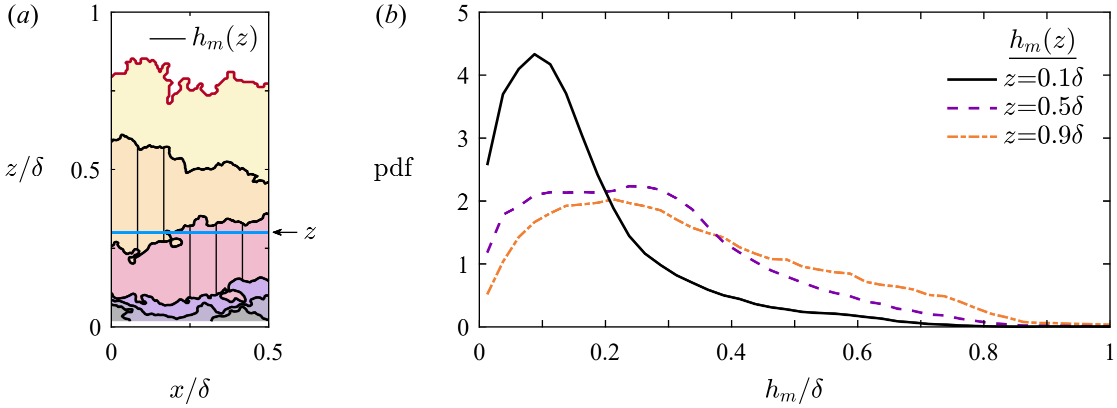

Figure 45. Example compilation of UMZ thickness statistics for the probability analysis. (*a*) The statistics at a given position z (blue line) include every thickness h_m where the UMZ intersects with z. (*b*) Probability densities of $h_m(z)$ at three wall-normal positions from the DNS dataset. Adapted from Figure 5 of Heisel *et al.* (2020).

the more recent predictions $u_e = 1.62u_\tau$ and $\ell_e = 0.62z$ used in the model by (Bautista *et al.* 2019). The difference between the UMZ size $H_m \approx 0.74z$ and the common mixing length definition $\ell_e = \kappa z$ is not surprising considering κ originates from mean velocity measurements as previously discussed. The results provide a reminder that the coefficient κ is specifically associated with the ratio u_τ/z and it therefore does not quantify the precise size of energy-containing turbulent motions as is assumed by the definition $\ell_e = \kappa z$. Nevertheless, the UMZs and the hypothetical mixing length eddies both result in the same mean shear scaling and κ value in figure 44(*d*), and lead to the same log law of the wall in equation (5).

5.4 Momentum zone probability distributions

Thus far, the focus has been on the average UMZ properties. However, the probability distributions of Δu_m and h_m are also important, especially for high-order statistics beyond a simple mean value. Only the average value ΔU_m is provided by the calculation of the velocity difference, and the present section is limited to analysis of the UMZ thickness.

The previous shear scaling comparison in figure 44 required the use of a single representative height for each UMZ, i.e. the midheight $h_m(z_m)$. In a probability analysis, however, the influence of large UMZs extending to the near-wall region would be diminished by confining the UMZ to a single height z_m farther from the wall. To avoid this bias, I calculated the height-dependent probability statistics using a new selection criterion on the original h_m values. At a given wall-normal position z, the thickness statistic $h_m(z)$ includes every UMZ which reaches the position z as depicted in figure 45(*a*). The statistics are repeated for all z. Examples of $h_m(z)$ pdfs at three z positions for the DNS dataset are shown in figure 45(*b*).

The shape of the sample pdfs in figure 45(*b*) resemble a log-normal distribution. A detailed analysis of the pdf shape type was not conducted to fit the distribution definitively, and a distribution with a similar general shape such as gamma may be more correct. However, unlike the Gaussian distribution assumed by Bautista

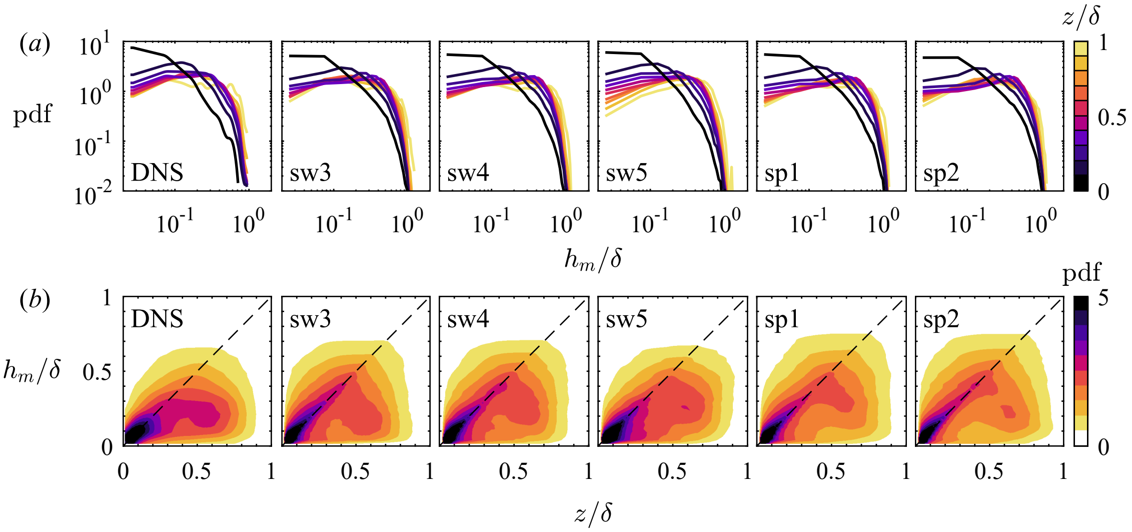

Figure 46. Probability density functions (pdfs) of UMZ thickness $h_m(z)$ for every dataset where the field of view extended to $z = \delta$. (*a*) Separate pdfs for different wall-normal positions z indicated by the line color. (*b*) Joint pdfs of h_m and z, where the dashed line represents $h_m(z) = z$. Columns correspond to the indicated experiments.

et al. (2019), the h_m distribution is skewed, positive-definite, and has a heavier tail.

Figure 46 shows the resulting probability distributions of $h_m(z)$ for the datasets where the field of view included the full boundary layer thickness. The distributions could not be calculated for the datasets with a more limited field of view because the true extent of UMZs exceeding the field of view is not known. The plots in figure 46(*a*) suggest that the distribution tail is always limited by $h_m \lesssim \delta$ regardless of position z, which is expected. At any position, the largest structures are limited in size by the outer boundary condition δ. However, for small z/δ in the log region, these δ-scaled structures are rarely occurring such that the influence of δ on the mean behavior is small. As the wall-normal distance increases, the outer condition δ limits the size of an increasing proportion of the identified structures. The behavior of the probability tail may explain the decreasing trend in figure 44(*c*), where h_m/z decreases slowly with z as δ becomes increasingly relevant.

The joint probabilities of h_m and z in figure 46(*b*) more clearly shows the departure from wall-dependent behavior in the log region to outer (δ) scaling in the wake region. The small differences between cases are likely due to differences in the experimental measurement resolution and variability in the detection process. The consistent trend across datasets is that the most probable UMZ thickness follows $h_m(z) = z$ up to $z/\delta \approx 0.5$, above which the probability distribution transitions to being independent of wall-normal distance as δ becomes the primary length scale. The probability analysis reveals the competing influence of multiple scales, in this case z and δ. In the next chapter, a similar probabilistic approach is used to reveal scaling behavior that is not apparent simply from the mean value.

6 Vortex cores and internal shear layers

Preliminary analysis of vortices using the SLPIV data in §4.4 demonstrated that the strong prograde vortex cores primarily appear within the internal shear layers. In this chapter, I use the same suite of experimental datasets as the UMZ analysis to compare the properties of the vortex cores across a wide range of Reynolds number and surface conditions. The goal of the analysis is to identify commonalities between the vortex and ISL behavior to better understand how they relate to each other.

The experimental datasets used in chapter 5 are summarized again in table V. Additional information pertinent to the vortex and shear layer analysis is provided in the new table, namely the measurement spatial resolution. For the DNS experiment from Sillero *et al.* (2013), the resolution given in table V corresponds to the streamwise grid spacing; the wall-normal spacing was non-uniform, with higher resolution nearer to the wall in order to fully resolve all flow scales. The HRNBLWT PIV experiments from the University of Melbourne in chapter 5 used a large-field-of-view camera configuration to capture an extensive streamwise distance (de Silva *et al.* 2014). The same flow conditions were also captured with a high-resolution tower configuration (Squire *et al.* 2016a). The tower PIV data are used in this chapter because the focus is now smaller-scale structures. The sandpaper surface roughness PIV experiments are included in the shear layer findings, but excluded from the vortex results presented here. These datasets were analyzed, but issues with the vectors fields and vortex detection led to unreliable statistics. As a reminder, the velocity profiles for the experimental datasets are plotted together in figure 41.

6.1 Parameterizing the small scales

Assessing the behavior of the small turbulent features requires accurate estimates of the possible governing parameters. The relevant parameters include the Kolmogorov microscales: length $\eta \equiv (\nu^3/\epsilon)^{1/4}$, velocity $u_\eta \equiv (\nu\epsilon)^{1/4}$, and time $\tau_\eta \equiv (\nu/\epsilon)^{1/2}$ (Pope 2000). These scales define the smallest turbulent fluctuations, as motions smaller than the Kolmogorov scale are dominated by viscosity.

By their definition, estimating the Kolmogorov microscales requires knowledge of the energy dissipation rate ϵ, which is difficult to measure directly. Various estimation methods for ϵ were used depending on the dataset. For the ASL dataset, the measurement resolution of both the SLPIV and the sonic anemometer were coarse relative to the Kolmogorov scales. The dissipation was therefore estimated using a scaling argument $\epsilon \approx u_\tau^3/\kappa z$. The argument is based on an assumption of energy equilibrium in the log region as discussed in 3.3.1. The scaling parameters for the HRNBLWT datasets were provided in the transfer of data during the collaboration with the University of Melbourne. Using hotwire anemometer measurements, the dissipation had been estimated as $\epsilon \approx 15\nu\langle(\partial u/\partial x)^2\rangle$ which assumes locally isotropic conditions (Pope 2000). I calculated the SAFL dataset parameters also using hotwire anemometry measurements. I estimated ϵ based on the turbulent energy density in the inertial subrange using the longitudinal second-order structure function $D_{11}(r) = \langle[u(x+r) - u(x)]^2\rangle$, where I converted the hotwire temporal series to x with Taylor's

Table V. Spatial resolution for the experimental datasets introduced in table 4. In this chapter, the HRNBLWT measurements are from the high-resolution tower configuration, as opposed to the large-field-of-view configuration in chapter 5. The comparison of the interrogation window size w_I with the Kolmogorov length scale η and Taylor microscale λ_T uses the average η and λ_T values within the approximated log region. The vector spacing is $\Delta x = w_I$ for the DNS case and $\Delta x = w_I/2$ for the PIV data. Further measurement details are given in Sillero *et al.* (2013) for the DNS, Squire *et al.* (2016a) for HRNBLWT, §5.2.2 for SAFL, and chapter 3 for Eolos.

Dataset	Symbol	Facility	Re_τ	k_s^+	w_I^+	w_I/η	w_I/λ_T
direct numerical simulation	$*$	computation	2 000	–	6.3	1.9	0.06
smooth wall	$\times$	SAFL	3 800	–	26	6.1	0.20
smooth wall	$+$	SAFL	4 700	–	36	8.4	0.22
smooth wall	○	HRNBLWT	6 600	–	7.6	1.8	0.05
smooth wall	□	HRNBLWT	12 300	–	14	2.8	0.06
smooth wall	◊	HRNBLWT	17 000	–	20	3.7	0.08
mesh roughness	△	SAFL	10 100	430	38	7.8	0.18
mesh roughness	▽	SAFL	13 900	620	55	10	0.22
sandpaper roughness	▷	HRNBLWT	12 100	64	15	2.9	0.07
sandpaper roughness	◁	HRNBLWT	18 400	104	19	3.3	0.06
atmospheric surface layer	•	Eolos	$O(10^6)$	30 000	6,400	800	4

hypothesis. Specifically, the method estimates ϵ from the theoretical inertial subrange expression $D_{11}(r) = C\epsilon^{2/3}r^{2/3}$, where $C \approx 1.9$ is a universal constant and the inertial subrange is identified by premultiplying D_{11} by $r^{-2/3}$ (Saddoughi & Veeravalli 1994). I estimated the dissipation for the DNS dataset using the same structure function method with the streamwise signals $u(x)$. The viscosity ν was known based on the temperature for each experiment, and the calculation of the Kolmogorov microscales was straightforward following the estimation of ϵ.

A second parameter worth considering is the Taylor microscale λ_T, an intermediate length scale. Previous studies have shown the average shear layer thickness is proportional to λ_T (Eisma *et al.* 2015; de Silva *et al.* 2017). The definition of the Taylor microscale is statistical, and there is not a robust physical interpretation of λ_T in turbulence theory. The meaning of the Taylor microscale is discussed further in chapter 7. As with ϵ, there are multiple methods for calculating λ_T. The direct equation for the transverse Taylor microscale, based on the autocorrelation function, is $\lambda_T = \sqrt{u_{rms}^2/\langle(\partial u/\partial x)^2\rangle}$ (Pope 2000), where u_{rms} is the streamwise rms velocity. I calculated λ_T using this equation for the DNS and Melbourne datasets. As before, hotwire measurements were used rather than the PIV data for parameterizing the wind tunnel cases. The cross-hotwire anemometers used in the SAFL wind tunnel have a substantial control volume relative to the Kolmogorov scales. As the velocity derivative statistic in the λ_T definition is governed by the dissipative scales, the cross-wire underestimated the derivative rms term. The preferred method for the SAFL cases was therefore to assume local isotropy and estimate λ_T from the expression $\epsilon = 15\nu u_{rms}^2/\lambda_T^2$, which combines the λ_T and ϵ expressions to circumvent the derivative term. The dissipation, calculated from inertial subrange statistics at scales larger than the derivative rms, is not subject to the same underestimation. The field measurements were also too coarse to resolve the velocity derivative statistic and the same isotropic expression as the SAFL cases was instead employed. Using the previous ϵ estimate yielded the Taylor microscale $\lambda_T \approx 13$ cm in the ASL case.

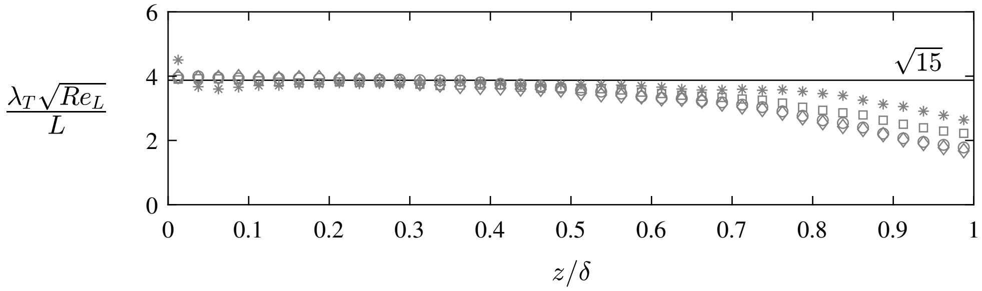

Figure 47. Wall-normal profile of the functional relationship between the Taylor microscale λ_T, integral length scale L, and Reynolds number Re_L. Values are shown only in intervals of 0.025δ for clarity. Data symbols correspond to the experimental datasets in table V.

The yet larger motions correspond to the integral scales. These scales are important in the context of the Taylor microscale because of their close functional dependence, i.e. $\lambda_T{\sim}LRe_L^{-1/2}$ where L is the integral length scale. Here, I used the streamwise velocity parameter u_{rms} to estimate the integral scales. Specifically, I calculated the integral length scale as $L = u_{rms}^3/\epsilon$ and the turnover time as $T = u_{rms}^2/\epsilon$. The turnover time is related to the classical energy cascade timescale (Pope 2000) and is distinct from the integral time scale L/U. The integral Reynolds number is $Re_L = u_{rms}L/\nu$. The relationship between λ_T and L is shown in figure 47. The proportional coefficient, i.e. the vertical axis value, is approximately constant throughout the majority of the outer region within each case. The SAFL and ASL cases are excluded from figure 47 because the estimation methods described above yield the trivial ratio $\sqrt{15} \approx 3.87$ regardless of the measurements. The value close to $\sqrt{15}$ for the DNS case supports the assumption of local isotropy used in the other cases, except for far into the wake region.

The possible relevance of multiple parameters for vortices and ISLs is a consequence of the multi-scale dynamics of turbulence. The Kolmogorov- and integral-scaled motions do not evolve in isolation from one another, and are in fact connected through energy transfer processes and so-called scale interaction. Statistics resulting from these properties may therefore have a signature behavior at multiple scales. In these cases, the mean statistic may not tell the whole story, so to speak, or the mean may not even have any relevance. The following analysis therefore focuses primarily on probability distributions, and only resorts to mean statistics when necessary.

6.2 The model vortex and detection algorithm

The previous vortex analysis for the ASL case in §4.4 successfuly demonstrated that the strong prograde vortices primarily occur within the internal shear layers. However, the analysis was limited by the subjectivity of the cutoff threshold, in addition to the SLPIV spatial resolution. Here, in the comparison of vortex properties across flow conditions, a model vortex is preferred. Parameters such as the size and velocity of the vortex are determined by fitting the local vector field to a vortex model defined by these parameters. Previous studies used the following model vortex in cylindrical coordinates (Carlier & Stanislas 2005; Herpin *et al.* 2013):

$$\mathbf{u} = \mathbf{u}_\omega + \frac{\Gamma}{2\pi r}\left[1 - \exp\left(-\frac{r^2}{r_\omega^2}\right)\right]\mathbf{e}_\theta, \tag{14}$$

where $\mathbf{u}_\omega$ is the advection velocity of the vortex, Γ is the circulation, r is the radial distance from the vortex center, r_ω is the vortex radius, and $\mathbf{e}_\theta$ is the unit vector in the azimuthal direction. The model incorporates Biot-Savart law for the velocity induced by a vortex line, i.e. $u_\theta \propto \Gamma/2\pi r$. Equation (14) is based on the Oseen vortex model (1912), which is consistent with the Navier-Stokes equations in its three-dimensional definition. The difference between this Oseen model and the Burgers vortex (1948) is that the Oseen model does not consider any radial velocity or vortex stretching in the axial direction.

In the original vortex definition by Oseen (1912), the radius is given by the term $r_\omega = 2\sqrt{\nu t}$, where the radius is zero at time t=0 and the vortex grows in time via viscous diffusion. The radius r_ω is inferred to be the location of the maximum azimuthal velocity. In the vortex model by Burgers (1948), the radius is given by $r_\omega = 2\sqrt{\nu/\alpha}$, where α is the strain rate. Rather than growing in time, the Burgers vortex size is steady due to a balance between outward diffusion and inward radial velocity induced by the vortex stretching mechanism (Burgers 1948). This distinction between the two models becomes important for interpreting the later results.

I conducted the vortex detection using the Oseen model in equation (14) following the procedure of Herpin *et al.* (2013), which is summarized here. I identified possible vortex cores based on vector regions where $\lambda_{ci} > 1.5\lambda_{rms}$. This threshold introduces selection bias on the vortices, but the threshold is not applied in the later model fit. Based on a test using one dataset, changing the threshold factor from 1.5x to 2x or 2.5x resulted in the detection of fewer vortices, but resulted in no statistically significant changes to the vortex properties. A notable deviation to the original procedure was to apply a Gaussian filter to the wind tunnel PIV fields prior to vortex detection. The filter removed small-scale noise in the gradients which significantly improved the performance of the fitting algorithm. The selected size of the Gaussian filter, i.e. its standard deviation, corresponded to approximately 2η in the log region for each case. The filter was not applied to the DNS or SLPIV vector fields.

I used the properties of the core region as initial guesses for the six vortex model parameters: the center position given by x_ω and z_ω, the advection velocity components u_ω and w_ω, the circulation Γ, and the radius r_ω. The initial value for Γ was calculated from the core area and out-of-plane vorticity ω_y within the core region. Based on the initial guesses for r_ω, x_ω, and z_ω, I extracted the local velocity vector field within $2r_\omega$ of the vortex center. I then fitted the extracted vector field to equation (14) using the initial guesses and a non-linear least-squares fitting algorithm. The algorithm outputted values for the six model parameters defined above that resulted in a model vortex most closely matching the vector field within and around the vortex core. An example vector field and closest model fit are shown in figure 48(*a*).

In some cases, the fitted radius was much larger than the initial guess. To ensure an accurate fit, I wrote a condition in the fitting algorithm to extract a larger vector field around the vortex and repeat the model fit if the fitted radius was more than twice the initial guess. I also only saved the vortex properties if the following criteria were met:

1. The R-squared value of the model vortex fit exceeded 0.5.
2. The vortex did not overlap with the field of view limits.

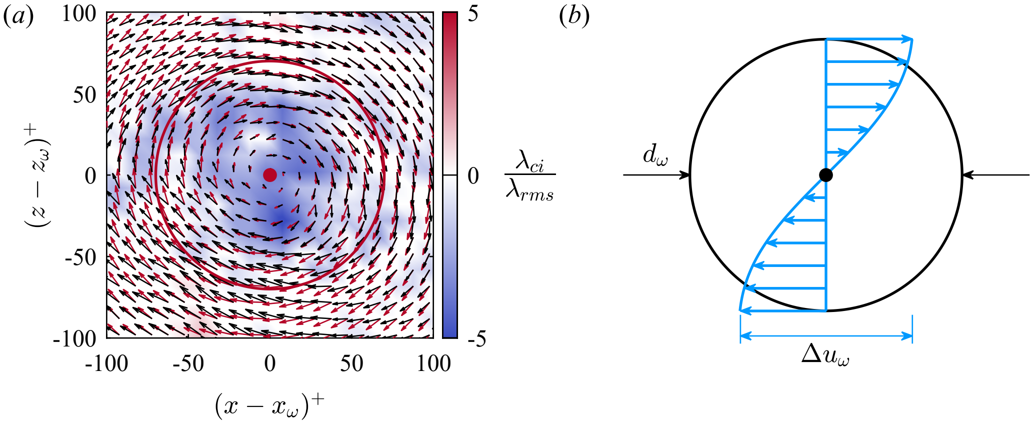

Figure 48. Example of a model Oseen vortex fitted to a velocity vector field following the methodology of Herpin *et al.* (2013). (*a*) Comparison of measured velocities (black vectors) with the closest Oseen model (red vectors) whose radius is indicated by the red circle. (*b*) Notation for the diameter d_ω and velocity difference Δu_ω across the diameter of the fitted model vortex.

3. The fitted vortex center was close to the initial guess center, i.e. within one vortex radius. This condition prevented the vortex fit from converging to a separate nearby core.

The detection algorithm was conducted for all experimental datasets in table V, including a re-analysis of the vortices in the ASL case. Besides the advection velocity, the characteristic velocity of each vortex is the maximum azimuthal velocity difference Δu_ω across the vortex. This velocity, shown in figure 48(*b*), is twice the azimuthal velocity at the edge of the vortex $r = r_\omega$ due to axisymmetry and the definition of the radius. From equation (14), the velocity is therefore $\Delta u_\omega = \frac{1}{\pi}\Gamma r_\omega^{-1}\left(1 - e^{-1}\right)$.

6.2.1 Sources of uncertainty

As with the previous chapters, the spatial resolution provides a source of error and limits the detection of the motions finer than the measurement grid. One benefit of focusing the analysis on probability distributions rather than mean statistics is that the resolution effects are easier to recognize and account for: the distribution behavior at the smallest sizes is the least reliable, and conclusions are drawn only from the other regions of the distribution.

I conducted extensive analysis on the effect of the grid spacing Δx. The findings are summarized here rather than presented in full detail. The average vortex properties D_ω and ΔU_ω are both sensitive to the experimental resolution. Downscaling the resolution with a low-pass filter increases the average values as expected. The downscaling did not influence the conclusions of the probability analysis except for very coarse effective resolutions where $\Delta x \gtrsim \lambda_T$ such that the shear layers were represented by one or fewer points.

This coarsened resolution is similar to the SLPIV measurements. The SLPIV vortex properties are therefore not used to make any new interpretations. However, the SLPIV vortex velocity statistics are found to be consistent with the other cases, and are included for comparison. The correct velocity behavior of the vortices may be captured by the SLPIV vector field due to either smoothing effects or inertia of the snow particles. The strong vortices likely ejected the larger snow particles through centrifugal acceleration. If these ejected particles still exhibited the azimuthal velocity behavior of the vortex, the effect of the particles would be to enlarge the vortex footprint to an area captured by the SLPIV grid.

Finally, an important limitation of fitting a model vortex is selection bias: the algorithm only accepts vortices that resemble the form of the model. Despite this, a large number of Oseen-type vortices were found in every case. Approximately 22 000 Oseen vortices were accepted for the SLPIV case, and more than 100 000 were accepted for every other dataset. Recalling that the algorithm considers the flow field in the neighborhood of the vortex, the smallest detected vortices in each case are fitted based on the flow outside the vortex moreso than inside. The flow outside the vortex model is non-zero and slowly decays with increasing radial distance in equation (14). These small vortices match the Oseen model external to the vortex core, but it cannot also be said that the interior core necessarily matches the model.

6.3 Vortex size

For this analysis, the vortex size is presented as the diameter d_ω. The probability distributions of d_ω for prograde vortices in each experimental dataset are shown in figure 49. To improve the statistical convergence of the probability tails, I used logarithmic spacing for the histogram binning intervals. The proper normalization of the histogram as a pdf is then achieved by dividing the value of each bin by its respective bin width and the total number of occurrences in the histogram. Logarithmic bin intervals are also used in later figures where the horizontal axis is shown with logarithmic scaling. Six orders of probability magnitude are observed with the large number of detected vortices.

Most previous literature studies have described the vortex size distribution mode, i.e. the most probable size, in terms of the Kolmogorov scale η. The mode for the DNS case is approximately 10η, which is between the values 8–10η observed by Tanahashi *et al.* (2004) and 12–13η by Herpin *et al.* (2013). However, it is not clear from a comparison across datasets which scaling parameter is appropriate for describing the mode. There is a range of diameter mode 10–20η in figure 49(*a*) and 0.3–$0.4\lambda_T$ in figure 49(*c*). The observed range for both normalizations may be due, to some extent, to variability in the measurements across PIV experiments. Based on the parameter ratio in figure 47, the most probable detected vortex size was approximately $LRe_L^{-1/2}$ for each case except for the SLPIV measurements whose spatial resolution was coarser than the mode. It is perhaps worth noting that the most probable size is $O(LRe_L^{-1/2})$ for each case based on the parameter ratio in figure 47, except for the SLPIV measurements whose spatial resolution was coarser than the mode.

Regarding the distribution shape, Herpin *et al.* (2013) showed that the size probability approximately follows a log-normal distribution with a somewhat thicker tail than expected. The figure 49 distributions are consistent with these findings. With logarithmic axes, the log-normal probability p should follow a second-order polynomial of the form $\ln(p) = -a\ln(x)^2 + b\ln(x) + c$, where the coefficients are determined by the

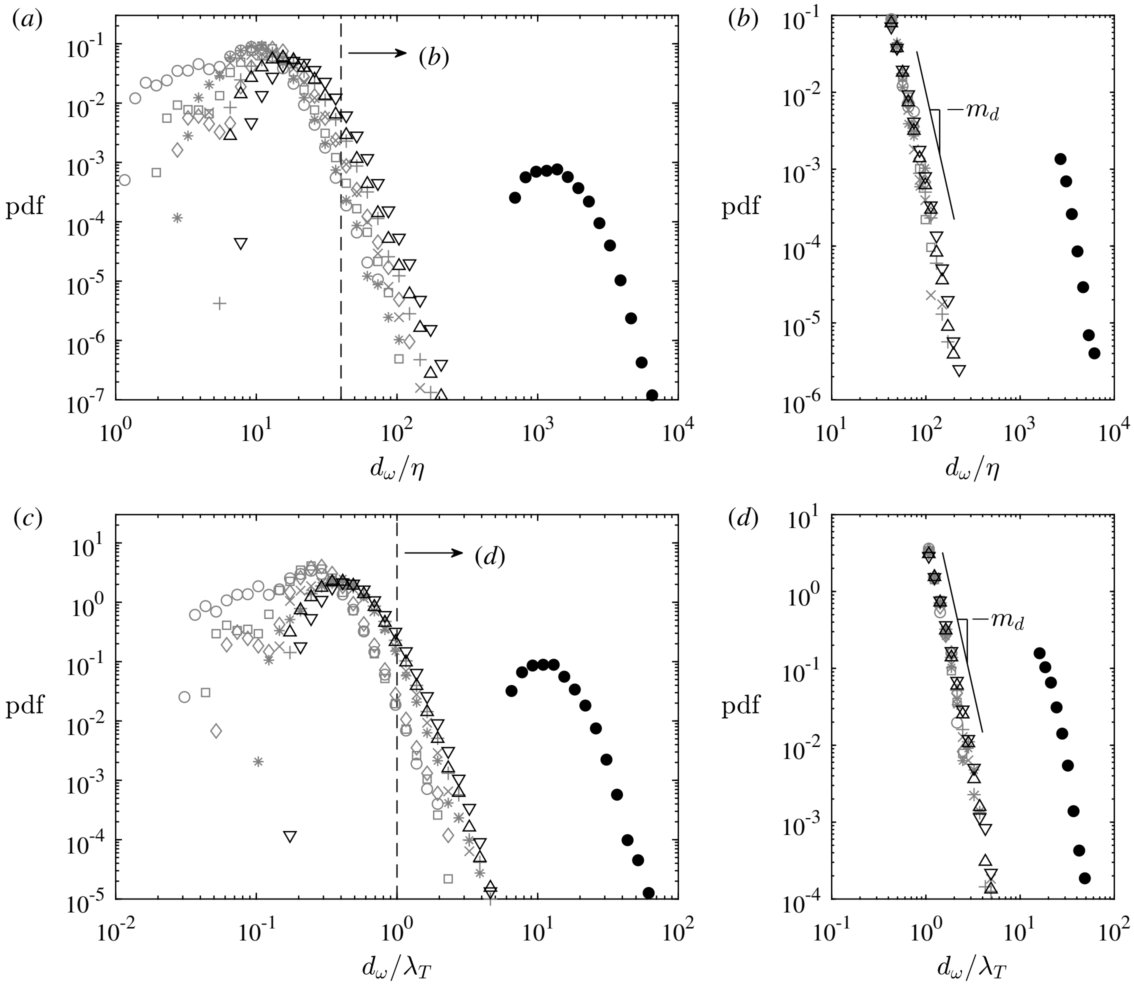

Figure 49. Probability distributions of diameter d_ω for all prograde vortices in the outer region: (*a,b*) normalized by the Kolmogorov lengthscale η; (*c,d*) normalized by the Taylor microscale λ_T. The right-hand side pdfs (*b,d*) show the distribution tails re-scaled to achieve area unity under each tail. Data symbols correspond to the experimental datasets in table V.

distribution mean and standard deviation[6]. However, the tail deviates from the second-order behavior and approximates a linear function consistent with a power law.

The probability tails shown in figure 49(*b,d*) are the regions to the right of the dashed lines in 49(*a,c*). The pdfs in figure 49(*b,d*) are re-scaled to achieve area unity under the tail region. The re-scaling is equivalent to a conditional pdf, i.e. $p(d_\omega \,|\, d_\omega{>}\lambda_T)$, which allows for a comparison of the tail shape across cases. The power law distribution is given by $p(d_\omega) \propto d_\omega^{-m_d}$, where $m_d \approx 6{-}7$ is the linear slope in figure 49(*b,d*). The relevant scaling parameter cannot be determined by the shape of the power law, as m_d is independent of the normalization. The slope is the same for the ASL case, and also does not vary with wall-normal position.

---

[6] Specifically, $a = 1/2\sigma^2$, $b = (\mu/\sigma^2 - 1)$ and $c = -\mu^2/2\sigma^2 - \ln(\sigma\sqrt{2\pi})$, where μ and σ are the respective mean and standard deviation of $\ln(x)$. I derived this by taking the logarithm of the log-normal distribution.

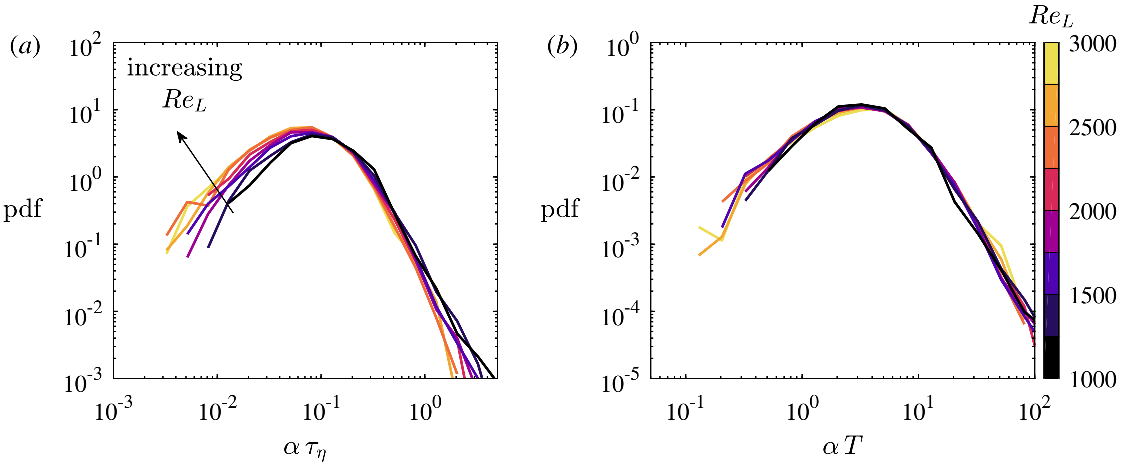

Figure 50. Probability distributions of the strain rate α determining the vortex diameter $d_\omega = \sqrt{8\nu/\alpha}$: ($a$) normalized by the Kolmogorv time scale $\tau_\eta = \sqrt{\nu/\epsilon}$; ($b$) normalized by the turnover time scale $T = u_{rms}^2/\epsilon$. Data shown are for the DNS case in intervals of the local integral Reynolds number Re_L determined by the wall-normal position of the vortex.

One potentially meaningful aspect of the tail is that the largest vortices have size $O(\lambda_T)$ in every case, noting the larger ASL vortices likely result from artificial augmentation by the resolution and snow particles. While the tail may not be an exact power law, the very steep slope $m_d \approx 6{-}7$ and limit $O(\lambda_T)$ indicate the largest vortices are confined by the same scaling that describes the internal shear layer thickness.

Figure 49 provides promising results regarding the possible influence of λ_T on the size of the largest vortices. However, a trend in the probability mode cannot be discerned across the experiments. Further, there is only a weak Reynolds dependence $\eta/\lambda_T \sim Re_L^{-1/4}$ such that the limited separation between η and λ_T in laboratory experiments makes it difficult to distinguish scaling trends. I therefore turn to the strain rate $\alpha = 16\nu/d_\omega^2$ for the DNS case only. The Reynolds dependence is amplified for the strain rate, and a comparison within the computational experiment has reduced uncertainty. Figure 50 shows probability distributions of α for intervals of Re_L. I determined the Re_L interval for a given vortex based on the vortex position z_ω and the local mean values for u_{rms} and L at the same wall-normal position. Here, the relevant parameters for comparison are the Kolmogorov time scale $\tau_\eta = \sqrt{\nu/\epsilon}$ and turnover time scale $T = L/u_{rms}$. Inserting these time scales into the expression $d_\omega \sim \sqrt{\nu t}$ returns the Kolmogorov length scale $\sqrt{\nu\tau_\eta} = (\nu^3/\epsilon)^{1/4} = \eta$ and Taylor microscale $\sqrt{\nu T} = L/\sqrt{Re_L} \sim \lambda_T$.

In figure 50(a) with τ_η normalization, there is a clear Reynolds number trend in the mode and left shoulder of the distribution. When the strain is instead normalized by T in figure 50(b), the Reynolds number trend is accounted for, the position of the mode is $\alpha\,T{\sim}O(1)$, and there is strong agreement across the range of Re_L represented. Note that grouping the strain statistics in intervals of z/δ rather than Re_L is less successful due to the non-monotonic profile of $Re_L(z)$. The results suggest that the size of the detected Oseen-type vortices in the outer region is better described by λ_T than η in both the probability mode and large-diameter tail. This result is interpreted in the context of turbulence phenomenology in chapter 7.

Similar to the pdfs for d_ω, the pdf shape for α in figure 50 resembles a log-normal distribution with overly thick tails. Given the relationship $d_\omega = 4\sqrt{\nu/\alpha}$, and assuming the strain pdf is log-normal, the diameter pdf is also log-normal. This is a derived distribution resulting from several lines of math not included here[7].

6.4 Vortex velocity

Specifically discussed here is the azimuthal velocity difference Δu_ω across the vortex diameter. The advection of vortices is discussed in the next section. The velocity probability distributions for prograde vortices are shown in figure 51 using the same format as the diameter pdfs. The distributions again contain several decades of probability which facilitates characterization of the shape. Unlike the size statistics, the velocity distributions are shown with linear scaling of the horizontal axis. The probability tails are consistently linear in this plotted format, indicative of an exponential probability function[8] $p \propto \exp(-\Delta u_\omega / m_u)$. There is scatter in the velocity mode in terms of both u_η in figure 51(*a*) and u_τ in 51(*c*), which again may be due to variability in the experiment apparatus. Note the mode position in terms of u_τ likely changes moderately with wall-normal position, based on later findings.

As seen in figure 51(*b,d*), the friction velocity also yields better agreement across cases in the probability tail slope. The u_τ agreement extends to the ASL case as well, providing strong evidence for the friction velocity scaling. The tail slope in figure 51 is given as $1/m_u$ rather than the reciprocal because the mean of an exponential distribution is defined by m_u. However, the pdf is not fully exponential as indicated by the presence of the mode, and the mean in this case is larger than m_u. While it does not exactly describe the mean for this study, m_u is the most relevant parameter for the distribution and is critical to the central moment statistics. Hereon I refer to m_u as a shape parameter for the distribution. I used a linear fit on the pdf tails to estimate m_u for each dataset. In addition the pdfs shown in figure 51 which include the vortices throughout the outer region, I also estimated m_u for vortices in intervals of the wall-normal position based on the vortex center z_ω. The resulting parameter values are shown in figure 52.

The shape parameter increases with Reynolds number Re_τ when normalized by u_η, and is approximately constant across three decades of Re_τ when normalized by u_τ. This again supports the u_τ scaling for the probability tail suggested visually in figure 51, both in the mode position and the tail shape. Similar to the analysis for d_ω, it is not easy to distinguish the relevant scaling across a small Reynolds number range. To demonstrate the weak Reynolds number dependence, I assume here that u_τ and δ are the same order as the integral scales. This is a fair assumption given u_{rms} and the large scale motions are described in terms of u_τ and δ, respectively, in the outer region. The Kolmogorov and outer length scales are then related as $\eta/\delta \sim Re_\tau^{-3/4}$, which comes from the same expression with L and Re_L (Pope 2000). Given $\eta = \nu/u_\eta$ and $\delta = \nu Re_\tau / u_\tau$ by the definitions of Re_η and Re_τ, respectively, the velocity scales are related as $u_\tau/u_\eta \sim Re_\tau^{1/4}$. Figure 51(*a*) supports this relationship, where the shape parameter exhibits the same weak Reynolds number dependence $m_u/u_\eta \sim Re_\tau^{1/4}$.

---

[7] Footnote version of derived distributions: given $d_\omega = \mathrm{f}(\alpha) = 4\sqrt{n\nu/\alpha}$ and the pdf $p_\alpha(\alpha)$, the derived distribution is $p_d(d_\omega) = p_\alpha(\mathrm{f}^{-1}(d_\omega))|\partial \mathrm{f}^{-1}(d_\omega)/\partial d_\omega|$, where $\mathrm{f}^{-1}(d_\omega)$ is the inverse function relateing α to d_ω. From this expression, for the given function it can be shown that if p_α is log-normal, p_d is also log-normal, and the distribution parameters are related as $\mu_d = \frac{1}{2}(\ln(16\nu) - \mu_\alpha)$ and $\sigma_d = \frac{1}{2}\sigma_\alpha$, where μ and σ are defined in the previous footnote.

[8] Taking the logarithm of both sides yields the linear form $\ln(p) = -\Delta u_\omega / m_u$ shown in figure 51.

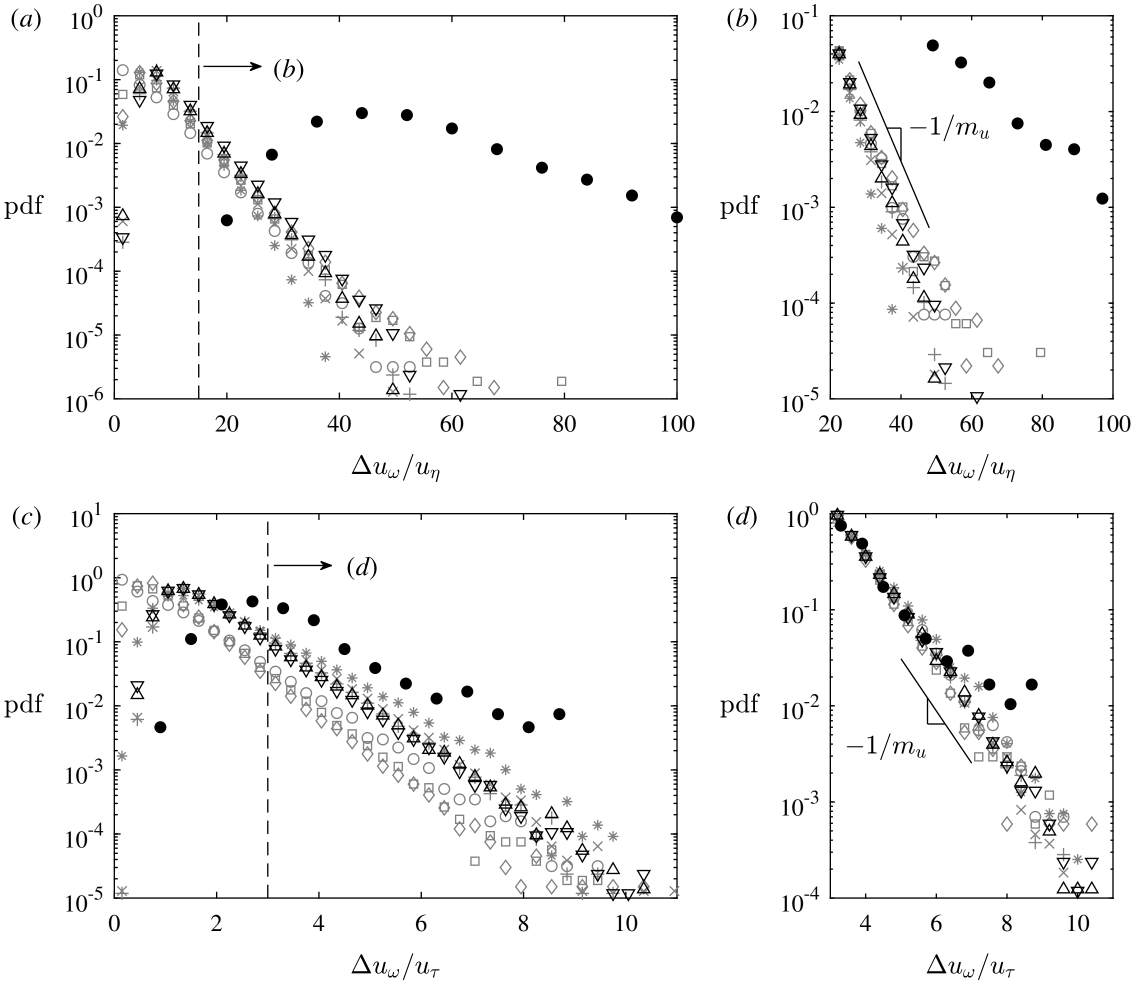

Figure 51. Probability distributions of velocity Δu_ω for all prograde vortices: (*a,b*) normalized by the Kolmogorov velocity u_η; (*c,d*) normalized by the friction velocity u_τ. The right-hand side pdfs (*b,d*) show the distribution tails re-scaled to achieve area unity under each tail. Data symbols correspond to the experimental datasets in table V.

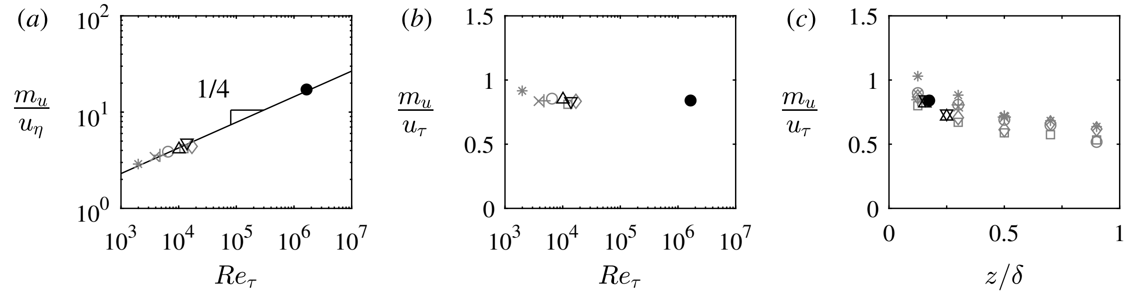

Figure 52. The shape parameter m_u describing the exponential relationship $p \propto \exp(-\Delta u_\omega / m_u)$ of the vortex azimuthal velocity distribution tail: (*a,b*) as a function of Re_τ when normalized by u_η and u_τ, respectively; (*c*) wall-normal profile normalized by u_τ. Data symbols correspond to the experimental datasets in table V.

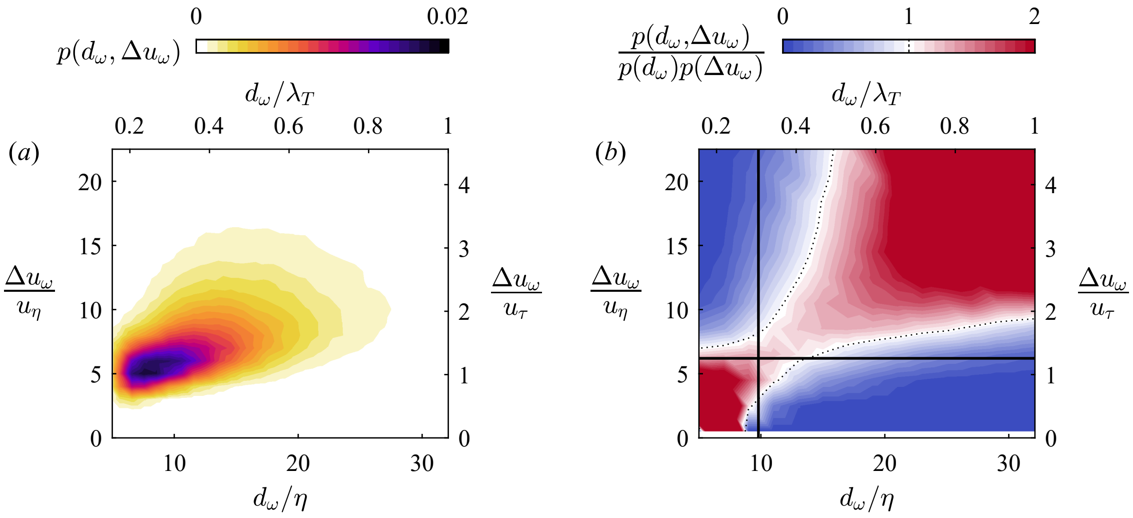

Figure 53. (*a*) Joint probability distribution $p(d_\omega, \Delta u_\omega)$ of vortex diameter d_ω and azimuthal velocity difference Δu_ω for the $Re_\tau = 3\,800$ smooth wall case. (*b*) The same joint distribution normalized by the individual pdfs. The normalized distribution indicates the probability relative to if the two variables were independent. The dotted black lines in (*b*) correspond to normalized probability equal to one and the solid lines correspond to the modes of the individual probabilities $p(d_\omega)$ and $p(\Delta u_\omega)$.

In figure 51(*c*), m_u decreases moderately with increasing wall-normal distance. The trend matches the behavior of the velocity difference ΔU_m across internal shear layers. The value for ΔU_m, shown in figure 44 in the previous chapter, is approximately twice m_u throughout the boundary layer, with the same wall-normal dependence. Given m_u represents an underestimated value of the statistical mean ΔU_ω for the modified exponential distributions in figure 51, the vortex azimuthal velocity ΔU_ω follows the same scaling and is quantitatively similar to the shear layer velocity ΔU_m.

Another aspect of the azimuthal velocity Δu_ω is its correlation with the vortex size d_ω in addition to the circulation Γ. These properties are related through the functional dependence $\Delta u_\omega \propto \Gamma d_\omega^{-1}$. The circulation is also related to the total vorticity within the area of the vortex core: $\Gamma \propto \omega d_\omega^2$. Combined with the first dependence, this yields an expected relationship where the vortex velocity and size are positively correlated rather than inversely related. The correlation is apparent through the joint probability distribution $p(d_\omega, \Delta u_\omega)$ of vortex diameter and velocity. An example distribution for the $Re_\tau = 3\,800$ smooth wall case of table V is shown in figure 53(*a*). The inclination of the joint probability contours suggests the two parameters are positive correlated.

A more quantitative test requires comparison of the joint probability with the independent case. If d_ω and Δu_ω are statistically independent (uncorrelated), then the joint probability reduces to $p(d_\omega, \Delta u_\omega) = p(d_\omega)p(\Delta u_\omega)$ throughout the range of size and velocity. The ratio of the joint probability and the independent case is plotted in figure 53(*b*). Red regions where the ratio exceeds unity indicate greater probability than if the variables were independent, and blue regions less than unity indicate lower probability. The positive correlation is confirmed by figure 53(*b*): smaller vortices are more likely to have lower velocity, and larger vortices have higher velocity.

The positive correlation is itself neither surprising nor particularly revealing. The more interesting result is the presence of four distinct probability regions. The division of the four regions corresponds approximately to the modes of the individual pdfs indicated by the solid black lines in figure 53(*b*) : $d_\omega \approx 0.3\lambda_T$ (10η) and $\Delta u_\omega \approx 1.2u_\tau$ (6η). Here, I infer these modes to represent transition points between the Kolmogorov- and intermediate-scaled vortices. The probability modes then represent a combination of larger-than-average Kolmogorov-scaled vortices and smaller-than-average intermediate-scaled vortices. Mixed-scale vortices, e.g. with $d_\omega > 0.3\lambda_T$ and $\Delta u_\omega < 6u_\eta$, correspond closely with the blue regions where the probability becomes negligibly small. The smallest vortices are thus Kolmogorov-scaled in both their size and velocity. Additionally, the probability tails in the previous figures are closely related through the joint probability in figure 53, where a vortex whose size is within the diameter distribution tail will very likely have a characteristic velocity within the exponential tail. Note that this joint probability behavior was exhibited by the other experimental datasets, but only one case is shown and discussed here for brevity.

6.5 Vortex advection

The vortex advection velocity (u_ω,w_ω) describes the bulk movement of the vortex core. The advection was estimated from the Oseen model fit, and is likely closely related to the average of the velocity vectors in the vortex vicinity that contribute to the fitting procedure. The advection estimate is therefore inferred, rather than observed from the vortex core trajectory across multiple instances in time. For the wall-normal component w_ω, I subtracted the local mean $W(z_\omega)$ from the advection velocity. The SLPIV measurements are affected by the snow settling speed, and the laboratory-scale cases have a weak non-zero $W(z)$ profile based on the growth of the boundary layer along the streamwise direction. The advection is less susceptible to spatial resolution effects such that the mean statistics are more reliable than for the vortex size and azimuthal velocity. The mean values are presented first, followed by probability statistics.

To construct profiles of the average vortex advection velocity, I calculated the average values for u_ω and w_ω in intervals of z/δ. I chose the corresponding interval for each vortex based on the wall-normal position of its center z_ω. The resulting advection velocity profiles are shown in figure 54. Throughout the outer region, the streamwise advection in figure 54(*a*) is approximately 1 to 2% slower than the local time-averaged mean velocity, including for the ASL case. Approaching the wall, the advection transitions to being faster than the mean velocity.

The wall-normal advection is weakly positive throughout the boundary layer outer region in figure 54(*a*), but transitions to net downward motions approaching the wall. The observed trend is not an artifact of subtracting the mean W; the subtraction reduces W_ω by approximately 50% in the outer region. The streamwise and wall-normal advection results are both remarkably consistent with trends in the Reynolds shear stress balance: ejection-type events ($u'{<}U, w'{>}0$) contribute more to the Reynolds shear stress in the buffer layer and roughness sublayer, whereas sweep-type events ($u'{>}U, w'{<}0$) are relatively more important throughout the outer region (Raupach 1981). This result suggests a connection between the vortex core advection and Reynolds shear stress events.

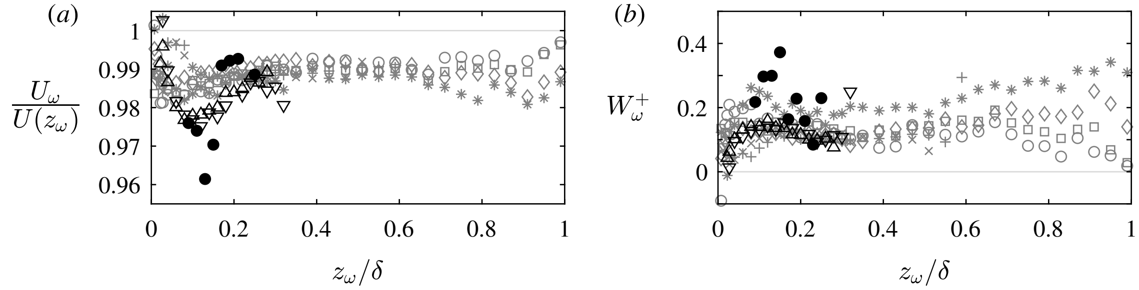

Figure 54. Profiles of average prograde vortex advection velocity: (*a*) streamwise advection U_ω relative to the time-averaged mean $U(z_\omega)$ at the vortex wall-normal position z_ω; (*b*) wall-normal advection W_ω. Data symbols correspond to the experimental datasets in table V.

The resemblance of the advection statistics to the turbulents shear stresses is further seen in joint probabilities of u_ω and w_ω. The joint pdfs for each case in table V are provided in figure 55. The vortex events contributing to the joint pdfs are limited to those within the log region of each boundary layer. The resulting joint distributions have the same shape as joint pdfs of u' and w' (see, e.g., figure 15). Consistent with the mean advection, the figure 55 distributions are stretched farther into the second quadrant corresponding to ejections than the fourth quadrant for sweeps. This behavior matches the observations of Raupach (1981), where the most intense stress events away from the wall are more likely to be ejections than sweeps.

While figures 54 and 55 suggest a relationship between the strong vortices and the stress events, the exact nature of the relationship is not provided by the present results. My interpretation, based to some extent on speculation, is provided in chapter 7.

6.6 Internal shear layer size and advection

Certain attributes of the internal shear layers have already been presented. Namely, the u_τ scaling of the velocity difference ΔU_m across shear layers was demonstrated in §5.3. The detection of these ISLs and the conditioning of statistics relative to the interface position z_i were previously detailed in §4.3 and §5.2.3. For the extended ISL analysis in this section, I used the same detected shear regions from the UMZ study in chapter 5. The only difference is that here the high-resolution tower PIV results are presented rather than the large-field-of-view measurements.

Following the same format as figure 35, the conditionally averaged shear layer profiles for each experimental dataset are shown in figure 56. The ASL case is excluded here because the limited SLPIV spatial resolution does not allow for a proper comparison with the laboratory-scale flows. Figure 56 shows that the Taylor microscale provides the best agreement across flow conditions in describing the overall layer thickness, as suggested by previous studies (Eisma *et al.* 2015; de Silva *et al.* 2017). I note here that the shear layer may have a central, Kolmogorov-scaled core region that is not captured in these experiments (Chini *et al.* 2017).

One method of calculating the average ISL thickness δ_ω was previously given in equation (13). As discussed in §4.3, the estimate of δ_ω using the maximum velocity gradient within the layer $\partial\langle u-u_i\rangle/\partial z|_{max}$

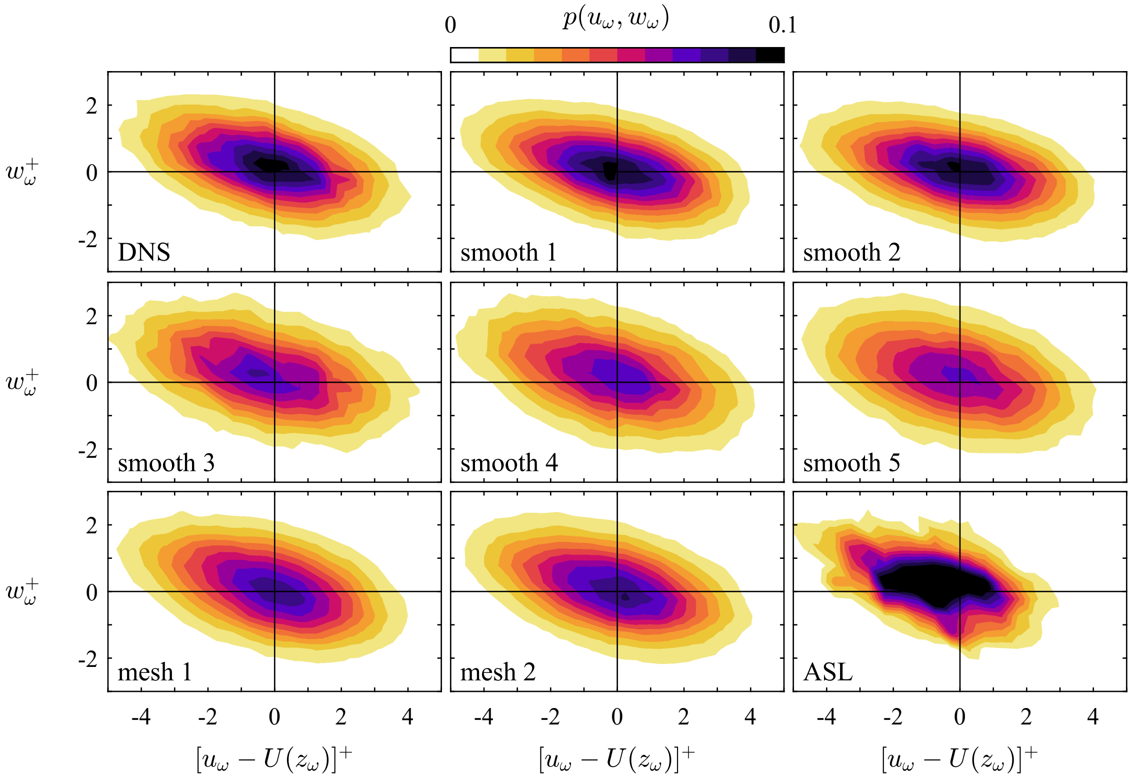

Figure 55. Joint probability of vortex advection velocities u_ω and w_ω for every experimental dataset in table V. The vortex events are limited to those in the log region. The figure representation is analogous to the quadrant classification of $u'-w'$.

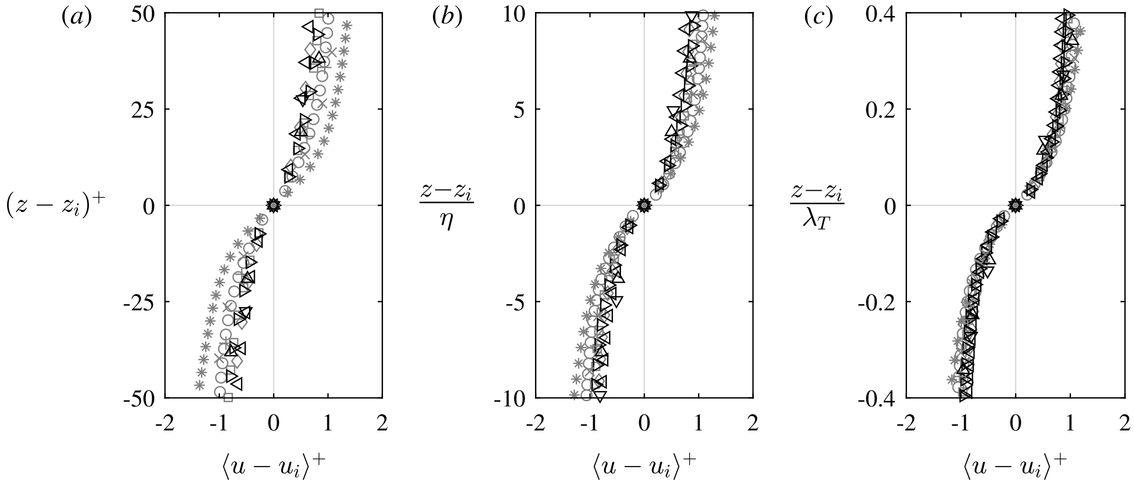

Figure 56. Average streamwise velocity profile relative to the shear layer velocity u_i and midheight z_i: (*a*) normalized by the viscous length ν/u_τ; (*b*) normalized by the Kolmogorov length η; (*c*) normalized by the Taylor microscale λ_T. Data symbols correspond to the experimental datasets in table V.

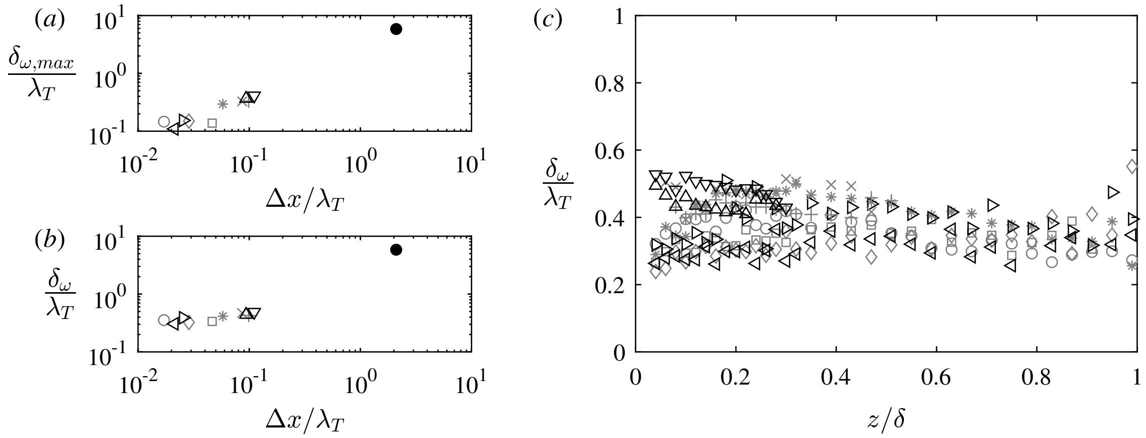

Figure 57. Estimated average thickness δ_ω of internal shear layers normalized by λ_T: (*a,b*) as a function of grid spacing where δ_ω is estimated from (*a*) the maximum gradient within the interface $\partial\langle u - u_i\rangle/\partial z|_{max}$ and (*b*) the thickness across the velocity jump ΔU_m; (*c*) wall-normal profile using the method in (*b*). Data symbols correspond to the experimental datasets in table V.

is susceptible to the spatial resolution. The gradient reaches its maximum at the center of the layer and quickly decreases away from the center. The observed maximum therefore depends strongly on the spacing of the grid points Δx in the vicinity of the layer center where the derivative is estimated. The effect of resolution is demonstrated in figure 57(*a*), which shows the calculated thickness δ_ω as a function of the grid spacing Δx. As expected, the calculated thickness increases for coarser resolutions that measure a smaller maximum shear.

The thickness can more simply be estimated as the distance across which the velocity difference ΔU_m occurs (Eisma *et al.* 2015). In addition to being less sensitive to measurement resolution, this estimate is more representative of the overall shear layer. The velocity thickness ΔU_m is determined independently based on the flow external to the layer as depicted in figure 35(*b*). I therefore considered δ_ω in this estimation to be the wall-normal distance spanning the velocity range representing ΔU_m. The resulting δ_ω values are shown in figure 57(*b*). This simpler method removes the spatial resolution trend in δ_ω, but only for datasets where the resolution was finer than the ISL thickness. In other words, the method using the distance across ΔU_m is preferred for datasets with $\Delta x \lesssim 0.1\lambda_T$, but for coarser resolution such as the SLPIV data the δ_ω value will be overestimated regardless of the method.

The wall-normal profiles of δ_ω calculated using the average gradient are shown in figure 57(*c*). The thickness, when normalized by λ_T, is constant throughout the boundary layer with a value between 0.3-$0.5\lambda_T$, which is in close agreement with the observed thickness $\delta_\omega \approx 0.4\lambda_T$ from Eisma *et al.* (2015) and $\delta_\omega \approx 0.5\lambda_T$ from de Silva *et al.* (2017). In terms of the integral scales, the average thickness is close to $LRe_L^{-1/2}$, and is similar to the mode of the pdf for d_ω/λ_T. The scatter between datasets is likely within the combined uncertainty of δ_ω and λ_T and the residual effects of spatial resolution. There is no apparent trend in either the Reynolds number or the surface roughness. Ebner *et al.* (2016) proposed that significant roughness may affect the thickness of the shear layers and the overall organization of UMZs. However, the required roughness in terms of k_s/δ for this effect to occur may be too great to maintain outer layer similarity.

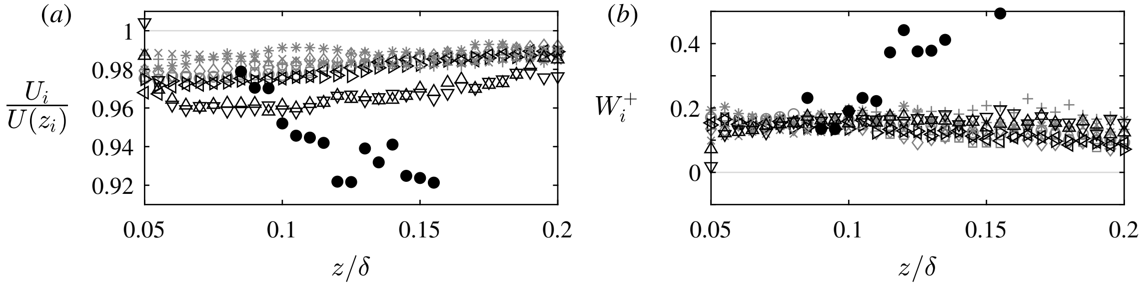

Figure 58. Wall-normal profile of the average shear layer advection within the log region: (*a*) streamwise advection U_i relative to the time-averaged mean $U(z_i)$ at the shear layer height z_i; (*b*) wall-normal advection W_i. Data symbols correspond to the experimental datasets in table V.

For each detected ISL, I used the velocity vector closest to the shear layer midpoint as the representative advection velocity. This inference is similar to the vortex analysis in that the advection is estimated from the local flow field and is not directly observed from the shear layer evolution. As before, I subtracted the weak mean wall-normal velocity W from the wall-normal advection. Following the same format as figure 54, profiles of the average streamwise U_i and wall-normal W_i advection velocity of the shear layers are plotted in figure 58. The profiles are focused within the log region of the boundary layer. The shear layer advection matches the behavior of the vortex cores: the layers advect somewhat slower than the time-averaged mean, and there is a weak mean upward advection. This consistency suggests that the possible relationship between the turbulent shear stress events and the vortex advection can be extended to include the ISLs.

The deficit in streamwise advection is greater for the shear layers than the vortices, particularly for the mesh roughness and ASL cases. The deficit increases with surface roughness k_s^+, indicating a possible effect of roughness. However, this trend was not exhibited by the vortex cores, and additional work is required to confirm and interpret any such trends.

6.7 Where are all the Kolmogorov-scaled vortices?

In the present analysis, the most probable vortex size in figure 49 is in good agreement with the average ISL thickness in figure 57. The strain rate distribution in figure 50 suggests the local integral scales are relevant to the vortex behavior, and the most probable vortex azimuthal velocity corresponds to the friction velocity. From this, the governing parameters for the vortex size and velocity seem to be intermediate scales λ_T and u_τ, respectively, rather than the Kolmogorov scales. However, I must consider the methodology as a possible explanation for the general absence of a small-scale (Komogorov) signature on the probability statistics.

The most likely culprit for masking the smallest vortices is the definition of the vortex size. Specifically, the Oseen model assumes the azimuthal velocity reaches a maximum at the radius of the vortex core, then decreases with increasing outward radial distance. This radius may work well for vortices isolated in an otherwise uniform flow field, but these vortices are clustered within thin shear layers (see, e.g., §4.4). A strong velocity gradient is present across the Taylor-microscale thickness of these ISLs. It is possible that many of the smallest spanwise vortices within the ISLs are not well fit by the Oseen model because the background velocity gradient is contrary to the assumed decreasing azimuthal velocity external to the vortices. In this sense, the Oseen model may be most useful for detecting vortical motions that span the majority of the ISL thickness, which is consistent with the results of my vortex analysis. This possibility is also consistent with the findings of da Silva & Taveira (2010), who found large vortices spanning the TNTI thickness and separate, smaller Kolmogorov-scaled worm-like vortices.

The radius definition employed here is not unique to a model Oseen or Burgers vortex. Tanahashi *et al.* (2004) found a similar vortex size distribution with mode 8–10η by using the same radius definition without imposing a model. A new radius definition may be required to detect and characterize the smallest vortices within the shear layers. I leave this task to another intrepid researcher, however, as my focus is on the relationship between the ISLs and vortical motions. I have already demonstrated that many spanwise, prograde vortices within the boundary layer have similar characteristic size, velocity, and advection to ISLs. The important message here regarding the Kolmogorov-scaled vortices is that they likely were present but not detected due to the methodology. The present finding are therefore specific to vortices well-described by the Oseen model. Depending on how you choose to define a vortex, the probability distributions for the vortex properties in this chapter may be missing information at the smallest scales.

7 Phenomenological interpretation of the results

To this point, I have attempted to avoid speculative claims regarding the experimental results. I have been saving such speculations for the present chapter, in which I untether myself from the chains of scientific rigor and the peer-review process to offer my unproven opinions[9]. As such, chapter 7 should be read as a speculative discussion of the results rather than a robust extension of the findings.

The scientific opinions contained here relate mostly to the vortex and shear layer dynamics studied in chapter 6. The UMZ scaling results in chapter 5 are more robust, and a discussion of these results was already included in §5.3. The earlier chapters, for the most part, developed the foundation for the all-important UMZ and vortex scaling analyses.

7.1 The interaction of momentum zones and shear layers

One of the most revealing results of the previous chapter is the influence of the turnover time scale T on the strain rate α associated with the vortex size, see e.g. figure 50(*b*). Coupled with the importance of u_τ to the vortex azimuthal velocity, the results suggest the local large-scale motions determine the properties of the smaller vortical motions. Assuming the large-scale motions are represented by the UMZs, there must be an important dynamic relationship between the UMZs, the ISLs, and the vortices.

The possible nature of the scale interactions is already provided by the Burgers vortex model (1948). In the model, the local flow field around the vortex induces an extensional strain which acts to stretch the vortex. The stretching induces inward radial flow from outside the vortex by continuity. The radial flow balances the outward growth of the vortex by viscous diffusion, providing a steady solution for the state of the vortex tube. The same principle can be applied to a sheet such as the internal shear layers, rather than a tube. Applying this stretching model to the UMZ and ISLs, the UMZs impose a strain rate α on the ISLs that leads to stretching in the spanwise direction and net flow from the UMZs into the shear layers and vortices.

There is a limited extent to which the strain and stretching mechanism can be proven with the current experimental observations. The net flow into the vortices and ISLs can (and will) be supported using the measurements in the $x-z$ plane. However, the axial stretching and strain rate α, both in the spanwise direction, cannot be identified. I assume here that there is a consistent aspect ratio between the streamwise and spanwise large-scale parameters. By this assumption, the spanwise equivalent of the turnover time scale is proportional to the streamwise component such that the streamwise value can be used as a proxy. Figure 50(*b*) already demonstrated the assumption to be reasonable, where the streamwise turnover time T describes well the strain rate of the spanwise vortices. Owing to these assumptions and limitations, the evidence provided here is supportive of the stretching mechanism rather than definitive proof.

---

[9] These chains are normally beneficial, but you cannot fault me for turning to dramatic phrasing in the one research document where I have the freedom to do so.

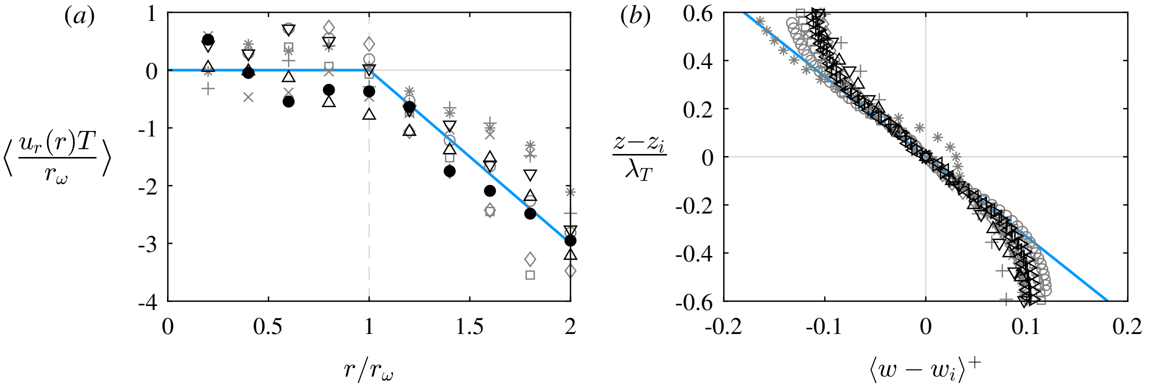

Figure 59. Average velocity profiles demonstrating the net flow inward towards the vortices and shear layers. (*a*) Radial velocity $u_r(r)$ relative to the prograde vortex center, normalized by its radius r_ω and the turnover time scale T. (*b*) Wall-normal velocity w relative to the shear layer velocity w_i and midheight z_i, normalized by the Taylor microscale λ_T and the friction velocity u_τ. Data symbols correspond to the experimental datasets in table V.

For each tracked vortex in every dataset, I used the local flow field around the fitted vortex center to compile a profile of the radial velocity component $u_r(r)$ as a function of radial distance r from the vortex center. To average the profile across all vortices, I normalized r by the vortex radius r_ω such that $r/r_\omega = 1$ always corresponded to the edge of each vortex core. The average radial profile of u_r is provided in figure 59(*a*) for every dataset. Note that the Oseen vortex model used to detect the vortices assumes $u_r(r) = 0$, and any deviations from zero thus indicate robust behavior that overcomes the imposed model. The average radial velocity is close to zero within the vortex core, i.e. $r/r_\omega < 1$, and follows an approximately linear trend of increasingly negative flow outside the core. There is generally good agreement across datasets, including the ASL case, with u_r normalized by r_ω/T. Assuming $1/T$ is representative of the strain rate α as suggested by figure 50(*b*), the linear trend outside the vortices in figure 59(*a*) is consistent with the profile $u_r(r) = -\alpha r$ predicted by the Burgers vortex. The result confirms that the flow field around the vortex on average moves towards the vortex core at a speed proportional to the integral strain rate $1/T$. The overall shape of the profile may in part be due to the fitted model, and should be confirmed using an independent method.

To assess the net flow relative to the ISLs, I computed the same conditionally averaged shear layer profiles as in figure 56, except here I used the wall-normal velocity component w. The average profile of w relative to the ISL midpoint is shown in figure 59(*b*). The best agreement across datasets was achieved using the same normalization parameters as for the streamwise velocity case: λ_T for the relative position $z{-}z_i$ and u_τ for the relative velocity $w{-}w_i$. In the ISL reference frame, the average flow above the ISL is moving down into the shear layer ($w{<}w_i$) and the flow below the is move up into the shear layer ($w{>}w_i$). Within the ISL, i.e. $|z{-}z_i| \lessapprox 0.25\lambda_T$, the profile is approximately linear which is consistent with the predicted profile $w{-}w_i = -\alpha(z{-}z_i)$.

The normalization of the velocity $w{-}w_i$ by the strain parameter λ_T/T yielded relatively less agreement across experimental datasets compared to u_τ. There may be multiple processes resulting in the figure 59(*b*) profile such that straining mechanism does not govern the scaling of the average velocity. For instance, I showed in §6.6 that the ISLs have a net positive wall-normal velocity W_i, see e.g. figure 58(*b*). The average

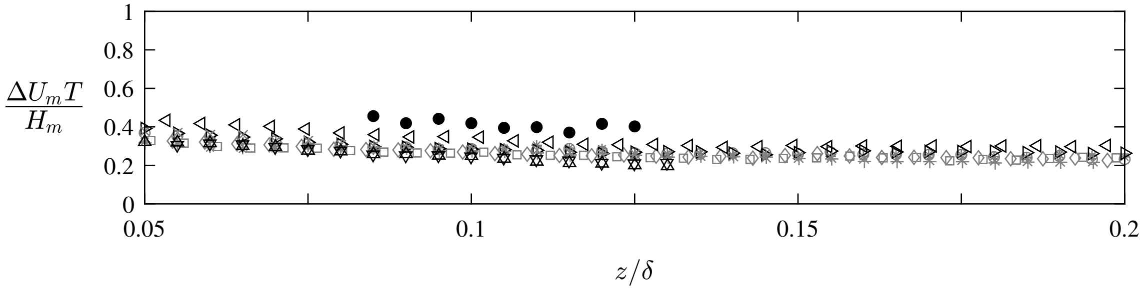

Figure 60. Wall-normal profile of the strain rate scaling argument for local UMZs $\alpha(z) = \Delta U_m/H_m$. The value is normalized by the turnover time scale T which represents the most probable vortex strain rate from the chapter 6 analysis. Data symbols correspond to the experimental datasets in table V.

relative velocity $\langle w - w_i \rangle$ may therefore be a combined result of the ISL advection W_i associated with shear stress events and the local compressive flow W into the ISL. For most of the datasets, the average value of the strain parameter λ_T/T in the log region is approximately half the average value of W_i, and the ratio decreases for increasing Reynolds number.

A notable deviation in figure 59(*b*) is the center-most region of the profile for the DNS case. The DNS profile has a center layer approximately 3η thick where the wall-normal velocity is uniform. The velocity profile is asymmetrical outside the center, i.e. there is a larger velocity difference above the center than below. I assumed this central layer was not resolved by the remaining experimental datasets, and offset the DNS profile center to match the bulk velocity difference outside the ISL. The result suggests a possible core region of the ISL scaling with η (Chini *et al.* 2017).

I have demonstrated in figures 50 and 59 that the relevant strain rate α for the large vortices is connected to the turnover time scale T. The further connection to the UMZs has thus far been through the assumption that the UMZ properties are consistent with the turnover time and other integral-scale parameters. Using the average UMZ profiles in figure 44, I constructed a presumed average strain rate $\alpha(z) = \Delta U_m/H_m$ corresponding to the UMZs. A comparison of this UMZ strain rate with the turnover time scale in the log region is shown in figure 60. The profile is relatively flat throughout the log region, and there is reasonable agreement across all experimental datasets. The profile suggests there is a proportional relationship between the UMZ properties and the turnover time, such that it is reasonable to assume the T-scaled strain field acting on the ISLs and vortices corresponds to the UMZs.

In addition to linking the UMZ properties to the integral scales, figure 44 also implies a connection between the average shear and the strain field acting on the smaller structures. Based on the result in figure 44(*d*), the UMZ strain rate is approximately equivalent to the average shear $S = \partial u/\partial z \approx \Delta U_m/H_m$. This connection provides a means to potentially infer the properties of the intermediate-scale structures governed by α simply by knowing the mean velocity profile. The implication for the UMZ-ISL organization is that the UMZ flow states both lead to the mean velocity profile and also impose a strain field that governs the evolution of structures within the ISLs.

This proposed interaction between the UMZs and ISLs is depicted in the figure 61 cartoon. The average UMZ and ISL properties observed experimentally are shown in the left-side panel. The properties of the

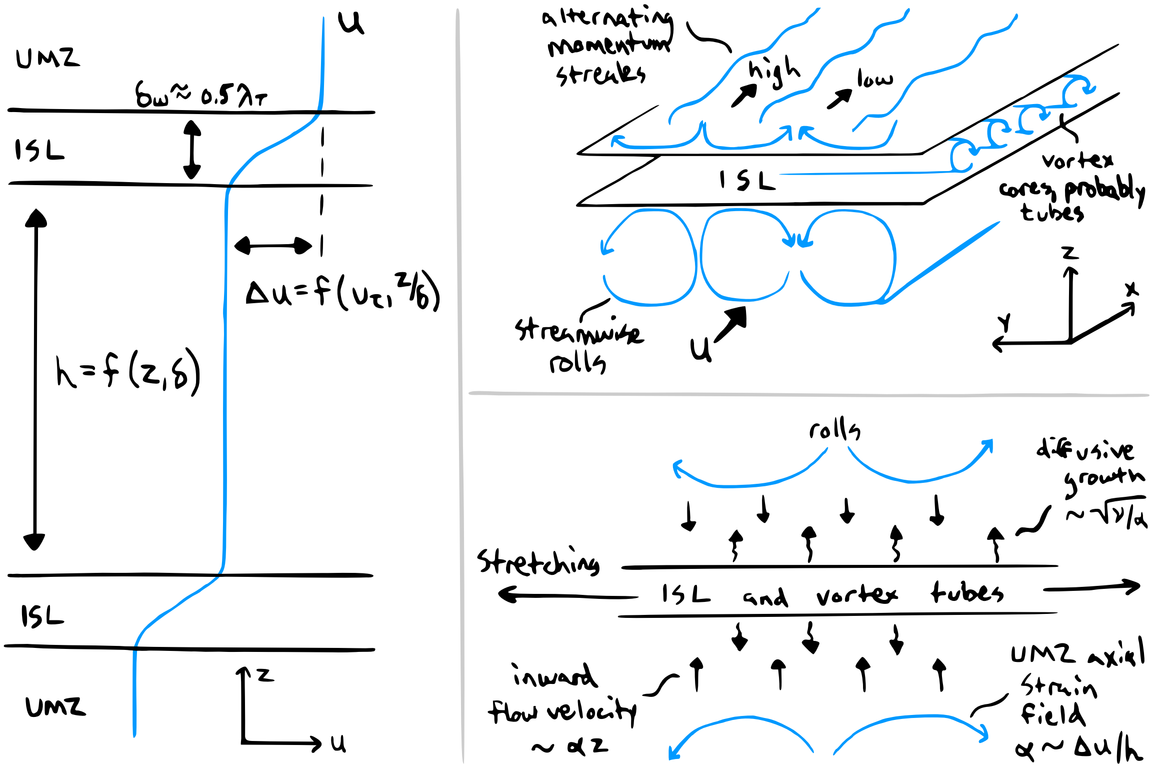

Figure 61. Cartoon depicting the proposed dynamic relationship between UMZs and ISLs. (*left*) The scaling of the UMZ-ISL organization observed experimentally. (*upper right*) An idealized two-dimensional ISL populated by vortex tubes and bounded by UMZs resembling streamwise rolls and alternating momentum streaks. (*lower right*) UMZ-ISL interactions in the $y-z$ plane: spanwise motion of the rolls leads to axial strain and stretching, which induces flow into the shear layer that counters the diffusive growth.

uniform flow regions are determined by the global geometry and boundary conditions, i.e. size dependent on z and/or δ and velocity difference dependent on u_τ. While I do not know the genesis of the UMZs (there may indeed be more than one mechanism), the independence of the UMZ properties from the ISL behavior makes it difficult to imagine that the shear layers are responsible for directly initiating UMZs. As for the origin of the ISLs, it is reasonable to expect the interaction of two UMZs with different momentum to initiate a shear layer that develops vortex structures through a shear instability and vortex roll-up mechanism (Sreenivasan *et al.* 1989). It is possible that the spanwise vortices detected in chapter 6 correspond to these roll-up vortex structures, given the conspicuous absence of Kolmogorov-scaled vortices from the results.

The observed δ-scaled streamwise extent of the UMZs and ISLs indicate these features are relatively long-lived. Yet the ISLs exhibit a generally consistent thickness, suggesting the state of the shear layers is usually steady and the thickness does not grow indefinitely. These anecdotal observations are consistent with the steady conditions afforded by the stretching mechanism depicted in the lower-right panel of figure 61. The inward flow $u_r \propto -\alpha r$ and diffusive growth $d_\omega \propto \sqrt{\nu/\alpha}$ based on an assumed UMZ strain field $\alpha \sim 1/T \sim \Delta U_m/H_m$ are both supported here by experimental evidence.

The assumed strain field requires the UMZs to have a diverging spanwise velocity component to exert a tensile stress on the shear regions. This requirement is fulfilled if the UMZs have a weak streamwise rotation similar to the behavior of streamwise rolls depicted in figure 14. Previous studies discussed in §2.2 support the existence of self-similar streamwise rolls throughout the log region including for atmospheric flows (see, e.g., Foster *et al.* 2006; Jiménez 2018). These rolls are associated with alternating high- and low-momentum streaks (Dennis & Nickels 2011; Smits *et al.* 2011; Hutchins *et al.* 2012), whose signature tends to be longer than the rolls (Jiménez 2018). The velocity structures related to the UMZs are depicted in the upper-right panel of figure 61. The depiction is similar to the self-sustaining mechanism proposed by Chini *et al.* (2017) involving ISLs and streamwise rolls.

The vortex stretching mechanism has been applied to isotropic turbulence for several decades (Taylor 1937, 1938). However, to my knowledge, its application in boundary layer flows has primarily been for transition to turbulence (Stuart 1965; Orszag & Patera 1983). Further proof of axial (spanwise) stretching in high-Reynolds-number turbulence is required to support my speculations.

The idealized cartoon in figure 61 is an incomplete description of the structural organization of boundary layer turbulence. The average long-lived ISL is inclined (Squire 2017) and exhibits fractal behavior (de Silva *et al.* 2017). Further, the depiction lacks three-dimensionality. It is possible the downward rotation of a streamwise roll below an ISL draws a vortex tube downward. This vortex tube behavior is consistent with the partial hairpin arches and legs that are common in outer region turbulence (Dennis & Nickels 2011), which could explain the success of the Λ-eddy packet as a representative eddy. Lastly, the proposed stretching only provides a local mechanism to sustain an individual ISL. It does not explain the generation of new structures.

The final connection to be made here is between the ISLs and intense Reynolds shear stress events. The advection results for ISLs and vortices in chapter 6 are consistent with observed Reynolds shear stress behavior: the correlation of streamwise and wall-normal advection is dominated by sweep- and ejection-type events, and on average ejections are favored (Raupach 1981). I do not believe the advected shear layers represent directly the sweep and ejection events, as the majority of the Reynolds shear stress corresponds to large-scale motions. Rather, I find it more likely that the Reynolds shear stress events correspond to large, relatively uniform regions moving in the wall-normal direction, particularly for sweep events. Following my previous speculation, shear layers are initiated along the interface of these regions. The uniform regions advect the shear layers and embedded vortices in the same wall-normal direction such that the ISL and vortex statistics carry the signature of the shear stress events.

7.2 The Taylor microscale

Perhaps the most confounding parameter in turbulence, to me at least, is the Taylor microscale λ_T. While λ_T corresponds statistically to several features in turbulence, its physical representation is more elusive. I compiled here my various notes on λ_T and formulated a physical definition that most closely matches the present findings for boundary layer turbulence. The following is a list of various relationships and descriptions for λ_T I have come across:

1. The original definition given by G. I. Taylor $\lambda_T = \sqrt{u_{rms}^2/\langle(\partial u/\partial x)^2\rangle}$, which he described as the

"average size of the smallest eddies responsible for the dissipation of energy" (Taylor 1935).

2. The size of the most well-correlated eddies, from the parabolic fit of the autocorrelation function which is mathematically related to number 1 and was included in the original definition.
3. An intermediate length scale between L and η, where $\lambda_T/L \sim Re_L^{-1/2}$, $\eta/\lambda_T \sim Re_\lambda^{-1/2}$, and $\lambda_T \sim \eta^{2/3}L^{1/3}$ (Pope 2000).
4. The mean frequency of zero crossings in a fluctuating signal, mathematically related to number 1 (Liepmann 1949; Sreenivasan *et al.* 1983).
5. The scale approximately separating the inertial subrange from the dissipative motions in the spectrum of turbulence (Cava *et al.* 2012).
6. The approximate thickness of shear layers in isotropic turbulence (Ishihara *et al.* 2009; Elsinga *et al.* 2017), the TNTI in jet turbulence (da Silva & Taveira 2010), the TNTI in boundary layer turbulence (Chauhan *et al.* 2014), and internal shear layers (Eisma *et al.* 2015; de Silva *et al.* 2017).
7. The largest length scale at which the viscosity affects turbulent vortices[10] (da Silva *et al.* 2014).

In the present work, λ_T was defined using item #1 above. The value corresponds to thickness δ_ω of the ISLs in figure 57 across a wide range of Reynolds number and surface roughness, in accordance with item #6. The largest vortices in figure 49 consistently correspond to $d_\omega \approx \lambda_T$. Following item #7 and figure 61, these sizes are directly affected by the viscosity through the diffusion relationship $\delta_\omega \sim d_\omega \sim \sqrt{\nu/\alpha}$. Given the viscosity is important for motions smaller than λ_T, it is reasonable for these motions to correspond to the scales where energy is directly dissipated into heat through viscosity (item #5). The appropriate strain rate is due to the local UMZ properties which correspond to the turnover time scale T. Using $\alpha = 1/T$ in the diffusion relation above yields $\delta_\omega \sim \sqrt{\nu/\alpha} \sim LRe_L^{-1/2}$ which is consistent with item #3. These observations leads to a description of λ_T that combines several of the items above:

> The Taylor microscale in boundary layer turbulence is a statistical parameter describing the thickness of the largest shear and vorticity structures that are strongly affected by viscosity. The microscale is governed by the mutual interaction of these structures with local integral-scale velocity structures.

By this definition, λ_T is a dynamically important parameter, even for high-Reynolds-number cases such as in the ASL. However, λ_T is often difficult to estimate in atmospheric flows unless high-frequency ($f_s \geq$ 50 Hz) sonic anemometers are available. The ability to predict the Taylor microscale *a priori* would be useful in both field studies with limited measurement resolution and in determining the mesh spacing for high-resolution LES experiments. The previously discussed connection between the strain rate α and the average shear S provides a method to estimate the microscale as $\lambda_T \sim \sqrt{\nu S}$. In the log region of neutrally stratified conditions, this relationship simplifies to $\lambda_T \sim \sqrt{\nu u_\tau/z}$. The accuracy of this relationship and the extent to which it applies for convective and stably stratified flows are topics of future research.

---

[10] This is similar to the definition currently given on Wikipedia.

7.3 A thought on the incremental energy cascade

In an attempt to invoke even more clichés of turbulence research, I now enter the topic of the turbulent energy cascade. The concept of the cascade, briefly introduced in §2.2, was first proposed by Richardson (1920), though the term cascade is attributed to Onsager (1949). In the classical view of the cascade, the energy of the largest eddies is transferred to incrementally smaller eddies until the energy is dissipated into heat through viscosity. The concept is succinctly summarized in Richardson's short poem (1922, p. 66):

> *Big whirls have little whorls,*
> *which feed on their velocity.*
> *And little whorls have lesser whorls*
> *and so on to viscosity.*

The cascade was formalized by Kolmogorov (1941), who used a similarity hypothesis to predict the self-similar power law behavior of the energy spectrum E and structure function D in the inertial subrange. The spectrum E quantifies the energy density of velocity fluctations in Fourier space, D quantifies the velocity difference as a function of separation in physical space, and the two can be related through the correlation function[11]. Kolmogorov's 1941 hypothesis predicted $E \sim k^{-5/3}$ where k is the wavenumber and $r \sim D^{2/3}$ for the second-order structure function whose definition is given in §6.1. These predictions have been well borne out in experiments, as shown in the example streamwise spectrum E_{11} and second-order structure function D_{11} in figure 62. Note the spectrum is plotted as a function of the streamwise linear wavelength $\Lambda_x = 1/k_x$. The incremental cascade is often inferred from these slopes, where there is a self-similar decrease in energy content for decreasing eddy size. The approximate boundaries for the inertial subrange are related to λ_T and L as seen in figure 62. In the log region, the upper limit is often expressed as u_τ^3/ϵ (Davidson & Krogstad 2014) or a factor of the wall-normal distance z (Saddoughi & Veeravalli 1994; de Silva *et al.* 2015).

Outside the inertial subrange, there has been considerable success in attributing the shape of E_{11} and D_{11} to the behavior of coherent structures. The so-called production range above the inertial subrange is characterized by $E_{11} \sim k_x^{-1}$ (Tchen 1953) and $D_{11} \sim \ln r_x$ (Davidson *et al.* 2006). These functional forms in the production range are only apparent for high Reynolds numbers (Nickels *et al.* 2005), and the sample case in figure 62 has insufficient Re_τ to observe a distinct, extended production range. The production range behavior is the result of wall-dependent or "attached" structures scaling with z such as UMZs or Λ-eddy packets (Perry *et al.* 1986). The largest structures scale in size with the outer condition δ and are considered "inactive" in terms of their contribution to the mean shear and production (Townsend 1976). At the other end of the spectrum, scales smaller than the inertial subrange are characterized by high dissipation and enstrophy (Davidson 2015). This region represents vortical motions and other structures governed by viscosity which directly dissipate energy into heat, causing a sharp change in E_{11}.

The structures associated with the inertial subrange and energy cascade are more of a mystery, based on my incomplete knowledge of the literature. The cascade has been attributed to or associated with several processes including vortex stretching (Taylor 1937), fractal behavior (Sreenivasan 1991), rapid distortion (Hunt

---

[11] Specifically, $E_{11} = \frac{1}{2\pi}\int \rho_{11}(r)e^{-\mathrm{i}kr}dr$ and $D_{11} = 2\sigma^2[1-\rho_{11}(r)]$ following a few assumptions.

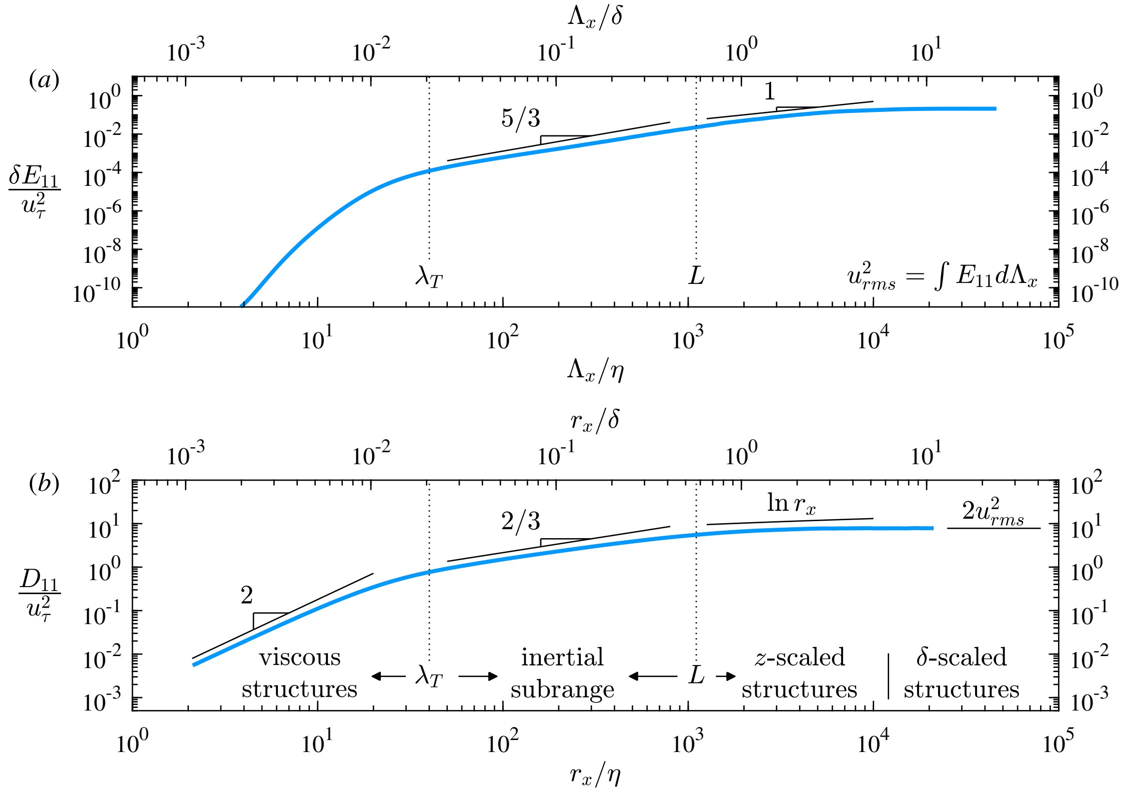

Figure 62. Scale-dependent turbulent energy based on (*a*) the streamwise velocity spectrum E_{11} as a function of streamwise wavelength Λ_x and (*b*) second-order streamwise structure function D_{11} as a function of streamwise separation r_x. The coherent structures associated with each scaling region are given in (*b*), where the inertial subrange structures are not well understood. From hotwire measurement for the $Re_\tau = 10\,100$ mesh roughness case at z= 0.15δ.

et al. 2014), and strain self-amplification (Carbone & Bragg 2020), to name a few. Most of these examples are directly related to the strain field. Perhaps controversially, I propose separating the energy cascade from the inertial subrange power law behavior, or at least avoiding an assumption of mutual inclusivity. The inertial subrange in D_{11} contains no information relating to how energy is transferred to smaller scales. Rather, E_{11} as a statistic describes the contribution of each wavelength (or separation distance for D_{11}) to the overall velocity variations. Given the intermittency and clustering of the strongest velocity gradients into thin shear layers, it is likely the properties of these shear layers are critical to the distribution of velocity difference captured by E_{11} and D_{11}. In this sense, these statistics help to answer the following question: what is the physical spacing between the shear layers, i.e. how many of these layers, on average, are present within a given distance?

Experimental evidence, both here and in previous studies, suggests the shear layers in boundary layer turbulence have average thickness λ_T and length L (de Silva *et al.* 2017), where the latter corresponds to the size of the velocity structures bounding the shear layers. In the structural representation of the energy spectrum, these average properties seem to constitute a gap within the inertial subrange. However, the shear

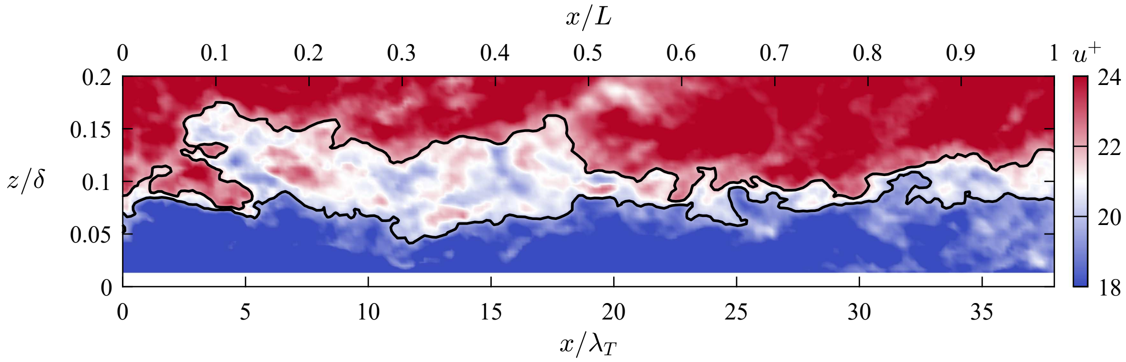

Figure 63. Color plot of streamwise velocity isolating a single internal shear layer. The black contour lines are the approximate limits of the shear region. From PIV measurements for the $Re_\tau = 12\,300$ smooth wall case. The axes are scaled such that a 1:1 aspect ratio is maintained.

layers do not form along a straight path, and instead their shape exhibits fractal-like behavior, which has been a subtopic of turbulence research for some time (Mandelbrot 1974; Sreenivasan 1991; Meneveau & Sreenivasan 1991). The average fractal dimension increases with wall-normal position (de Silva *et al.* 2017), perhaps due to increasing time scale of the structure. Consider the example internal shear layer in figure 63, where the streamwise extent shown is one integral length $x = L$. The shear layer is significantly thicker on the left side of the figure, where it may be connected to the spanwise edge of a velocity structure that only partially extends into the measurement plane. The signal $u(x, z{=}0.1\delta)$ passes through the same shear layer numerous times within one integral length, and the separation distance between crossings are generally within the inertial subrange $\lambda_T < x < L$. Each of these crossing produces a significant velocity gradient that contributes to the scale-dependent E_{11} and D_{11} statistics. I therefore believe the convoluted internal shear layers where the velocity gradients are concentrated may be important to the self-similar power law of the inertial subrange.

These shear layer crossings do not directly reflect the down-scale energy transfer, but the fractal geometry may be a consequence of the transfer. This topic, and small-scale dynamics in general, are not my area of expertise. The possible connection between the energy transfer and the shear layer geometry warrants future research, hopefully in collaboration with researchers who have greater knowledge on the subject. Nevertheless, the results in §7.1 suggest the coherent structures associated with the energy cascade are related to the UMZ-ISL self-organization. The local strain field around each ISL leads to energy transfer from the relatively uniform velocity structures into the shear layer. The small-scale structures embedded within the shear layer, e.g. vortices and possibly other viscous structures such as dissipation sheets, then do the work of directly dissipating the energy. This turbulent energy pathway is diagrammed in figure 64.

Previous studies have proposed similar structures to be related to the cascade in the log region, specifically streamwise rolls (Q2–Q4 pairs) and a corresponding vortex cluster (Flores & Jiménez 2010; Jiménez 2012). The rolls contribute to UMZs as depicted in figure 61, and the vortex cluster is qualitatively similar to the ISLs with embedded vortices. In this framework, the interior of UMZs lack the little whorls described

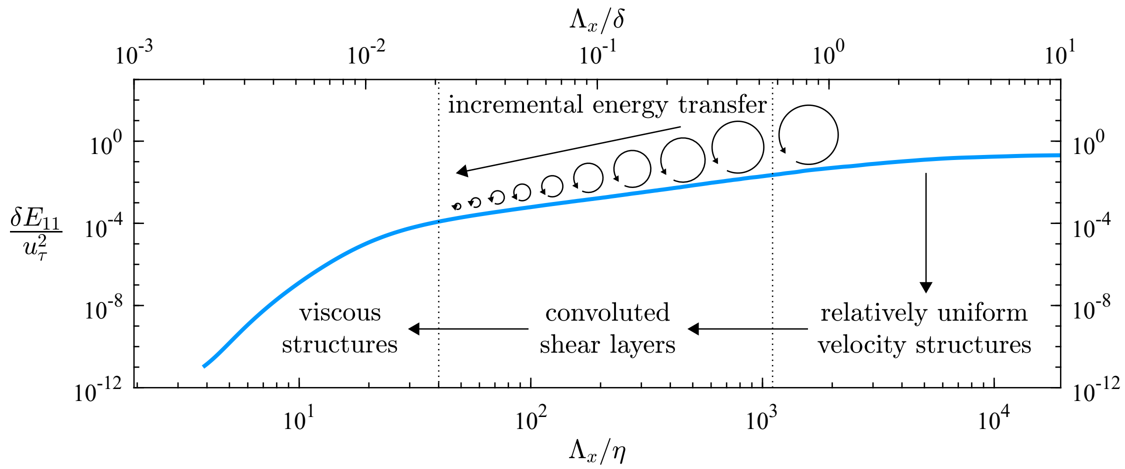

Figure 64. Diagram of turbulent energy transfer across scales using the streamwise velocity spectrum E_{11} from figure 62. The classical description involves transfer to incrementally smaller eddies. The present results suggest a direct transfer from large-scale velocity structures to shear regions of thickness $O(\lambda_T)$ and length $O(L)$.

in Richardson's poem, which does not account for the intermittent nature of the turbulence organization. Tsinober (2001) previously pointed out that a more accurate poetic description is given by Betchov (1976). Betchov's words below (1976, p. 845) are certainly better aligned with the present observations and the phenomenology proposed in this chapter:

> *Big whirls lack smaller whirls,*
> *to feed on their velocity.*
> *They crash and form the finest curls*
> *permitted by viscosity.*

One necessary clarification is that these 'finest curls', i.e. internal shear layers and embedded vortices, are long-lived features in boundary layer flows. The evidence here suggests the longevity is facilitated by strain and possibly stretching. In other words: the whirls strain, the curls stretch, and develop sinuosity.

8 Concluding remarks

Congratulations, we made it! We endured a snowy blizzard and overcame a mountain of clichés. Readers who have skipped ahead to this point will not be rewarded with an exhaustive summary. Rather, the primary focus of this conclusion is an outlook on future research efforts.

The present thesis used extensively the UMZ framework introduced by Meinhart & Adrian (1995), which identifies the organization of the boundary layer outer region into large-scale velocity structures and thin shear layers. The main utility of the framework, in my opinion, is its ability to comprehensively detect the properties of this organization. Indeed, the comparison of UMZ properties across a range of flow conditions in chapter 5 revealed the connection between the structural organization and the mean velocity profile. Yet the current framework is unable to detect certain details such as axial strain, which may be critical to the dynamic interaction of UMZs and ISLs based on my interpretation in figure 61. In this regard, a logical progression of UMZ analysis is to extend the detection of UMZs beyond u structures in the $x-z$ plane to additional velocity components and in three dimensions. Previous works have already established the relationship between UMZs and hairpin-type packets (Adrian *et al.* 2000b), bulges (Saxton-Fox & McKeon 2017), momentum streaks (Hwang & Sung 2018), and shear stress events (Laskari *et al.* 2018). Extending the UMZ detection to additional velocity components will provide a more quantitative connection to streamwise rolls, sweeps, and ejections. With additional details, we may also learn that certain UMZ structures, especially in the wake region, are not well described by any current structural classification.

Given current experimental capabilities, analysis of UMZs in three dimensions will likely be limited to numerical simulations (see, e.g., Chen *et al.* 2020). The Reynolds number is then limited to the moderate values afforded by DNS, i.e. $Re_\tau \sim O(10^3)$, unless it is demonstrated that LES can properly resolve the internal shear layer dynamics. Studying the UMZ-ISL organization in three dimensions is necessary for further exploring the possible scale interactions identified in chapter 7. Fortunately, these interactions appear to be independent of Reynolds number based on the range of cases studied here, where the results using the DNS of Sillero *et al.* (2013) are in agreement with the higher-Reynolds-number experiments.

The second utility of the UMZ-ISL framework, and perhaps the more important for practical advancements, is reduced-order modeling. The analysis of de Silva *et al.* (2016) and in chapter 4 showed the UMZ-ISL organization to be statistically robust: turbulence within the detected UMZs is small, and a majority of the shear and vortices are aligned with the detected ISLs. Statistics can then be approximated using only information on the UMZ size and velocity and ISL size. The approximation is reasonably successful for velocity statistics governed primarily by large-scale features (Bautista *et al.* 2019), but would underestimate velocity gradient statistics which are associated with the dissipative scales. A reduced-order UMZ representation of turbulence is therefore more useful as a kinematic model similar to the AEM (Marusic & Monty 2019). The stochastic properties of the UMZs and ISLs presented in this thesis can be used to improve the predictions of the existing AEM and UMZ models.

For such a model to be of practical use in atmospheric sciences, the effect of buoyancy on coherent structures and the UMZ-ISL organization must be understood. Qualitatively, the UMZs become shorter (in x) and more inclined under increasingly positive buoyancy as convective cells form (Salesky *et al.* 2017). For negative buoyancy in stably stratified flows, the shear layers become less inclined, but the primary turbulence generation is still by shear production (Sullivan *et al.* 2016; Shah & Bou-Zeid 2014). A more quantitative analysis of the changes in the UMZ and ISL properties for each thermal stability case is warranted. Observing how buoyancy effects lead to changes in the structural organization and subsequent changes in the velocity profiles could provide a better phenomenological understanding of empirical similarity equations (Monin & Obukhov 1954) for which the theoretical basis is limited (Katul *et al.* 2011). A stochastic approach to describing the structural organization of atmospheric turbulence could also have implications for many atmospheric models, which typically use mean parameterization that does not account for the full range of flow states.

While the modeling aspect of the work is left as a long-term research goal, the prospect at least seems feasible. In neutrally stratified conditions, the present thesis provides convincing evidence that the organization of outer region structures is universal in accordance with Townsend's similarity hypothesis (1976). The apparent universality makes it possible to extend a structural model to any flow conditions so long as the appropriate parameters are known. If scaling behavior can be attributed to caring, the large-scale velocity structures only care about the wall shear stress (u_τ) and their position within the flow geometry (z/δ), and the shear layers likely only care about the local large-scale properties. This personification may seem unscientific, but for me it is the only natural conclusion to a close five-year companionship with boundary layer turbulence.

References

Abraham, A., Dasari, T., and Hong, J. (2019). Effect of turbine nacelle and tower on the near wake of a utility-scale wind turbine. *J. Wind Eng. Ind. Aerod.*, 193, 103981.

Abraham, A. and Hong, J. (2020). Dynamic wake modulation induced by utility-scale wind turbine operation. *Appl. Energy*, 257, 114003.

Adrian, R. J. (1984). Scattering particle characteristics and their effect on pulsed laser measurements of fluid flow: speckle velocimetry vs particle image velocimetry. *Appl. Optics*, 23 (11), 1690–1691.

Adrian, R. J. (1991). Particle-imaging techniques for experimental fluid mechanics. *Annu. Rev. Fluid Mech.*, 23, 261–304.

Adrian, R. J. (2007). Hairpin vortex organization in wall turbulence. *Phys. Fluids*, 19, 041301.

Adrian, R. J., Christensen, K. T., and Liu, Z.-C. (2000a). Analysis and interpretation of instantaneous turbulent velocity fields. *Exp. Fluids*, 29 (3), 275–290.

Adrian, R. J., Meinhart, C. D., and Tomkins, C. D. (2000b). Vortex organization in the outer region of the turbulent boundary layer. *J. Fluid Mech.*, 422, 1–54.

Adrian, R. J. and Westerweel, J. (2011). *Particle Image Velocimetry*. Cambridge University Press, 1st edition.

del Álamo, J. C., Jiménez, J., Zandonade, P., and Moser, R. D. (2006). Self-similar vortex clusters in the turbulent logarithmic region. *J. Fluid Mech.*, 561, 329–358.

Anderson, J. D. (2016). *Introduction to Aerodynamics*. McGraw-Hill Education, 6th edition.

Baars, W. J., Hutchins, N., and Marusic, I. (2017). Self-similarity of wall-attached turbulence in boundary layers. *J. Fluid Mech.*, 823 (R2), 1–12.

Balakumar, B. J. and Adrian, R. J. (2007). Large- and very-large-scale motions in channel and boundary-layer flows. *Phil. Trans. R. Soc. A*, 365, 665–681.

Barenblatt, G. I. (1993). Scaling laws for fully developed turbulent shear flows. part 1. basic hypotheses and analysis. *J. Fluid Mech.*, 248, 513–520.

Bautista, J. C. C., Ebadi, A., White, C. M., Chini, G. P., and Klewicki, J. C. (2019). A uniform momentum zone–vortical fissure model of the turbulent boundary layer. *J. Fluid Mech.*, 858, 609–633.

Betchov, R. (1976). On the non-Gaussian aspects of turbulence. *Archiwum Mechaniki Stosowanej*, 28 (5-6), 837–845.

Blackwelder, R. F. and Eckelmann, H. (1979). Streamwise vortices associated with the bursting phenomenon. *J. Fluid Mech.*, 94 (3), 577–594.

Blasius, H. (1912). Das aehnlichkeitsgesetz bei reibungsvorgängen. *Z. Ver. Dtsch. Ing.*, 56 (16), 639–643.

Boussinesq, J. (1887). Essai sur la théorie des eaux courantes. *Mémoires présentés par divers savants à l'Académie des Sciences*, 23 (1).

Boussinesq, J. (1897). *Théorie de l'écoulement tourbillonnant et tumultueux des liquides dans les lits rectilignes a grande section*. Gauthier-Villars et fils, Imprimeurs-Libraires.

Brandes, E. A., Ikeda, K., Zhang, G., Schönhuber, M., and Rasmussen, R. M. (2007). A statistical and physical description of hydrometeor distributions in colorado snowstorms using a video disdrometer. *J. Appl. Meteorol. Climatol.*, 46 (5), 634–650.

Brown, G. L. and Roshko, A. (1974). On density effects and large structure in turbulent mixing layers. *J. Fluid Mech.*, 64 (4), 775–816.

Brutsaert, W. (1982). *Evaporation into the Atmosphere: Theory, History and Applications*, volume 1. Springer Science & Business Media.

Burgers, J. M. (1948). A mathematical model illustrating the theory of turbulence. In *Advances in Applied Mechanics*, volume 1, pages 171–199. Academic Press Inc.

Carbone, M. and Bragg, A. (2020). Is vortex stretching the main cause of the turbulent energy cascade? *J. Fluid Mech.*, 883, R2.

Carlier, J. and Stanislas, M. (2005). Experimental study of eddy structures in a turbulent boundary layer using particle image velocimetry. *J. Fluid Mech.*, 535, 143–188.

Cava, D., Katul, G. G., Molini, A., and Elefante, C. (2012). The role of surface characteristics on intermittency and zero-crossing properties of atmospheric turbulence. *J. Geophys. Res.*, 117, D01104.

Chakraborty, P., Balachandar, S., and Adrian, R. J. (2005). On the relationships between local vortex identification schemes. *J. Fluid Mech.*, 535, 189–214.

Chauhan, K., Philip, J., de Silva, C. M., Hutchins, N., and Marusic, I. (2014). The turbulent/non-turbulent interface and entrainment in a boundary layer. *J. Fluid Mech.*, 742, 119–151.

Chauhan, K. Hutchins, N., Monty, J., and Marusic, I. (2013). Structure inclination angles in the convective atmospheric surface layer. *Boundary-Layer Meteorol.*, 147, 41–50.

Chen, X., Chung, Y. M., and Wan, M. (2020). Uniform-momentum zones in a turbulent pipe flow. *J. Fluid Mech.*, 884, A25.

Cheng, C., Li, W., Lozano-Durán, A., and Liu, H. (2019). Identity of attached eddies in turbulent channel flows with bidimensional empirical mode decomposition. *J. Fluid Mech.*, 870, 1037–1071.

Chini, G. P., Montemuro, C., White, C. M., and Klewicki, J. C. (2017). A self-sustaining process model of inertial layer dynamics in high Reynolds number turbulent wall flows. *Phil. Trans. R. Soc. A*, 375, 20160090.

Chow, V. T. (1959). *Open-channel Hydraulics*. McGraw-Hill Book Company Inc.

Christensen, K. T. and Adrian, R. J. (2001). Statistical evidence of hairpin vortex packets in wall turbulence. *J. Fluid Mech.*, 431, 433–443.

Chung, D., Monty, J. P., and Ooi, A. (2014). An idealised assessment of townsends outer-layer similarity hypothesis for wall turbulence. *J. Fluid mech.*, 742, R3.

Clarke, R. H., Dyer, A. J., Brokk, R. R., Reid, D. G., and Troup, A. J. (1971). The Wangara experiment: boundary-layer data. *CSIRO Div. of Met. Phys. Tech. Paper 19*.

Coles, D. (1956). The law of the wake in a turbulent boundary layer. *J. Fluid Mech.*, 1 (2), 191–226.

Corino, E. R. and Brodkey, R. S. (1969). A visual investigation of the wall region in turbulent flow. *J. Fluid Mech.*, 37 (1), 1–30.

Coriolis, G. G. (1835). Mémoire sur les équations du mouvement relatif des systèmes de corps. *J. de l'école Polytechnique*, 15, 142–154.

Corrsin, S. (1957). Some current problems in turbulent shear flows. In *Proc. 1st Symp. on Naval Hydrodyn.* NAS-NRC Publ. 515.

Crowe, C. T., Schwarzkopf, J. D., Sommerfeld, M., and Tsuji, Y. (1998). *Multiphase Flows with Droplets and Particles*. CRC Press.

Dasari, T., Wu, Y., Liu, Y., and Hong, J. (2019). Near-wake behaviour of a utility-scale wind turbine. *J. Fluid Mech.*, 859, 204–246.

Davidson, P. A. (2015). *Turbulence: An Introduction for Scientists and Engineers*. Oxford University Press, Second edition.

Davidson, P. A. and Krogstad, P. A. (2014). A universal scaling for low-order structure functions in the log-law region of smooth- and rough-wall boundary layers. *J. Fluid Mech.*, 752, 140–156.

Davidson, P. A., Nickels, T. B., and Krogstad, P. A. (2006). The logarithmic structure function law in wall-layer turbulence. *J. Fluid Mech.*, 550, 51–60.

Deardorff, J. W. (1970). A numerical study of three-dimensional turbulent channel flow at large Reynolds numbers. *J. Fluid Mech.*, 41 (2), 453–480.

Dennis, D. J. and Nickels, T. B. (2011). Experimental measurement of large-scale three-dimensional structures in a turbulent boundary layer. Part 1. Vortex packets. *J. Fluid Mech.*, 673, 180–217.

Drobinski, P., Carlotti, P., Newsom, R. K., Banta, R. M., Foster, R. C., and Redelsperger, J. L. (2004). The structure of the near-neutral atmospheric surface layer. *J. Atmos. Sci.*, 61 (6), 699–714.

Durbin, P. A. (2018). Some recent developments in turbulence closure modeling. *Annu. Rev. Fluid Mech.*, 50, 77–103.

Ebner, R. L., Mehdi, F., and Klewicki, J. C. (2016). Shared dynamical features of smooth-and rough-wall boundary-layer turbulence. *J. Fluid Mech.*, 792, 435–469.

Eisma, J., Westerweel, J., Ooms, G., and Elsinga, G. E. (2015). Interfaces and internal layers in a turbulent boundary layer. *Phys. Fluids*, 27 (5), 055103.

Elghobashi, S. (1994). On predicting particle-laden turbulent flows. *Appl. Sci. Res.*, 52, 309–329.

Elsinga, G. E. and Marusic, I. (2010). Universal aspects of small-scale motions in turbulence. *J. Fluid Mech.*, 662, 514–539.

Elsinga, G. E., Scarano, F., Wieneke, B., and van Oudheusden, B. W. (2006). Tomographic particle image velocimetry. *Exp. Fluids*, 41, 933–947.

Elsinga, G. E. Ishihara, T., Goudar, M. V., da Silva, C. B., and Hunt, J. C. R. (2017). The scaling of straining motions in homogeneous isotropic turbulence. *J. Fluid Mech.*, 829, 31–64.

Etling, D. and Brown, R. A. (1993). Roll vortices in the planetary boundary layer : A review. *Boundary-Layer Meteorol.*, 65, 215–248.

Fan, D., Xu, J., Yao, M. X., and Hickey, J. P. (2019). On the detection of internal interfacial layers in turbulent flows. *J. Fluid Mech.*, 872, 198–217.

Flack, K. A. and Schultz, M. P. (2014). Roughness effects on wall-bounded turbulent flows. *Phys. Fluids*, 26 (10), 101305.

Flack, K. A., Schultz, M. P., and Connelly, J. S. (2007). Examination of a critical roughness height for outer layer similarity. *Phys. Fluids*, 19 (9), 095104.

Flores, O. and Jiménez, J. (2010). Hierarchy of minimal flow units in the logarithmic layer. *Phys. Fluids*, 22 (7), 071704.

Flores, O., Jiménez, J., and del Álamo, J. C. (2007). Vorticity organization in the outer layer of turbulent channels with disturbed walls. *J. Fluid Mech.*, 591, 145–154.

Foster, R. C., Vianey, F., Drobinski, P., and Carlotti, P. (2006). Near-surface coherent structures and the vertical momentum flux in a large-eddy simulation of the neutrally-stratified boundary layer. *Boundary-Layer Meteorol.*, 120, 229–255.

Frank, J. M., Massman, W. J., and Ewers, B. E. (2013). Underestimates of sensible heat flux due to vertical velocity measurement errors in non-orthogonal sonic anemometers. *Agricultural and Forest Meteorol.*, 171-172, 72–81.

Ganapathisubramani, B., Hutchins, N., Hambleton, W. T., Longmire, E. K., and Marusic, I. (2005). Investigation of large-scale coherence in a turbulent boundary layer using two-point correlations. *J. Fluid Mech.*, 524, 57–80.

Ganapathisubramani, B., Longmire, E. K., and Marusic, I. (2003). Characteristics of vortex packets in turbulent boundary layers. *J. Fluid Mech.*, 478, 35–46.

Ganapathisubramani, B., Longmire, E. K., and Marusic, I. (2006). Experimental investigation of vortex properties in a turbulent boundary layer. *Phys. Fluids*, 18 (5), 055105.

Gao, Q., Ortiz-Dueñas, C., and Longmire, E. K. (2011). Analysis of vortex populations in turbulent wall-bounded flows. *J. Fluid Mech.*, 678, 87–123.

Garratt, J. R. (1994). *The Atmospheric Boundary Layer*. Cambridge University Press.

George, W. K. (2007). Is there a universal log law for turbulent wall-bounded flows? *Phil. Trans. R. Soc. A*, 365 (1852), 789–806.

Graftieaux, L., Michard, M., and Grosjean, N. (2001). Combining piv, pod and vortex identification algorithms for the study of unsteady turbulent swirling flows. *Meas. Sci. Tech.*, 12 (9), 1422–1429.

Grant, A. L. M. and Watkins, R. D. (1989). Errors in turbulence measurements with a sonic anemometer. *Boundary-Layer Meteorol.*, 46 (1-2), 181–194.

Grass, A. J. (1971). Structural features of turbulent flow over smooth and rough boundaries. *J. Fluid Mech.*, 50 (2), 233–255.

Guala, M., Hommema, S. E., and Adrian, R. J. (2006). Large-scale and very-large-scale motions in turbulent pipe flow. *J. Fluid Mech.*, 554, 521–542.

Guala, M., Metzger, M., and McKeon, B. J. (2011). Interactions within the turbulent boundary layer at high Reynolds number. *J. Fluid Mech.*, 666, 573–604.

Guala, M., Tomkins, C. D., Christensen, K. T., and Adrian, R. J. (2012). Vortex organization in a turbulent boundary layer overlying sparse roughness elements. *J. Hydraul. Res.*, 50 (5), 465–481.

Haller, G. (2005). An objective definition of a vortex. *J. Fluid Mech.*, 525, 1–26.

Hama, F. R., Long, J. D., and Hegarty, J. C. (1957). On transition from laminar to turbulent flow. *J. Appl. Phys.*, 28 (4), 388–394.

Hartmann, D. (2016). *Global Physical Climatology*. Elsevier, 2nd edition.

Head, M. R. and Bandyopadhyay, P. (1981). New aspects of turbulent boundary-layer structure. *J. Fluid Mech.*, 107, 297–338.

Hearst, R. J. and Ganapathisubramani, B. (2015). Quantification and adjustment of pixellocking in particle image velocimetry. *Exp. Fluids*, 56, 191.

Heisel, M., Dasari, T., Liu, Y., Hong, J., Coletti, F., and Guala, M. (2018). The spatial structure of the logarithmic region in very-high-Reynolds-number rough wall turbulent boundary layers. *J. Fluid Mech.*, 857, 704–747.

Heisel, M., de Silva, C. M., Hutchins, N., Marusic, I., and Guala, M. (2020). On the mixing length eddies and logarithmic mean velocity profile in wall turbulence. *J. Fluid Mech.*, 887, R1.

Herpin, S., Stanislas, M., Foucaut, J. M., and Coudert, S. (2013). Influence of the Reynolds number on the vortical structures in the logarithmic region of turbulent boundary layers. *J. Fluid Mech.*, 716, 5–50.

Heymsfield, A. J., Bansemer, A., Schmitt, C., Twohy, C., and Poellot, M. R. (2004). Effective ice particle densities derived from aircraft data. *J. Atmos. Sci.*, 61 (9), 982–1003.

Hinze, J. O. (1975). *Turbulence*. McGraw-Hill.

Högström, U., Hunt, J. C. R., and Smedman, A. (2002). Theory and measurements for turbulence spectra and variances in the atmospheric neutral surface layer. *Boundary-Layer Meteorol.*, 103 (1), 101–124.

Hommema, S. E. and Adrian, R. J. (2003). Packet structure of surface eddies in the atmospheric boundary layer. *Boundary-Layer Meteorol.*, 106 (1), 147–170.

Hong, J., Katz, J., and Schultz, M. P. (2011). Near-wall turbulence statistics and flow structures over three-dimensional roughness in a turbulent channel flow. *J. Fluid Mech.*, 667, 1–37.

Hong, J., Toloui, M., Chamorro, L. P., Guala, M., Howard, K. B., Riley, S., Tucker, J., and Sotiropoulos, F. (2014). Natural snowfall reveals large-scale flow structures in the wake of a 2.5-mw wind turbine. *Nat. Commun.*, 5, 4216.

Hultmark, M., Vallikivi, M., Bailey, S. C. C., and Smits, A. J. (2013). Logarithmic scaling of turbulence in smooth- and rough-wall pipe flow. *J. Fluid Mech.*, 728, 376–395.

Hunt, J. C. R. and Carlotti, P. (2001). Statistical structure at the wall of the high Reynolds number turbulent boundary layer. *Flow Turbul. Combust.*, 66 (4), 453–475.

Hunt, J. C. R., Eames, I., Westerweel, J., Davidson, P. A., Voropayev, S., Fernando, J., and Braza, M. (2010). Thin shear layers – the key to turbulence structure? *J. Hydro-environ. Res.*, 94 (2), 75–82.

Hunt, J. C. R., Ishihara, T., Worth, N. A., and Kaneda, Y. (2014). Thin shear layer structures in high Reynolds number turbulence. *Flow Turbul. Combust.*, 92 (3), 607–649.

Hutchins, N., Chauhan, K., Marusic, I., Monty, J. P., and Klewicki, J. C. (2012). Towards reconciling the large-scale structure of turbulent boundary layers in the atmosphere and laboratory. *Boundary-Layer Meteorol.*, 145 (2), 273–306.

Hutchins, N. and Marusic, I. (2007a). Evidence of very long meandering features in the logarithmic region of turbulent boundary layers. *J. Fluid Mech.*, 579, 1–28.

Hutchins, N. and Marusic, I. (2007b). Large-scale influences in near-wall turbulence. *Phil. Trans. R. Soc. A*, 365, 647–664.

Hutchins, N. Hambleton, W. T. and Marusic, I. (2005). Inclined cross-stream stereo particle image velocimetry measurements in turbulent boundary layers. *J. Fluid Mech.*, 541, 21–54.

Hwang, J. and Sung, H. J. (2018). Wall-attached structures of velocity fluctuations in a turbulent boundary layer. *J. Fluid Mech.*, 856, 958–983.

Hwang, Y. (2015). Statistical structure of self-sustaining attached eddies in turbulent channel flow. *J. Fluid Mech.*, 767, 254–289.

Hwang, Y. and Cossu, C. (2010). Self-sustained process at large scales in turbulent channel flow. *Phys. Rev. Lett.*, 105 (4), 044505.

Ishihara, T., Gotoh, T., and Kaneda, Y. (2009). Study of highReynolds number isotropic turbulence by direct numerical simulation. *Annu. Rev. Fluid Mech.*, 41 (1), 165–180.

Ishihara, T., Kaneda, Y., and Hunt, J. C. R. (2013). Thin shear layers in high Reynolds number turbulence – DNS results. *Flow Turbul. Combust.*, 91 (4), 895–929.

Jiménez, J. (1998). The largest scales of turbulent wall flows. Annual Research Briefs 1998, Center for Turbulence Research, Stanford University.

Jiménez, J. (2004). Turbulent flows over rough walls. *Annu. Rev. Fluid Mech.*, 36 (1), 173–196.

Jiménez, J. (2012). Cascades in wall-bounded turbulence. *Annu. Rev. Fluid Mech.*, 44 (1), 27–45.

Jiménez, J. (2013). Near-wall turbulence. *Phys. Fluids*, 25, 101302.

Jiménez, J. (2018). Coherent structures in wall-bounded turbulence. *J. Fluid Mech.*, 842, P1.

Jiménez, J. and Moin, P. (1991). The minimal flow unit in near-wall turbulence. *J. Fluid Mech.*, 225, 213–240.

Jiménez, J., Wray, A. A., Saffman, P. G., and Rogallo, R. S. (1993). The structure of intense vorticity in isotropic turbulence. *J. Fluid Mech.*, 255, 65–90.

Jodai, Y. and Elsinga, G. E. (2016). Experimental observation of hairpin auto-generation events in a turbulent boundary layer. *J. Fluid Mech.*, 795, 611–633.

Kaimal, J. C. and Finnigan, J. J. (1994). *Atmospheric boundary layer flows*. Oxford University Press.

Kang, S. J., Tanahashi, M., and Miyauchi, T. (2007). Dynamics of fine scale eddy clusters in turbulent channel flows. *J. Turbul.*, 8, N52.

von Kármán, T. (1930). Mechanische ähnlichkeit und turbulenz. *Gött. Nachr.*, 5, 58–76.

Katul, G. G., Konings, A. G., and Porporato, A. (2011). Mean velocity profile in a sheared and thermally stratified atmospheric boundary layer. *Phys. Rev. Lett.*, 107, 268502.

Kevin, Monty, J., and Hutchins, N. (2019). The meandering behaviour of large-scale structures in turbulent boundary layers. *J. Fluid Mech.*, 865, R1.

Kim, J., Moin, P., and Moser, R. (1987). Turbulence statistics in fully developed channel flow at low Reynolds number. *J. Fluid Mech.*, 177, 133–166.

Kim, K. C. and Adrian, R. J. (1999). Very large-scale motion in the outer layer. *Phys. Fluids*, 11 (2), 417–422.

Klebanoff, P. S., Tidstrom, K. D., and Sargent, L. M. (1962). The three-dimensional nature of boundary-layer instability. *J. Fluid Mech.*, 12 (1), 1–34.

Klewicki, J. C. (2013a). A description of turbulent wall-flow vorticity consistent with mean dynamics. *J. Fluid Mech.*, 737, 176–204.

Klewicki, J. C. (2013b). Self-similar mean dynamics in turbulent wall flows. *J. Fluid Mech.*, 718, 596–621.

Klewicki, J. C., Fife, P., and Wei, T. (2009). On the logarithmic mean profile. *J. Fluid Mech.*, 638, 73–93.

Klewicki, J. C., Metzger, M. M., Kelner, E., and Thurlow, E. M. (1995). Viscous sublayer flow visualizations at $r_\theta \simeq 1\,500\,000$. *Phys. Fluids*, 7 (4), 857–863.

Kline, S. J., Reynolds, W. C., Schraub, F. A., and Runstadler, P. W. (1967). The structure of turbulent boundary layers. *J. Fluid Mech.*, 30 (4), 741–773.

Kline, S. J. and Runstadler, P. W. (1959). Some preliminary results of visual studies of the flow model of the wall layers of the turbulent boundary layer. *J. Appl. Mech.*, 26, 166–170.

Kokhanovsky, A. A. and Zege, E. P. (2004). Scattering optics of snow. *Appl. Optics*, 43 (7), 1589–1602.

Kolmogorov, A. N. (1941). The local structure of turbulence in an incompressible viscous fluid for very large Reynolds numbers. *Dokl. Akad. Nauk SSSR*, 30, 299–303.

Kovasznay, L. S. G., Kibens, V., and Blackwelder, R. F. (1970). Large-scale motion in the intermittent region of a turbulent boundary layer. *J. Fluid Mech.*, 41 (2), 283–325.

Krogstad, P. A. and Antonia, R. A. (1994). Structure of turbulent boundary layers on smooth and rough walls. *J. Fluid Mech.*, 277, 1–21.

Krogstad, P. A. and Antonia, R. A. (1999). Surface roughness effects in turbulent boundary layers. *Exp. Fluids*, 27, 450–460.

Krogstad, P. A., Antonia, R. A., and Browne, L. W. B. (1992). Comparison between rough- and smooth-wall turbulent boundary layers. *J. Fluid Mech.*, 245, 599–617.

Krug, D., Philip, J., and Marusic, I. (2017). Revisiting the law of the wake in wall turbulence. *J. Fluid Mech.*, 811, 421–435.

Kunkel, G. J. and Marusic, I. (2006). Study of the near-wall-turbulent region of the high-Reynolds-number boundary layer using an atmospheric flow. *J. Fluid Mech.*, 548, 375–402.

Kwon, Y. S., Philip, J., de Silva, C. M., Hutchins, N., and Monty, J. P. (2014). The quiescent core of turbulent channel flow. *J. Fluid Mech.*, 751, 228–254.

Laskari, A., de Kat, R., Hearst, R. J., and Ganapathisubramani, B. (2018). Time evolution of uniform momentum zones in a turbulent boundary layer. *J. Fluid Mech.*, 842, 554–590.

Laurenza, D. and Kemp, M. (2019). *Leonardo da Vinci's Codex Leicester: A New Edition*, volume 1. Oxford University Press.

Lee, J., Lee, J. H., Choi, J. I., and Sung, H. J. (2014). Spatial organization of large- and very-large-scale motions in a turbulent channel flow. *J. Fluid Mech.*, 749, 818–840.

Lee, J. H. and Sung, H. J. (2011). Very-large-scale motions in a turbulent boundary layer. *J. Fluid Mech.*, 673, 80–120.

Lee, M. and Moser, R. D. (2015). Direct numerical simulation of turbulent channel flow up to $Re_\tau \approx 5200$. *J. Fluid Mech.*, 774, 395–415.

Li, C., Abraham, A., Li, B., and Hong, J. (2020). Incoming flow measurements of a utility-scale wind turbine using super-large-scale particle image velocimetry. *J. Wind Eng. Ind. Aerod.*, 197, 104074.

Liepmann, H. W. (1949). Application of a theorem on the zeros of stochastic functions to turbulence measurements. *Helv. Phys. Acta*, 22 (2), 119–126.

Lin, C. L., McWilliams, J. C., Moeng, C. H., and Sullivan, P. P. (1996). Coherent structures and dynamics in a neutrally stratified planetary boundary layer flow. *Phys. Fluids*, 8 (10), 2626–2639.

Liu, H.-Y., Bo, T.-L., and Liang, Y.-R. (2017). The variation of large-scale structure inclination angles in high Reynolds number atmospheric surface layers. *Phys. Fluids*, 29, 035104.

Long, R. R. and Chen, T. C. (1981). Experimental evidence for the existence of the 'mesolayer' in turbulent systems. *J. Fluid Mech.*, 105, 19–59.

Louis, J. F. (1979). A parametric model of vertical eddy fluxes in the atmosphere. *Boundary-Layer Meteorol.*, 17, 187–202.

Lozano-Durán, A., Flores, O., and Jiménez, J. (2012). The three-dimensional structure of momentum transfer in turbulent channels. *J. Fluid Mech.*, 694, 100–130.

Luchini, P. (2017). Universality of the turbulent velocity profile. *Phys. Rev. Lett.*, 118, 224501.

L'vov, V. S., Procaccia, I., and Rudenko, O. (2008). Universal model of finite Reynolds number turbulent flow in channels and pipes. *Phys. Rev. Lett.*, 100, 054504.

Mahrt, L. (2014). Stably stratified atmospheric boundary layers. *Annu. Rev. Fluid Mech.*, 46, 23–45.

Makkonen, L., Lehtonen, P., and Helle, L. (2001). Anemometry in icing conditions. *J. Atmos. Oceanic Tech.*, 18, 1457–1469.

Mandelbrot, B. B. (1974). Intermittent turbulence in self-similar cascades: divergence of high moments and dimension of the carrier. *J. Fluid Mech.*, 62 (2), 331–358.

Manneville, P. (2010). *Instabilities, Chaos, and Turbulence*. World Scientific, 2nd edition.

Marusic, I. (2001). On the role of large-scale structures in wall turbulence. *Phys. Fluids*, 13 (3), 735–743.

Marusic, I. and Hutchins, N. (2008). Study of the log-layer structure in wall turbulence over a very large range of Reynolds number. *Flow Turbul. Combust.*, 81 (3), 115–130.

Marusic, I. and Monty, J. P. (2019). Attached eddy model of wall turbulence. *Annu. Rev. Fluid Mech.*, 51, 49–74.

Marusic, I., Monty, J. P., Hultmark, M., and Smits, A. J. (2013). On the logarithmic region in wall turbulence. *J. Fluid Mech.*, 716 (R3), 1–11.

Maxey, M. R. and Riley, J. J. (1983). Equation of motion for a small rigid sphere in a nonuniform flow. *Phys. Fluids*, 26 (4), 883–889.

McKeon, B. (2019). Self-similar hierarchies and attached eddies. *Phys. Rev. Fluids*, 4 (8), 082601(R).

Mehdi, F., Klewicki, J. C., and White, C. M. (2013). Mean force structure and its scaling in rough-wall turbulent boundary layers. *J. Fluid Mech.*, 731, 682–712.

Meinhart, C. D. and Adrian, R. J. (1995). On the existence of uniform momentum zones in a turbulent boundary layer. *Phy. Fluids*, 7 (4), 694–696.

Meneveau, C. and Katz, J. (2000). Scale-invariance and turbulence models for large-eddy simulation. *Annu. Rev. Fluid Mech.*, 32, 1–32.

Meneveau, C. and Sreenivasan, K. R. (1991). The multifractal nature of turbulent energy dissipation. *J. Fluid Mech.*, 224, 429–484.

Metzger, M. and Klewicki, J. C. (2001). A comparative study of near-wall turbulence in high and low Reynolds number boundary layers. *Phys. Fluids*, 13 (3), 692–701.

Millikan, C. M. (1938). A critical discussion of turbulent flows in channels and circular tubes. In *Proceedings of the Fifth International Congress for Applied Mechanics*. Wiley.

Mizuno, Y. and Jiménez, J. (2013). Wall turbulence without walls. *J. Fluid Mech.*, 723, 429–455.

Moin, P. and Mahesh, K. (1998). DIRECT NUMERICAL SIMULATION: A tool in turbulence research. *Annu. Rev. Fluid Mech.*, 30, 539–578.

Moisy, F. and Jiménez, J. (2004). Geometry and clustering of intense structures in isotropic turbulence. *J. Fluid Mech.*, 513, 111–133.

Monin, A. S. and Obukhov, A. M. (1954). Basic laws of turbulent mixing in the atmosphere near the ground. *Trudy Akad. Nauk SSSR Geophiz. Inst.*, 24 (151), 163–187.

Monin, A. S. and Yaglom, A. M. (1971). *Statistical Fluid Mechanics: Mechanics of Turbulence*, volume 1. MIT Press, 1st edition.

Monty, J. P., Stewart, J. A., Williams, R. C., and Chong, M. S. (2007). Large-scale features in turbulent pipe and channel flows. *J. Fluid Mech.*, 589, 147–156.

Moody, L. F. (1944). Friction factors for pipe flows. *ASME Trans.*, 66, 671–684.

Morrill-Winter, C., Squire, D. T., Klewicki, J. C., Hutchins, N., Schultz, M. P., and Marusic, I. (2017). Reynolds number and roughness effects on turbulent stresses in sandpaper roughness boundary layers. *Phys. Rev. Fluids*, 2 (5), 054608.

Morris, S. C., Stolpa, S. R., Slaboch, R. E., and Klewicki, J. C. (2007). Near-surface particle image velocimetry measurements in a transitionally rough-wall atmospheric boundary layer. *J. Fluid Mech.*, 580, 319–338.

Nakagawa, H. and Nezu, I. (1977). Prediction of the contributions to the Reynolds stress from bursting events in open-channel flows. *J. Fluid Mech.*, 80 (1), 99–128.

Nakaya, U. (1954). *Snow Crystals: Natural and Artificial*. Harvard University Press, 1st edition.

Navier, C. L. (1821). Sur les lois des mouvements des fluides, en ayant égard à l'adhésion des molecules. *Annales de Chimie et de Physique*, XIX, 244–260.

Nemes, A., Dasari, T., Hong, J., Guala, M., and Coletti, F. (2017). Snowflakes in the atmospheric surface layer: observation of particle-turbulence dynamics. *J. Fluid Mech.*, 814, 592–613.

Nemes, A., Jacono, D. L., Blackburn, H. M., and Sheridan, J. (2015). Mutual inductance of two helical vortices. *J. Fluid Mech.*, 774, 298–310.

Newton, I. (1687). *Philosophiæ Naturalis Principia Mathematica*. 1st edition.

Nicholson, S. E. (1975). A pollution model for street-level air. *Atmos. Environ.*, 9 (1), 19–31.

Nickels, T. B., Marusic, I., Hafez, S., and Chong, M. S. (2005). Evidence of the k_1^{-1} law in a high-Reynolds-number turbulent boundary layer. *Phys. Rev. Lett.*, 95 (7), 074501.

Nickels, T. B., Marusic, I., Hafez, S., Hutchins, N., and Chong, M. S. (2007). Some predictions of the attached eddy model for a high Reynolds number boundary layer. *Phil. Trans. R. Soc. A*, 365, 807–822.

Nikuradse, J. (1933). Strömungsgesetze in rauhen rohren. *VDI-Forsch.*, 4, 361.

Offen, G. R. and Kline, S. J. (1975). A proposed model of the bursting process in turbulent boundary layers. *J. Fluid Mech.*, 70 (2), 209–228.

Onsager, L. (1949). Statistical hydrodynamics. *Il Nuovo Cimento*, 6, 279–287.

Orszag, S. A. and Patera, A. T. (1983). Secondary instability of wall-bounded shear flows. *J. Fluid Mech.*, 128, 347–385.

Oseen, C. W. (1912). Über die wirbelbewegung in einer reibenden flüssigkeit. *Ark. Mat. Astro. Fys.*, 7, 14–26.

Panton, R. L. (2002). Evaluation of the Barenblatt-Chorin-Prostokishin power law for turbulent boundary layers. *Phys. Fluids*, 14 (5), 1806–1808.

Passot, T., Politano, H., Sulem, P. L., and Angilella, J. R. (1995). Instability of strained vortex layers and vortex tube formation in homogeneous turbulence. *J. Fluid Mech.*, 282, 313–338.

Perry, A. E. and Abell, C. J. (1975). Scaling laws for pipe-flow turbulence. *J. Fluid Mech.*, 67 (2), 257–271.

Perry, A. E. and Abell, C. J. (1977). Asymptotic similarity of turbulence structures in smooth- and rough-walled pipes. *J. Fluid Mech.*, 79 (4), 785–799.

Perry, A. E. and Chong, M. S. (1982). On the mechanism of wall turbulence. *J. Fluid Mech.*, 119, 173–217.

Perry, A. E., Henbest, S., and Chong, M. S. (1986). A theoretical and experimental study of wall turbulence. *J. Fluid Mech.*, 165, 163–199.

Perry, A. E., Lim, T. T., and Teh, E. W. (1981). A visual study of turbulent spots. *J. Fluid Mech.*, 104, 387–405.

Perry, A. E. and Marusic, I. (1995). A wall-wake model for the turbulence structure of boundary layers. Part 1. extension of the attached eddy hypothesis. *J. Fluid Mech.*, 298, 361–388.

Petersen, A. J., Baker, L., and Coletti, F. (2019). Experimental study of inertial particles clustering and settling in homogeneous turbulence. *J. Fluid Mech.*, 864, 925–970.

Pirozzoli, S. (2012). On the velocity and dissipation signature of vortex tubes in isotropic turbulence. *Physica D*, 241 (3), 202–207.

Pope, S. B. (2000). *Turbulent Flows*. Cambridge University Press, 1st edition.

Prandtl, L. (1904). Über flüssigkeitsbewegung bei sehr kleiner reibung. *Verhandlg. III. Intern. Math. Kong. Heidelberg*, pages 484–491.

Prandtl, L. (1925). Bericht über untersuchungen zur ausgebildeten turbulenz. *ZAMM. Z. Angew. Math. Mech.*, 5, 136–139.

Prandtl, L. (1932). Zur turbulenten strömung in röhren und längs platten. *Ergebn. Aerodyn. Versuchsanst*, 4, 18–29.

Prandtl, L. and Schlichting, H. (1934). Das widerstandsgesetz rauher platten. *Werft-Redeerei-Hafen*, 15.

Praturi, A. K. and Brodkey, R. S. (1978). A stereoscopic visual study of coherent structures in turbulent shear flow. *J. Fluid Mech.*, 89 (2), 251–272.

Priyadarshana, P. J. A., Klewicki, J. C., Treat, S., and Foss, J. F. (2007). Statistical structure of turbulent-boundary-layer velocity–vorticity products at high and low Reynolds numbers. *J. Fluid Mech.*, 570, 307–346.

Pruppacher, H. R. and Klett, J. D. (1997). *Microphysics of Clouds and Precipitation*. Springer.

Raffel, M., Willert, C. E., Wereley, S. T., and J., K. (2007). *Particle Image Velocimetry: A Practical Guide*. 2nd edition.

Raupach, M. R. (1981). Conditional statistics of Reynolds stress in rough-wall and smooth-wall turbulent boundary layers. *J. Fluid Mech.*, 108, 363–382.

Raupach, M. R., Antonia, R. A., and Rajagopalan, S. (1991). Rough-wall turbulent boundary layers. *Appl. Mech. Rev.*, 44 (1), 1–25.

Reiss, L. P. and Hanratty, T. J. (1963). An experimental study of the unsteady nature of the viscous sublayer. *AIChE J.*, 9 (2), 154–160.

Reynolds, O. (1883). An experimental investigation of the circumstances which determine whether the motion of water shall be direct or sinuous, and of the law of resistance in parallel channels. *Phil. Trans. R. Soc.*, 174, 935–982.

Reynolds, O. (1895). On the dynamical theory of incompressible viscous fluids and the determination of the criterion. *Phil. Trans. R. Soc. A*, 186, 123–164.

Richardson, L. F. (1920). The supply of energy from and to atmospheric eddies. *Proc. R. Soc. Lond. A*, 97 (686), 354–373.

Richardson, L. F. (1922). *Weather Prediction by Numerical Processes*. Cambridge University Press, 1st edition.

Robinson, S. K. (1991). Coherent motions in the turbulent boundary layer. *Annu. Rev. Fluid Mech.*, 23, 601–639.

Roth, G. I. and Katz, J. (2001). Five techniques for increasing the speed and accuracy of piv interrogation. *Meas. Sci. Technol.*, 12 (3), 238–245.

Ruetsch, G. R. and Maxey, M. R. (1992). The evolution of smallscale structures in homogeneous isotropic turbulence. *Phys. Fluids A*, 4 (12), 2747–2760.

Runstadler, P. W., Kline, S. J., and Reynolds, W. C. (1963). An experimental investigation of the flow structure of the turbulent boundary layer. Report No. MD-8, Stanford University.

Saddoughi, S. G. and Veeravalli, S. V. (1994). Local isotropy in turbulent boundary layers at high Reynolds number. *J. Fluid Mech.*, 268, 333–372.

Salesky, S. T. and Anderson, W. (2018). Buoyancy effects on large-scale motions in convective atmospheric boundary layers: implications for modulation of near-wall processes. *J. Fluid Mech.*, 856, 135–168.

Salesky, S. T., Chamecki, M., and Bou-Zeid, E. (2017). On the nature of the transition between roll and cellular organization in the convective boundary layer. *Boundary-Layer Meteorol.*, 163, 41–68.

Saxton-Fox, T. and McKeon, B. J. (2017). Coherent structures, uniform momentum zones and the streamwise energy spectrum in wall-bounded turbulent flows. *J. Fluid Mech.*, 826 (R6), 1–12.

Scarano, F. (2001). Iterative image deformation methods in PIV. *Meas. Sci. Technol.*, 13 (1), R1–R19.

Schlichting, H. and Gersten, K. (1999). *Boundary-Layer Theory*. Springer, 8th revised edition.

Schmid, P. J., Violato, D., and Scarano, F. (2012). Decomposition of time-resolved tomographic piv. *Exp. Fluids*, 52, 1567–1579.

Schultz, M. P. and Flack, K. A. (2007). The rough-wall turbulent boundary layer from the hydraulically smooth to the fully rough regime. *J. Fluid Mech.*, 580, 381–405.

Shah, S. K. and Bou-Zeid, E. (2014). Direct numerical simulations of turbulent Ekman layers with increasing static stability: modifications to the bulk structure and second-order statistics. *J. Fluid Mech.*, 760, 494–539.

Sharma, A. S. and McKeon, B. J. (2013). On coherent structure in wall turbulence. *J. Fluid Mech.*, 728, 196–238.

Sharma, A. S., Moarref, R., and McKeon, B. J. (2017). Scaling and interaction of self-similar modes in models of high Reynolds number wall turbulence. *Phil. Trans. R. Soc. A*, 375, 20160089.

She, Z. S., Jackson, E., and Orszag, S. A. (1990). Intermittent vortex structures in homogeneous isotropic turbulence. *Nature*, 344 (3), 226–228.

She, Z. S. and Leveque, E. (1994). Universal scaling laws in fully developed turbulence. *Phys. Rev. Lett.*, 72 (3), 336–339.

Sillero, J. A., Jiménez, J., and Moser, R. D. (2013). One-point statistics for turbulent wall-bounded flows at Reynolds numbers up to $\delta^+ \approx 2000$. *Phys. Fluids*, 25, 105102.

da Silva, C. B., Hunt, J. C. R., Eames, I., and Westerweel, J. (2014). Interfacial layers between regions of different turbulence intensity. *Annu. Rev. Fluid Mech.*, 46, 567–590.

da Silva, C. B. and Taveira, R. (2010). The thickness of the turbulent/nonturbulent interface is equal to the radius of the large vorticity structures near the edge of the shear layer. *Phys. Fluids*, 22 (12), 021702.

de Silva, C. M., Gnanamanickam, E. P., Atkinson, C., Buchmann, N. A., Hutchins, N., Soria, J., and Marusic, I. (2014). High spatial range velocity measurements in a high Reynolds number turbulent boundary layer. *Phys. Fluids*, 26, 025117.

de Silva, C. M., Hutchins, N., and Marusic, I. (2016). Uniform momentum zones in turbulent boundary layers. *J. Fluid Mech.*, 786, 309–331.

de Silva, C. M., Marusic, I., Woodcock, J. D., and Meneveau, C. (2015). Scaling of second- and higher-order structure functions in turbulent boundary layers. *J. Fluid Mech.*, 769, 654–686.

de Silva, C. M., Philip, J., Chauhan, K., Menevau, C., and Marusic, I. (2013). Multiscale geometry and scaling of the turbulent-nonturbulent interface in high Reynolds number boundary layers. *Phys. Rev. Lett.*, 111, 044501.

de Silva, C. M., Philip, J., Hutchins, N., and Marusic, I. (2017). Interfaces of uniform momentum zones in turbulent boundary layers. *J. Fluid Mech.*, 820, 451–478.

Simiu, E. and Yeo, D. H. (2019). *Wind Effects on Structures: Modern Structural Design for Wind*. Wiley-Blackwell, 4th edition.

Smith, C. R. (1984). A synthesized model of the near-wall behavior in turbulent boundary layers. In *Proc. 8th Smyp. Turbul.*

Smits, A. J., McKeon, B. J., and Marusic, I. (2011). High-Reynolds number wall turbulence. *Annu. Rev. Fluid Mech.*, 43 (1), 353–375.

Spalart, P. R. (1986). Direct simulation of a turbulent boundary layer up to Re_θ=1410. Tech. Memo. 89407, NASA.

Squire, D. (2017). *The structure and scaling of rough-wall turbulent boundary layers*. PhD thesis, University of Melbourne.

Squire, D. T., Morrill-Winter, C., Hutchins, N., Marusic, I., Schultz, M. P., and Klewicki, J. C. (2016a). Smooth- and rough-wall boundary layer structure from high spatial range particle image velocimetry. *Phys. Rev. Fluids*, 1 (6), 064402.

Squire, D. T., Morrill-Winter, C., Hutchins, N., Schultz, M. P., Klewicki, J. C., and Marusic, I. (2016b). Comparison of turbulent boundary layers over smooth and rough surfaces up to high Reynolds numbers. *J. Fluid Mech.*, 795, 210–240.

Sreenivasan, K. R. (1991). Fractals and multifractals in fluid turbulence. *Annu. Rev. Fluid Mech.*, 23, 539–600.

Sreenivasan, K. R. and Antonia, R. A. (1997). The phenomenology of small-scale turbulence. *Annu. Rev. Fluid Mech.*, 29, 435–472.

Sreenivasan, K. R., Prabhu, A., and Narasimha, R. (1983). Zero-crossings in turbulent signals. *J. Fluid Mech.*, 137, 251–272.

Sreenivasan, K. R., Ramshankar, R., and Meneveau, C. (1989). Mixing, entrainment and fractal dimensions of surfaces in turbulent flows. *Proc. R. Soc. A*, 421, 79–108.

Stevens, R. and Meneveau, C. (2017). Flow structure and turbulence in wind farms. *Annu. Rev. Fluid Mech.*, 49 (1), 311–339.

Stokes, G. G. (1845). On the theories of the internal friction of fluids in motion and of the equilibrium and motion of elastic solids. *Trans. Cambridge Phil. Soc.*, 8, 287–305.

Stokes, G. G. (1851). On the effect of the internal friction of fluids on the motion of pendulums. *Trans. Cambridge Phil. Soc.*, 9, 8–106.

Stuart, J. T. (1965). The production of intense shear layers by vortex stretching and convection. Report No. 514, AGARD.

Stull, R. B. (1988). *An Introduction to Boundary Layer Meteorology*. Kluwer Academic Publishers.

Sullivan, P. P., Weil, J. C., Patton, E. G., Jonker, H. J. J., and Mironov, D. V. (2016). Turbulent winds and temperature fronts in large-eddy simulations of the stable atmospheric boundary layer. *J. Atmos. Sci.*, 73 (4), 1815–1840.

Sutton, O. G. (1953). *Micrometeorology*. McGraw-Hill.

Tanahashi, M., Kang, S. J., Miyamoto, T., Shiokawa, S., and Miyauchi, T. (2004). Scaling law of fine scale eddies in turbulent channel flows up to $Re_\tau{=}800$. *Int. J. Heat Fluid Flow*, 25 (3), 331–340.

Tani, I. (1977). History of boundary-layer theory. *Annu. Rev. Fluid Mech.*, 6, 87–111.

Taylor, G. I. (1935). Statistical theory of turbulence: Parts I-III. *Proc. R. Soc. A*, 151 (873), 421–464.

Taylor, G. I. (1937). The statistical theory of isotropic turbulence. *J. Aeronaut. Sci.*, 4 (8), 311–315.

Taylor, G. I. (1938). Production and dissipation of vorticity in a turbulent fluid. *Proc. R. Soc. A*, 164 (916), 15–23.

Tchen, C. M. (1953). On the spectrum of energy in turbulent shear flow. *J. Res. Natl. Bur. Stand.*, 50 (1), 51–62.

Tennekes, H. and Lumley, J. L. (1972). *A First Course in Turbulence*. The MIT Press, 1st edition.

Theodorsen, T. (1952). Mechanism of turbulence. In *Proc. 2nd Midwestern Conf. Fluid Mech.* Ohio State University.

Thompson, G., Field, P. R., Rasmussen, R. M., and Hall, W. D. (2008). Explicit forecasts of winter precipitation using an improved bulk microphysics scheme. part ii: Implementation of a new snow parameterization. *Mon. Weath. Rev.*, 136 (12), 5095–5115.

Thorpe, S. A. (2005). *The Turbulent Ocean*. Cambridge University Press.

Tieleman, H. W. (2008). Strong wind observations in the atmospheric surface layer. *J. Wind Eng. Ind. Aerod.*, 96 (1), 41–77.

Toloui, M., Riley, S., Hong, J., Howard, K. B., Chamorro, L. P., Guala, M., and Tucker, J. (2014). Measurement of atmospheric boundary layer based on super-large-scale particle image velocimetry using natural snowfall. *Exp. Fluids*, 55 (5), 1737.

Tomkins, C. D. and Adrian, R. J. (2003). Spanwise structure and scale growth in turbulent boundary layers. *J. Fluid Mech.*, 490, 37–74.

Townsend, A. A. (1961). Equilibrium layers and wall turbulence. *J. Fluid Mech.*, 11 (1), 97–120.

Townsend, A. A. (1976). *The Structure of Turbulent Shear Flow*. Cambridge University Press, 2nd edition.

Träumner, K., Damian, T., Stawiarski, C., and Wieser, A. (2015). Turbulent structures and coherence in the atmospheric surface layer. *Boundary-Layer Meteorol.*, 154, 1–25.

Tsinober, A. (2001). *An Informal Introduction to Turbulence*. Springer Netherlands.

Vanderwel, C. and Tavoularis, S. (2011). Coherent structures in uniformly sheared turbulent flow. *J. Fluid Mech.*, 689, 434–464.

Vincent, A. and Meneguzzi, M. (1994). The dynamics of vorticity tubes in homogeneous turbulence. *J. Fluid Mech.*, 258, 245–254.

Vogel, A. and Lauterborn, W. (1988). Time resolved particle image velocimetry. *Opt. Lasers Eng.*, 9 (3-4), 277–294.

Volino, R. J., Schultz, M. P., and Flack, K. A. (2007). Turbulence structure in rough- and smooth-wall boundary layers. *J. Fluid Mech.*, 592, 263–293.

Wallace, J. M. (2016). Quadrant analysis in turbulence research: History and evolution. *Annu. Rev. Fluid Mech.*, 48, 131–158.

Wallace, J. M., Eckelmann, H., and Brodkey, R. S. (1972). The wall region in turbulent shear flow. *J. Fluid Mech.*, 54 (1), 39–48.

Wang, G. and Zheng, X. (2016). Very large scale motions in the atmospheric surface layer: a field investigation. *J. Fluid Mech.*, 802, 464–489.

Warhaft, Z. (2009). Why we need experiments at high Reynolds numbers. *Fluid Dyn. Res.*, 41, 021401.

Wei, L., Elsinga, G. E., Brethouwer, G., Schlatter, P., and Johansson, A. V. (2014). Universality and scaling phenomenology of small-scale turbulence in wall-bounded flows. *Phys. Fluids*, 26 (3), 035107.

Wei, T., Fife, P., Klewicki, J. C., and McMurtry, P. (2005). Properties of the mean momentum balance in turbulent boundary layer, pipe and channel flows. *J. Fluid Mech.*, 522, 303–327.

Westerweel, J. (1997). Fundamentals of digital particle image velocimetry. *Meas. Sci. Technol.*, 8 (12), 1379–1392.

Westerweel, J. and Scarano, F. (2005). Universal outlier detection for PIV data. *Exp. Fluids*, 39 (6), 1096–1100.

Wilczak, J. M. and Tillman, J. E. (1980). The three-dimensional structure of convection in the atmospheric surface layer. *J. Atmos. Sci.*, 37, 2424–2443.

Williams, O. J. H., Shoo, D., Baumgartner, M. L., and Smits, A. J. (2018). Experiments on the structure and scaling of hypersonic turbulent boundary layers. *J. Fluid Mech.*, 834, 237–270.

Woodcock, J. D. and Marusic, I. (2015). The statistical behaviour of attached eddies. *Phys. Fluids*, 27 (1), 015104.

Wu, X. and Moin, P. (2009). Direct numerical simulation of turbulence in a nominally zero-pressure-gradient flat-plate boundary layer. *J. Fluid Mech.*, 650, 5–41.

Wu, Y. and Christensen, K. T. (2006). Population trends of spanwise vortices in wall turbulence. *J. Fluid Mech.*, 568, 55–76.

Zhou, J., Adrian, R. J., Balachandar, S., and Kendall, T. M. (1999). Mechanisms for generating coherent packets of hairpin vortices in channel flow. *J. Fluid Mech.*, 387, 353–396.